Cold gas in distant galaxies

Boogaard, L.A.

Citation

Boogaard, L. A. (2021, February 25). *Cold gas in distant galaxies*. Retrieved from https://hdl.handle.net/1887/3147175

Version: Publisher's Version

License: Licence agreement concerning inclusion of doctoral thesis in the Institutional Repository of the University of Leiden

Downloaded from: https://hdl.handle.net/1887/3147175

Note: To cite this publication please use the final published version (if applicable).

Cover Page

Universiteit Leiden

Leiden University Repository

The handle http://hdl.handle.net/1887/3147175 holds various files of this Leiden University dissertation.

Author: Boogaard, L.A.
Title: Cold gas in distant galaxies
Issue date: 2021-02-25

Cold gas in distant galaxies

Cold gas in distant galaxies

Koud gas in verre sterrenstelsels

Proefschrift

ter verkrijging van
de graad van Doctor aan de Universiteit Leiden,
op gezag van Rector Magnificus prof. dr. ir. H. Bijl,
volgens besluit van het College voor Promoties
te verdedigen op donderdag 25 februari 2021
klokke 16.15 uur

door

Lein Adriaan Boogaard

geboren te Oegstgeest
in 1992

Promotor:	Prof. dr. P. P. van der Werf	
Co-promotor:	Dr. R. J. Bouwens	
Promotiecommissie:	Prof. dr. H. J. A. Röttgering	
	Prof. dr. J. Schaye	
	Prof. dr. S. Viti	
	Dr. J. A. Hodge	
	Dr. J. Brinchmann	Universidade do Porto (Portugal)
	Dr. F. Walter	MPIA, Heidelberg (Germany)
	Prof. dr. I. R. Smail	Durham University (UK)

Voor mijn ouders

&

Voor Elisabeth

Copyright © 2021 L. A. Boogaard

Printed by: Gildeprint

Cover design: Arjen Wiersma

Cover images: The Hubble Ultra Deep Field, *credit: NASA, ESA, and S. Beckwith (STScI) and the HUDF Team (front)*, and a 3D rendering of the ALMA Spectroscopic Survey of the HUDF 3 mm datacube *(back)*.

An electronic copy of this thesis can be found at https://openaccess.leidenuniv.nl

ISBN 978 94 6419 120 2

Contents

1 **Introduction** 1

1.1 From effect to cause 2
1.2 The theory 4
1.2.1 Cosmology, galaxy formation and the baryon cycle 4
1.2.2 Star formation and the cold interstellar medium 6
1.2.3 The light from galaxies across the electromagnetic spectrum 11
1.3 The instruments 12
1.3.1 Multi Unit Spectroscopic Explorer (MUSE) 13
1.3.2 Atacama Large Millimeter Array (ALMA) 13
1.3.3 Other facilities 13
1.4 The state of the art 14
1.4.1 Star formation in galaxies across cosmic time 14
1.4.2 Molecular gas in distant galaxies 15
1.4.3 The need for molecular deep fields 17
1.5 The ALMA Spectroscopic Survey of the HUDF 18
1.5.1 Motivation 18
1.5.2 Observing strategy 19
1.5.3 Data products: two cubes and two images 19
1.6 The thesis 23
1.6.1 This thesis 23
1.6.2 Related science with ASPECS 25
1.7 The future 26
1.7.1 The cosmic baryon cycle 26
1.7.2 Science and facilities 27

2 **Constraining the low-mass end of the M_*–SFR relation at $z < 1$** 29

2.1 Introduction 30
2.2 Observations and methods 32
2.2.1 Observations, data reduction, and spectral line fitting 33
2.2.2 Sample selection 34
2.2.3 Stellar masses 37
2.2.4 Star formation rates 38

2.3 Consistency of SFR indicators 39
2.4 Bayesian model 42
  2.4.1 Definition 42
  2.4.2 Execution 44
  2.4.3 Model and data limitations 45
2.5 Star formation sequence 45
  2.5.1 Global sample 45
  2.5.2 Low-mass sample ($\log M_*[M_\odot] < 9.5$) 49
  2.5.3 The effect of redshift bins (2D) 49
2.6 Discussion 51
  2.6.1 Comparison with the literature 51
  2.6.2 The MS slope — a quantitative comparison to models 55
  2.6.3 Implications of a shallow slope 57
2.7 Summary and conclusions 58
Appendix 2.A Simulations 60
  2.A.1 Selection function and completeness 60
  2.A.2 Transformation 61

3 The nature and physical properties of gas-mass selected galaxies 65
3.1 Introduction 66
3.2 Observations 67
  3.2.1 ALMA Spectroscopic Survey 67
  3.2.2 MUSE HUDF Survey 68
  3.2.3 Multi-wavelength data (UV–radio) and MAGPHYS 70
  3.2.4 X-ray photometry 71
3.3 The ASPECS-LP sample 72
  3.3.1 Identification of the line search sample 72
  3.3.2 Additional sources with MUSE redshift priors at $z < 2.9$ 75
  3.3.3 Full sample redshift distribution 78
3.4 Physical properties 79
  3.4.1 Star formation rates from MAGPHYS and [O II] 79
  3.4.2 Metallicities 81
  3.4.3 Molecular gas properties 81
3.5 Results: Global sample properties 83
  3.5.1 Stellar mass and SFR distributions 83
  3.5.2 AGN fraction 85
  3.5.3 Obscured and unobscured star formation rates 85
  3.5.4 Metallicities at $1.0 < z < 1.42$ 86
3.6 Discussion 87
  3.6.1 Sensitivity limit to molecular gas reservoirs 87
  3.6.2 Molecular gas across the galaxy main sequence 89
  3.6.3 Evolution of molecular gas content in galaxies 92
3.7 Summary 93
Appendix 3.A Source description and redshift identifications 95

Appendix 3.B MAGPHYS fits for all CO-detected galaxies 104

4 CO excitation, [C I] and ISM conditions in galaxies at $z = 1 - 3$ 105
4.1 Introduction 106
4.2 Observations and ancillary data 108
4.2.1 ALMA Spectroscopic Survey Data Reduction 108
4.2.2 ASPECS Sample 110
4.2.3 Very Large Array Observations (VLASPECS) 111
4.2.4 Multi-wavelength data and SED fitting 112
4.3 Methods 112
4.3.1 Spectral line analysis 112
4.3.2 Deriving line luminosities and molecular gas masses 115
4.4 Results 115
4.4.1 Observed emission lines from CO and [C I] 115
4.5 CO excitation 117
4.5.1 Individual sources 117
4.5.2 Stacked line fluxes 120
4.5.3 LVG modeling 122
4.5.4 Dust-continuum versus low-J CO 125
4.6 Atomic carbon 129
4.6.1 Atomic carbon abundances 129
4.6.2 PDR modeling 132
4.7 Discussion 134
4.7.1 Modest excitation in mid-J lines at $z = 1.0 - 1.6$ 134
4.7.2 Increasing excitation with redshift 136
4.7.3 The low-J excitation 138
4.7.4 Broader implications of the flux-limited survey 140
4.7.5 Implications for the cosmic molecular gas density 140
4.8 Summary and Conclusions 141
Appendix 4.A Similar widths for the low-J and high-J CO lines 143
Appendix 4.B Spectral line fits 144

5 Line-luminosity functions and the cosmic density of molecular gas 153
5.1 Introduction 154
5.2 Observations 156
5.2.1 ALMA data 156
5.2.2 Ancillary data 158
5.3 Analysis and Results 158
5.3.1 Line search at 1.2 mm 158
5.3.2 Line fluxes 160
5.3.3 Line identification and redshifts 160
5.3.4 Line luminosities and molecular gas masses 163
5.3.5 Luminosity functions and ρ_{H_2} 166
5.4 Discussion 166

5.4.1 CO luminosity functions 166
5.4.2 [C I] and [C II] luminosity functions 169
5.4.3 ρ_{H_2} vs redshift 170
5.5 Conclusions 172
Appendix 5.A Tabulated luminosity functions 173
Appendix 5.B Cosmic variance 175
Appendix 5.C Identification of line candidates without near-infrared counterparts 178

6 The average molecular gas content of star-forming galaxies at $z = 3 - 4$ 181
6.1 Introduction 182
6.2 Observations and sample selection 183
6.2.1 Parent sample selection and physical properties 183
6.2.2 Measurement of systemic redshifts 185
6.2.3 Final systemic redshift sample 188
6.3 Results 190
6.3.1 Velocity offsets 190
6.3.2 ALMA Stacking 191
6.4 Discussion 194
6.4.1 Molecular gas masses 194
6.4.2 Low metallicity driving a high molecular gas mass-to-light ratio . . 196
6.4.3 Contribution to the cosmic molecular gas density 201
6.4.4 Implications for observing cold gas in low metallicity galaxies at high redshift 201
6.5 Summary and conclusions 203
Appendix 6.A Table 205
Appendix 6.B Spectra 208

Bibliography 211

Publication list 221

Nederlandse samenvatting 227

Curriculum Vitae 233

Acknowledgements 235

1 | Introduction

Abstract

The formation and evolution of galaxies is fundamentally driven by the formation of new stars out of cold gas. Observations of young stars in distant galaxies in the early universe, such as we can see in the *Hubble* Ultra Deep Field, have unveiled how the cosmic star formation rate density evolves. Yet, while the *effect* of star formation—the young stars—has been mapped in ever-increasing detail, the *cause*—the cold molecular gas that fuels star formation—has been elusive. This thesis presents an observational study of the cold interstellar medium of distant galaxies in the early universe, using the most sensitive submillimeter telescope to date, the *Atacama Large Millimeter Array*, together with new integral-field spectrographs, such as the *Multi Unit Spectroscopic Explorer* on the *Very Large Telescope*. It unveils the physical properties of star-forming galaxies and their molecular gas reservoirs, and describes the evolution of the cosmic molecular gas density—*the fuel for star formation*.

1.1 From effect to cause

Since the discovery that our home galaxy, the Milky Way, and other galaxies are separate islands of stars in the universe, and their earliest classifications into spirals and ellipticals (Hubble, 1926), it has become clear that galaxies can be broadly subdivided into two categories: galaxies with large amounts of gas, and galaxies with little gas. The gas-rich galaxies often appear disk-like or irregular, with lanes of dust obscuring their starlight, hosting young and blue stars, and are actively *star-forming*. The gas-poor galaxies host older and redder stellar populations and appear as *quiescent* spheroids of stars. One of the primary goals of modern day astronomy is to explain how this beautifully varied galaxy population has formed and evolved over time.

The gas and dust that fills the space between the stars is aptly described as the *interstellar medium* (ISM). The gas consists mostly of hydrogen and helium, that is enriched with heavier elements formed by nuclear fusion in the centres of stars. It can cool, or be heated by the stars and the supermassive black hole that lies at the centre of most galaxies, and cycle through different phases where it is in equilibrium: the molecular medium (H_2), the neutral medium (H I), and the ionised medium (H II). Galaxies grow through the formation of new stars, which are born in the cold and dense molecular gas, as it collapses under the influence of gravity. Evidently, a central role in the process of galaxy formation and evolution is played by the cold molecular gas, *the fuel for star formation*.

The processes involved in the formation and evolution of a single galaxy take millions or even billions of years and therefore cannot be observed directly by humankind. Instead, the evolution of galaxies is studied by observing the population at different epochs in the past, tracing the evolution of galaxies through time in a statistical manner. This is possible because light emitted by more distant galaxies takes a longer time to reach our telescopes, because it cannot travel faster than the finite speed of light.[1] The distant galaxies we see today therefore appear to us the way they were when the universe was much younger. The fabric of space and time itself is not static either. It is distorted by the objects that reside within it (gravity; as described by the theory of general relativity) and expands at an accelerating rate. The expansion of the universe shifts the wavelength of a photon that travels towards an observer by a factor $1 + z$, where z is called the *redshift*.[2] The redshift of distant galaxies is therefore a measurement of their distance and the age of the universe at the time of emission.

Arguably the most beautiful and distant views into the past have been obtained by the *Hubble Space Telescope*, through its deep field campaigns in northern, southern and equatorial regions of the sky (Williams et al., 1996; Casertano et al., 2000; Beckwith et al., 2006). The *Hubble* Ultra Deep Field (HUDF), shown in Figure 1.1, is the latest installment and reveals a universe that is filled with galaxies. The most distant galaxies in this image emitted their light when the universe was only a few hundred million years old. They reveal a past galaxy

---

[1] 299 792 458 $\mathrm{m\,s^{-1}}$ (BIPM, 2019), denoted by c.

[2] $1 + z = a(t_{\mathrm{obs}})/a(t_{\mathrm{emit}}) = \lambda_{\mathrm{obs}}/\lambda_{\mathrm{emit}}$, where $a(t)$ is the scale factor of the expansion at the cosmic time, t, of emission (emit) and observation (obs). The name redshift originates from the fact that, for a distant source, the observed wavelength, λ_{obs}, is greater than the emitted wavelength, λ_{emit}, and the light therefore appears redder. The relation holds inversely for frequencies, $\nu = c/\lambda$. Note the present day universe corresponds to $z = 0$, whereas higher redshifts refer to progressively earlier times in cosmic history, in a non-linear fashion.

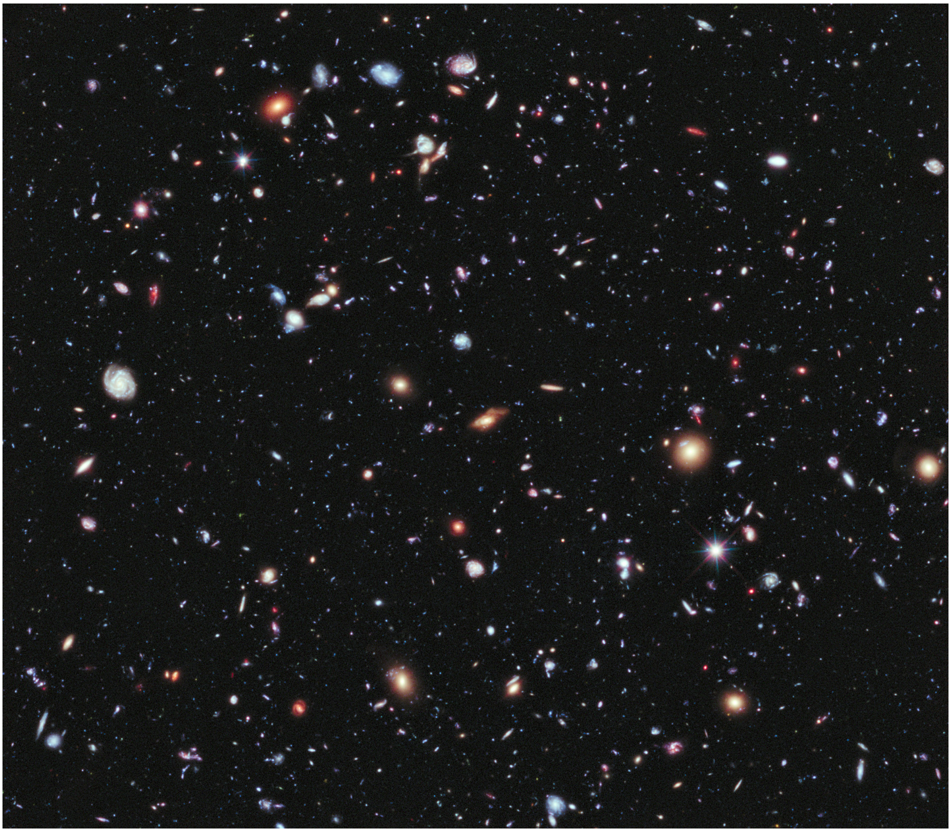

Figure 1.1: A zoom-in on the *Hubble* Ultra Deep Field (HUDF). There are more than 5000 galaxies visible in the image. Some galaxies are so far away that their light, seen in this image, was emitted only a few hundred million years after the big bang. The width of the image on sky is about the same as that of a tennis ball seen across a football field. *Technical details: North points 50° counterclockwise from the top and the image extends* $2\overset{\prime}{.}3 \times 2\overset{\prime}{.}0$ *on sky. The total exposure time is about 22.5 days (2 million seconds); see Illingworth et al. (2013). The observations in different filters are combined to an RGB image as follows. Blue: F435W + F606W; Green: F775W + F814W + F850LP; Red: F105W + F125W + F160W. Credit: NASA, ESA, G. Illingworth, D. Magee, P. Oesch, R. Bouwens, and the HUDF09 Team.*

population that looks both remarkably similar and very different from the one we see today. The light seen by *Hubble* has been emitted by the stars and hot gas in distant galaxies, and can be used to trace the formation of new stars and the build-up of their stellar content over cosmic time. These images also testify to the common assumption in cosmology that the universe is spatially homogeneous and isotropic,[3] which allows us to make inferences about galaxy evolution.

---

[3] While the individual galaxies are different in each image, the universe, when averaged over large enough volumes, looks the essentially same in all directions and earth is in no special place (that is, in a spatial sense; temporally speaking, it is a interesting fact that humankind exists on earth at this specific cosmic time).

Surveys across the electromagnetic spectrum and large computer simulations have greatly advanced our understanding of the formation and evolution of the galaxy population throughout cosmic time. A fundamental aspect of galaxy formation and evolution is to understand where, when and how the stars in galaxies have formed. The *effect* of star formation, the rate at which galaxies form new stars and the build-up of their stellar mass, has been mapped in distant galaxies in ever-increasing detail. In contrast, our knowledge of the *cause*, the cold gas that fuels the star formation, has remained limited, as it difficult to measure in distant galaxies. This has now changed, through advances that have been made in astronomical instrumentation in the last decade. In this thesis, we use these novel instruments to study of the cold gas in distant galaxies, and its implication for our understanding of galaxy formation.

The questions that are central to this thesis are: How does the cold molecular interstellar medium of galaxies evolve over cosmic time, in relation to their star-forming properties, and how does this dictate their evolution? How do galaxies cycle gaseous material in and out of their interstellar medium, driving their evolution over cosmic time?

1.2 The theory

Galaxy formation and evolution is a complex phenomenon that involves processes operating over a vast range of scales in both space and time. On one hand, the formation of stars itself takes place deep inside the cold ISM of galaxies, on scales that are much smaller than the size of a single galaxy. On the other hand, it relies on the potential of fueling star formation over time, through the accretion and cooling of gas from large distances, on scales much larger the size of a single galaxy. The formation and evolution of a galaxy therefore cannot be viewed independently from its place in the universe and the cosmological context in which it evolves.

1.2.1 Cosmology, galaxy formation and the baryon cycle

The current best description of the content of the universe is contained in what is called the concordance model of cosmology; the Λ cold dark matter (ΛCDM) paradigm. Here Λ is the cosmological constant originally defined by Einstein (1917), that describes the accelerated expansion of the universe (Riess et al., 1998; Perlmutter et al., 1999). We observe the universe through the light emitted by the ordinary baryonic[4] matter, which can interact with electromagnetic radiation. However, the baryonic matter alone is insufficient to explain the gravity of, for example, (clusters of) galaxies. This has lead to the postulation of *dark matter* (that does not, or extremely weakly, interact via electromagnetic radiation), which has been a very successful paradigm to explain the dynamic nature of the anomalous gravity in the universe. According to recent measurements, the universe consists of about 5% baryonic matter and 26% dark matter, while the cosmological constant (due to its unknown nature also referred to as *dark energy*) contains around 69% of the total energy density (Planck Collaboration et al.,

---

[4] It is common in cosmology to refer to all visible matter (consisting of protons, neutrons, and electrons) as baryonic, even though the electron is a lepton and not a baryon.

2020). Reversing the cosmological model in time, we infer that the universe is around 13.8 billion years old and started hot and dense in what is known as the *big bang*.

The process of galaxy formation can be traced back to the *Cosmic Microwave Background* (CMB). This afterglow of the hot and dense gas in the early universe, that decoupled once the gas became neutral, still permeates the present day universe (Penzias & Wilson, 1965). Minute variations in the temperature of the CMB are believed to reflect small density fluctuations in the otherwise homogeneous and isotropic gas in the early universe, and as such the initial conditions for galaxy formation. The composition of this primordial gas is set by the nucleosynthesis of elements that occurred after the big bang and almost exclusively consists of hydrogen ($\approx$ 75%) and helium-4 ($\approx$ 25%), with traces of heavier elements at the $\leq 0.1\%$ level (e.g., Schramm & Turner, 1998). This epoch where the universe is filled with neutral gas is referred to as the *dark ages* and lasts until the escaping ionising radiation from the first galaxies initiates a global phase-transition back to the ionised state, during what is called the *epoch of reionisation*, which ends when the universe is around 1 billion years old (e.g., Barkana & Loeb, 2001; Loeb & Barkana, 2001).

As the universe expands, the matter inside expands with it, while slightly overdense regions are being pulled together by gravity at the same time. When the density in a region exceeds a certain threshold (around 200 times the background density), it collapses. The dark matter cannot cool radiatively and forms what is known as a dark matter halo. The gas can fall into these halos to form the visible parts of a galaxy. Over time, the dark matter halos, and the galaxies that reside within them, can grow hierarchically through merging (White & Rees, 1978; Blumenthal et al., 1984; White & Frenk, 1991). On the largest scales, gravity shapes these overdensities into the large scale filamentary structure of the universe that is known as the *cosmic web*.

In contrast to the dark matter, the baryonic matter inside a halo can further cool radiatively and neutral gas (H I) can settle in the centre of the potential well. This is where the gas can cool even further to feed the central supermassive black hole,[5] or convert into dense clouds of molecular gas (H_2) that can gravitationally collapse to form stars. This process is central to galaxy formation: as long as cold gas can be supplied and collapse to form stars, galaxies can continue to build up their stellar mass.

In their core, stars fuse the primordial elements into all the heavier elements that we are so familiar with on earth, such as carbon, nitrogen, oxygen, and iron. These elements are returned into the ISM through stellar winds or supernova explosions. As such, the ISM enriches in metals and dust over time and subsequent generations of stars that are born out of more metal rich gas have higher *metallicity*,[6] such as our Sun (Asplund et al., 2009). A significant fraction of these elements are locked into solid-phase dust grains, which play an important role in the heating and cooling of the ISM and the formation of molecules.

During various stages of their evolution, stars and black holes can drive out gas through their ionising radiation, winds, supernovae, or by accretion onto the supermassive black hole

---

[5] The formation and (co)evolution of the central supermassive black hole (e.g., Kormendy & Ho, 2013) is another important aspect of galaxy evolution, that we will not focus on here.

[6] In astronomy, all elements more massive than hydrogen and helium (the two elements that together make up $>$ 99% of the cosmic mass budget) are collectively referred to as metals. The mass fraction of these metals in a particular environment is called its metallicity.

(giving rise to an active galactic nucleus; AGN). This *feedback* can suppress or completely halt the gas accretion, blowing gas from the ISM back into the circumgalactic medium, or even out of the halo into the intergalactic medium. These processes may quench the star formation in galaxies temporarily or even permanently. The process where the matter in the universe is heated and cooled and transfers through the various phases (molecular, neutral, ionised, and in-and-out-of stars) both in- and outside galaxies is called the *baryon cycle* (e.g., Tumlinson et al., 2017; Péroux & Howk, 2020). One particularly relevant aspect of the baryon cycle is to understand what fraction of the gas was situated in-and-around galaxies, and available for the formation of stars through cosmic time (e.g., Walter et al., 2020).

It should be mentioned that our understanding of the process of galaxy formation, as outlined above, is greatly aided by numerical simulations on supercomputers. These can compute the evolution of astronomical systems through cosmic time, from single stars and molecular clouds, to galaxies, and even complete universes (including dark and/or baryonic matter). Modern and large cosmological hydrodynamic simulations (e.g., Schaye et al., 2015; Crain et al., 2015; Pillepich et al., 2018; Nelson et al., 2018) include many physical processes and provide an accurate description of a wide range of galaxy properties. Truly *ab initio* cosmological simulations of galaxy formation are still beyond the capabilities of modern computational facilities, however, due to the vast range of spatial scales involved (see Somerville & Davé 2015 and Naab & Ostriker 2017 for recent reviews). They typically rely on subgrid physics to describe the processes that happen below the resolution limit with preset (tunable) parameters, such as star formation (that is, the efficiency with which gas is converted to stars, as they generally do not resolve the cold ISM) and the strength of feedback (e.g., Schaye et al., 2010). A different approach is taken by semi-analytical models, that do not solve the fundamental physical equations at certain resolution, but instead use equations to describe the flow of bulk material between different phases. Studies of the cold ISM in cosmological simulations typically resort to refining the simulated gas into the different cold phases during post-processing of cosmological simulations, or by using semi-analytical models (e.g., Popping et al., 2019). Testing and breaking these (and future) simulations with improved observations is important to forward our understanding of the physical processes involved. Conversely, the predictions from simulations are a valuable tool to understand the limitations and improve the design of observations.

1.2.2 Star formation and the cold interstellar medium

In the Milky Way and other galaxies, star formation takes place inside *Giant Molecular Clouds* (GMCs) of cold ($T = 10 - 50$ K) and dense gas ($n_{\rm H} \geq 10^3$ cm^{-3}) with sizes ranging from a few parsec[7] up to roughly 100 pc (e.g., Solomon et al., 1987; McKee & Ostriker, 2007; Bolatto et al., 2008).[8, 9] These GMCs fragment into clumps and cores and are the birthplace of populations of stars. The detailed physics of this process is a field of study on its own and we will not

---

[7] A parsec (pc) is a measure of distance and equals about 3.262 light years or 30.86 trillion (10^{12}) kilometres.

[8] A possible exception being the first generation of stars.

[9] Giant Molecular Clouds can be part of larger (gravitationally bound) 'complexes' while individual clouds can fragment into 'cores' and 'clumps'. While individual GMCs often have reasonably well-defined boundaries, there is no universal definition of this delineation. These numbers should therefore be taken as indicative, see Draine (2011).

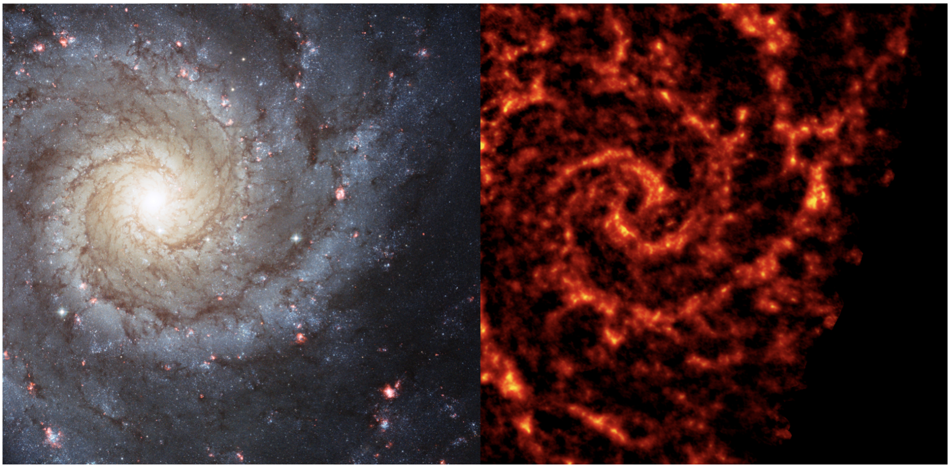

Figure 1.2: The spiral galaxy Messier 74 (NGC 628) lies at distance of about 10 Mpc. The images show a zoom-in of the face of the disk of about 10 kpc on each side. The *Hubble* image (*left*) shows the starlight, that appears bluer in the spiral arms and redder towards the nucleus. Lanes of dust obscuring the starlight appear as filamentary brown structures. The bright red spots show emission from ionised hydrogen in the H II regions around recently formed stars. The ALMA image (*right*) shows the cold molecular gas in giant molecular clouds, as traced by emission from carbon monoxide, at 50 pc resolution. The cold molecular gas is coincident with the dust and the spiral arms where new stars are formed. *Left: Blue: F435W, Green: F555W, Red: F656N (Hα + [N II]) + F814W. Right: Emission from CO* $J = 2 \rightarrow 1$*; the black area towards the bottom right of the panel lacks observations. Credits: NASA, ESA, and the Hubble Heritage Collaboration, R. Chandar and J. Miller (left). ALMA (ESO/NAOJ/NRAO), NRAO/AUI/NSF and the PHANGS collaboration, B. Saxton (right).*

concern ourselves with it here (the interested reader can start exploring in, e.g., McKee & Ostriker, 2007). The reason is that the substructure of GMCs has been (and still is) very difficult to resolve in all but the most nearby galaxies. In the context of galaxy formation and evolution, studies have therefore long focused on linking the surface density of star formation and cold (H I and H_2) gas over larger scales (Schmidt, 1959; Kennicutt, 1998b). More detailed observations now show that the star formation rate correlates with the H_2 density over wide range of surface densities, both in regions where H I is absent or the dominant gas component (e.g., Leroy et al., 2008; Bigiel et al., 2008; Schruba et al., 2011; Leroy et al., 2013), while the denser gas may connect even more strongly (e.g., Gao & Solomon, 2004). This supports the long-standing picture that cold molecular H_2 gas is the fuel for star formation in galaxies (e.g., Young & Scoville, 1991). The right panel of Figure 1.2 shows observations of the cold molecular gas in a nearby galaxy, which reach the scale of individual GMCs ($\approx$ 50 pc; Kreckel et al. 2018), that are now possible with state-of-the-art submillimeter interferometers (§ 1.3.2).

Observations in the local universe show that galaxies globally consume their gas at, to first order, similar timescales (e.g., Leroy et al., 2013). However, there is still quite a diversity throughout the larger galaxy population (e.g., Saintonge et al., 2016, 2017). To what extent the 'laws' that guide star formation are universal, and to what extent they apply to, for example,

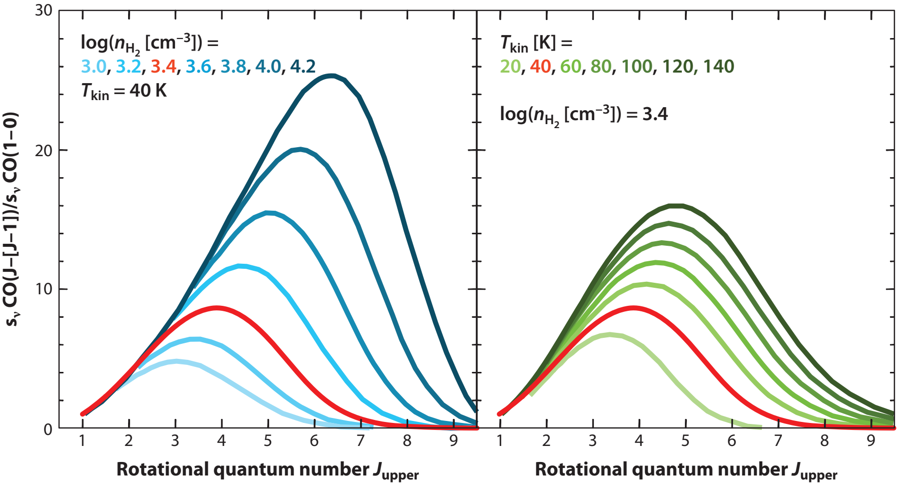

Figure 1.3: Illustration of how the measured CO excitation ladder changes as a function of density and kinetic temperature. *Left:* The effect of changing density at a fixed temperature ($T_{\rm kin} = 40$ K). *Right:* The effect of changing temperature at fixed density ($n_{\rm H_2} = 10^{3.4}$ cm^{-3}). Both panels have been normalised to the CO $J = 1 \rightarrow 0$ transition. High CO excitation is obtained through a combination of high kinetic temperature and high density. *Figure taken from Carilli & Walter (2013).*

starburst galaxies with very high surface densities of gas and star formation, or galaxies with very low metallicities, is a topic of debate (e.g., Kennicutt & Evans, 2012). As the physical conditions in and around galaxies in the distant universe are quite likely different from those in present day galaxies, this raises the question what extent the process of star formation operates in the same fashion, and if not what drives the differences.

Measuring molecular gas

Tracing the mass and distribution of the cold ISM, which consists almost entirely of H_2, is not trivial. Because H_2 is a homonuclear, diatomic molecule, it does not posses a permanent dipole moment with corresponding electric dipole transitions. More importantly, because H_2 is such a low-mass molecule, the lowest energy rotational quadrupole transitions (from the ground state of para- and ortho-H_2) have upper-level energies of $E/k \simeq 510$ K and 1015 K and are not excited inside cold GMCs (and the same is true for the lowest energy vibrational transitions, which require even higher temperatures to excite). As a result, the cold H_2 that makes up most of the ISM is practically invisible in emission (Bolatto et al., 2013).

Trace species must therefore be used to measure the molecular gas mass. The next most abundant element, the helium atom, suffers from similar observability problems as H_2. Fortunately, the cold interstellar medium is also the site where hydrogen and the more abundant elements such as carbon, nitrogen and oxygen, can enter into richer chemistry, forming molecules. Besides molecules, the cold ISM also harbours significant amounts of dust. The dust plays an important role in the chemistry of the ISM, being a catalyst for the formation of H_2, and can be observed in both absorption and emission.

Carbon monoxide is the most abundant molecule in the cold ISM and $^{12}C^{16}O$ (hereafter, CO) is its most abundant isotopologue. In contrast to H_2, the heteronuclear CO molecule has a weak permanent dipole moment and its rotational transitions (denoted by their rotational quantum number J) have a very low excitation temperature. The upper level energy of the first excited state is $E/k = 5.53\,\mathrm{K}$, which is easily excited even in cold molecular clouds. The CO $J = 1 \rightarrow 0$ transition lies at $\nu_0 = 115.27\,\mathrm{GHz}$ (or $\lambda_0 = 2.60\,\mathrm{mm}$) and is easily observable at through a transparent atmospheric window (at $z = 0$). As a result, emission from CO has become the workhorse tracer of molecular gas.

Converting the integrated CO luminosity to a molecular gas mass requires a mass-to-light ratio, known as α_{CO}.[10] The value of α_{CO} is calibrated locally, through independent measurements of the total mass of a molecular cloud from, for example, dust emission or extinction, gamma-ray emission, or the virial theorem (see Bolatto et al., 2013, for a recent review). The value of α_{CO} is dependent on the abundance of CO (related to the metallicity), the density and temperature of the emitting medium, and, because the CO emission is optically thick under most circumstances, the geometry. Even after more than half a century of observations, the value of α_{CO} is an important source of uncertainty in determining gas masses, and knowledge of the physical properties of the system under study are essential to make an informed decision about its value. Averaged over galactic scales, there are average values of α_{CO} that seem to apply within reasonable uncertainties, for certain types of galaxies.

The higher-J rotational transitions of CO (with $J > 1$) are also observable, being relatively closely spaced at J-multiples of ν_0. This excitation 'ladder' of rotational transitions is sensitive to (and can be used to constrain) the density and temperature of the cold ISM, and the radiation field (see Figure 1.3). Conversely, knowledge of the CO excitation is crucial to determine gas masses when only higher-J transitions of CO are observed, in order to convert back to the ground-state transition to which α_{CO} is calibrated. This is particularly common at higher redshifts, as transitions may shift to inaccessible parts of frequency space.

An alternative tracer for the cold gas mass is the thermal continuum emission from dust (e.g., Hildebrand, 1983). The Rayleigh-Jeans tail of the dust blackbody at long-wavelengths is most sensitive to the cold dust grains that contain most of the dust mass (the peak of the dust emission is driven by the temperature of the warm grains, which do not contain most of the mass). Because this tail is optically thin, the emission is directly proportional to the dust mass. Deriving the dust mass requires knowledge of the (mass-weighted) temperature of the cold dust, its composition and size distribution, and the corresponding emissivity as a function of wavelength (e.g., Draine & Li, 2001; Li & Draine, 2001). Furthermore, to convert the dust mass to a gas mass requires knowledge of the gas-to-dust ratio. Because the mass in dust is built up over time (until it reaches an equilibrium between formation and destruction) the gas-to-dust ratio can vary from source to source, and is sensitive to the metallicity of the medium (e.g., Rémy-Ruyer et al., 2014). Again, knowledge of the physical conditions of system under study are key to make justified assumptions, while over galactic scales average values may apply within reasonable uncertainty (e.g. Scoville et al., 2016).

---

[10] Directly related is the well-known conversion factor X_{CO}, that is, the ratio between the (resolved) CO intensity and the hydrogen column density. In this thesis we will exclusively deal with unresolved observations and therefore α_{CO}. The adopted α_{CO} in this work includes a correction factor for the abundance heavy elements, such that the results refer to the total molecular gas mass (not just the mass in H_2).

Other species can also potentially be used to trace (different parts) of molecular clouds. However, their emission lines are generally much fainter than those of CO and therefore difficult, if not impossible, to detect in distant galaxies, even with modern instruments (though see chapter 4 and chapter 6 for notable exceptions).

Measuring star formation

Once a stellar population is formed, the ionising radiation from the young, hot, blue stars disperse the birth cloud and give rise to an H II region of ionised gas. These can been seen as knots of bright red emission in the left panel of Figure 1.2. The interface between the ionised and molecular medium is called a photodissociation region (PDR; Hollenbach & Tielens 1999), where through an ionisation- and photodissociation front the gas transitions smoothly back from the ionised, to the neutral, to the molecular phase. Inside the hot H II regions the ionised hydrogen atoms recombine with their electrons giving rise to recombination radiation (through the Lyman, Balmer, Paschen, Brackett, etc., series). Ionised and neutral species of carbon, nitrogen and oxygen atoms are often observed in emission through their (semi-) forbidden lines (for example, [O II] $\lambda\lambda$3727, 3730, [O III] $\lambda\lambda$4960, 5008) and fine structure lines (for example, [C I] λ370 μm, [C II] λ158 μm, [O III] λ88 μm). While more complex molecules can radiate from the colder phases (like CO). Together, the emission lines that arise in the different phases of the gas can be used as a direct and indirect diagnostic for the physical properties of the gas, such as its density, temperature, and metallicity, as well as the radiation field and the (ionising) sources that give rise to it, such as stars or an AGN (e.g., Osterbrock & Ferland, 2006; Draine, 2011).

The hottest stars emit most of the ionising radiation and are very short lived ($\leq$ 10 Myr). The number of massive stars can therefore be converted to a total number of recently formed stars, under the assumption an initial mass function (IMF), which is the stellar mass distribution of a population of newly formed stars (throughout this thesis, we adopt the IMF from Chabrier 2003). This star formation rate (SFR) can be measured either from the direct ultraviolet (UV) radiation of the young hot stars, or indirectly by the way the it affects the ISM (see, e.g., Kennicutt & Evans, 2012). An example of the latter are the recombination lines from hydrogen, which trace the SFR well because their recombination rate is directly proportional to the ionising flux, with limited sensitivity to the density and temperature (and metallicity) of the H II region.

The presence of dust grains along the line of sight can have a strong attenuating effect on UV and optical radiation, which proves a significant complication when inferring (for example) the SFR, and needs to be corrected for (e.g., Charlot & Fall, 2000). At the same time, the absorption increases the temperature of the dust grains, which re-emit the radiation at longer wavelengths, in the infrared (IR) and (sub)millimeter (e.g., Galliano et al., 2018). The emission from (warm) dust (including polycyclic aromatic hydrocarbons; PAHs, Tielens 2008) can therefore also be used as a tracer of star formation, either directly, or in combination with the UV.

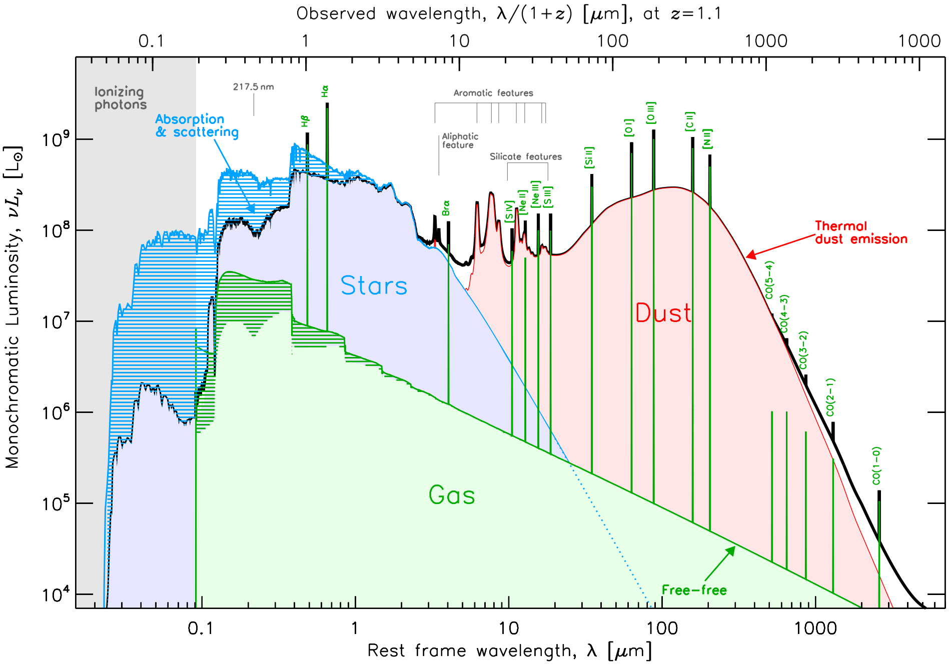

Figure 1.4: An illustration of the spectral energy distribution of a galaxy from the ultraviolet to the millimeter regime. The overall shape (black) is a combination of different components. The emission from stars and gas are show in blue and green, respectively, with the hashed region indicating the fraction of light scattered and absorbed by the dust (which is re-radiated at long-wavelengths). The emission from dust and PAHs (polycyclic aromatic hydrocarbons) is shown in red. Some emission lines from the ionised, neutral and molecular interstellar medium, including several that are relevant to this work, are indicated in green (real galaxies show many more lines that are not shown, for clarity). The top ordinate shows the shift in observed wavelength, for a distant galaxy at $z = 1.1$. *Figure adapted from Galliano et al. (2018), credit: F. Galliano.*

1.2.3 The light from galaxies across the electromagnetic spectrum

A model of the complete *spectral energy distribution* (SED) of a galaxy is shown in Figure 1.4. It emphasises the emission from the stars (at UV, optical and near-IR wavelengths), the emission from the dust (at mid- and far-IR, as well as (sub)millimeter wavelengths), and the emission from the gas (ionised, neutral, and molecular; across the spectrum). The total amount of starlight from galaxies can be modeled to infer the total mass in stars and the techniques to do so have become increasingly sophisticated. Modern approaches aim to describe the overall SED of galaxies across all wavelengths, by modeling the birth and evolution of individual populations of stars over time, including the chemical evolution, and the reprocessing of the light by dust (e.g., Conroy 2013, in some cases also including other phases, such as the ionised gas and associated emission lines). Observations of the colours of galaxies (as measured with broad-band filters with cameras on telescopes, like *Hubble*, cf. Figure 1.1), can be sufficient

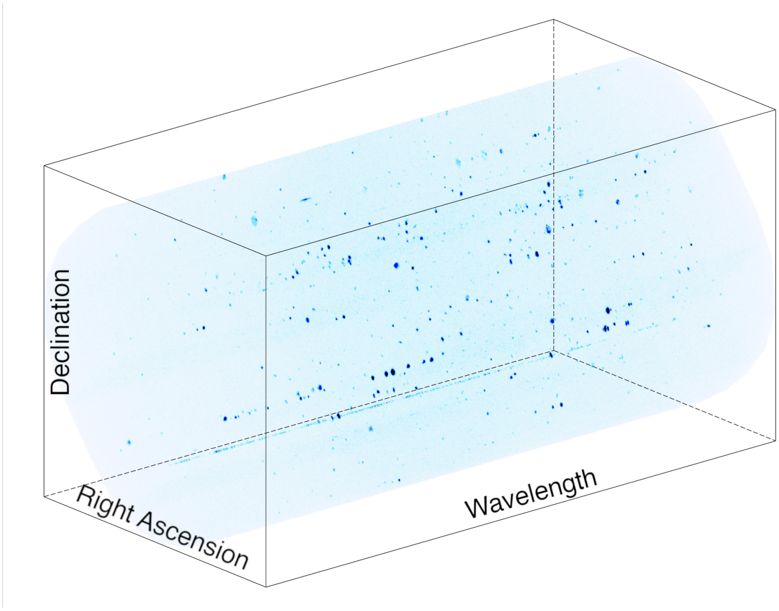

Figure 1.5: Three-dimensional rendering of (part of) the MUSE *Hubble* Ultra Deep Field Survey signal-to-noise cube, that corresponds to the ASPECS field. The (starlight) continuum emission has been subtracted so that the bright emission lines from the hot gas in galaxies are clearly visible as bright spots in the cube. *The rendition uses the 10 h data (Bacon et al., 2017) and spans about 2.′5 in the spatial directions, covering the full wavelength range of MUSE.*

to constrain the overall shape of the SED, from which the total mass in old and young stars can be inferred to within reasonable accuracy. To measure the molecular gas masses and star formation rates from the emission lines (§ 1.2.2), however, requires spectroscopic instruments that break up the light with sufficient resolution, ideally for large numbers of galaxies simultaneously.

1.3 The instruments

Observational astronomy is driven by the development of new telescopes and instruments that improve and expand our view of the sky. Two facilities stand out as being essential to the work presented here and are described in detail below. While both are very different (from a technical point of view) they achieve the same result, that is: to provide spectroscopy for all galaxies within the field of view simultaneously, enabling the study of their properties without any *a priori* target selection. In addition to these two instruments, the work builds on observations of the HUDF taken with a range of instruments, many ground-breaking at the time they became available (and some still are).

1.3.1 Multi Unit Spectroscopic Explorer (MUSE)

The *Multi Unit Spectroscopic Explorer* (MUSE) instrument was installed in 2014 at the Very Large Telescope (VLT) at the European Southern Observatory (ESO) in Paranal, Chile (Bacon et al., 2010; Bacon et al., 2014). MUSE is an optical (4750 – 9300Å), integral-field spectrograph with a square arcminute field of view. It takes an image, but splits the light into a spectrum at every pixel, such that an observation results in a datacube of the sky with wavelength as the third dimension. An example of a MUSE datacube can be seen in Figure 1.5. When observing a deep field with MUSE, the resulting datacube provides a spectrum for every galaxy in the field, that can be used to measure its redshift and infer different physical properties (depending on the redshift).

The HUDF has been extensively observed with MUSE during the Guaranteed Time Observations. The observations consists of a mosaic of 10 h exposures with covering the full field and a single, 30 h exposure in the central region of the field, both taken as part of the MUSE HUDF Survey (Bacon et al., 2017), as well as an ultra-deep series of exposures reaching a total depth of 140 h called the MUSE eXtreme Deep Field (MXDF; R. Bacon, et al., *in prep.*). In total, the MUSE observations provide spectroscopic redshifts for over 10× more galaxies than all previous spectroscopic surveys measured together, which will prove to be essential for the work in this thesis.

1.3.2 Atacama Large Millimeter Array (ALMA)

The *Atacama Large Millimeter/submillimeter Array* (ALMA) started its operations in 2011 and is currently the largest (sub-)millimeter telescope in the world (Wootten & Thompson, 2009). It is a radio-interferometer, consisting of 66 individual antennae operating in different bands that cover the transparent windows in the atmosphere between 84 and 950 GHz (extending down to 35 GHz, once complete). The antennae can be moved around in a variable configuration, from compact (160 m) to extended (16 km), to provide a range from sensitive low-resolution images, to extremely high resolution images. ALMA is the most sensitive telescope to detect emission from in particular the gas and dust in the cold and warm interstellar medium. It is now revolutionising observations of the cold ISM in all facets of astronomy, from the inside of protoplanetary disks around newly forming stars, to the evolution of the cosmic cold molecular gas content of galaxies. The ALMA observations of the HUDF studied in this thesis are presented in § 1.5.

1.3.3 Other facilities

Besides MUSE and ALMA, this thesis builds on the work done by the *Hubble Space Telescope* and other observatories on earth and in space, such as *Chandra* in the X-rays, and *Spitzer* and *Herschel* in the near- and far-IR. The rest-frame optical wavelength regime shifts to the near-IR for galaxies at higher redshift. For the last chapter, we therefore obtained rest-frame optical spectroscopy taken with the *K-band Multi Object Spectrograph* (KMOS) at the VLT and the *Multi-Object Spectrometer For Infra-Red Exploration* (MOSFIRE) at the Keck Observatory on Hawai'i. Taken together, all these instruments provide unprecedented constraints on the

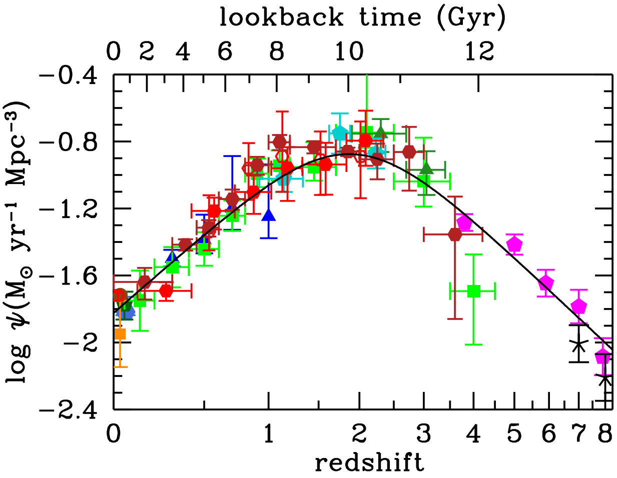

Figure 1.6: The cosmic star formation rate density (SFRD, ψ; per comoving volume) as a function of redshift and lookback time (shown on the bottom and top abscissa, respectively). The coloured points show measurements from different surveys and the solid line shows the best-fit. The SFRD increases with time up to a broad peak roughly 10 billion years ago, followed by a factor ≈ 8 decrease towards the present day. *Figure taken from Madau & Dickinson (2014).*

SED of distant galaxies in the HUDF and work towards an integrated view of their physical properties.

1.4 The state of the art

1.4.1 Star formation in galaxies across cosmic time

Observations of star-forming galaxies have revealed how the cosmic star formation rate density (SFRD) evolves with time in increasing detail (e.g., Lilly et al., 1996; Madau et al., 1996; Hopkins & Beacom, 2006; Madau & Dickinson, 2014), out to when universe was only a few hundred million years old (e.g., Bouwens et al., 2015). The SFRD is shown in Figure 1.6. From the formation of the first galaxies at *cosmic dawn*, the SFRD of the universe has increased with time, up to a broad peak around 10 billion years ago (between redshift $1-3$), often referred to as *cosmic noon*. Since then, it has declined by a factor ≈ 8 towards the present day. The detailed evolution of the SFRD beyond the peak (towards the earliest times) is uncertain, however, in particular because of the difficulty in constraining the amount of dust-obscured star formation (e.g., Casey et al., 2018; Bouwens et al., 2020). Explaining what drives the drives the evolution in the average star formation rate of galaxies is one of the defining features of a successful theory of galaxy formation. In theoretical work, using large computer simulations, the increase at high redshift is limited by the build-up of dark matter halos, while the subsequent evolution is driven by the balance between in- and outflows of gas and star formation (e.g., Schaye et al., 2010) and the effectiveness of each of these processes as a function of the halo mass (e.g. Behroozi et al., 2013b). At the same time, theory predicts that, due to self-regulation, the evolution of the SFRD is relatively insensitive to the details of the star formation efficiency (or gas consumption time scale; Schaye et al. 2010; Behroozi et al. 2013a; Somerville et al. 2015). To some extent, the SFRD by itself is therefore a limited probe to understand the details of the process of star formation inside galaxies. However, by comparing the (evolution of the) cosmic SFRD to the other baryonic components, such as the cosmic atomic and molecular gas densities, it does provide insight into where the baryons reside over cosmic time, the baryon cycle of galaxies, and the global process of star- and galaxy formation. For example, were galaxies more efficient in converting their cold ISM into stars 10 billion years ago, or were they simply more cold gas-rich?

The individual star-forming galaxies (that make up the SFRD) are observed to follow a broad correlation between their stellar mass and (recent) star formation rate (Brinchmann et al., 2004; Noeske et al., 2007a), see Figure 2.7 and Figure 3.10. This relation has become known as the *main sequence of star-forming galaxies*.[11] Galaxies with a significantly higher SFR than the population average at fixed stellar mass are called *starburst galaxies*, while (massive) galaxies with relatively little star formation are considered to be *quenched*. The physical processes that drive the shape of the relation, the scatter around it, and its evolution with time, hold valuable clues about galaxy formation. While the shape and scatter are still an active topic of study (see chapter 2), it is clear that the normalisation of the relation increases out to $z \approx 3$ (e.g., Whitaker et al., 2014; Schreiber et al., 2015; Tomczak et al., 2016), in line with the cosmic SFRD. The present and future evolution of a galaxy in this parameter space is necessarily linked to the availability of cold gas to fuel the star formation, as surveys in the local universe have demonstrated (e.g., Saintonge et al., 2016, 2017). To understand this interplay over cosmic time in detail, surveys of the cold molecular gas content of galaxies with average star formation rates for their stellar mass—galaxies 'on the main sequence'—are required.

1.4.2 Molecular gas in distant galaxies

There is a long history of molecular gas observations in distant galaxies. Given the fundamental importance of molecular gas for star formation, however, it has remained surprisingly difficult to study in distant galaxies. Advances in the field have continuously been driven by the availability of more sensitive (sub)millimeter instruments, in particular interferometers.

Ever since the first detection of CO in a high-redshift galaxy, the $z = 2.28$ quasar *IRAS* F10214+4724 (Brown & vanden Bout, 1991; Solomon et al., 1992a), the number of CO detections in distant galaxies has been steadily increasing. By the time of the review by Solomon & Vanden Bout (2005), a few dozen detections of CO were made in galaxies at $z > 1$. Most of these galaxies were first identified as strong emitters at far-infrared/submillimeter wavelengths, with high far-IR luminosities (greater than 10^{12} $\mathrm{L}_\odot$). These were selected either directly from submillimeter surveys, or by following up radio galaxies or large optical surveys of high-redshift quasars. Key to the detection of CO in these sources was prior knowledge of their redshift from optical spectroscopy, because of the narrow bandwidth of the (sub)millimeter instruments. As more sensitive (sub)millimeter interferometers became available in the following decade, large reservoirs of cold gas as were confirmed in an increasing number of galaxies. Importantly, these instruments also enabled the first studies of optically-selected star-forming galaxies at $z > 1$. The total number of CO detections in distant galaxies increased to close to 200 by the review of Carilli & Walter (2013). Since then there have been major developments in the field. In particular ALMA, with its unparalleled sensitivity and angular resolution, has greatly improved our view of the molecular gas content of distant galaxies.

---

[11] The name resembles the *main sequence* of stars in the Hertzsprung-Russell diagram that are powered by nuclear fusion of hydrogen and form a tight locus along which they evolve in equilibrium. However, the relation between the SFR of galaxies and its integral over time (the stellar mass that has been built-up) is not equally straightforward. It is perhaps best considered as a cross-sectional snapshot of the population at a specific time, in which each galaxy evolves along its own star formation history (which can vary on both short and long timescales), and care should thus be expressed when interpreting its parameters (e.g., Abramson et al. 2016; Matthee & Schaye 2019, see also the recent discussion in Förster Schreiber & Wuyts 2020). In chapter 2, that deals specifically with this topic, we therefore avoid this connotation and consequently refer to the 'stellar mass – star formation rate relation'. In later chapters, however, we will use the now commonly adopted and brief term '(galaxy) main sequence'.

Submillimeter-selected galaxies (SMGs; Smail et al. 1997; Blain et al. 2002) have been among the prime targets for cold-gas observations as their high dust luminosities are indicative of large amounts of gas and dust. Observing their CO emission has been challenging, however, as the large dust attenuation often causes them to be extremely faint at optical wavelengths, making redshift determinations challenging (even to date, e.g., Danielson et al., 2017). In addition, the low angular resolution ($\geq 15''$) of the single-dish telescopes with which they were initially selected, as well as later far-IR instruments such as *Herschel*, gave rise to significant source blending and challenges in identifying the counterparts of the SMGs at other wavelengths. As such, understanding the nature of SMGs and their relation to the overall population of star-forming galaxies has been challenging. The field is now rapidly developing with ALMA (see Hodge & da Cunha, 2020, for a review). Recent studies confirm that SMGs are mostly massive and highly star-forming galaxies ($M_* \sim 10^{11}$ $\mathrm{M}_\odot$ with SFR between 10^2 and 10^3 $\mathrm{M}_\odot\,\mathrm{yr}^{-1}$), with most of the submm emission arising in a compact (starburst) region (though they may still host more extended disks). While SMGs have been portrayed as the high-redshift analogues of (U)LIRGS,[12] and as such the starburst outliers of the galaxy population, this picture is debatable, and SMGs are likely a diverse population of objects. While the brightest sources are linked to extreme galaxies, the boundary between faint SMGs and massive, optically-selected, star-forming galaxies is starting to fade[13] with sensitive submm telescopes (Hodge & da Cunha, 2020). SMGs generally host large reservoirs of cold gas (see Carilli & Walter, 2013, for a review), though their precise gas mass is uncertain because of the difficulty in constraining the α_{CO} (which is commonly assumed to be low, (U)LIRG like). The diversity among SMGs is also seen in their gas conditions, as reflected by the variety in their CO excitation ladders. These imply SMGs have dense and warm gas in comparison to local star-forming galaxies (Danielson et al., 2011; Bothwell et al., 2013; Birkin et al., 2020), although, given their diverse nature, an average CO ladder that applies to 'all' SMGs is not to be expected (Casey et al., 2014).

---

[12] (Ultra) Luminous Infrared Galaxies in the local universe with high infrared luminosities above (10^{12}) 10^{11} $\mathrm{L}_\odot$, that predominantly host (merger-driven) starbursts and/or an AGN, and make up a very small fraction of the overall galaxy population (Sanders & Mirabel, 1996).

[13] Note that the average (main-sequence) galaxy with a stellar mass of 5×10^{10} $\mathrm{M}_\odot$ is in fact a LIRG by $z \approx 1$ and a ULIRG at $z \approx 3$.

The first studies of optically-selected star-forming galaxies showed that they were surprisingly gas rich (Daddi et al., 2010a; Tacconi et al., 2010; Riechers et al., 2010; Tacconi et al., 2013), with fairly large reservoirs of warm gas compared to local spiral galaxies (Daddi et al., 2015). These galaxies were typically selected to be 'less extreme' than SMGs in terms of their SFR, though to enable detections, most were still selected to be massive (with M_* around 10^{10} to 10^{11} $\mathrm{M}_\odot$) and highly star-forming (SFRs of 10 to 100 $\mathrm{M}_\odot\ \mathrm{yr}^{-1}$), with IR luminosities in excess of 10^{11} $\mathrm{L}_\odot$, though morphologically disk-like (e.g., Daddi et al., 2010a; Tacconi et al., 2013). These results indicated that the average cold gas fraction of star-forming galaxies at $z = 2$ is several times higher than in the local universe, and increases out to at least $z = 3$, while the depletion time decreases mildly over the same time (Tacconi et al., 2010; Geach et al., 2011; Tacconi et al., 2013), though it may show potential differences between disk-like galaxies and nuclear starburst (e.g., Daddi et al., 2010a; Genzel et al., 2010, albeit degenerate with the assumptions for α_{CO}). Large (literature) studies are now trying to constrain the evolution of the scaling relations of molecular gas fraction (f_{gas}) and depletion time (t_{depl}) (Genzel et al., 2015; Tacconi et al., 2018, 2020), and simultaneous efforts take place to constrain these from the dust-continuum emission (e.g., Scoville et al., 2017; Liu et al., 2019). Still, significant uncertainties persist in these scaling relations. Besides challenges in deriving stellar masses and SFRs for a variety of sources in a consistent and accurate way (for example, highly obscured sources such as SMGs), and biases that arise when combining large-but-incomplete samples of galaxies, there are still fundamental uncertainties in deriving gas masses for galaxies at high redshift, due to the limited knowledge about the conditions in the ISM, which drive the conversion factors. Again, submm interferometers like ALMA are now enabling progress on this front, as (larger samples of) massive star-forming galaxies can be studied in multiple tracers (in particular from CO and [C I], e.g., Popping et al., 2017b; Bourne et al., 2019; Brisbin et al., 2019; Valentino et al., 2018; Valentino et al., 2020a,b, see chapter 4).

While not strictly dealing with the cold molecular gas, this brief review would not be complete without mentioning the impact of ALMA by its ability of observing the fine-structure lines in the highest-redshift galaxies, in particular [C II] $\lambda 158\,\mu$m. While only the brightest and most extreme sources were previously observable at $z \geq 5$, massive star-forming galaxies at these redshifts can be detected in half an hour with ALMA, making it one of the prime tools for searching and spectroscopically confirming high-z galaxies. This is sparking studies of the galaxy population at $z = 5 - 6$ (e.g., Capak et al., 2015; Le Fèvre et al., 2020), spectral scan surveys for galaxies at $z = 6 - 8$ (e.g., Smit et al., 2018), and has led to the highest spectroscopic redshift to date at $z = 9.1$ (Hashimoto et al., 2018, via [O III] $\lambda 88\,\mu$m). ALMA also enables more systematic studies of the highest redshift quasars, and their companions, at sub-kpc resolution (e.g., Decarli et al., 2017, 2018; Venemans et al., 2018, 2019)

1.4.3 The need for molecular deep fields

What becomes clear from § 1.4.2 is that a significant limitation in our knowledge of the cold gas content of galaxies comes from the fact that most observations have been restricted to targets that were preselected based on their UV–FIR emission (cf. Carilli & Walter 2013).

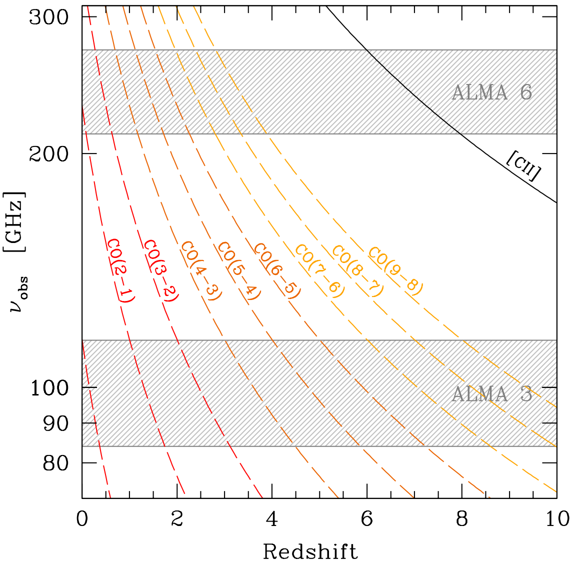

Figure 1.7: The observed frequency of the rotational transitions of carbon monoxide (up to CO $J = 9 \rightarrow 8$) as they shift with increasing redshift. The ASPECS tunings, scanning through the entire ALMA bands 3 and 6, provide almost continuous coverage of the CO signal, out to high redshift (there is only a tiny gap between $0.6309 < z < 0.6950$). Also indicated is the [C II] $\lambda 158\,\mu$m line. The transitions from atomic carbon, topic of chapter 4, follow tracks close to CO $J = 4 \rightarrow 3$ and CO $J = 7 \rightarrow 6$. See Figure 3.1 and Figure 4.1 for an alternative presentation. *Figure taken from Walter et al. (2016).*

While this approach is efficient, it leaves the possibility that a significant fraction of the molecular gas is missed, because it is not associated with the galaxies that are *a priori* expected to be most gas rich. In order to obtain a more complete picture of the molecular gas content of distant star-forming galaxies, and to perform a census of the cosmic molecular gas content of the universe, an untargeted survey for the molecular gas signal throughout cosmic time is needed. Such a survey should be sensitive enough to detect the molecular gas in the average population of star-forming galaxies. ALMA is the only telescope with sufficient sensitivity to perform such a study continuously over the past 12 billion years cosmic history, as shown by several pilot programs (Walter et al., 2014, 2016, see also Riechers et al. 2019).

1.5 The ALMA Spectroscopic Survey of the HUDF

1.5.1 Motivation

The ALMA Spectroscopic Survey of the *Hubble* Ultra Deep Field (ASPECS) is a three dimensional survey for the emission from cold gas and dust throughout cosmic time. It is the first extragalactic Large Programme approved for ALMA, totaling 150 h of observations, lead by Principal Investigators (PIs): F. Walter, M. Aravena, and C. Carilli. The primary goal of ASPECS is to survey the cosmic molecular gas content of galaxies—the fuel for star formation—without performing any target preselection. In this way, ASPECS measures the cosmic molecular gas density, which is the necessary complement to the cosmic SFR density (SFRD) and an important missing piece in our picture of the baryon cycle.

1.5.2 Observing strategy

The ASPECS observations are specifically designed to detect emission from cold molecular gas in a well defined cosmic volume (that is, an area on the sky times a distance along the line of sight) and obtain a census of the cosmic molecular density through time, $\rho_{\mathrm{H}_2}(z)$. This goal is achieved by imaging a significant area on the sky in a mosaic of individual ALMA images, while at the same time scanning for emission from the bright lines of CO in frequency space, down to a predetermined sensitivity limit. The transitions between the higher rotational levels of CO lie at distinct frequencies (§ 1.2.2), which redshift through frequency space as galaxies are more distant. The *spectral scans* of ASPECS are chosen such that they encompass almost the complete atmospheric transmission windows at 3 mm (from 84 to 115 GHz; band 3) and 1.2 mm (from 212 to 272 GHz; band 6). Because the effective bandwidth of ALMA is (only) 4×1.875 GHz, five frequency tunings in band 3 and eight tunings in band 6 are needed to scan through the whole spectral range (Walter et al., 2016). The result is that ASPECS can detect emission from CO at essentially all redshifts, as shown in Figure 1.7. At the same time, the spectral scans are sensitive to any other transition that falls within the frequency coverage, such as [C II] for galaxies at $6 \leq z \leq 8$ and emission from [C I] at lower redshifts, as well as fainter emission (for example, from H_2O).

The field of choice for ASPECS is the *Hubble* Ultra Deep Field, which is ideally located on the sky for observations with ALMA (at −27° declination). The HUDF has been studied extensively with telescopes across the electromagnetic spectrum, providing excellent quality ancillary data both in depth and resolution. It will also be one of the prime targets for guaranteed time observations with the *James Webb Space Telescope*. The wealth of multi-wavelength data provides important constraints on the properties of the galaxies, such as their stellar mass, star formation rate, and AGN activity. Conversely, the ASPECS data greatly adds to the legacy value of the HUDF. The HUDF has also been an important target for MUSE (§ 1.3.1), which provides spectroscopic redshifts for more than 1500 galaxies in the field. This redshift information is particularly important, as it can be used to both identify the molecular gas emitters, as well as search for molecular gas below the formal detection threshold of ASPECS. The synergy between MUSE and ALMA is one of the main topics of this thesis.

1.5.3 Data products: two cubes and two images

The result of the ASPECS observations are a pair of three dimensional datacubes. Two axes of a cube are the location on the sky (in right ascension and declination) and the third axis is the observed frequency. The latter translates to a distance along the line of sight via the redshift, once the observed emission line has been identified. A rendering of the three dimensional datacubes from ASPECS can be seen in Figure 1.10. The bright spots correspond to emission lines from the cold molecular gas in galaxies, while the stripe(s) parallel to the frequency axis

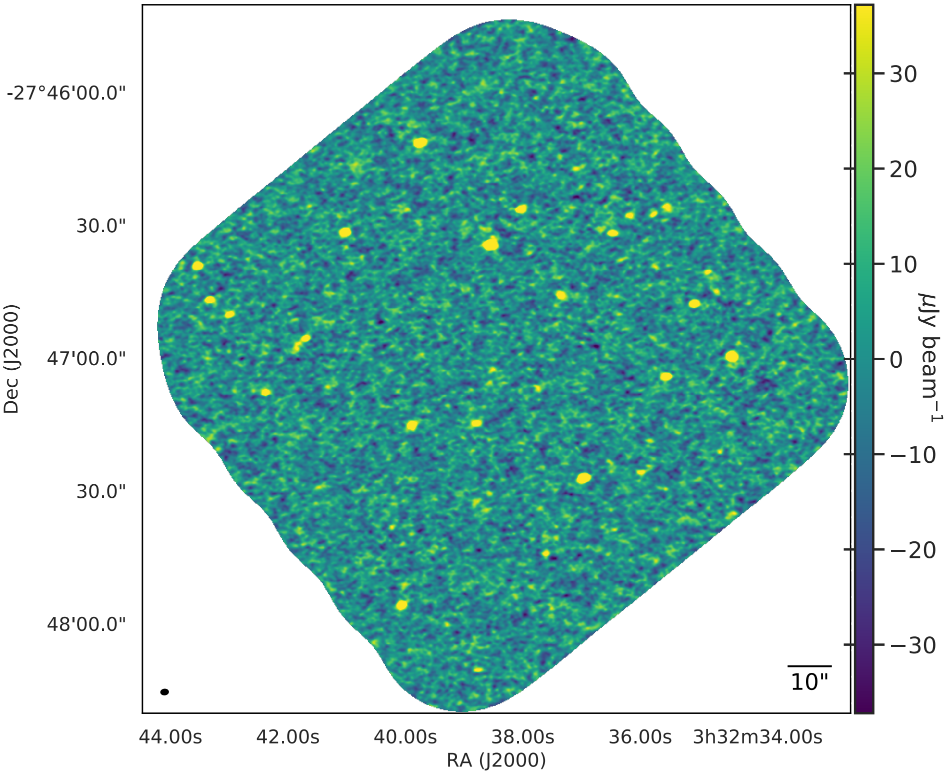
-27°46'00.0"
30.0"
47'00.0"
30.0"
48'00.0"
Dec (J2000)
44.00s
42.00s
40.00s
38.00s
36.00s
3h32m34.00s
RA (J2000)
10"
30
20
10
0
−10
−20
−30
μJy beam−1

Figure 1.8: The ASPECS-LP 1.2 mm continuum map (band 6), showing the continuum emission from the cold dust in galaxies in the *Hubble* Ultra Deep Field. This map is the deepest ALMA continuum map of a cosmological deep field obtained to date, reaching a root-mean-square noise level of 9.3 μJy beam^{-1}. *The map is naturally weighted and shown down to 10% of the primary beam response (without correcting for mosaic primary beam response), which corresponds to 4.2 arcmin*^{2} *on sky. Figure adapted from González-López et al. (2020).*

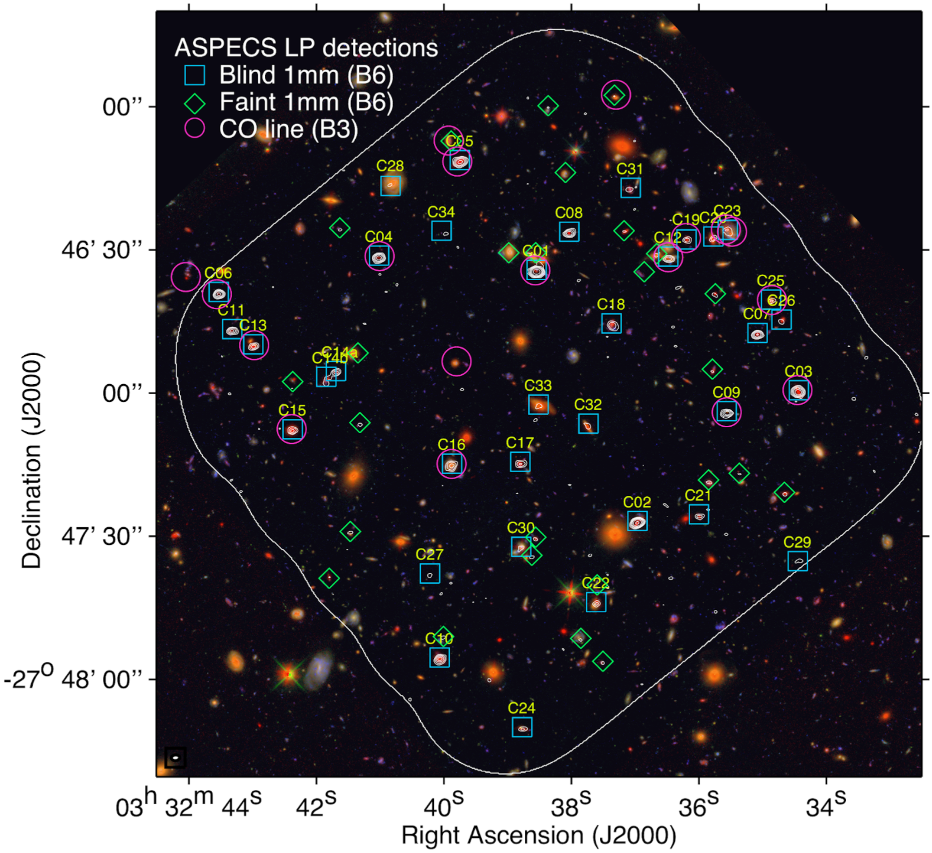
ASPECS LP detections
Blind 1mm (B6)
Faint 1mm (B6)
CO line (B3)
C01
C02
C03
C04
C05
C06
C07
C08
C09
C10
C11
C12
C13
C14a
C14b
C15
C16
C17
C18
C19
C20
C21
C22
C23
C24
C25
C26
C27
C28
C29
C30
C31
C32
C33
C34
00”
46’ 30”
00”
47’ 30”
-27° 48’ 00”
Declination (J2000)
03h 32m 44s
42s
40s
38s
36s
34s
Right Ascension (J2000)

Figure 1.9: *Hubble* image of the HUDF on which we highlight the dust continuum- and CO-selected samples from ASPECS. The purple circles show the galaxies that are detected by their CO-line emission, which are the topic of chapter 3. The blue squares and green diamonds indicate the galaxies that are detected in the dust continuum (without and with a prior, respectively). The intersection between these samples, and the subsequent implication for their physical conditions, is discussed as part of chapter 4. The white contours show the ASPECS-LP 1.2 mm dust-continuum emission (cf. Figure 1.8). *Red: F160W, Green: F850LP, Blue: F450W. Contours at the 3, 5, 7, 10 and 20σ level. Figure taken from Aravena et al. (2020).*

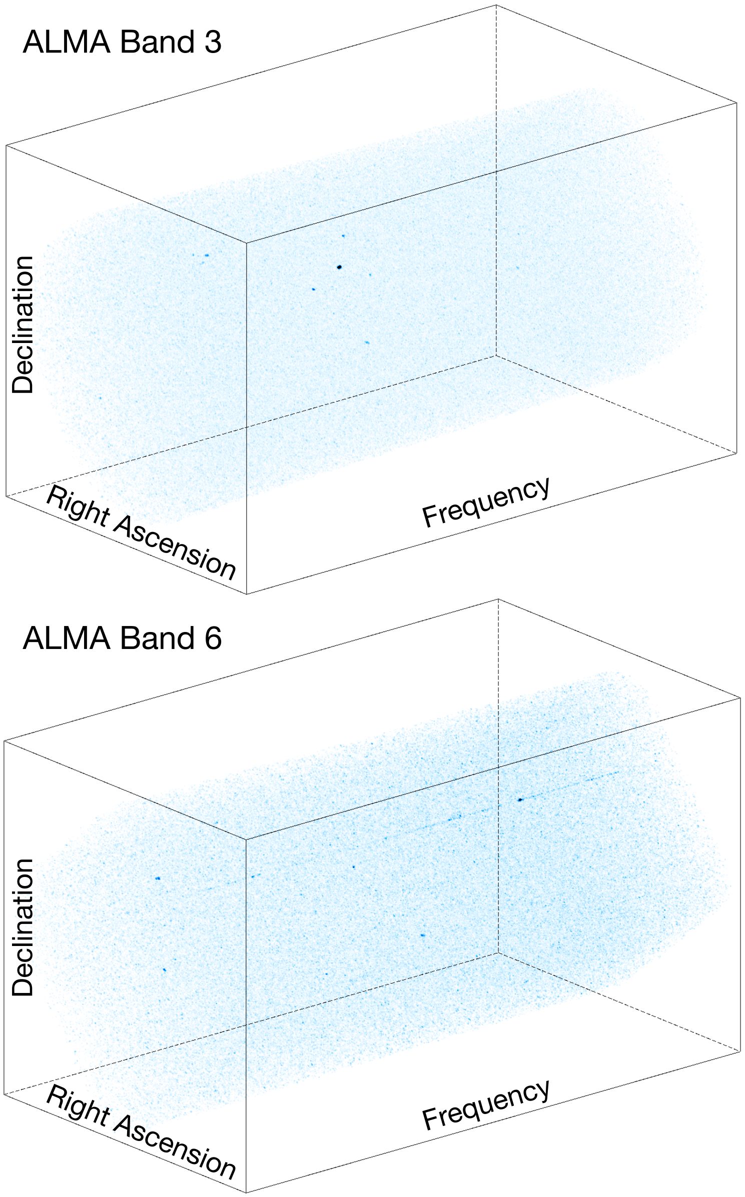
ALMA Band 3
Declination
Right Ascension
Frequency
ALMA Band 6
Declination
Right Ascension
Frequency

Figure 1.10: Three-dimensional rendering of the ASPECS band 3 and band 6 datacubes. The bright spots correspond to emission lines from cold gas in galaxies, while the fainter dots are increasingly due to noise fluctuations. The horizontal stripe that is clearly visible in the band 6 data is due to strong dust-continuum emission from the brightest galaxy (compare Figure 4.3). *Both renditions span about* $2\overset{\prime}{.}5$ *in the spatial directions and cover the full frequency range of the band 3 and band 6 scans.*

are due to continuum emission. The emission lines of varying brightness (including those that are not directly visible in this image) are identified through a statistical analysis of the noise.

By collapsing the cubes along the frequency axis, images of the dust continuum are obtained at the average frequency of the spectral scans. These are very sensitive, because of the sensitivity of each tuning in combination with the number of tunings, spanning a large frequency range. The band 6 image at 1.2 mm is shown in Figure 1.8 and represents one of the deepest continuum images of an extragalactic field to date.[14] The number of sources in the image that is detected above a certain sensitivity limit (the *number counts*) shows a strong flattening at the faintest levels, which implies that the observations are reaching the limits of submillimeter imaging at these frequencies, in the sense that deeper observations will not yield many additional sources. Indeed, ASPECS identifies the individual galaxies that together are responsible for almost all ($\approx$ 93%) of the *Extragalactic Background Light* at 1.2 mm in the HUDF (González-López et al., 2020; Popping et al., 2020)

1.6 The thesis

1.6.1 This thesis

This thesis presents a series of studies of the cold molecular gas in distant galaxies in the *Hubble* Ultra Deep Field. These are enabled through deep spectroscopic surveys with MUSE and ALMA, in particular ASPECS. The central question throughout these studies is: how does the cold, molecular interstellar medium of galaxies evolve over cosmic time, in relation to their star-forming properties, and how does this dictate their evolution?

The logical flow of the thesis can be understood as follows. We first study the relation between the star formation rate and stellar mass (the galaxy main sequence) in low-mass galaxies in chapter 2. We then shift focus to the cold molecular gas. We identify which galaxies are rich in molecular gas and study the conditions in their cold ISM, in relation to their star formation rate, stellar mass, and other physical properties (chapter 3 and chapter 4). We then use this information to measure the cosmic molecular gas content of the universe back in time, from the present day to when the universe was only 1.5 billion years old, and discuss how future studies can improve on these constraints (chapter 5 and chapter 6).

Chapter 2: In the hierarchical framework of galaxy formation, low-mass galaxies play a fundamental role. However, studies of the main sequence have been limited to more massive galaxies. In this initial chapter, we use MUSE to study the low-mass end of the stellar mass–star formation rate relation, a poorly sampled part of parameter space, for a flux-limited sample of galaxies in the HUDF. We use robust, dust extinction-corrected, Balmer line-derived star formation rates and apply a novel, Bayesian statistical model that jointly constrains the intrinsic scatter. We find an increased intrinsic scatter, which may signal increasingly stochastic star formation histories in low-mass galaxies, and discuss why previous work may have underestimated the scatter. We also find a flatter slope than predicted by simulations, which suggests that the modeling of feedback processes in low-mass halos is still to be improved.

---

[14] It is at least a factor 4 deeper than other deep field surveys with ALMA, that often consist of 1.2 mm dust continuum imaging in a single frequency tuning over a larger area of the sky (e.g., Kohno et al., 2016; Dunlop et al., 2017; González-López et al., 2017a,b; Franco et al., 2018; Hatsukade et al., 2018), see also Hodge & da Cunha (2020).

Chapter 3 answers perhaps the most simple question one can ask when doing a survey like ASPECS: what is the nature and what are the physical properties of the galaxies we detect in a flux-limited survey for molecular gas as traced by CO? We identify all the emission lines as redshifted CO, arising from the cold molecular gas in galaxies that are visible to *Hubble*. Using the MUSE spectra, we measure that the gas in galaxies at $z \leq 1.5$ has a solar metallicity, which supports the use of a Galactic conversion factor ($\alpha_{\rm CO}$) to measure their molecular gas mass. The results show that ASPECS unveils the molecular gas in the majority of the massive, star-forming galaxies at cosmic noon. The low SFR of some detected galaxies, however, highlights that previous, star formation-based selection methods can miss part of the gaseous galaxy population.

Chapter 4 studies the physical conditions in the ISM of the ASPECS-detected galaxies, by means of their CO excitation, atomic carbon emission, and dust-continuum emission. Combining the ALMA observations with those from the VLA, we measure and predict (using theoretical models) the average low-, mid- and high-J excitation for the galaxies observed with ASPECS. Focusing on the results from CO, we find that the excitation, and thus the average density and temperature in the cold ISM, increases with redshift. At the same time, the ASPECS galaxies show less excited CO ladders than earlier samples of optically- and submillimeter-selected galaxies at comparable redshifts. Both phenomena can be explained by the (lower) star formation rate surface densities of our galaxies (compared to earlier surveys).

Chapter 5: Building on the foundation laid out in chapters 3 and 4, all aspects come together in this chapter, where an inventory and a statistical analysis of the multi-line signal in the ASPECS data is performed. We combine the necessary redshift and metallicity information (chapter 3) together with knowledge we obtained about the CO excitation and the conditions in the ISM (chapter 4) to construct the cosmic molecular gas density, $\rho_{\rm H_2}(z)$. The main result is that $\rho_{\rm H_2}(z)$ increases with cosmic time, up to a peak at $z \sim 1.5$, followed by a drop towards the present day, in agreement with the evolution of the cosmic star formation rate density. This implies that the rise and fall of the cosmic star formation rate density is indeed linked to the increased gas content of galaxies at cosmic noon, and that the molecular gas depletion time in galaxies is approximately constant with redshift, after averaging over the galaxy population.

Chapter 6: In this final chapter ASPECS is pushed one step further. Starting from the large number of Lyα-redshifts from MUSE, we determine the systemic redshifts of $z = 3 - 4$ galaxies from other spectral features at restframe UV and optical wavelengths, through near-IR spectroscopy. Using the exact distance information, we stack the molecular gas and dust signal in these low-mass galaxies, observed when the universe was only $\sim$ 2 Gyr old. We show that the molecular gas and dust is very hard to detect, because the metallicity in the ISM of these galaxies is significantly sub-solar, as it is still being enriched with metals. We conclude by pointing in future directions that could be taken to measure the cold gas reservoirs in these galaxies.

1.6.2 Related science with ASPECS

The ASPECS observations enable a wide range of science beyond what is presented in the following chapters. This is reflected in the well over a dozen publications from the ASPECS team, as well as others that have used the pubicly available data.[15] Here we briefly summarise some of these studies, in relation to this thesis, in particular those that are not discussed in as much detail in the following chapters.

Aravena et al. (2019) discuss the evolution of the molecular gas content and star-forming properties of the CO-selected ASPECS galaxies (studied in chapter 3 and chapter 4), in the broader context of the galaxy scaling relations between molecular gas factions, depletion times, and distance from the galaxy main sequence. Most galaxies from the flux-limited sample follow the relations (to within uncertainties), although there is some tension with galaxies that would be missed by earlier (targeted) observations (see also chapter 3). A follow-up study of the dust continuum-selected sample is presented in Aravena et al. (2020). Both studies conclude that galaxies with an average star formation rate are the dominant contributors to the overall molecular gas density. Figure 1.9 provides an overview of the HUDF galaxies that are detected through their low-J CO and/or 1.2 mm dust-continuum emission.

Inami et al. (2020) leverage the MUSE redshifts to study CO emission below the formal detection threshold of ASPECS (see also chapter 3) and perform a CO-stacking study to constrain the molecular gas content of galaxies up to $z = 3$ (stacking results at $z \geq 3$, where MUSE alone is insufficient, are discussed in chapter 6). They detect CO in individually undetected galaxies at $z \sim 1.5$ and place constrains on the gas fractions of galaxies towards lower stellar masses. They find limited additional signal at higher redshift, in good agreement with the ASPECS intensity mapping study from Uzgil et al. (2019).

Magnelli et al. (2020) study the evolution of the cosmic densities of dust and molecular gas as a function of time, through a dust continuum-stacking analysis of all H-band selected galaxies in the HUDF. They find an early rise, peak at $z \sim 2$, and decline towards the present, similar to the cosmic SFRD, and consistent with the result from chapter 5. Their results imply that by a large fraction ($\sim 90\%$) of the dust formed in galaxies across cosmic time has either been destroyed or ejected into the intergalactic medium by $z = 0$.

Bouwens et al. (2020) study the obscured star formation of distant (Lyman break-selected) galaxies, out to the first 500 million years of cosmic time ($z = 10$). Updating constraints on the correlation between the dust extinction and re-emission in the IR (the IRX–β-relation), they refine the estimates of the cosmic SFRD at $z > 3$ and show how relative fraction of obscured versus unobscured star formation evolves as a function of cosmic time.

Kaasinen et al. (2020) perform a detailed study of three ASPECS galaxies at higher resolution, comparing the spatial extent of their CO, dust, and (rest-frame optical) stellar emission. They find a variety of morphologies, with both compact and extended ISM distributions (despite similar selection criteria), and emphasise the importance of surveys that are not biased to submm bright sources, which are more likely to show compact dust emission.

---

[15] https://www.aspecs.info

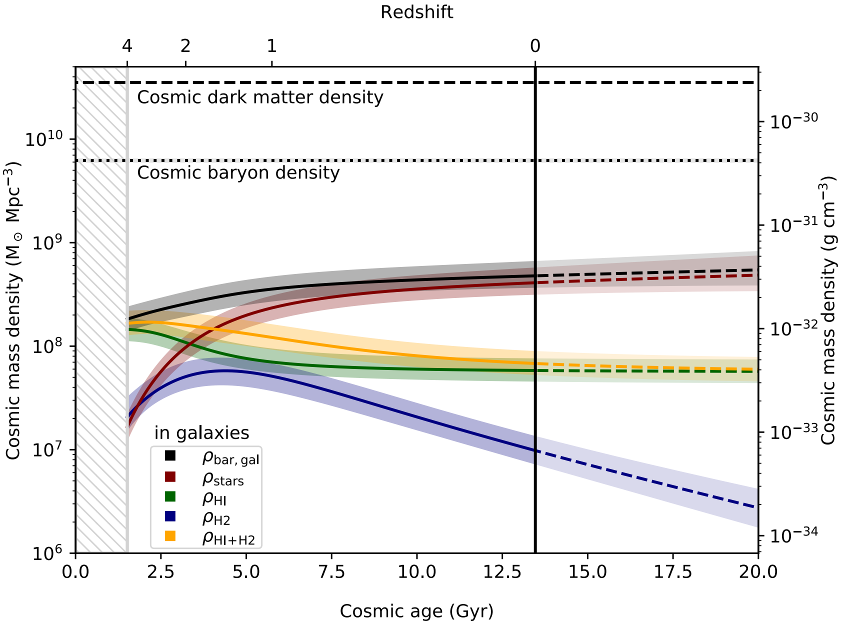

Figure 1.11: The evolution, as a function of cosmic time, of the cosmic mass densities of: stars (red, cf. Figure 1.6), neutral hydrogen (H I, green, as derived by Walter et al., 2020), and molecular gas, H_2, as derived by ASPECS (blue). The latter is the topic of this thesis and is discussed extensively in chapter 5 and is shown in Figure 5.9. Also shown are the the sum of the gaseous components (yellow, H I + H_2) and the sum of all the baryons (grey, the sum of all curves), and the cosmic baryon and dark matter densities (dotted and dashed lines, respectively). The lower abscissa indicates the cosmic age of the universe and the upper abscissa the corresponding redshift. The figure starts 1.5 Gyr after the big bang (at redshift $z = 4$) and shows the measured evolution towards the present day ($z = 0$). The dashed segments are a hypothetical extrapolation into the future, under the assumption of continuity and that the current physical processes continue to dominate. *Figure taken from Walter et al. (2020).*

1.7 The future

1.7.1 The cosmic baryon cycle

The evolution of the cosmic molecular gas density, as measured in chapter 5, can be combined with the evolution of the cosmic densities of stellar mass, star formation rate, and neutral gas to constrain the evolution of the baryons associated with galaxies, averaged over space and time. This analysis is presented in Walter et al. (2020) and briefly summarised here. Figure 1.11 shows the evolution of the cosmic mass densities. The cosmic density of H I has slowly declined over the past 12 billion years (cf. Neeleman et al., 2016), while the density of H_2 increases and decreases, similar to the evolution of the SFR (chapter 5). Significant accretion of gas onto galaxies is required in order to sustain the star formation needed to form the bulk of the stellar mass seen in galaxies in the last 9 billion years. The relative evolution of the atomic and molecular mass densities can be explained via a two-phase accretion process: (i) the inflow of diffuse (ionised) gas into the (extended) H I reservoir of a galaxy and (ii) the subsequent inflow of atomic gas towards the centre of the potential well, the conversion to molecular gas, and the formation of stars. This is in line with the observation that the star formation rate surface density in galaxies is correlated with the molecular gas density (§ 1.2.2). The cosmic star formation rate density is then driven by the net availability of molecular gas, as it is (indirectly) accreted onto galaxies. A comparison to numerical simulations suggest that the decreased gas accretion rates in the last 9 billion years are the result of the decreased growth of dark matter halos (partly due to the expansion of the universe), combined with the effects of feedback from stars and accreting black holes. Extrapolating the evolution of the mass densities into the hypothetical future paints a picture in which the molecular gas density continues to decline, with limited growth in the stellar mass density, as the cosmic star formation rate density steadily diminishes.

1.7.2 Science and facilities

Because of its unparalleled scale and sensitivity, ALMA will continue to play a central role in the study of cold gas in distant galaxies (and submm science in general) in the years to come. It is not even at its full potential: certain aspects of the observatory are still being completed and further technological developments are marked on the ALMA roadmap (Carpenter et al., 2019) that improve the sensitivity, frequency coverage, bandwidth and angular resolution of the instrument. Particularly relevant are the planned Band 1 and 2 receivers, that will enable the observations of CO $J = 1 \rightarrow 0$ in galaxies up to $z = 2$, removing the need for the uncertain excitation corrections—that play a central role in this thesis—and anchor ρ_{H_2} even more firmly. Increasing the bandwidth for ALMA is another important avenue—ideally to cover the entire atmospheric transmission windows all at once. This will allow for much greater efficiency of spectral scan surveys, which are becoming increasingly popular (note three of the four large programs in the “Cosmology and High Redshift Universe” Science Category to date are spectral scans[16]). At the same time, this will greatly increase the continuum sensitivity, which will also help reduce the increasing demand in the total observing time. These improvements will allow an increasing investment in large(r) programs, which are instrumental for the study of distant galaxies. Indeed, in light of the monumental time investments of the great observatories in the extragalactic deep fields, the ASPECS program should not be seen as the end point, but only as the beginning.

Future studies of cold gas in distant galaxies, with a range of different submm facilities, should focus on different aspects to advance our insight into the process of galaxy assembly. In addition to spectral scan surveys (mentioned above), and studies of larger samples in single, well-calibrated tracers, targeted multi-line studies will provide insight into the cold ISM conditions and should (eventually) aim at mapping the ‘complete’ (sub)mm spectra of different classes of galaxies. At the same time, while expensive in terms of observation time, higher resolution observations of both the dust and gas (kinematics) of larger samples of galaxies are much-needed, to peer into the cold ISM of distant galaxies and probe the interplay between stars, gas and dust, and the physics of star formation at smaller scales.

---

[16] Besides ASPECS and ALPINE (The ALMA Large Program to INvestigate [C II] at Early Times, PI: Olivier Lé Fevre; which is not a spectral scan survey), these are the ALMA Lensing Cluster Survey (PI: K. Kohno) and the Reionization Era Bright Emission Line Survey, REBELS (PI: R. Bouwens).

Finally, several new windows on distant galaxies will be provided in the near future through instrumental advances across the electromagnetic spectrum. Two facilities that are particularly relevant are the *James Webb Space Telescope* and the *Extremely Large Telescope*. Together, these will provide much-needed advances in terms of spatial resolution, sensitivity and wavelength coverage, to study the stellar populations, the build-up of dust and metals, and the (co)evolution galaxies and their supermassive black holes in distant galaxies.

2 | The MUSE Hubble Ultra Deep Field Survey: XI. Constraining the low-mass end of the stellar mass – star formation rate relation at $z < 1$

Abstract

Star-forming galaxies have been found to follow a relatively tight relation between stellar mass (M_*) and star formation rate (SFR), dubbed the 'star formation sequence'. A turnover in the sequence has been observed, where galaxies with $M_* < 10^{10}\,\mathrm{M}_\odot$ follow a steeper relation than their higher-mass counterparts, suggesting that the low-mass slope is (nearly) linear. In this paper, we characterise the properties of the low-mass end of the star formation sequence between $7 \leq \log M_*[\mathrm{M}_\odot] \leq 10.5$ at redshift $0.11 < z < 0.91$. We use the deepest MUSE observations of the *Hubble* Ultra Deep Field and the *Hubble* Deep Field South to construct a sample of 179 star-forming galaxies with high signal-to-noise emission lines. Dust-corrected SFRs are determined from Hβ λ4863 and Hα λ6565. We model the star formation sequence with a Gaussian distribution around a hyperplane between $\log M_*$, $\log \mathrm{SFR}$, and $\log(1 + z)$, to simultaneously constrain the slope, redshift evolution, and intrinsic scatter. We find a sub-linear slope for the low-mass regime where $\log \mathrm{SFR}[\mathrm{M}_\odot\,\mathrm{yr}^{-1}] = 0.83^{+0.07}_{-0.06} \log M_*[\mathrm{M}_\odot] + 1.74^{+0.66}_{-0.68} \log(1 + z)$, increasing with redshift. We recover an intrinsic scatter in the relation of $\sigma_{\mathrm{intr}} = 0.44^{+0.05}_{-0.04}$ dex, larger than typically found at higher masses. As both hydrodynamical simulations and (semi-)analytical models typically favour a steeper slope in the low-mass regime, our results provide new constraints on the feedback processes which operate preferentially in low-mass halos.

L. A. Boogaard, J. Brinchmann, N. Bouché, M. Paalvast, *et al.*
Astronomy & Astrophysics, 619, A27 (2018)

2.1 Introduction

How galaxies grow is one of the fundamental questions in astronomy. The picture that has emerged is that a galaxy builds up its stellar mass mainly through star formation, which is triggered by gas accretion from the cosmic web (e.g. Dekel et al., 2009; van de Voort et al., 2012), while mergers with other galaxies play only a minor role (except for massive systems; Bundy et al., 2009).

In the past decade, star-forming galaxies have been found to form a reasonably tight quasi-linear relation between stellar mass (M_*) and star formation rate (SFR) (Brinchmann et al., 2004; Noeske et al., 2007a; Elbaz et al., 2007; Daddi et al., 2007; Salim et al., 2007) over a wide range of masses and out to high redshifts (Pannella et al., 2009; Santini et al., 2009; Oliver et al., 2010; Peng et al., 2010; Rodighiero et al., 2010; Karim et al., 2011; Bouwens et al., 2012; Whitaker et al., 2012; Stark et al., 2013; Whitaker et al., 2014; Ilbert et al., 2015; Lee et al., 2015; Renzini & Peng, 2015; Schreiber et al., 2015; Shivaei et al., 2015; Salmon et al., 2015; Tasca et al., 2015; Gavazzi et al., 2015; Kurczynski et al., 2016; Tomczak et al., 2016; Santini et al., 2017; Bisigello et al., 2018), which is often referred to as the 'main sequence of star-forming galaxies' or the 'star formation sequence'. In contrast, galaxies that are undergoing a starburst or have already quenched their star formation respectively lie above and below the relation. This main sequence is close to a similar scaling relation for halos (Birnboim et al., 2007; Neistein & Dekel, 2008; Genel et al., 2008; Fakhouri & Ma, 2008; Correa et al., 2015a,b) where the growth rate increases super-linearly[17] with halo mass, and this has been interpreted as supporting the picture where galaxy growth is driven by gas accretion from the cosmic web (e.g. Bouché et al., 2010; Lilly et al., 2013; Rodríguez-Puebla et al., 2016; Tacchella et al., 2016).

This interpretation is supported by hydrodynamical simulations of galaxy formation (Schaye et al., 2010; Haas et al., 2013a,b; Torrey et al., 2014; Hopkins et al., 2014; Crain et al., 2015; Hopkins et al., 2016), where a global equilibrium relation is found between the inflow and outflow of gas and star formation in galaxies. In this picture the star formation acts as a self-regulating process, where the inflow of gas, through cooling and accretion, is balanced by the feedback from massive stars and black holes (e.g. Schaye et al., 2010). Furthermore, semi-analytical models (e.g. Dutton et al., 2010; Mitchell et al., 2014; Cattaneo et al., 2011, 2017) and relatively simple analytic theoretical models which connect the gas supply (from the cosmological accretion) to the gas consumption can also reproduce the main features of the main sequence rather well (e.g. Bouché et al., 2010; Davé et al., 2012; Lilly et al., 2013; Dekel et al., 2013; Dekel & Mandelker, 2014; Mitra et al., 2015; Rodríguez-Puebla et al., 2016, 2017).[18]

The parameters of the M_*-SFR relation (i.e. slope, normalisation, and scatter) are thus important, as they provide us with insight into the relative contributions of different processes operating at different mass scales, in particular when comparing the values of the parameters to their counterparts in dark matter halo scaling relations. The normalisation of the star formation sequence is governed by the change in cosmological gas accretion rates and gas

---

[17] There is a tension between the shallow slope of the observed main sequence with the super-linear slope expected in models, which is set by the index of the initial dark matter power spectrum (Birnboim et al., 2007; Neistein & Dekel, 2008; Correa et al., 2015a,b).

[18] For an alternative interpretation, cf. Gladders et al. (2013); Kelson (2014); Abramson et al. (2016).

depletion timescales. The slope can be sensitive to the effect of various feedback processes acting on the accreted gas, which prevent (or enhance) star formation. The intrinsic scatter around the equilibrium relation is predominantly determined by the stochasticity in the gas accretion process (e.g. Forbes et al., 2014; Mitra et al., 2017), but can also be driven by dynamical processes that rearrange the gas inside galaxies (Tacchella et al., 2016). The M_*-SFR relation is observed to be reasonably tight, with an intrinsic scatter of only ≈ 0.3 dex (Noeske et al., 2007a; Salmi et al., 2012; Whitaker et al., 2012; Guo et al., 2013; Speagle et al., 2014; Schreiber et al., 2015; Kurczynski et al., 2016, though we caution against a blind comparison as different observables probe star formation on different timescales). Yet, it has proven to be challenging to place firm constraints on the intrinsic scatter as one needs to deconvolve the scatter due to measurement uncertainty (e.g. Speagle et al., 2014; Kurczynski et al., 2016; Santini et al., 2017).

Observationally, the slope has been difficult to measure, particularly at the low-mass end, as most studies have been sensitive to galaxies with stellar masses above $\log M_*[\mathrm{M}_\odot] \sim 10$ and often lack dynamical range in mass. In addition, while it is well known that there is significant evolution in the normalisation of the sequence with redshift, most studies have measured the slope in bins of redshift. For a flux limited sample this could introduce a bias in the slope because overlapping populations at different normalisations are not sampled equally in mass within a single redshift bin. The slope may also be mass dependent and indeed recent studies have observed that the relation turns over around a mass of $M_* \sim 10^{10}\ \mathrm{M}_\odot$ (Whitaker et al., 2012, 2014; Lee et al., 2015; Schreiber et al., 2015; Tomczak et al., 2016) and shows a steeper slope below the turnover mass. In the low-mass regime, a (nearly) linear slope has generally been expected (e.g. Schreiber et al., 2015; Tomczak et al., 2016), motivated also by the fact that there is very little evolution in the faint-end slope of the blue stellar mass function with redshift (Peng et al., 2014). Leja et al. (2015) showed that the sequence cannot have a slope $a < 0.9$ at all masses because this would lead to a too high number density between $10 < \log M_*[\mathrm{M}_\odot] < 11$ at $z = 1$.

In addition to the observational challenges, careful modelling is required to get reliable constraints on the parameters (slope, normalisation, scatter) of the star formation sequence. It is important to properly take selection effects into account as well as the uncertainties on both the stellar masses and star formation rates (and, if spectroscopy is lacking, also on the photometric redshifts). The latter in particular, due to the fact that there is intrinsic scatter in the relation that needs to be deconvolved from the measurement errors. Common statistical techniques do not take these complications into account self-consistently, which leads to biases in the results.

Putting the existing observations in perspective, it is clear that a large dynamical range in mass is necessary to measure the slope of the star formation sequence in the low-mass regime. Deep field studies, that can blindly detect large numbers of galaxies down to masses much below $10^{10}\ \mathrm{M}_\odot$, are invaluable in this regard (e.g. Kurczynski et al., 2016). Yet, such studies are challenged by having to measure all observables, distances as well as stellar masses and star formation rates, from the same photometry. This can lead to undesirable correlations between different observables. At the same time the measurements suffer from the uncertainties associated with photometric redshifts. Spectroscopic follow up is crucial in this regard, but can suffer from biases due to photometric preselection.

With the advent of the *Multi Unit Spectroscopic Explorer* (MUSE; Bacon et al. 2010) on the VLT it is now possible to address these concerns. With the deep MUSE data obtained over the *Hubble* Ultra Deep Field (HUDF; Bacon et al., 2017) and *Hubble* Deep Field South (HDFS; Bacon et al., 2015), we can 'blindly' detect star-forming galaxies in emission lines down to very low levels ($\sim 10^{-3}\,\mathrm{M}_{\odot}\,\mathrm{yr}^{-1}$) and obtain a precise spectroscopic redshift estimate at the same time (Inami et al., 2017). These data provides a unique view into the low-mass regime of the star formation sequence.

In this paper we present a characterisation of the low-mass end of the M_*-SFR relation, using deep MUSE observations of the HUDF and HDFS. We characterise the properties of the M_*-SFR relation down stellar masses of $M_* \sim 10^8\,\mathrm{M}_{\odot}$ and SFR $\sim 10^{-3}\,\mathrm{M}_{\odot}\,\mathrm{yr}^{-1}$, out to $z < 1$, and trace the SFR in individual galaxies with masses as low as $M_* \leq 10^7\,\mathrm{M}_{\odot}$ at $z \sim 0.2$. We model the relation using a self-consistent Bayesian framework and describe it with a Gaussian distribution around a plane in (log mass, log SFR, log redshift)-space. This allows us to simultaneously constrain the slope and evolution of the star formation sequence as well as the amount of intrinsic scatter, while taking into account heteroscedastic errors (i.e. a different uncertainty for each data point).

The structure of the paper is as follows. In § 2.2 we first introduce the MUSE data set and outline the selection criteria used to construct our sample of star-forming galaxies. We then go into the methods used to determine a robust stellar mass and a SFR from the observed emission lines. Before looking at the results, we discuss the consistency of our SFRs in § 2.3. We then introduce the framework of our Bayesian analysis used to characterise the M_*-SFR relation (§ 2.4) and present the results in § 2.5. We discuss the robustness of the derived parameters in § 2.A.1. Finally, we discuss our results in the context of the literature and models, and the physical implications (§ 2.6). We summarise with our conclusions in § 2.7. Throughout this paper we assume a Chabrier (2003) stellar initial mass function and a flat ΛCDM cosmology with $H_0 = 70\,\mathrm{km\,s^{-1}\,Mpc^{-1}}$, $\Omega_m = 0.3$ and $\Omega_\Lambda = 0.7$.

2.2 Observations and methods

To study the properties of the galaxy population down to low masses and star formation rates, deep spectroscopic observations are required for a large number of sources. We exploit the unique observations taken with the MUSE instrument over the *Hubble* Ultra Deep Field (Bacon et al., 2017) and the *Hubble* Deep Field South (Bacon et al., 2015) to investigate the star formation rates in low-mass galaxies at $0.11 < z < 0.91$. We provide a brief presentation of the observations and data reduction in the next section, but refer to the corresponding papers for details.

The MUSE instrument is an integral-field spectrograph situated at UT4 of the Very Large Telescope. It has a field-of-view of $1' \times 1'$ when operating in wide-field-mode, which is fed into 24 different integral-field units. These sample the field-of-view at $0.2''$ resolution. The spectrograph covers the spectrum across 4650Å - 9300 Å with a spectral resolution of $R \equiv \lambda/\Delta\lambda \simeq 3000$. The result of a MUSE observation is a data cube of the observed field, with two spatial and one spectral axes, i.e. an image with spectroscopic information at every pixel.

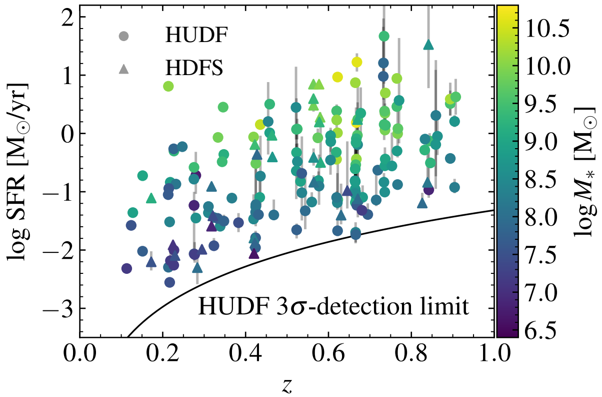

Figure 2.1: Redshift distribution of our galaxies plotted against their (dust-corrected) SFR (1σ error bars are in grey). The colour denotes the stellar mass. The solid line depicts the lowest uncorrected SFR from Hβ λ4863 we can detect in the HUDF at each redshift (which is effectively determined by the requirement that S/N(Hγ λ4342) > 3; see § 2.2.4).

2.2.1 Observations, data reduction, and spectral line fitting

The HUDF (Beckwith et al., 2006) was observed with MUSE in a layered strategy. The deepest region consists of a single $1' \times 1'$ pointing with a total integration depth of 31 hours. This deep region lies embedded in a larger $3' \times 3'$ mosaic consisting of 9 individual MUSE pointings, each of which is 10 hours deep. The average full width at half maximum (FWHM) seeing measured in the data cubes is 0.6 ″ at 7750 Å. For the purpose of this work we use all galaxies from the `mosaic` region, including the deep (`udf10`) region, which we refer to collectively as the (MUSE) HUDF.

Because of its similar depth, we also include the MUSE observation of the HDFS (Williams et al., 2000) which was observed as part of the commissioning activities. These observations consist of a single deep field ($1' \times 1'$) with a total integration time of 27 hours and a median seeing of 0.7 ″.

The full data acquisition and reduction of the HUDF is detailed in Bacon et al. (2017) (for a description of the MUSE data reduction pipeline see Weilbacher et al., in prep.[19]). The data reduction of the HUDF is essentially based on the reduction of the HDFS, which is detailed in Bacon et al. (2015), with several improvements. We use HUDF version 0.42 and HDFS version 1.0, which reach a 3σ-emission line depth for a point source (1 ″) of 1.5 and 3.1×10^{-19} erg s^{-1} cm^{-2} (`udf10` and `mosaic`) and 1.8×10^{-19} erg s^{-1} cm^{-2} (HDFS), measured between the OH skylines at 7000 Å.

Sources in the HUDF were identified using both a blind and a targeted approach. The latter uses the sources from the UVUDF catalogue (Rafelski et al., 2015) as prior information to extract objects from the MUSE cube. A blind search of the full cube was also conducted, using a tool specifically developed for MUSE cubes called ORIGIN (Bacon et al. 2017; Mary et al., in prep.[20]). A similar approach was already followed for the HDFS. Here sources were identified based on the Casertano et al. (2000) catalogue and blind emission line searches of the data cube were done with the automatic detection tools MUSELET[21] and LSDCat (Herenz & Wisotzki, 2017) as well as through visual inspection, and cross-correlated with the corresponding photometric catalogue, as described in Bacon et al. (2015).

---

[19] Weilbacher et al. (2020)

The process of determining redshifts and constructing a full catalogue from the extracted sources is described in Inami et al. (2017) for the HUDF (and a similar approach was followed for the HDFS). In short, redshifts were determined semi-automatically by cross-matching template spectra with the identified sources and subsequently inspected and confirmed by at least two independent investigators. For emission line galaxies an additional constraint comes from the requirement that the emission line flux is coherent in a narrow band image around the line in the MUSE cube. The typical error on the MUSE spectroscopic redshifts is $\sigma_z = 0.00012(1 + z)$ (Inami et al., 2017), which we will take into account in the modelling (conservatively taking $\sigma_{\log(1+z)} = 0.0005$ for all galaxies; § 2.4)

For all detected sources one dimensional spectra are extracted using a straight sum extraction over an aperture around each source (based on the MUSE point spread function convolved with the Rafelski et al. (2015) segmentation map, see Bacon et al. 2017). From the extracted 1D spectra emission line fluxes are fitted in velocity space, using an updated version of the PLATEFIT code described in Tremonti et al. (2004) and Brinchmann et al. (2004, 2008). PLATEFIT assumes a Gaussian line profile for all lines, with the same intrinsic width and velocity. The result is a measurement of the flux and equivalent width of all emission lines present, with the uncertainties obtained from propagating the original pipeline errors. We define the signal-to-noise (S/N) in a particular spectral line as the line flux over the line flux error. We also determine the strength of the 4000 Å break, $D_n(4000)$, measured over 3850 − 3950Å and 4000 − 4100Å (Kauffmann et al., 2003). We note that the stellar absorption underlying the emission lines is taken into account by PLATEFIT.

2.2.2 Sample selection

From the HUDF and HDFS catalogues we construct our sample of star-forming galaxies using the following constraints:

1. We use Hβ λ4863 or Hα λ6565 to derive the SFR (see § 2.2.4) and in either case we always need Hβ λ4863 (to directly probe the SFR or to correct for dust extinction in Hα λ6565). As a result, we are limited to the range of redshifts where Hβ λ4863 falls within the MUSE spectral range. Subsequently, we only take objects into account that have a redshift $z < (9300/4861) - 1 = 0.913$.

2. In order to derive a robust SFR and dust correction, we only allow objects with a signal-to-noise ratio > 3 in the relevant pair of Balmer lines. This means S/N > 3 in either Hβ λ4863 and Hγ λ4342 (for Hβ λ4863 derived SFRs) or Hα λ6565 and Hβ λ4863 (for Hα λ6565 derived SFRs).

---

[20] Mary et al. (2020)

[21] https://mpdaf.readthedocs.io/en/latest/muselet.html

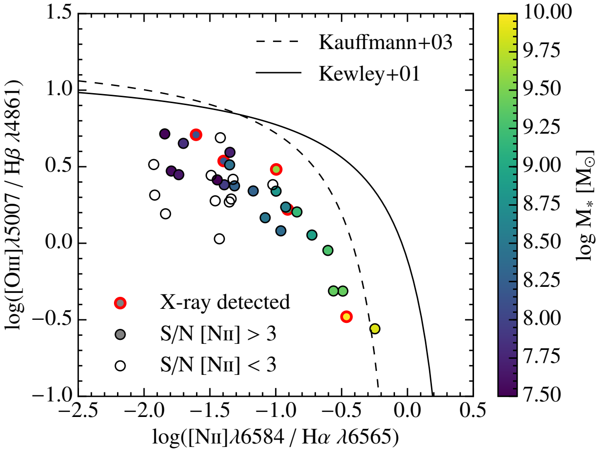

Figure 2.2: BPT-diagram (Baldwin et al., 1981) of the sources in our Hα λ6565-subsample for which we measure [N II] λ6585. All galaxies fall in the star-forming region of the diagram. The filled and open circles have S/N([N II] λ6585) > 3 and < 3, respectively, and the 5 sources encircled in red are detected in X-rays (Luo et al., 2017). The solid and dashed curve show the AGN boundary and maximum starburst line from Kauffmann et al. (2003) and Kewley et al. (2001), respectively.

Included in the above criteria are some galaxies that are not actively star-forming and lie on the 'red-sequence'. Since these galaxies are not expected to lie on the M_*-SFR relation, we exclude them from the analysis based on their spectral features:

3. We remove 12 galaxies with a strong 4000 Å break by only allowing galaxies with a $D_n(4000) < 1.5$.

4. We omit galaxies with a rest-frame equivalent width in either Hα λ6565 or Hβ λ4863 of < 2Å.[22] This removed an additional 7 and 5 objects, respectively.

In addition, three sources were removed from the sample due to severe artefacts in their emission lines (see § 2.3). All sources selected based on the MUSE data are detected in the *HST* imaging. However, four sources were removed because there photometry was severely blended, prohibiting a mass estimate.

5. We remove potential AGN from our sample in the HUDF by cross-matching our sources with the *Chandra* Deep Field South 7Ms X-ray catalogue (Luo et al., 2017). We also confirm the location of the sources in the star-forming region of different emission line diagnostic diagrams.

A total of 16 galaxies with $z < 0.913$ from the MUSE catalogue are detected in X-rays. Five of these sources (including one AGN) show passive spectra without emission lines and did not

---

[22] Following the convention that emission-line equivalent widths (EQW) are negative, this translates to excluding EQW > −2Å.

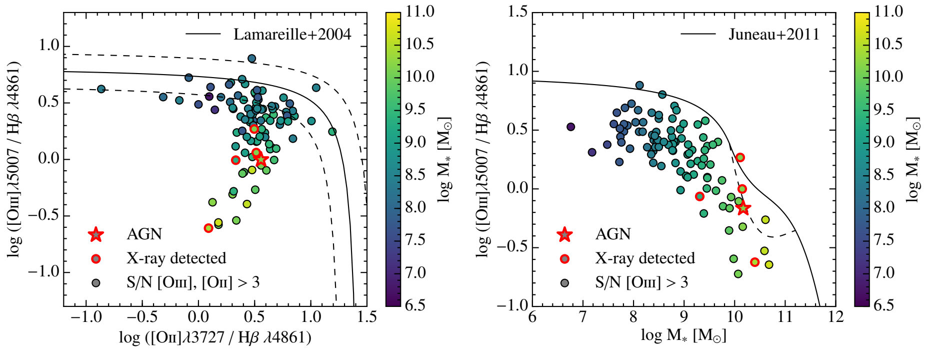

Figure 2.3: AGN diagnostics for the sources in our Hβ λ4863-subsample, including all sources which have S/N> 3 in the relevant emission lines. Overall, our sample is consistent with star-forming galaxies. We remove one X-ray detected AGN from the sample. Left: The [O ii] λλ3727, 3730/Hβ vs. [O iii] λλ4960, 5008/Hβ diagnostic from Lamareille et al. (2004) (solid line, with the uncertainty indicated by the dashed lines). Right: The mass-excitation diagram from Juneau et al. (2011). Galaxies in the region between the dashed and solid lines are on average identified as intermediate between AGN and SF.

pass the previous criteria. Cross-matching our star-forming sample (after applying criteria 1 through 4) left 11 galaxies that were detected in X-rays. Five of these sources (ID#855, 861, 863, 895, and 902) are in the Hα-subsample and six (ID#867, 869, 874, 875, 884, and 905) are in the Hβ-subsample. All of these sources were classified as 'Galaxy' in the Luo et al. (2017) catalogue (according to their 6 criteria based on X-ray luminosity, spectral index, flux-ratios and previous spectroscopic identification), except for ID# 875 which was classified as an AGN and which we subsequently removed from the sample. Luo et al. (2017) caution however that sources classified as 'Galaxy' may still host low-luminosity or heavily obscured AGN.

We plot all sources from our Hα λ6565-subsample for which we have a measurement of [N ii] λ6585 in the BPT-diagram (Baldwin et al., 1981) in Figure 2.2. We include sources for which we have a low S/N (<3) measurement of [N ii] λ6585 as open circles. While we can only put a subsample of our sources on this diagram, all are in the star-forming region, including the 5 galaxies which have an X-ray detection. None of the X-ray sources classified as 'Galaxy' show spectral signatures of AGN activity. In Figure 2.3 we show a similar consistency check for the Hβ λ4863-subsample. Because we lack access to the BPT diagram at these redshift, we instead use the diagnostics from both Lamareille et al. (2004) and Juneau et al. (2011). Reassuringly, our sample is overall consistent with star-forming galaxies and none of the galaxies show line-ratios clearly powered by AGN activity (including, perhaps surprisingly, the single X-ray classified AGN). There is only one source which is above the discriminating line in both plots (ID#1114), however, it is consistent within errors with being dominated by star formation and not detected in X-rays. Furthermore, its high [O iii] flux can very well be driven by star formation and indeed it is part of the sample of high-[O iii]/[O ii] galaxies identified by Paalvast et al. (2018). Hence, except for X-ray detected AGN ID#875, we do not

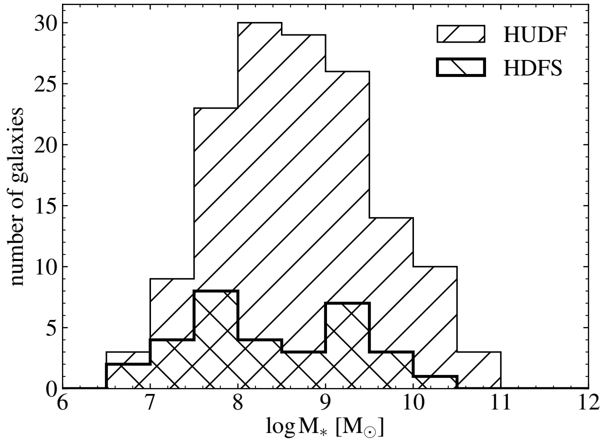

Figure 2.4: Histograms of the stellar mass distributions of the MUSE detected galaxies in the HUDF and the HDFS. The deep 30h observations allow us to detect and subsequently infer a stellar mass and SFR for galaxies down to $\sim 10^7$ M$_\odot$.

remove any additional sources from the sample. Finally, we note that none of the methods to identify AGN are individually foolproof. Therefore, we check the impact of potential misclassification of AGN and confirm that excluding (1) the sources that are above the pure star-forming line in either of the diagnostic diagrams or (2) all galaxies that are detected in X-rays (even when consistent with star formation) does not significantly affect the results.

The final sample then consists of 179 star-forming galaxies, 147 from the HUDF, all with the highest redshift confidence (Inami et al., 2017), and 32 from the HDFS, between $0.11 < z < 0.91$ with a mean redshift of 0.53 (see Figure 2.1).

2.2.3 Stellar masses

The stellar masses of the galaxies were estimated using the Stellar Population Synthesis (SPS) code FAST (Kriek et al., 2009). The SPS-templates were χ^2-fitted to the broad-band photometry of the different fields for a range of parameters. For the HUDF, we rely on the deep *HST* photometry from the UVUDF catalogue (Rafelski et al., 2015) (containing WFC3/UVIS F225W, F275W and F336W; ACS/WFC F435W, F606W, F775W, and F850LP and WFC/IR F105W, F125W, F140W and F160W) while for the HDFS we take the WFPC2 photometry from Casertano et al. (2000) (F330W, F450W, F606W, and F814W). The SPS-templates were constructed from the Conroy et al. (2010) (FSPS) models using a discrete range of metallicities ($Z/Z_\odot = [0.04, 0.20, 0.50, 1.0, 1.58]$). We assumed a Chabrier (2003) initial mass function with an exponentially declining star formation history (SFR $\propto \exp(-t/\tau)$ with $8.5 < \log(\tau/\mathrm{yr}) < 10$ in steps of 0.2 dex). The redshifts were fixed to the accurate spectroscopic values determined from the MUSE spectra. Ages were allowed to vary between $8 < \log \mathrm{Age/yr} < 10.2$ in steps of 0.2 dex. We parameterised the dust attenuation curve according to the Calzetti et al. (2000) dust law with the dust extinction in the visual taken to be within $0 < A_V < 3$ ($\Delta A_V = 0.1$ magnitudes). For all the parameters error estimates were obtained through Monte Carlo methods, by re-running the fitting 500 times while varying the input photometry within their photometric errors (see Kriek et al. 2009 for details).

Stellar masses were determined for all 179 objects in the final sample. The distribution of masses is shown in Figure 2.4. With these deep MUSE observations we are mainly probing low-mass ($<10^{9.5}$ M$_\odot$) galaxies and we can still detect star formation from emission lines in galaxies with mass $\sim10^7$ M$_\odot$. The mass estimates with their upper and lower confidence intervals are shown for the individual objects in Figure 2.7. The mean and standard deviation of the average errors on the mass estimates are 0.19 ± 0.06 dex for the HUDF and 0.22 ± 0.12 dex for the HDFS.

2.2.4 Star formation rates

The star formation rates are inferred from the flux in the H$\alpha\,\lambda$6565 or H$\beta\,\lambda$4863 recombination lines emitted by H II regions, which primarily trace recent ($\sim$10 Myr) massive star formation. Before we can infer a SFR we need to correct the measured flux in the emission lines for the attenuation by dust along the line of sight. We do this assuming a dust law according to Charlot & Fall (2000) (i.e. $\tau \propto \lambda^{-1.3}$, appropriate for birth clouds) and using the intrinsic ratio of the Balmer recombination lines ($j_{\mathrm{H}\alpha}/j_{\mathrm{H}\beta} = 2.86$ and $j_{\mathrm{H}\beta}/j_{\mathrm{H}\gamma} = 2.14$; Hummer & Storey (1987), for an electron temperature and density of $T = 10\,000$ K and $n_e = 10^3$ cm^{-3}). Hence, to derive an SFR(H$\alpha\,\lambda$6565) we also require a measurement of H$\beta\,\lambda$4863 and likewise for SFR(H$\beta\,\lambda$4863) we also require H$\gamma\,\lambda$4342. After the dust correction we can convert the intrinsic flux to a luminosity using the measured redshift, given the assumed ΛCDM cosmology.

To determine the SFR we follow the treatment by Moustakas et al. (2006), which is essentially based on the relations from Kennicutt (1998a). Out of the SFR indicators that MUSE has access to, the H$\alpha\,\lambda$6565 line presents the least systematic uncertainties, but it is only available at low redshifts ($z \leq 0.42$ for MUSE at 9300 Å; 47 galaxies). We convert the Kennicutt (1998a) relation from a Salpeter to a Chabrier IMF ($0.1 < M[\mathrm{M}_\odot] < 100$) by multiplying by a factor 0.62 (which is derived by computing the difference in total mass in both IMFs, while assuming the same number of massive ($>$10 M$_\odot$) stars):

$$\mathrm{SFR}(\mathrm{H}\alpha\,\lambda6565) = 4.9 \times 10^{-42} \frac{L(\mathrm{H}\alpha\,\lambda6565)}{\mathrm{ergs}^{-1}} \mathrm{M}_\odot\,\mathrm{yr}^{-1}, \tag{2.1}$$

where $L(\mathrm{H}\alpha\,\lambda6565)$ is the dust-corrected luminosity. We note that this calibration assumes case B recombination and solar metallicity.

Because H$\alpha\,\lambda$6565 moves out of the optical regime at $z > 0.42$, the H$\beta\,\lambda$4863 luminosity is the primary tracer of SFR for the majority of our sample (132 galaxies). Given the intrinsic flux ratio between H$\alpha\,\lambda$6565 and H$\beta\,\lambda$4863, we can convert equation Equation 2.1 into a SFR for $L(\mathrm{H}\beta\,\lambda4863)$:

$$\mathrm{SFR}(\mathrm{H}\beta\,\lambda4863) = 1.4 \times 10^{-41} \frac{L(\mathrm{H}\beta\,\lambda4863)}{\mathrm{ergs}^{-1}} \mathrm{M}_\odot\,\mathrm{yr}^{-1}, \tag{2.2}$$

where $L(\mathrm{H}\beta\,\lambda4863)$ is corrected for dust. We note that the Hβ λ4863 derived SFR inherits all the uncertainties from SFR(Hα λ6565), including variations in dust reddening (Moustakas et al., 2006).

We also investigate the SFR using the [O ii] $\lambda\lambda$3727, 3730 nebular emission line. Here we use the calibration for the Hα λ6565 SFR (Equation 2.1), where we assume an intrinsic flux ratio between [O ii] $\lambda\lambda$3727, 3730 and Hα λ6565 of unity (Moustakas et al., 2006). Since [O ii] $\lambda\lambda$3727, 3730 is closest to Hβ λ4863, we use the Hβ λ4863/Hγ λ4342 ratio to determine the dust correction, scaled to the appropriate wavelength. The consequence of this is that the addition of the [O ii] $\lambda\lambda$3727, 3730 line as a tracer of SFR will not add any new objects to the sample. Instead, it can be used as a useful comparison, which will be discussed in § 2.3.

To estimate the uncertainty in the SFR estimates (and dust corrections), we use Monte Carlo methods to derive a confidence interval on the SFR of every individual galaxy. We create a posterior distribution on the SFR by doing 1000 draws from a Gaussian distribution centred on the measured flux, with the variance set by the measurement error squared. The median posterior SFR can then be determined, as well as the $\pm1\sigma$ confidence intervals, by taking the 50$^{\mathrm{th}}$, 16$^{\mathrm{th}}$ and 84$^{\mathrm{th}}$ percentile from the derived posterior distribution.

2.3 Consistency of SFR indicators

Before turning to the results, we first consider the consistency of the derived SFRs, by comparing the SFR estimates from different tracers for the same galaxies. In the remainder of the paper we only use the dust-corrected Balmer lines as tracers of star formation.

For a significant fraction of our galaxies ($\approx$ 40%) we find that the Balmer line ratios are below their case B values (as stated in § 2.2.4), indicative of a negative dust correction. While this might seem surprising, this is not uncommon and similar ratios have been seen in spectra from, e.g. the SDSS (Groves et al., 2012), MOSDEF (Reddy et al., 2015), KBSS (Strom et al., 2017) and ZFIRE (Nanayakkara et al., 2017). While 'unphysical', these ratios are not entirely unexpected and can have several causes.

First, these deviations can be caused by noisy spectra. Most galaxies in our sample are not very dusty and hence have a ratio close to case B. In $>$ 50% of the cases with deviant ratios, the case B ratio is indeed within the 1σ error bars. We conservatively apply no dust correction for all these galaxies. The mean dust correction for all galaxies in our sample is $\tau(\mathrm{H}\beta/\mathrm{H}\gamma) \approx 0.6$ (setting galaxies with a negative dust correction to zero) or $\tau(\mathrm{H}\beta/\mathrm{H}\gamma) \approx 1$ (including only galaxies with a positive dust correction).

Secondly, there could be a problem with the measurement. Three objects that were significantly offset from the rest of the sample showed particular problems in their emission lines. In one object (ID#971) Hγ λ4342 was severely affected by an emission line from a nearby source ([O iii] λ4960 from ID#874 at $z = 0.458$, another galaxy in our sample, coincidentally almost exactly at the observed wavelength of Hγ). For five other objects there was a clear problem with the fit to the Hβ λ4863 (ID#894, #896, #1027) or Hα λ6565 (ID#2, #1426) emission lines. We subsequently removed the first four sources from the analysis; for the latter two we disregarded the Hα λ6565 SFR and use the Hβ λ4863 SFR.

A third, intriguing option is that theses objects are real. Indeed, there remains a small

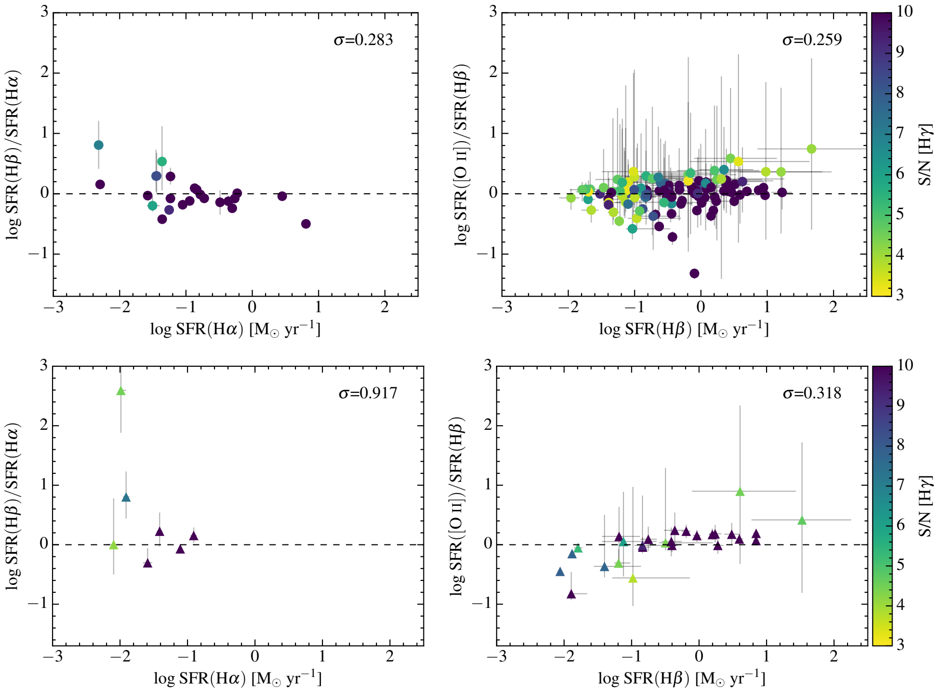

Figure 2.5: A comparison of the derived star formation rate (SFR) from the Hα λ6565, Hβ λ4863 and [O II] $\lambda\lambda$3727, 3730 luminosities for the HUDF (top panels, circles) and the HDFS (bottom panels, triangles). The left panels show the logarithm of the SFR from Hα λ6565 vs. the difference between the log Hβ λ4863 and log Hα λ6565 SFRs. The right panels show the same for Hβ λ4863 vs. [O II] $\lambda\lambda$3727, 3730. In the top right corners σ indicates the standard deviation (in dex) around the one-to-one relation. Colour indicates the signal-to-noise ratio (S/N) in the faintest line; Hγ λ4342. Only galaxies that allowed for more than one SFR indicator are included in the plot. Overall the SFRs from Hβ λ4863 and [O II] $\lambda\lambda$3727, 3730 agree reasonably well, considering we have not taken into account the metallicity dependence in SFR([O II] $\lambda\lambda$3727, 3730). The scatter in Hα λ6565 vs. Hβ λ4863 SFR is largely driven by Hγ λ4342 S/N.

number of galaxies which have high-S/N spectra, but still show Balmer ratio's below their case B values.[23] Similar objects have also been observed in the other surveys already referenced, such as SDSS (Jarle Brinchmann, private communication, see also Groves et al. 2012). While these are very interesting objects on their own, a detailed analysis of these sources is beyond the scope of this paper. To be conservative and consistent, we apply no dust correction for these sources.

For some objects in the sample we measure multiple emission lines, which allows us to infer a SFR from different tracers. In any case a pair of Balmer lines (either Hα/Hβ or Hβ/Hγ)

---

[23] It is important to point out that this is not caused by stellar absorption in the continuum as this is taken into account when modelling the emission lines with PLATEFIT.

is available (§ 2.2.2), to allow for a dust correction. The majority of our sample lies at $z > 0.42$ for which Hα λ6565 is not available, but (dust-corrected) [O II] $\lambda\lambda$3727, 3730 is available as an SFR indicator. In Figure 2.5 we show a comparison for all galaxies that allowed both Hα λ6565 and Hβ λ4863 (only some galaxies at $z < 0.42$) and Hβ λ4863 and [O II] $\lambda\lambda$3727, 3730 derived SFRs (all redshifts). We note that Hβ λ4863 and [O II] $\lambda\lambda$3727, 3730 derived SFRs are corrected for dust using the same Hβ/Hγ-ratio.

In the right panels of Figure 2.5 we see that the Hβ λ4863 and [O II] $\lambda\lambda$3727, 3730 derived SFRs agree remarkably well (standard deviation $\sigma \leq 0.28$ dex), considering that we have not taken into account the metallicity dependence of the [O II] $\lambda\lambda$3727, 3730 luminosity in the SFR conversion factor (e.g. Kewley et al., 2004). A few points scatter quite a bit, most of which have large error bars. At lower SFRs we do see that [O II] $\lambda\lambda$3727, 3730 predicts a lower SFR than Hβ λ4863, which is probably because at low SFR we are also probing low-mass and low-metallicity galaxies. Stars with a lower metallicity have a higher UV flux, which causes the ionisation equilibrium for oxygen to shift from [O II] to [O III] which diminishes the observed [O II] $\lambda\lambda$3727, 3730 flux. Because of the opposite effect [O II] $\lambda\lambda$3727, 3730 occasionally predicts a higher SFR than Hβ λ4863 at the high-SFR end.

For a limited number of objects all three Balmer lines are in the spectral range of MUSE ($0.09 < z < 0.42$). We compare the Hα λ6565 and Hβ λ4863 derived SFRs in the left panel of Figure 2.5, where we find reasonable agreement (in the HUDF, where we have most sources, they have a factor of ~ 2 scatter). Most of the scatter is found at low SFR, where (on average) the S/N is also the lowest. In the HDFS one object (at low S/N) is a strong outlier, but removing this source yields a similar scatter to the HUDF. Intuitively the SFRs from Hα and Hβ should agree very well, which warrants some deeper investigation into the outliers at low SFR.

The main uncertainty in the SFR estimate is the amount of dust attenuation. In Figure 2.6 we compare the inferred optical depth from the Hβ/Hγ-ratio (τ[Hβ/Hγ]) to the optical depth determined from the Hα/Hβ ratio (τ[Hα/Hβ]). We note though that Figure 2.6 shows the measured optical depth, while we set negative τ to zero before computing the SFR. Indeed, while many sources agree well, we see that the amount of dust correction estimated from the Balmer lines is not consistent for several objects, leading to a different SFR estimate from Hα λ6565 and Hβ λ4863.

This tension is in part caused by the nature of the experiment, which requires that all three Balmer lines are in the spectral range of MUSE simultaneously. Necessarily then, Hα λ6565 will be at the long wavelength end of the spectrograph where skylines are more prevalent, occasionally adding uncertainty to its measurement. For the low-SFR sources, however, Hγ λ4342 might not be very bright, adding uncertainty to the dust correction of SFR(Hβ λ4863) for these sources (as seen at lower SFR in the left panels of Figure 2.5). Indeed, most of the outliers have a low S/N in Hγ λ4342 (as stated earlier, for the objects with a negative dust correction from Hβ/Hγ, we leave the often lower S/N measurement of Hγ λ4342 out of the analysis by setting τ(Hβ/Hγ) to zero). On the other hand, the converse is not quite true: for a large number of sources with a low S/N in Hγ λ4342 we do have a consistent SFR estimate. For all objects we use the highest S/N lines available to infer a dust-corrected SFR, i.e. for objects which have a measurement of all three Balmer line we use the Hα λ6565, Hβ λ4863 pair to infer a dust-corrected SFR, which generally has the highest S/N.

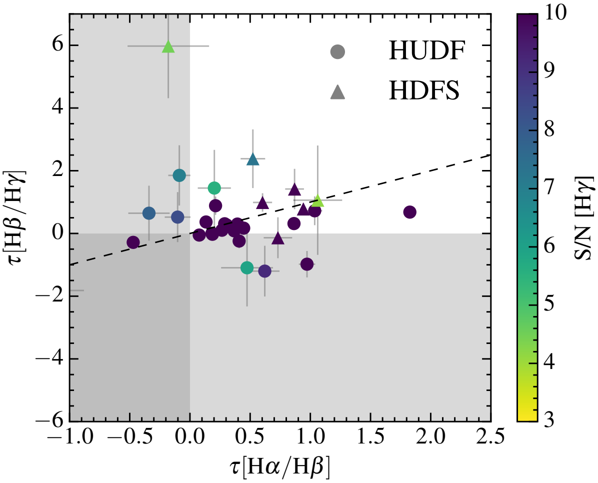

Figure 2.6: Optical depths at the wavelength of Hβ λ4863 as derived from both the Hβ λ4863/Hγ λ4342 and the Hα λ6565/Hβ λ4863-ratio, coloured by Hγ λ4342 signal-to-noise (S/N). The dashed line is the one-to-one relation. Overall the optical depths agree reasonably well, unless the Hγ S/N is low. Most galaxies actually show little dust (τ close to zero). The shaded area shows the regions of (unphysical) negative optical depth for each axis. We set the optical depth to zero for galaxies with negative τ as this is often consistent with the error bars and the offset is due to noise in the spectra. We note that some of the high-S/N outliers actually have discrepant Balmer ratios. If the inferred optical depth is very different, this will affect the comparison of the dust-corrected SFR from Hβ λ4863 and Hα λ6565 (see Figure 2.5).

In summary, we have dust-corrected SFR measurement from the Hα λ6565 and Hβ λ4863 spectral lines for all galaxies at $z < 0.42$ and the Hβ λ4863, Hγ λ4342-pair at higher redshifts. Comparing Hα λ6565 and Hβ λ4863 SFRs, we conclude that the dust correction is the largest uncertainty on the derived SFR. We always use the highest S/N line-pair available to compute a dust-corrected SFR. Comparing the Hβ λ4863 SFRs with [O II] $\lambda\lambda$3727, 3730 at all redshifts, we see a very consistent picture (they have ≤ 0.3 dex scatter in both fields). Naturally, some variations between Hβ λ4863 and [O II] $\lambda\lambda$3727, 3730 SFRs are expected given the metallicity dependent nature of [O II] $\lambda\lambda$3727, 3730.

2.4 Bayesian model

2.4.1 Definition

The star formation sequence is commonly described by a power-law relation between stellar mass (M_*) and star formation rate (SFR), which evolves with redshift (z):

$$\mathrm{SFR} \propto M_*^a (1+z)^c, \tag{2.3}$$

where a and c are the power law exponents. It has been suggested that the slope (a) becomes shallower in the high-mass regime ($M_* > 10^{10}\,\mathrm{M}_\odot$). In this work we will focus on the low-mass regime, for which we assume the slope is constant with mass. We will revisit this assumption in § 2.5.2. Given the lack of homogeneous studies with redshift it is still unclear whether the low-mass slope of the relation evolves with redshift. Here, we assume that the low-mass slope is independent of redshift over the range that we probe in this study. Likewise, given the large uncertainties in (the evolution of) the intrinsic scatter, we limit the number of free parameters in the model and assume that the intrinsic scatter does not depend on any of the other model parameters.

Following this description, we model the star formation sequence by a plane in ($\log M_*$, $\log(1+z)$, $\log \mathrm{SFR}$)-space:

$$\log \mathrm{SFR}[\mathrm{M}_\odot\,\mathrm{yr}^{-1}] = a \log\left(\frac{M_*}{M_0}\right) + b + c \log\left(\frac{1+z}{1+z_0}\right), \tag{2.4}$$

where b is now a normalisation constant. We take $M_0 = 10^{8.5}\,\mathrm{M}_\odot$ and $z_0 = 0.55$ (close to the medians of the data) without the loss of generality. Galaxies scatter around this relation with an amount of intrinsic scatter in the vertical (i.e. $\log \mathrm{SFR}$) direction, which we denote by σ_{intr}. In the lack of an obvious alternative, we take the intrinsic scatter to be Gaussian in our model.

In a statistical sense we can then say that our observations ($\log M_*$, $\log(1+z)$, $\log \mathrm{SFR}$) are drawn from a Gaussian distribution around the plane defined by Equation 2.4. To recover this distribution, we need to take a careful approach, taking into account the heteroscedastic errors of the measurements.

We adopt a Bayesian approach to determine the posterior distribution of the model parameters (a, c, b, σ_{intr}) (see Andreon & Hurn (2010) for a lucid description of the Bayesian methodology in an astronomical context). Different approaches to construct the likelihood have been presented in the literature (see e.g. Kelly 2007 or Hogg et al. 2010). We choose to adopt a parameterisation of the likelihood following Robotham & Obreschkow (2015) (hereafter R15).

First, we state that our knowledge about galaxy i (determined by the observations) is encompassed by the probability density function of a multivariate Gaussian distribution, $\mathcal{N}(\mathbf{x}_i, C_i)$, with a mean value of:

$$\mathbf{x}_i = (\log M_{*,i}, \log(1+z_i), \log \mathrm{SFR}_i) \tag{2.5}$$

and a diagonal covariance matrix:

$$C_i = \begin{pmatrix} \sigma^2_{\log M_*,i} & 0 & 0 \\ 0 & \sigma^2_{\log(1+z),i} & 0 \\ 0 & 0 & \sigma^2_{\log \mathrm{SFR},i} \end{pmatrix} \tag{2.6}$$

containing the variance in each parameter. This is justified as both stellar mass and star formation rate are measured independently from different data. The covariance with redshift is negligible as the error on the spectroscopic redshift is very small.

Secondly, we parameterise the model given by Equation 2.4 (which is a plane in three dimensions) in terms of its normal vector $\mathbf{n}$, to avoid optimisation problems (R15). The galaxies scatter around this plane with an amount of intrinsic Gaussian scatter, perpendicular to the plane, which we denote by $\sigma_\perp$. We note that perpendicular scatter $\sigma_\perp$ is distinct from the (commonly reported) vertical scatter σ_{intr} which lies in the log SFR direction. After the analysis, we can simply transform the parameters $(\mathbf{n}, \sigma_\perp^2)$ back into familiar parameters $(a, c, b, \sigma_{\text{intr}}^2)$ (using R15, Eq. 9).

Given the above definitions, we can express our log-likelihood[24] as the sum over N data points (see also R15):

$$\ln \mathcal{L} = -\frac{1}{2} \sum_{i=1}^{N} \left[\ln \left(\sigma_\perp^2 + \frac{\mathbf{n}^\top C_i \mathbf{n}}{\mathbf{n}^\top \mathbf{n}} \right) + \frac{(\mathbf{n}^\top [\mathbf{x}_i - \mathbf{n}])^2}{\sigma_\perp^2 \mathbf{n}^\top \mathbf{n} + \mathbf{n}^\top C_i \mathbf{n}} \right], \tag{2.7}$$

where all the parameters have been defined earlier.

Lastly, we have to define our priors on each component of $\mathbf{n}$ and on $\sigma_\perp^2$. As we want to impose limited prior knowledge, we express our priors as uniform distributions, with large bounds compared to the typical values of the parameters (we confirm that the results are robust, irrespective of the exact choice of bounds).

$$\begin{aligned} \mathbf{n} &\sim \mathcal{U}^3(-1000, 1000) \\ \sigma_\perp^2 &\sim \mathcal{U}(0, 1000), \end{aligned} \tag{2.8}$$

where $\mathcal{U}^n$ is the n-dimensional multivariate uniform distribution and we take into account the fact that variance is always positive.

2.4.2 Execution

With the likelihood and priors in hand we determine the posterior using *Markov chain Monte Carlo* (MCMC) methods. We use the Python implementation called EMCEE (Foreman-Mackey et al., 2013), which utilises the affine-invariant ensemble sampler for MCMC from Goodman & Weare (2010). EMCEE samples the parameter space in parallel by setting off a predefined number of 'walkers', which we take to be 250.

Following Foreman-Mackey et al. (2013), we first initialise the walkers randomly in a large volume of parameter space. We then restart the walkers in a small Gaussian ball around the median of the posterior distribution (i.e. around the 'best solution'). We (generously) burn in for a quarter of the total amount of iterations for each walker which we take to be 20000 for the main run (§ 2.5.1; roughly four hundred times the autocorrelation time). We note that for all subsequent runs described below we follow the same procedure, with similar results.

We take several steps to check whether the EMCEE algorithm has properly converged. As an indication, one can look at both the mean acceptance fraction of the samples as well as the autocorrelation time (Foreman-Mackey et al., 2013). For the main run the acceptance fraction that resulted from the modelling (0.45) was well within range advocated by Foreman-Mackey

---

[24] Throughout this paper we consistently use 'log' for the base-10 logarithm and 'ln' for the base-e logarithm, with one exception: we stick to standard terminology and call $\ln \mathcal{L}$ the 'log-likelihood'.

et al. (2013) (0.2 - 0.5). The autocorrelation time was also relatively short and we let the walkers sample the posterior well over the autocorrelation time. Furthermore, we confirmed that the walkers properly explored the parameter space.

Combining the results from all walkers then gives the posterior distribution over which we can marginalise to find the posterior probability distributions for the model parameters. We will discuss the results of the modelling in § 2.5.

2.4.3 Model and data limitations

The unique aspect of the likelihood in Equation 2.7 is that it captures both the heteroscedastic errors on the observables as well as the intrinsic scatter around the plane. Furthermore, it can simultaneously describe both the slope of the sequence as well as the evolution with redshift.

It is important to determine how well we can recover the 'true' parameters with the observed data at hand. Our MUSE observations are constrained by the fact that we can only detect galaxies in a certain redshift range and cannot detect galaxies below the flux limit of the instrument (see Figure 2.1). As the flux limit varies with redshift, this could introduce a bias in our inferred parameters. The reason behind this is that the lack of low-SFR galaxies at higher redshift will bias the posterior towards shallower slopes, with a steeper redshift evolution (see Figure 2.11 for an illustration). In order to correct for such a bias, we analyse a series of simulated observations. We briefly outline the procedure here, which is described in detail in § 2.A.

In order to characterise the bias in the inferred parameters, we simulate galaxies from a mock star formation sequence for a range of values in each parameter, which we call $\mathbf{x}_{\mathrm{true,k}}$ (see Table 2.2). After applying the redshift-dependent flux limit to the mock data, we model the remaining galaxies as described in § 2.4 and recover the parameters, $\mathbf{x}_{\mathrm{out,k}}$. We then fit the transformation between the true and recovered parameters with an affine transformation ($\mathbf{x}_{\mathrm{out,k}} = A\mathbf{x}_{\mathrm{true,k}} + \mathbf{b}$) as outlined in § 2.A.2. The inverse of the best-fit transformation (Equation 2.19) can then be used to correct the posterior density distribution as measured from the MUSE data. In the following, we provide both the uncorrected (directly fitted) and the corrected values for reference.

2.5 Star formation sequence

2.5.1 Global sample

With a reliable SFR estimate in hand, we can turn to the star formation sequence between $0.11 < z < 0.91$ as observed by MUSE. Figure 2.7 shows a plot of stellar mass (M_*) versus star formation rate (SFR) for all the galaxies in the sample. The figure is based on two dust-corrected SFR indicators: the Hβ λ4863 and Hα λ6565 luminosities (Eqs. (2.2) and (2.1)). The vertical grey lines indicate the errors in ($\log M_*$, $\log$ SFR) for each of the individual galaxies. The mean average error on the SFR is ≈ 0.2 dex in both the HUDF and the HDFS.

We are able to detect star formation in galaxies down to star formation rates as low as $0.003\ \mathrm{M_\odot\ yr^{-1}}$. The galaxies appear to follow the M_*-SFR trend closely over the complete

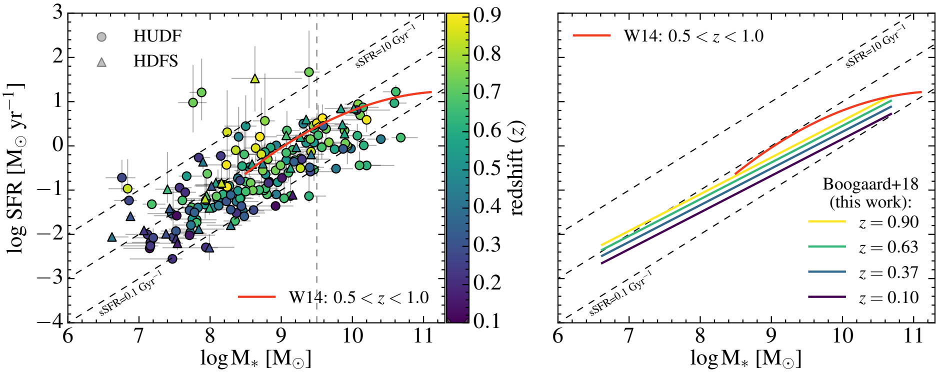

Figure 2.7: Left panel: The sample of 179 star-forming galaxies observed with MUSE, plotted on the M_*-SFR plane. The symbols indicate the field and colour indicates the redshift. The dashed lines show a constant sSFR, which is equivalent to a linear relationship: SFR $\propto M_*$. The red curve shows the model of the star formation sequence from Whitaker et al. (2014) for $0.5 < z < 1.0$. The vertical grey dashed line indicates the selection for the low-mass fit (§ 2.5.2). Right panel: Same as the left panel but with the data points removed, showing (the evolution of) the star formation sequence as seen by MUSE, according to Equation 2.11.

mass range, down to the lowest masses we can probe here $\sim 10^7$ M$_\odot$. At the high-mass end it appears we are starting to witness a flattening off of the trend, although we are primarily sensitive to the intermediate and low-mass galaxies.

We model the M_*-SFR relation with the Bayesian MCMC methodology described in detail in § 2.4. We show the resulting posterior probability density distribution for the parameters in Figure 2.8. By marginalising over the various parameters, we recover the posterior probability distributions for the individual parameters of interest (a, c, b, $\sigma_{\rm intr}$). These are plotted as histograms above the various axes in Figure 2.8. By taking the median and the 16th and 84th percentile from the posterior distributions we derive the median posterior value and a 1σ confidence interval for the parameters of interest.

The (uncorrected) best-fit (i.e. median posterior) parameters of the distribution (with their confidence intervals) that describe the star formation sequence are:

$$\begin{aligned}\log \mathrm{SFR}[\mathrm{M}_\odot\,\mathrm{yr}^{-1}] = 0.79^{+0.05}_{-0.05} \log\left(\frac{M_*}{M_0}\right) - 0.77^{+0.04}_{-0.04} \\ + 2.78^{+0.78}_{-0.78} \log\left(\frac{1+z}{1+z_0}\right) \pm 0.46^{+0.04}_{-0.03},\end{aligned} \tag{2.9}$$

analogous to Equation 2.4. The final term represents the intrinsic scatter ($\sigma_{\rm intr} = 0.46^{+0.04}_{-0.03}$) in the vertical (log SFR) direction. We note that while it is a perfectly valid option for the parameterisation of the likelihood, the posterior distribution does not favour models with zero intrinsic scatter.

Figure 2.8 shows that some correlations exist between the different parameters of the

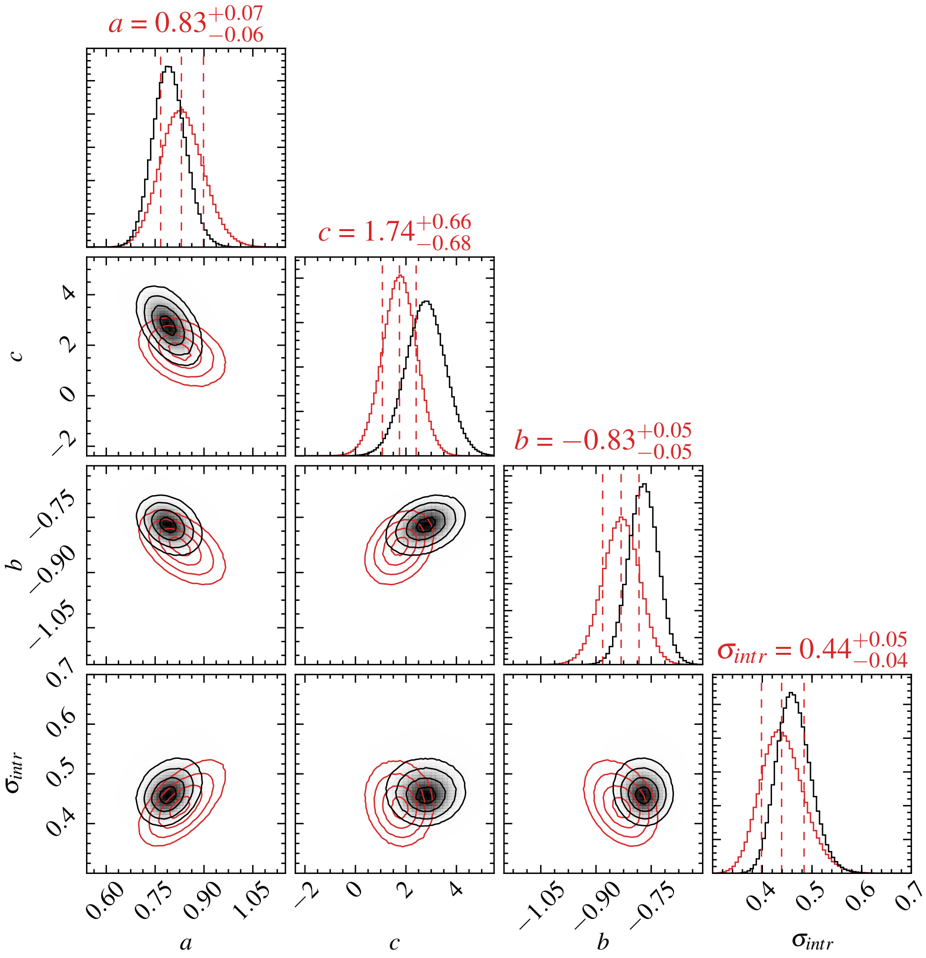

Figure 2.8: Projections of the 4D posterior distribution for the model parameters: slope (a), evolution (c), normalisation (b) and intrinsic scatter (σ_{intr}). The histograms on top show the marginalised distributions of the model parameters. The bias-corrected posterior median value and the 16th and 84th percentile are denoted by the dashed lines and by the values above the histograms. The contours show the 0.5, 1, 1.5 and 2 σ levels. The posterior directly from the modelling is shown in black, red indicates the posterior after applying the bias correction (Equation 2.19). Figure created using the `corner.py` module (Foreman-Mackey, 2016).

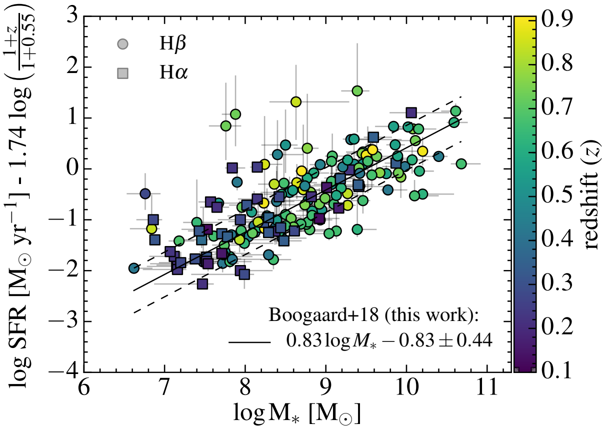

Figure 2.9: The best-fit star formation sequence for the 179 star-forming galaxies observed with MUSE. The symbols indicate the dust-corrected tracer used to infer the SFR. The solid line shows best-fit relation, as presented in Equation 2.11, and the dashed lines show the 1σ intrinsic scatter. We subtract the evolution from the y-axis and scale to the average redshift of the sample; $z = 0.55$. After accounting for evolution, the galaxies clearly follow the star formation sequence, down to the lowest masses and SFRs. The slightly larger fraction of galaxies that scatter into the high-mass, low-SFR regime may be a result of the flattening of the relation above $M_* = 10^{10}\,\mathrm{M}_\odot$.

model, which is expected. The strongest correlation exists between slope and redshift evolution as a less steep slope requires more evolution in the normalisation to be compatible with the data. The complete covariance matrix between the different parameters is:

$$\Sigma(a, c, b, \sigma_{\mathrm{intr}}) = \begin{pmatrix} 0.003 & -0.019 & -0.001 & 0.000 \\ -0.019 & 0.620 & 0.011 & 0.000 \\ -0.001 & 0.011 & 0.002 & 0.000 \\ 0.000 & 0.000 & 0.000 & 0.001 \end{pmatrix}. \tag{2.10}$$

We correct the posterior for observational bias, by applying Equation 2.19, which is indicated by the red contours in Figure 2.8. This yields a steeper slope, with a significantly shallower redshift evolution:

$$\begin{aligned} \log \mathrm{SFR}[\mathrm{M}_\odot\,\mathrm{yr}^{-1}] = {} & 0.83^{+0.07}_{-0.06} \log\left(\frac{M_*}{M_0}\right) - 0.83^{+0.05}_{-0.05} \\ & + 1.74^{+0.66}_{-0.68} \log\left(\frac{1+z}{1+z_0}\right) \pm 0.44^{+0.05}_{-0.04}, \end{aligned} \tag{2.11}$$

At the same time, the transformation has little effect on the intrinsic scatter. The covariance in the corrected posterior is essentially the same as the uncorrected one, with a slight increase in covariance with intrinsic scatter.

$$\Sigma(a, c, b, \sigma_{\mathrm{intr}}) = \begin{pmatrix} 0.004 & -0.016 & -0.002 & 0.002 \\ -0.016 & 0.459 & 0.010 & -0.003 \\ -0.002 & 0.010 & 0.002 & -0.001 \\ 0.002 & -0.003 & -0.001 & 0.002 \end{pmatrix}. \tag{2.12}$$

We compare the generative distribution (i.e. Equation 2.9) with the data in Figure 2.9. As the plane is three dimensional, we show a projection where we have subtracted the evolution with redshift from the y-axis. Overall, the distribution appears to describe the data very well and the scatter in the observations has tightened with respect to Figure 2.7. For a more familiar representation we also show the resulting star formation sequence in the right panel of Figure 2.7, for a number of different redshifts.

2.5.2 Low-mass sample ($\log M_*[M_\odot] < 9.5$)

We are primarily interested in the low-mass end of the star formation sequence. Our deep MUSE sample spans a significant mass range, between $\log M_*[\mathrm{M}_\odot] = 6.5 - 11$. As several studies have suggested different characteristics for the star formation sequence above and below a turnover mass of $M_* \sim 10^{10}\mathrm{M}_\odot$ (e.g. Whitaker et al., 2014; Lee et al., 2015; Schreiber et al., 2015), we repeat the above analysis excluding galaxies above a certain mass threshold. To be on the conservative side, we choose this mass threshold to lie at $M_* = 10^{9.5}\mathrm{M}_\odot$. This excludes $31/179 \approx 17.5\%$ of the sample. We include this threshold as a dashed vertical line in Figure 2.7. We then repeat the modelling identically to what has been described in the previous sections.

The bias-corrected star formation sequence for galaxies that have a stellar mass below $M_* < 10^{9.5}\mathrm{M}_\odot$ is:

$$\begin{aligned} \log \mathrm{SFR}[\mathrm{M}_\odot\,\mathrm{yr}^{-1}] = 0.83^{+0.10}_{-0.09} \log\left(\frac{M_*}{M_0}\right) - 0.79^{+0.05}_{-0.05} \\ + 2.22^{+0.75}_{-0.76} \log\left(\frac{1+z}{1+z_0}\right) \pm 0.47^{+0.06}_{-0.05}. \end{aligned} \tag{2.13}$$

The result is essentially the same, with the main difference being a steeper redshift evolution. All parameters are within errors consistent with the relation for our complete sample (also for the uncorrected values, see Table 2.1). This reflects the fact that we are primarily sensitive to the low-mass end of the galaxy sequence. As this fit utilises only a part of the data we will refer primarily to the fit based on all the data, Equation 2.11, as the main result in the remainder of the paper. We report the (un)corrected values for all the fits in Table 2.1.

2.5.3 The effect of redshift bins (2D)

Most previous studies have not modelled the redshift evolution of the star formation sequence directly, but have instead divided the data into redshift bins and adopted a non-evolving relation: $\log \mathrm{SFR} = a \log M_* + b$. To facilitate the comparison with the literature, we adapt our

Table 2.1: Star formation sequence parameters for different samples.

Sample	Size	a	b	c	$\sigma_{\rm intr}$
3D	$\log {\rm SFR}[{\rm M}_\odot\,{\rm yr}^{-1}] = a\log(M_*/M_0) + b + c\log(1+z)/(1+z_0)$				
Full	179	$0.79^{+0.05}_{-0.05}$	$-0.77^{+0.04}_{-0.04}$	$2.78^{+0.78}_{-0.78}$	$0.46^{+0.04}_{-0.03}$
$\log M_*[{\rm M}_\odot] < 9.5$	148	$0.79^{+0.08}_{-0.07}$	$-0.73^{+0.04}_{-0.04}$	$3.39^{+0.91}_{-0.90}$	$0.49^{+0.04}_{-0.04}$
3D – bias corrected (via Equation 2.19)					
Full	179	$0.83^{+0.07}_{-0.06}$	$-0.83^{+0.05}_{-0.05}$	$1.74^{+0.66}_{-0.68}$	$0.44^{+0.05}_{-0.04}$
$\log M_*[{\rm M}_\odot] < 9.5$	148	$0.83^{+0.10}_{-0.09}$	$-0.79^{+0.05}_{-0.05}$	$2.22^{+0.75}_{-0.76}$	$0.47^{+0.06}_{-0.05}$
2D	$\log {\rm SFR}[{\rm M}_\odot\,{\rm yr}^{-1}] = a\log(M_*/M_0) + b$				
Full	179	$0.89^{+0.05}_{-0.05}$	$-0.82^{+0.04}_{-0.04}$		$0.49^{+0.04}_{-0.04}$
$0.1 < z \leq 0.5$	72	$0.86^{+0.09}_{-0.08}$	$-0.92^{+0.07}_{-0.07}$		$0.57^{+0.07}_{-0.06}$
$0.5 < z < 1.0$	107	$0.84^{+0.07}_{-0.06}$	$-0.73^{+0.06}_{-0.06}$		$0.46^{+0.05}_{-0.05}$

Notes. For a full description of the different samples, see § 2.5. $M_0 = 10^{8.5}\,{\rm M}_\odot$ and $z_0 = 0.55$.

model to fit the relation in the ($\log M_*$, $\log {\rm SFR}$)-plane, without taking the redshift evolution into account. This is easily done, by taking a two-dimensional version of our likelihood, disregarding the second, $\log(1+z)$-component in Eq. (2.5)–(2.8) — the rest of the modelling is be identical. We note that we still take both heteroscedastic errors as well as intrinsic scatter into account (see § 2.4.1), however, we do not apply the bias correction.

We model both the entire redshift range, as well as the $0.1 < z < 0.5$ and $0.5 < z < 1.0$ range separately (similar to other studies). The results are collected in Table 2.1. For the full sample the slope is significantly steeper than when we take into account the redshift evolution, when comparing to our uncorrected fits:

$$\log {\rm SFR}[{\rm M}_\odot\,{\rm yr}^{-1}] = 0.89^{+0.05}_{-0.05}\log\left(\frac{M_*}{M_0}\right) - 0.82^{+0.04}_{-0.04}. \tag{2.14}$$

This is also the case for the smaller samples in both redshift bins, although the results are consistent with Equation 2.9 within the error bars (which are larger due to lower number statistics). The resulting relations are, for $0.1 < z \leq 0.5$;

$$\log {\rm SFR}[{\rm M}_\odot\,{\rm yr}^{-1}] = 0.86^{+0.09}_{-0.08}\log\left(\frac{M_*}{M_0}\right) - 0.92^{+0.07}_{-0.07}, \tag{2.15}$$

and for $0.5 < z < 1.0$;

$$\log {\rm SFR}[{\rm M}_\odot\,{\rm yr}^{-1}] = 0.84^{+0.07}_{-0.06}\log\left(\frac{M_*}{M_0}\right) - 0.73^{+0.06}_{-0.06}. \tag{2.16}$$

Given the significant evolution we found in the star formation sequence with redshift, this result is expected. While incidently these slopes are similar to our corrected fits, we caution that this does not imply that not modelling the redshift evolution can circumvent biases introduced by flux-limited observations.

2.6 Discussion

We have modelled the star formation sequence down to 10^8 M$_\odot$ at $0.11 < z < 0.91$ using a Bayesian framework (§ 2.4) that takes into account both the heteroscedastic errors on the observations as well as the intrinsic scatter in the relation. One major advantage of our framework is that we simultaneously model both the slope and the evolution in the M_*-SFR relation, while most previous studies have modelled these separately by dividing their sample into different redshift bins. As demonstrated in § 2.5.3, these results are not necessarily consistent, which can be attributed to evolution taking place within a single redshift bin. Another important difference is that we use the Balmer lines to trace the (dust-corrected) star formation, while most other recent studies have relied on SFRs derived from UV+IR/SED-fitting, using different dust corrections (Whitaker et al., 2014; Lee et al., 2015; Schreiber et al., 2015; Kurczynski et al., 2016).

As described in § 2.5.1, we have found that the star formation sequence (shown in Figure 2.7 and Figure 2.9) is well described by Equation 2.11 (see also Table 2.1). We now compare our results to other literature measurements and discuss each aspect of the star formation sequence separately, i.e. the redshift evolution, intrinsic scatter and the slope. We focus particularly on the slope, for which we find the strongest constraints, and continue with a discussion of the physical implications of our results.

2.6.1 Comparison with the literature

Evolution with redshift

We find that the normalisation in the star formation sequence increases with redshift as $(1 + z)^c$ with $c = 1.74^{+0.66}_{-0.68}$ ($2.22^{+0.75}_{-0.76}$ for $M_* < 10^{9.5}$ M$_\odot$). The fact that the normalisation of the star formation sequence increases with redshift is well known and attributed to the change in cosmic gas accretion rates and gas depletion timescales. Most studies have probed the higher mass regime and report values in the range of sSFR $\equiv$ SFR$/M_* \propto (1 + z)^{2.5-3.5}$ at $0 < z < 3$ (e.g. Oliver et al., 2010; Karim et al., 2011; Ilbert et al., 2015; Schreiber et al., 2015; Tasca et al., 2015). Looking specifically at the low-mass regime, Whitaker et al. (2014) reports sSFR $\propto (1 + z)^{1.9}$, similar to our result. Their more massive end indeed shows stronger evolution sSFR $\propto (1 + z)^{2.2-3.5}$. Lee et al. (2015) on the other hand, find much steeper evolution, with sSFR $\propto (1 + z)^{4.12\pm0.1}$. We note that our parameterisation assumes a power-law type of evolution of the star formation sequence with redshift. We have decided to stick to this very common first-order approximation. Still, one should keep in mind that a more complex evolution with redshift is possible, both non-linear in time as well as a different evolution in different mass regimes. We do not find strong constraints on the redshift evolution due to our relatively small redshift range from $z = 0.1$ to $z = 0.91$. Still, the results from § 2.5.3 show that it is important to take the redshift evolution into account, in order to get a robust constraint on the slope.

Intrinsic scatter

Constraining the intrinsic scatter in the star formation sequence has proven to be challenging as one has to separate the intrinsic scatter from the measurement error (e.g. Noeske et al., 2007a; Salim et al., 2007; Salmi et al., 2012; Whitaker et al., 2012; Guo et al., 2013; Speagle et al., 2014; Schreiber et al., 2015). This challenge in particular motivates our adopted model, which directly constrains the amount of intrinsic scatter in the relationship, even in the presence of measurement errors. Meanwhile, our measurements are not affected by binning, e.g. we do not boost the scatter artificially because of evolution of the star formation sequence within a single bin.

In our best fit model we find $\sigma_{\mathrm{intr}} = 0.44^{+0.05}_{-0.04}$ dex, which is larger than the value of $\sim 0.2 - 0.4$ dex that is commonly found (e.g. Speagle et al., 2014; Schreiber et al., 2015). Kurczynski et al. (2016) determined an intrinsic scatter of $\sigma_{\mathrm{intr}} = 0.427 \pm 0.011$ in their lowest redshift bin ($0.5 < z < 1.0$) in the HUDF, similar to our result, but found significantly smaller scatter at higher redshifts. They determined the intrinsic scatter by decomposing the total scatter ($\sigma_{\mathrm{Tot}} = 0.525$) using the covariance matrix between M_* and SFR determined from their SED fitting.

There are several effects that could potentially affect the scatter. Measurement outliers are not a cause of concern for the intrinsic scatter as they are taken into account by the likelihood approach. However, if galaxies are included in the sample that are not on the M_*-SFR relation, such as red-sequence galaxies or starbursts, then these might artificially increase the scatter. We argue that the former is unlikely as our selection criteria based on the 4000 Å break and the Hα λ6565 or Hβ λ4863 equivalent width effectively remove all red-sequence galaxies from the sample. On the other hand, our sample does include a small number of galaxies that are offset from the relation towards high SFRs. We verified however that removing all galaxies with a sSFR $> 10\,\mathrm{Gyr}^{-1}$ from the sample does not significantly increase or decrease the scatter.

Hypothetically, if the error bars on the SFR are underestimated, this will artificially boost the intrinsic scatter in the relationship. To determine the influence of the size of the error bars we redid the modelling while folding in an additional error on the SFR of 0.2 dex in quadrature (effectively doubling the average error bars); this decreased the scatter by 20% to ~ 0.4 dex. The sample size does not seem to affect the measurement and splitting our sample did not yield significantly larger scatter (see § 2.5.3).

Assuming our measured scatter is real, it might be that previous studies have underestimated the amount of intrinsic scatter. One potential danger might lie in the derivation of both stellar mass and SFR from the same photometry. Especially in SED modelling this might introduce correlations between M_* and SFR as both are regularised through the same star formation history in the model spectrum which could artificially decrease the scatter.

More physically, the difference could also in part be due to the fact that the Balmer lines trace the SFR on shorter timescales (stars with ages ≤ 10 Myr and masses $> 10\,\mathrm{M}_\odot$) than the UV does (ages of ≤ 100 Myr and masses $> 5\,\mathrm{M}_\odot$; e.g. Kennicutt 1998a; Kennicutt & Evans 2012). Simulations have indeed found that SFRs averaged over timescales decreasing from 10^8 to 10^6 yr could be significantly larger (Hopkins et al., 2014; Sparre et al., 2015), particularly if star formation histories are bursty (e.g. Dominguez et al., 2015; Sparre et al., 2017).

Furthermore, as the recent star formation histories of low-mass galaxies are more diverse, it can be expected that there is more scatter in the star formation sequence at low stellar masses. This indeed has been predicted by simulations (e.g. Hopkins et al., 2014; Sparre et al., 2017) as well as semi-analytical models (e.g. Mitra et al., 2017). Observing such a trend requires a large and highly complete sample of galaxies over an extended mass range and hence evidence has been inconclusive. Using a large sample of galaxies from the SDSS, Salim et al. (2007) reported a decrease in the scatter of -0.11 dex^{-1} from $10^8 - 10^{10.5}$ M$_\odot$, but such a trend with mass has not been confirmed by studies at higher masses (Whitaker et al., 2012; Guo et al., 2013; Schreiber et al., 2015; Kurczynski et al., 2016). Recently though, Santini et al. (2017) have found indications of decreasing scatter with mass in the Frontier Fields, albeit at higher redshifts ($z > 1.3$).

A large and complete sample of galaxies, covering the ($\log M_*$, $\log$ SFR, $\log(1+z)$)-space, with independent stellar mass and SFR estimates, is required to get a firm handle on the intrinsic scatter in the star formation sequence.

Slope

We find a best-fit (median posterior) slope of the star formation sequence of $a = 0.83^{+0.07}_{-0.06}$ ($\log \mathrm{SFR} \propto a \log M_*$). This slope is determined from galaxies that are more than an order of magnitude lower in mass than most earlier studies at $z > 0$, i.e. at 10^8 to 10^{10} M$_\odot$, whereas most previous studies (e.g. Speagle et al., 2014; Lee et al., 2015; Schreiber et al., 2015) have been primarily sensitive to a higher mass range from $10^{9.5}$ M$_\odot$ to 10^{11} M$_\odot$. For reference, we plot the polynomial fit from Whitaker et al. (2014) (down to their mass completeness limit, based on stacking) in Figure 2.7.

Recent studies have typically observed a shallower slope at the high-mass end, i.e. above 10^{10} M$_\odot$ (e.g. Whitaker et al., 2014). Gavazzi et al. (2015) find a turnover mass of $M_* \sim 10^{9.7}$ M$_\odot$ at $z = 0.55$ (after converting their result to a Chabrier IMF), increasing with redshift. As discussed in § 2.5.2, excluding galaxies above $M_* > 10^{9.5}$ M$_\odot$ has no significant effect on the slope. Only $15/179 \approx 8.5\%$ of galaxies in our sample have $M_* > 10^{10}$ M$_\odot$ and thus our result is not very sensitive to this turn-over. In light of this, we limit the following discussion to studies which specifically probe the mass range below the turnover of the star formation sequence.

Our best-fit slope of $0.83^{+0.07}_{-0.06}$ is compared to the values found by other recent studies in Figure 2.10 where we focus on studies with similar redshift ranges (i.e. $0 < z < 1$) and which extend well below $M_* < 10^{10}$ M$_\odot$. The slope in this regime is notably steeper than the consensus relation from Speagle et al. (2014) who reported $a = 0.6 - 0.7$ at our redshifts, due to the fact that this compilation is for a mass range of $\log M_*[\mathrm{M}_\odot] = 9.7 - 11.1$, where the slope is significantly shallower. Our slope is shallower than the low-mass power-law slope from Whitaker et al. (2014) ($a = 0.94 \pm 0.03$ for $M_* < 10^{10.2}$ M$_\odot$) from the 3D-HST catalogues in CANDELS, but is consistent with the global slope of $a = 0.88 \pm 0.06$ reported by Lee et al. (2015) in a large sample of star-forming galaxies in COSMOS. Kurczynski et al. (2016) have also presented a characterisation of the star formation sequence in the HUDF, based on the CANDELS/GOODS-S (Santini et al., 2015) and UVUDF (Rafelski et al., 2015) catalogues. In their lowest redshift bin ($0.5 < z < 1.0$), which goes down to $M_* \sim 10^{7.5}$M$_\odot$ they find a

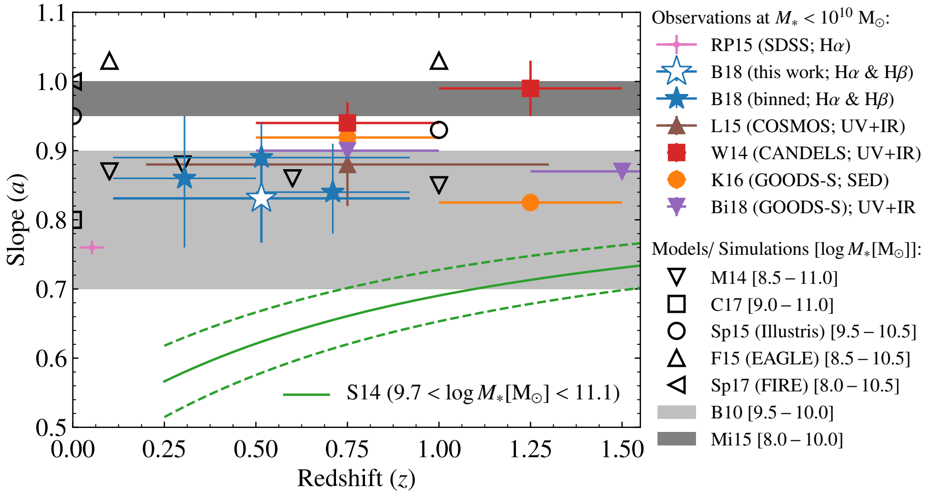

Figure 2.10: (a) A comparison of the slope (a) as a function of redshift (z) with studies from the literature that extend down to $M_* < 10^{10}$ $M_\odot$ near our redshift range. Our best-fit (bias-corrected) slope from Equation 2.11 is shown by the large star. As most studies have probed the slope in bins of redshift, we also include our results obtained using non-evolving redshift bins (Eqs. (2.14), (2.15) and (2.16); smaller blue stars). The literature results are from Renzini & Peng (2015, RP15), Kurczynski et al. (2016, K16), Bisigello et al. (2018, B18) and the low-mass ($M_* \lesssim 10^{10}$ $M_\odot$) power-law slopes from Whitaker et al. (2014, W14) and Lee et al. (2015, L15). We also add Speagle et al. (2014, SP14) for reference, though it is inferred at higher masses. We indicate the field and SFR-tracer in brackets, though note that distinct calibrations for the same tracer may be used in different studies. In addition, we add the slopes predicted by (semi-)analytical models; Bouché et al. (2010, B10), Mitchell et al. (2014, M14), Mitra et al. (2015, Mi15), Cattaneo et al. (2017, C17), and hydrodynamical simulations; Sparre et al. (2015, Sp15), Furlong et al. (2015, F15), Sparre et al. (2017, Sp17).

slope of $a = 0.919 \pm 0.017$, which is also steeper (marginally consistent) compared to what find. We note that they determined both masses and SFRs from the SED modelling, taking into account the correlations between the parameters, as their study was focused particularly on measuring the intrinsic scatter, see § 2.6.1. In the same field Bisigello et al. (2018) find a slope of 0.9 ± 0.01 ($0.5 \leq z < 1.0$), after selecting galaxies with $\log \mathrm{sSFR}[\mathrm{Gyr}^{-1}] < -9.8$.

The Sloan Digital Sky Survey (SDSS; York et al. 2000; Abazajian et al. 2009) serves as a natural reference for Balmer line-derived SFRs in the local universe and since Brinchmann et al. (2004) different studies have derived the star formation sequence slope (e.g, Salim et al., 2007; Elbaz et al., 2007). The most recent of these is Renzini & Peng (2015), who measure the slope of the ridge line in the $M_* - N \times$ SFR-plane (where N is the number of galaxies in every M_*-SFR bin) and find $a = 0.76 \pm 0.01$, which is significantly flatter than our results.

Taken at face value, our slope of $a = 0.83^{+0.07}_{-0.06}$ is inconsistent with a linear slope ($a = 1$). A value (close to) unity may have been expected on the basis of simulations (see next section), which is also evident from the fact that several parameterisations of the star formation sequence asymptote to a linear relation at low mass (e.g. Schreiber et al., 2015; Tomczak et al., 2016). An independent motivation for a near-linear value comes from the fact that there is very little evolution in the faint slope of the stellar mass function of star-forming galaxies up to $z = 2$ (see, e.g. Tomczak et al. (2014); Davidzon et al. (2017) for recent results). To first order, this may implies self-similar mass growth for low-mass galaxies (i.e. constant sSFR which implies a linear slope for the star formation sequence), unless balanced by mergers (Peng et al., 2014). Leja et al. (2015) investigated the link between the slope of the star formation sequence and the stellar mass function. While they do not provide precise constraints on the low-mass slope at low redshift (due to the challenge of disentangling growth through star formation and mergers), their results indicate that a sub-linear low-mass slope is still consistent with the stellar mass functions at $z < 1$.

Evolution of the low-mass slope

Combining results from the local universe out to redshift $z \sim 6$, Speagle et al. (2014) found evidence for an evolving slope at the high-mass end ($M_* > 10^{9.7}$ M$_\odot$), where the slope gets shallower with redshift (cf. Abramson et al., 2016, Fig. 5). Given the turnover in the star formation sequence at high mass, it is important to disentangle to what extent the evolution in the slope is due to different studies being sensitive to distinct mass regimes. Our data are too sparse in redshift space to simultaneously constrain the evolution of the slope (and hence we have adopted a single power-law slope for the sequence).

In light of the potential redshift evolution of the slope, we plot the slope as a function of redshift in Figure 2.10, compared to literature results which probe the mass range $M* < 10^{10}$ M$_\odot$ at $z < 1.5$. Figure 2.10 provides evidence for evolution of the low-mass slope with redshift. However, we caution against a too strong interpretation of such a trend as the literature suffers from studies probing distinct mass ranges (sometimes including the turn-over regime). What further complicates a fair comparison is that different tracers of star formation probe different timescales and additionally use varying dust corrections, which are not necessarily consistent (e.g. Davies et al., 2016). A consistent analysis of the low-mass galaxy population out to higher redshifts is important to quantify potential evolution in the low-mass slope.

2.6.2 The MS slope — a quantitative comparison to models

The galaxy main sequence (MS) is a natural outcome of hydrodynamical models (e.g. Fig. 1b in Bouche et al. 2005; Davé 2008; Genel et al. 2014; Torrey et al. 2014; Kannan et al. 2014; Hopkins et al. 2014; Sparre et al. 2015; Furlong et al. 2015) and in semi-analytical models (e.g. Somerville et al., 2008; Dutton et al., 2010; Cattaneo et al., 2011; Mitchell et al., 2014; Henriques et al., 2015; Hirschmann et al., 2016; Cattaneo et al., 2017). These models have reported a slope (and scatter) that, in general, is broadly consistent with observations, but the quantitative details regarding the slope and/or the evolution of the main sequence often do not match observations.

Since the pioneering work of Daddi et al. (2007) and Elbaz et al. (2007), it has been noted that the redshift evolution of the main sequence normalisation, in particular around $z = 2$, is a challenge for models (e.g. Davé, 2008; Damen et al., 2009; Bouché et al., 2010; Dutton et al., 2010; Dekel & Mandelker, 2014; Torrey et al., 2014; Genel et al., 2014; Mitchell et al., 2014; Furlong et al., 2015; Sparre et al., 2015; Abramson et al., 2016; Santini et al., 2017). Here, we focus on a quantitative comparison of the slope of the main sequence (SFR $\propto M_*^a$) with various models, given that our study yields the tightest constraint on this parameter (compared to the other parameters in the model).

The Illustris simulations (Vogelsberger et al., 2014; Genel et al., 2014; Sparre et al., 2015) produce a main-sequence with a slope a that is slightly sub-linear with $a \lessapprox 1.0$. In particular, Genel et al. (2014) noted that sSFR goes as $\simeq -0.1$ with stellar mass and using the results from Sparre et al. (2015), we find that the main sequence in Illustris goes as SFR $\propto M_*^{\approx 0.95}$. The EAGLE simulations (Schaye et al., 2015; Crain et al., 2015) also allow an investigation of the main sequence and Furlong et al. (2015, their Fig. 5), showed that the sSFR is constant with M_* from 10^8 to 10^{10} $\mathrm{M}_\odot$ at redshifts $z = 0.1$, 1.0 and 2.0, with a relatively steep decline above 10^{10} $\mathrm{M}_\odot$. Quantitatively, below 10^{10} $\mathrm{M}_\odot$, the slope of the main sequence a in Furlong et al. (2015) is $a \approx 1.04$. The MS slope for the Illustris and EAGLE simulations are shown in Figure 2.10 as the open circles and triangle symbols, respectively. In the FIRE simulations (Hopkins et al., 2014), Sparre et al. (2017) focused on studying the scatter in the main sequence for different tracers of SFR and shows a slope of $a \approx 0.98$ when using the FUV (their Fig. 2).

The MS slope has also been a challenge for semi-analytical models because different (regular) feedback prescriptions do not alter the MS slope as shown in Dutton et al. (2010) and discussed in Mitchell et al. (2014) (however, it can alter the slope in hydrodynamical simulations, e.g. Haas et al. 2013a,b; Crain et al. 2015). Mitchell et al. (2014) performed a detailed comparison between predictions from the GALFORM semi-analytical models with observations and their fiducial model produces a MS slope of $a \approx 0.85$ (shown in Figure 2.10 as the down-pointing triangles). Recently, the semi-analytical model of Cattaneo et al. (2017) using the GALICS2 code was set to reproduce the local luminosity function and the local MS slope simultaneously. Their MS slope is $a \approx 0.8$ (open square in Figure 2.10), but we caution their use of an extreme feedback model, where the mass loading η is $\eta \propto V^{-6}$, where V is the halo virial velocity. Such a steep scaling between galaxy mass and wind loading is not supported by the data (e.g. Schroetter et al., 2016).

Bouché et al. (2010) used a simple toy model for galaxy (self-)regulation with which they showed that variations in feedback prescriptions or in the laws of star formation have no impact on the MS slope. They argued that while ejective feedback alone is not sufficient to bring the theoretical slope of the main-sequence in agreement with observations, preventive feedback can easily do so as several studies have shown (Davé et al., 2012; Lu et al., 2015; Mitra et al., 2015, 2017). However, while the MS slope of Bouché et al. (2010) is sub-linear with $a \approx 0.8$, a quantitative analysis reveals that the slope varies rapidly with stellar mass, likely due to the limitations of the model. Indeed, the MS slope of Bouché et al. (2010) goes from 0.7 at $M_* \sim 10^{9.5}$ $\mathrm{M}_\odot$ to 0.9 at $M_* \sim 10^{10.5}$ $\mathrm{M}_\odot$. The range of values is indicated by the light grey box in Figure 2.10.

Mitra et al. (2015) expanded the self-regulation model of Bouché et al. (2010); Davé et al. (2012, and others) with physically motivated parameters and attempted to determine these parameters using a Bayesian MCMC approach on a set of observed scaling relations at $0 < z < 2$. Their fiducial model yields a MS with a slope that is quasi-linear with $a \sim 0.95$

in our mass regime, i.e. below 10^{10} $M_\odot$. Their MS slope is shown as the dark grey band in Figure 2.10.

Generally speaking, in the low-mass regime below 10^{10} $M_\odot$, hydrodynamical simulations have steeper MS slopes with $a \approx 1.0$ whereas our estimate ($a = 0.83^{+0.07}_{-0.06}$) at $z < 1$ and recent observations covering that mass range indicate $a < 1.0$ (see Figure 2.10). The reason that models tend to predict a steeper main sequence slope lies in the underlying feature in hydrodynamical simulations and semi-analytical models, where the growth rate for dark matter halos $\dot{M}_\mathrm{h}$ scales with mass as $\dot{M}_\mathrm{h} \propto M_\mathrm{h}^{1.15}$ (Birnboim et al., 2007; Genel et al., 2008; Dekel et al., 2009; Fakhouri & Ma, 2008; Neistein & Dekel, 2008), in combination with rapid gas cooling.

2.6.3 Implications of a shallow slope

As noted originally by Noeske et al. (2007b) and discussed in Mitchell et al. (2014) and Abramson et al. (2016), a MS with a sub-linear slope, SFR $\propto M_*^a$ with $a < 1$, implies downsizing where lower-mass galaxies have longer *e*-folding time and a later onset of star formation. This downsizing effect would be amplified if the MS slope is substantially flatter above 10^{10} $M_\odot$ as some studies have indicated (Whitaker et al., 2014; Schreiber et al., 2015; Lee et al., 2015; Tomczak et al., 2016). This turnover has generally been attributed to either a morphological transition, such as bulge growth (Abramson et al., 2014; Lee et al., 2015; Whitaker et al., 2015), or a reduced star formation efficiency (Schreiber et al., 2016).

Our result, that the slope of the main sequence is sub-linear in the low-mass regime, implies that there are processes at work which either: (1) affect the conversion of the accreted gas into stars through increased (supernova) feedback or a decrease in the SF efficiency; or (2) prevent the accretion of gas onto low-mass galaxies. These two processes might conspire with the fact that the gravitational potential is shallower in low-mass galaxies (Mitra et al., 2015).

In hydrodynamical simulations low-mass galaxies (up to halo masses of $\sim 10^{11.5}$ $M_\odot$) obtain their gas primarily through 'cold'-accretion (Kere et al., 2005; van de Voort et al., 2011), where the gas is never heated to the virial temperature, while 'hot' accretion, where gas is first shock heated to the virial temperature and then cools and accretes, is dominant for more massive galaxies. A candidate process is feedback from gravitational heating, due to the formation of virial shocks (e.g. Faucher-Giguère et al., 2011), which becomes more effective at higher masses, however, can still play a role down to halo masses of 10^{10} $M_\odot$. The heating of gas through winds (from either supernovae or black hole feedback) can also prevent the gas from flowing into the galaxy (Oppenheimer et al., 2010; Faucher-Giguère et al., 2011; van de Voort et al., 2011), in particular in low-mass galaxies. However, Schaye et al. (2010) pointed out that this type of feedback mainly has a regulatory effect on the gas infall.

As noted by Dutton et al. (2010), Bouché et al. (2010), and Mitchell et al. (2014), in semi-analytical models, the MS slope is rather insensitive to the ejective (regular) feedback mechanisms,[25] such as the heating of gas through winds and/or the star formation efficiency (Kennicutt, 1998a) because they act primarily on the gas content. Hence, the SFR and stellar mass are affected in a similar way, leaving the slope unchanged, unless the ejective feedback prescription is strongly mass dependent with $\eta \propto V^{-6}$, as in Cattaneo et al. 2017. In addition, Mitchell et al. (2014) showed that the slope is also insensitive to the gas re-incorporation prescription (see also Mitra et al., 2015).

---

[25] with mass loading $\eta \propto V^{-1}$ or $\eta \propto V^{-2}$ for momentum or energy-driven winds, respectively.

Preventive processes (Blanchard et al., 1992; Gnedin, 2000; Mo et al., 2005; Lu & Mo, 2007; Okamoto et al., 2008) that tend to be mass dependent can more easily impact the MS slope, the Tully-Fischer relation, and the luminosity function as argued by Bouché et al. (2010). A preventive process which can prevent the inflow of gas specifically in low-mass halos is photoionisation heating (Quinn et al., 1996). While it has been argued that this process is primarily effective in dwarf galaxies and becomes ineffective above halo masses of a few times 10^9 $M_\odot$ (e.g. Okamoto et al., 2008), Cantalupo (2010) suggest that photoionisation may still play a role for more massive halos if there is significant star formation.

2.7 Summary and conclusions

We have exploited the unique capabilities of the MUSE instrument to investigate the star formation sequence for low-mass galaxies at intermediate redshift ($0.11 < z < 0.91$). From the large number of sources detected with MUSE in the HUDF and HDFS we have constructed a sample of 179 star-forming galaxies down to $M_* \sim 10^8$ $M_\odot$, with a number of objects at even lower masses (Figure 2.4). The accurate spectroscopic redshifts from MUSE are combined with the deep photometry available over the HUDF and HDFS to determine a robust mass estimate for the galaxies in our sample through stellar population synthesis modelling.

With MUSE we can detect star-forming galaxies down to SFR $\sim 10^{-3}$ $M_\odot$ yr^{-1} (Figure 2.7). We show that we can determine robust, dust-corrected SFR estimates from Hα λ6565 and Hβ λ4863 recombination lines, by comparing the SFRs from different tracers (Figure 2.5). A dust-corrected star formation rate is inferred from the Hα λ6565 and Hβ λ4863 emission lines observed with S/N > 3 in the MUSE spectra.

We characterise the star formation sequence by a Gaussian distribution around a plane (Equation 2.4). This methodology is chosen to maximally exploit the data set taking into account heteroscedastic errors. We constrain the slope, normalisation, intrinsic scatter, and evolution with redshift from the posterior probability distribution via MCMC methods (Figure 2.8).

We analyse the robustness of our model and the influence of the MUSE detection limit on the derived properties of the star formation sequence, by determining how well we can recover the parameters from a sample of simulated relations (detailed in § 2.A). Using the results, we correct our inferred parameters for observational biases.

We report a best-fit description of the low-mass end of the galaxy star formation sequence of $\log \mathrm{SFR} = 0.83^{+0.07}_{-0.06} \log M_* - 0.83^{+0.05}_{-0.05} + 1.74^{+0.66}_{-0.68} \log(1+z)$ between $0.11 < z < 0.91$, shown in Figure 2.9. The full description of our parameters, including errors and normalisation, is found in Equation 2.11.

The intrinsic scatter around the sequence is found to be $\sigma_{\mathrm{intr}} = 0.44^{+0.05}_{-0.04}$ dex (in log SFR). This is notably higher than the average value reported in literature (~ 0.3 dex), which could be attributed to a combination of the Balmer lines probing star formation on shorter timescales and the star formation histories of low-mass galaxies being more diverse.

Excluding massive galaxies (with $M_* > 10^{9.5}$ $\mathrm{M}_\odot$) has no significant effect on the best-fit parameters, indicating we are primarily sensitive to low-mass galaxies. Notably though, we find that the slope steepens when splitting our sample into one or multiple redshift bins, with the values going up to $\log \mathrm{SFR}[\mathrm{M}_\odot\,\mathrm{yr}^{-1}] = 0.89^{+0.05}_{-0.05} \log M_*[\mathrm{M}_\odot]$. This shows the importance of taking into account the evolution with redshift when deriving the properties of the star formation sequence.

The slope of the star formation sequence is an important observable as it provides information on the processes that regulate star formation in galaxies. Our slope is shallower than most simulations and (semi-)analytical models predict, which find a (super-)linear slope essentially due to the growth rate of dark matter halos. Feedback processes operating specifically in the low-mass regime, which affect the accretion of gas onto galaxies and/or subsequent star formation, are required to reconcile these differences. Models suggest that supernova feedback or a decreased star formation efficiency do not affect the slope of the star formation sequence. Instead, processes that prevent the accretion of gas onto low-mass galaxies are thought to play an important role in determining the slope of the star formation sequence in the low-mass regime.

Acknowledgements

We would like to thank the referee for providing a constructive report that helped improve the quality of the paper. L.A.B. would like to thank the participants of the Lorentz Center Workshop on *A Decade of the Star-Forming Main Sequence* for beneficial discussions. We gratefully acknowledge the developers of IPYTHON, NUMPY, MATPLOTLIB, and ASTROPY (Perez & Granger, 2007; van der Walt et al., 2011; Hunter, 2007; The Astropy Collaboration et al., 2013) and TOPCAT (Taylor, 2005) for their development of the software used at various stages during this work. J.B. acknowledges support from Fundação para a Ciência e a Tecnologia (FCT) through national funds (UID/FIS/04434/2013) and Investigador FCT contract IF/01654/2014/CP1215/CT0003., and from FEDER through COMPETE2020 (POCI-01-0145-FEDER-007672). J.S. acknowledges support from the Netherlands Organisation for Scientific Research (NWO) through VICI grant 639.043.409. N.B. and T.C. acknowledge funding by the ANR FOGHAR (ANR-13-BS05-0010-02), the OCEVU Labex (ANR-11-LABX-0060), and the A*MIDEX project (ANR-11-IDEX-0001-02) funded by the "Investissements d'avenir" French government programme. R.B. acknowledges support from the ERC advanced grant 339659-MUSICOS. Based on observations made with ESO telescopes at the La Silla Paranal Observatory under programme IDs ID 060.A-9100(C), 094.A-2089(B), 095.A-0010(A), 096.A-0045(A), and 096.A-0045(B).

Appendix 2.A Simulations

2.A.1 Selection function and completeness

We have selected galaxies based on the signal-to-noise of their emission lines, without any photometric preselection. This means the selection function is essentially determined by the emission line sensitivity. In general, one might expect galaxies with higher S/N in their emission lines to have a higher SFR at a fixed mass, or similarly, for galaxies with the same S/N to have a higher SFR at higher redshift, which potentially introduces biases in our results. Additionally, we can only observe galaxies that have Balmer lines in the spectral range of MUSE ($z < 0.91$).

To investigate the influence of these selections, we determine how well we can recover the true parameters of the star formation sequence from a set of mock samples of galaxies, after applying the flux limit from our MUSE observations.

We determine the influence of the selection function on the inferred parameters by simulating mock data for a range of 'true' parameters. The range of values for each mock parameter is listed in Table 2.2, which combine to form a grid of $N = 1260$ points. The extent of grid is chosen such that it encompasses a wide range of possible parameters and we find that the results are consistent if we enlarge the grid even further (note that, if the grid is taken too large, non-linearities may arise at the extreme values which potentially bias the linear transformation approach of § 2.A.2). We denote each set of parameters as $\mathbf{x}_{\mathrm{true},k} = \left(\hat{a}, \hat{c}, \hat{b}, \hat{\sigma}_{\mathrm{intr}}\right)^T$ with $k = 1, \ldots, N$.

We generate realistic mock data for each set of parameters through the following procedure: We sample 100 galaxies from a uniform distribution in both mass ($7.0 < \log M_*[\mathrm{M}_\odot] < 10.5$) and redshift ($0.1 < z < 1$). Given the mass and redshift, we compute the SFR (via Equation 2.4), i.e. assuming a mock main sequence distribution with slope $\hat{a}$ and evolution $\hat{c}$. We choose our normalisation ($\hat{b}$) such that a 10^{10} $\mathrm{M}_\odot$ galaxy at $z = 0$ has a SFR of 1 $\mathrm{M}_\odot$/yr, similar to our results and, e.g. the Milky Way (Chomiuk & Povich, 2011), i.e. we take a zero-point of $b_0 = -10$. We then sample up to $b_{\mathrm{offset}} = \pm 0.4$ dex above and below this zero-point. We provide each galaxy with a random offset from the main sequence (perpendicular to the ($\log M_*$, $\log \mathrm{SFR}$)-relation) drawn from $\mathcal{N}(0, \hat{\sigma}_{\mathrm{intr}})$. Finally, we apply a random measurement error for each galaxy in both log stellar mass and log SFR of 0.3 dex (i.e. drawn from $\mathcal{N}(0, 0.3)$) and in log redshift of 5×10^{-4} dex ($\sim \mathcal{N}(0, 5 \times 10^{-4})$), similar to the observations.

We then apply the same flux limit as our shallowest MUSE observations, namely in the mosaic with 3×10^{-19} erg s^{-1} cm^{-2}, and mark all 'observed' galaxies as those that fall above our detection threshold (we do not take an additional factor for dust into account as our galaxies are not very dusty on average). We then fit the observed galaxies above the flux limit. Repeating this process 30 times for each individual set of parameters $\mathbf{x}_{\mathrm{true},}$ and marginalising over the combined posterior distribution, we determine the corresponding recovered parameters $\mathbf{x}_{\mathrm{out},k} = (a, c, b, \sigma_{\mathrm{intr}})^T$.

As an example, we show one the experiment for a particular set of parameters in Figure 2.11. It is clear that the recovered parameters are biased towards a shallower slope and a steeper redshift evolution. The magnitude of this bias depends on all the parameters and

Table 2.2: Grid values for our mock simulations.

	min	max	step
$\hat{a}$	0.7	1.1	0.05
$\hat{c}$	1.5	4.5	0.5
b_{offset}	-0.4	0.4	0.2
$\hat{\sigma}_{\text{intr}}$	0.3	0.6	0.1
$\hat{b} = \hat{a}\,(\log(M_0) - b_0) + \hat{c}\log(1+z_0) + b_{\text{offset}}$			

Notes. The normalisation ($b_0 = -10$) is chosen such that a 10^{10} $\mathrm{M}_\odot$ galaxy at $z = 0$ has a SFR of 1 $\mathrm{M}_\odot\,\mathrm{yr}^{-1}$.

becomes more severe for steeper slopes and shallower redshift evolutions.

To check our methods, we also fit all simulated galaxies (without discarding any data). Reassuringly, we recover our input parameters to within the errors, even when simulating only 100 galaxies. Since our actual sample size is 179 galaxies, we are in principle able to recover the true parameters of the relation, even in the case of intrinsic scatter and heteroscedastic errors. One feature that does draw attention is that the redshift evolution is marginally steeper than the input relation (but admittedly poorly constrained and still consistent within the error). This can be explained due to an intricacy of the model, which assumes that the intrinsic scatter about the relation is along the normal vector to the plane ($\sigma_\perp$ in § 2.4.1), i.e. also in the $\log(1+z)$-direction. If the data are truncated and there is a non-zero slope ($|c| > 0$) in redshift space, this may introduce an artificial bias in the corresponding slope (and scatter) as the truncation boundaries are not parallel to the normal vector. Given the fact that our data (and mock sample) are limited in redshift space by the spectral range of MUSE, this means that we may have slight artificial bias towards a steeper redshift evolution. For interpreting the intrinsic scatter this is not a problem as we can project the scatter along the (physical) log SFR-axis (which is our σ_{intr}).

With our simulations in hand however, we are now in place to apply a correction for both biases identified above.

2.A.2 Transformation

The simulations show a reasonably well behaved transformation between the true and recovered slope. We therefore model the mock data with an affine transformation, to be able to transform between the measured and true parameters.

We try to find the best transformation matrix A and vector $\mathbf{b}$ between the measured and true parameters. For each set of input ($\mathbf{x}_{\text{true},k}$) and output ($\mathbf{x}_{\text{out},k}$) parameters we have:

$$\mathbf{x}_{\text{out},k} \approx A\mathbf{x}_{\text{true},k} + \mathbf{b} \tag{2.17}$$

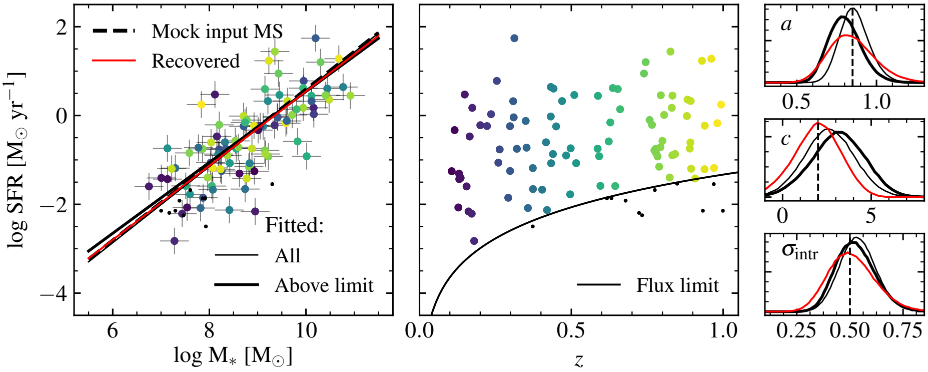

Figure 2.11: Illustration of the results of the recovery experiment on mock galaxies. The points in the left and centre panels show one of the 30 realisations of 100 galaxies in ($\log M_*$, $\log(1+z)$, log SFR)-space from a mock star formation sequence: $\log \mathrm{SFR} \propto a \log M_* + c \log(1+z)$, where in this particular case $a = 0.8$ and $c = 2.0$ with $\sigma_{\mathrm{intr}} = 0.5$ dex. The colour indicates redshift, unless a mock galaxy falls below the solid line in the centre panel, indicating the flux limit of $\sim 3 \times 10^{-19}$ erg s^{-1} cm^{-2}, in which case it is a black point. The rightmost panels show the marginalised distributions (slope, redshift evolution, and intrinsic scatter) from combining all 30 realisations. The thin and thick black lines indicate the results when taking into account all mock data and only the data above the flux limit, respectively, and are compared to the input values (dashed lines). With all data points (including noise), we can recover the input parameters sequence well. When applying the flux limit a slight bias towards a shallower slope and steeper redshift evolution appears. We plot all curves in the leftmost panel at the average redshift of the sample (z_0). The red line is obtained after applying the correction to the fit of the data above the limit. These recovered curves are plotted in the leftmost panel as well and compared to the input mock relation. With our correction, we can recover the true input parameters well, even in the case of limited data.

We minimise the function

$$S(A, \mathbf{b}) = \sum_{k=1}^{N} ||\mathbf{x}_{\mathrm{out},k} - A\mathbf{x}_{\mathrm{true},k} - \mathbf{b}||_2^2 \tag{2.18}$$

with respect to each component of A and $\mathbf{b}$ in order to find the best-fit transformation A and $\mathbf{b}$ (Späth, 2004). We note that we do not take the errors on each point $\mathbf{x}_{\mathrm{out}}$, k into account as their magnitudes are all comparable (essentially adding a constant to the equation).

With the best-fit A and $\mathbf{b}$ in hand, we can then invert the equation to obtain the relation between the observed and the recovered 'true' parameters, which denote as $\mathbf{x}'_{\mathrm{true}}$:

$$\mathbf{x}'_{\mathrm{true}} \approx A^{-1} (\mathbf{x}_{\mathrm{out}} - \mathbf{b}) \tag{2.19}$$

$$\begin{pmatrix} a' \\ c' \\ b' \\ \sigma'_{\mathrm{intr}} \end{pmatrix} = \begin{pmatrix} 1.336 & 0.014 & -0.150 & 0.171 \\ 0.638 & 0.863 & 0.574 & -2.621 \\ -0.178 & -0.008 & 1.175 & -0.185 \\ 0.285 & 0.009 & -0.044 & 1.091 \end{pmatrix} \left(\begin{pmatrix} a \\ c \\ b \\ \sigma_{\mathrm{intr}} \end{pmatrix} - \begin{pmatrix} 0.293 \\ 0.061 \\ -0.194 \\ 0.236 \end{pmatrix} \right) \tag{2.20}$$

For our simulated data, we show the distribution of the difference between the recovered parameters ($\mathbf{x}'_{\rm true}$) and the true parameters ($\mathbf{x}_{\rm true}$) in Figure 2.12. We recover the input parameters very well, with no mean offset between the recovered and the true parameter. This shows that the transformation (i.e. A and $\mathbf{b}$) are very well determined. Furthermore, the scatter in the differences is much smaller than the average uncertainty on each parameter obtained from the observations (of order $\sim$ 1%). As an illustration, we show the inverse transformation applied to the simulation by the red lines in Figure 2.11, which are now in good agreement with the true values (dashed lines).

In summary, the transformation obtained from the best-fit A and $\mathbf{b}$ is a very accurate description of the bias induced by the flux limit in our simulated data. We use the inverse of this transformation, Equation 2.19, in § 2.5 to correct our inferred posterior density distribution from modelling the MUSE data.

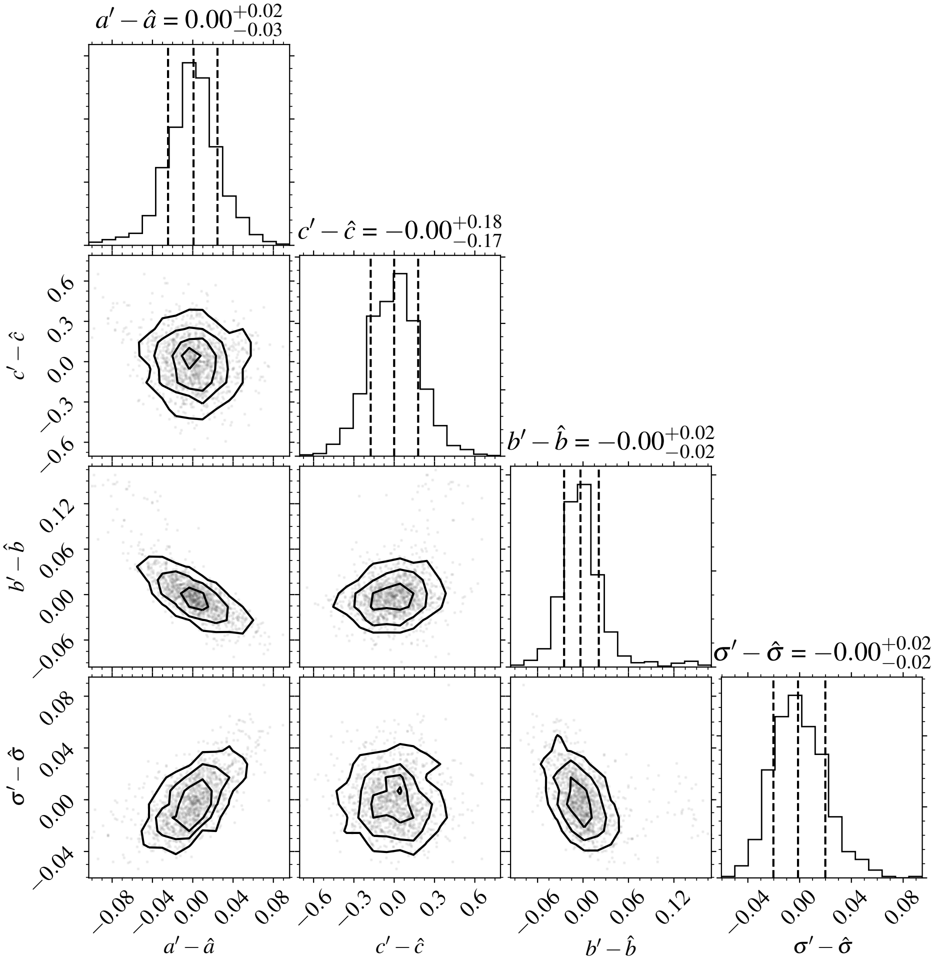

Figure 2.12: Plot of the differences between the recovered parameters, $\mathbf{x}'_{\mathrm{true}} = \left(a', c', b', \sigma'_{\mathrm{intr}}\right)^T$ and the true parameters, $\mathbf{x}_{\mathrm{true}} = \left(\hat{a}, \hat{c}, \hat{b}, \hat{\sigma}_{\mathrm{intr}}\right)^T$, for the $N = 1260$ points from our simulation; see Equation 2.19. We can recover the input parameters of our simulation very well, with no mean offset and very small scatter (compared to the uncertainty on each parameter obtained from the observations). Figure created using the `corner.py` module (Foreman-Mackey, 2016).

3 The ALMA Spectroscopic Survey in the HUDF: Nature and physical properties of gas-mass selected galaxies using MUSE spectroscopy

Abstract

We discuss the nature and physical properties of gas-mass selected galaxies in the ALMA spectroscopic survey (ASPECS) of the *Hubble* Ultra Deep Field (HUDF). We capitalize on the deep optical integral-field spectroscopy from the MUSE HUDF Survey and multiwavelength data to uniquely associate all 16 line emitters, detected in the ALMA data without preselection, with rotational transitions of carbon monoxide (CO). We identify ten as CO(2–1) at $1 < z < 2$, five as CO(3–2) at $2 < z < 3$ and one as CO(4–3) at $z = 3.6$. Using the MUSE data as a prior, we identify two additional CO(2–1)-emitters, increasing the total sample size to 18. We infer metallicities consistent with (super-)solar for the CO-detected galaxies at $z \leq 1.5$, motivating our choice of a Galactic conversion factor between CO luminosity and molecular gas mass for these galaxies. Using deep *Chandra* imaging of the HUDF, we determine an X-ray AGN fraction of 20% and 60% among the CO emitters at $z \sim 1.4$ and $z \sim 2.6$, respectively. Being a CO-flux-limited survey, ASPECS-LP detects molecular gas in galaxies on, above, and below the main sequence (MS) at $z \sim 1.4$. For stellar masses $\geq 10^{10}(10^{10.5})\,\mathrm{M}_{\odot}$, we detect about 40% (50%) of all galaxies in the HUDF at $1 < z < 2$ ($2 < z < 3$). The combination of ALMA and MUSE integral-field spectroscopy thus enables an unprecedented view of MS galaxies during the peak of galaxy formation.

L. A. Boogaard, R. Decarli, J. González-López, P. van der Werf, F. Walter, *et al.*
The Astrophysical Journal, 882, 140 (2019)

3.1 Introduction

Star formation takes place in the cold interstellar medium (ISM) and studying the cold molecular gas content of galaxies is therefore fundamental for our understanding of the formation and evolution of galaxies. As there is little to no emission from the molecular hydrogen that constitutes the majority of the molecular gas in mass, cold molecular gas is typically traced by molecules, such as the bright rotational transitions of $^{12}C^{16}O$ (hereafter CO).

Recent years have seen a tremendous advance in the characterization of the molecular gas content of high redshift galaxies (for a review, see Carilli & Walter, 2013). Targeted surveys with the Atacama Large Millimetre Array (ALMA) and the Plateau de Bure Interferometer (PdBI) have been instrumental in our understanding of the increasing molecular gas reservoirs of star-forming galaxies at $z > 1$ (Daddi et al., 2010a, 2015; Genzel et al., 2010; Tacconi et al., 2010, 2013; Silverman et al., 2015, 2018). Combining data across cosmic time, these provide constraints on how the molecular gas content of galaxies evolves as a function of their physical properties, such as stellar mass (M_*) and star formation rate (SFR; Scoville et al., 2014, 2017; Genzel et al., 2015; Saintonge et al., 2016; Tacconi et al., 2013, 2018). These surveys typically target galaxies with SFRs that are greater than or equal to the majority of the galaxy population at their respective redshifts and stellar masses (the 'main sequence' of star-forming galaxies; Brinchmann et al. 2004; Noeske et al. 2007a; Whitaker et al. 2014; Schreiber et al. 2015; Eales et al. 2018; Boogaard et al. 2018), and therefore should be complemented by studies that do not rely on such a preselection.

Spectral line scans in the (sub)millimeter regime in deep fields provide a unique window into the molecular gas content of the universe. As the cosmic volume probed is well defined, these scans play a fundamental role in determining the evolution of the cosmic molecular gas density through cosmic time. Through their spectral scan strategy, these surveys are designed to detect molecular gas in galaxies without any preselection, providing a flux-limited view on the molecular gas emission at different redshifts (Walter et al., 2014; Decarli et al., 2014; Walter et al., 2016; Decarli et al., 2016b; Pavesi et al., 2018; Riechers et al., 2019). By conducting 'spectroscopy-of-everything', these can in principle reveal the molecular gas content in galaxies that would not be selected in traditional studies (e.g., galaxies with a low SFR, well below the main sequence (MS), but with a substantial gas mass).

This paper is part of a series of papers presenting the first results from the ALMA Spectroscopic Survey Large Program (ASPECS-LP; Decarli et al. 2019). The ASPECS-LP is a spectral line scan targeting the *Hubble* Ultra Deep Field (HUDF). Here we use the results from the spectral scan of Band 3 (84–115 GHz; 3.6–2.6 mm) and investigate the nature and physical properties of galaxies detected in molecular emission lines by ALMA. In order to do so, it is important to know about the physical conditions of the galaxies detected in molecular gas, such as their ISM conditions, their (*HST*) morphology, and their stellar and ionized gas dynamics. The HUDF benefits from the deepest and most extensive multiwavelength data, and, as of recently, ultra-deep integral-field spectroscopy.

A critical step in identifying ALMA emission lines with actual galaxies relies on matching the galaxies in redshift. In this context, the Multi Unit Spectroscopic Explorer (MUSE, Bacon et al. 2010) HUDF survey, that provides a deep optical integral-field spectroscopic survey over the HUDF (Bacon et al., 2017), is essential. The MUSE HUDF is a natural complement to the ASPECS-LP in the same area on the sky, providing optical spectroscopy for all galaxies within the field of view, also without any preselection. In addition, the integral-field spectrograph provides redshifts for over a thousand of galaxies in the HUDF (increasing the number of previously known redshifts by a factor of ∼ 10×; Inami et al. 2017). Depending on the redshift, these data can provide key information on the ISM conditions (such as metallicity and dynamics) of the galaxies harboring molecular gas. As we will see throughout this paper, the MUSE data are a significant step forward in our understanding of galaxy population selected with ALMA.

The paper is organized as follows: we first introduce the spectroscopic and the multi-wavelength data (§ 3.2). We discuss the redshift identification of the CO-detected galaxies from the line search (González-López et al., 2019), using the MUSE and multiwavelength data, in § 3.3.1. Next, we leverage the large number of MUSE redshifts to separate real from spurious sources down to a significantly lower signal-to-noise ratio (S/N) than possible in the line search (§ 3.3.2). Together, these sources form the full ASPECS-LP Band 3 sample (§ 3.3.3). We then move on to the central question(s) of this paper: by doing a survey of molecular gas, in what kind of galaxies do we detect molecular gas emission at different redshifts, and what are the physical properties of these galaxies? We determine stellar masses, SFRs, and (where possible) metallicities for all sources in (§ 3.4) and link these to the molecular gas content (M_{H_2}) to derive the gas fraction (M_{H_2}/M_*, the molecular-to-stellar mass ratio) and depletion time ($t_{\mathrm{depl}} = M_{\mathrm{H}_2}/\mathrm{SFR}$). We first discuss the properties of the sample of CO-detected galaxies in the context of the overall population of the HUDF (§ 3.5.1) and investigate the X-ray AGN fraction among the detected sources (§ 3.5.2). Using the MUSE spectra, we determine the unobscured SFR (§ 3.5.3) and the metallicity of the $1 < z < 1.5$ sources (§ 3.5.4). Finally, we discuss the CO-detected galaxies from the flux-limited survey in the context of the galaxy MS (§ 3.6), focusing on the molecular gas mass, gas fraction, and depletion time. We discuss what fraction of the galaxy population in the HUDF we detect with increasing redshift. A further discussion of the molecular gas properties of these sources will be presented in Aravena et al. (2019).

Throughout this paper, we adopt a Chabrier (2003) IMF and a flat ΛCDM cosmology, with $H_0 = 70\,\mathrm{km\,s^{-1}\,Mpc^{-1}}$, $\Omega_m = 0.3$, and $\Omega_\Lambda = 0.7$. Magnitudes are in the AB system (Oke & Gunn, 1983).

3.2 Observations

3.2.1 ALMA Spectroscopic Survey

We focus on the ASPECS-LP Band 3 observations, that have been completed in ALMA Cycle 4. The acquisition and reduction of the Band 3 data are described in detail in Decarli et al. (2019). The final mosaic covers a 4.6 arcmin^2 area in the HUDF (where the primary beam response is > 50% of the peak sensitivity). The data are combined into a single spectral cube with a spatial resolution of $\approx 1\farcs75 \times 1\farcs49$ (synthesized beam with natural weighting at 99.5 GHz) and a spectral resolution of 7.813 MHz, corresponding to $\Delta v \approx 23.5\ \mathrm{km\,s^{-1}}$ at 99.5 GHz. The average root-mean-square (rms) sensitivity is ≈ 0.2 mJy beam^{-1} but varies across the frequency range, being deepest (≈ 0.13 mJy beam^{-1}) around 100 GHz and higher above 110 GHz, due to the spectral setup of the observations (see González-López et al. 2019 for details). Throughout this paper, we consider the area that lies within $> 40\%$ of the primary beam peak sensitivity, which is the shallowest part of the survey over which we still detect CO candidates without preselection (§ 3.3.1). When comparing to the *HST* reference frame, we take into account an astrometric offset of $\Delta\alpha = +0\farcs076$, $\Delta\delta = -0\farcs279$ (Dunlop et al., 2017; Rujopakarn et al., 2016).

We perform an extensive search of the cube for molecular emission lines, as is detailed in González-López et al. (2019) and § 3.3. With the Band 3 data alone, the ASPECS-LP is sensitive to different CO and [C I] transitions at specific redshift ranges which are indicated in the top panel of Figure 3.1.

3.2.2 MUSE HUDF Survey

The HUDF was observed with the MUSE as part of the MUSE *Hubble* Ultra Deep Field survey (Bacon et al., 2017). The location on the sky of the ASPECS-LP with respect to the MUSE HUDF is shown in Decarli et al. (2019), Fig. 1. The MUSE integral-field spectrograph has a $1' \times 1'$ field of view, covering the optical regime (4750 − 9300Å) at an average spectral resolution of $\lambda/\Delta\lambda \approx 3000$. The HUDF was observed in a two tier strategy, with the *mosaic*-region reaching a median depth of 10 hours in a $3' \times 3'$-region and the *udf10*-pointing reaching 31 hours depth in a $1' \times 1'$-region (3σ emission line depth for a point source of 3.1 and 1.5×10^{-19} erg s^{-1} cm^{-2} at 7000Å, respectively). The data acquisition and reduction as well as the automated source detection are described in detail in Bacon et al. (2017). The measured seeing in the reduced datacube is $0\farcs65$ full width at half maximum (FWHM) at 7000Å.

Redshifts were identified semiautomatically and the full spectroscopic catalog is presented in Inami et al. (2017). The spectra were extracted using a weighted extraction, where the weighting was based on the MUSE white light image, to obtain the maximal signal-to-noise. The spectra are modeled with a modified version of PLATEFIT (Tremonti et al., 2004; Brinchmann et al., 2004, 2008) to obtain line flux measurements and equivalent widths for all sources. The typical uncertainty on the redshift measurement is $\sigma_v = 0.00012(1 + z)$ or $\approx 40\ \mathrm{km\,s^{-1}}$ (Inami et al., 2017), which we use to compute the uncertainties in the relative velocities.

In order to compare in detail the relative velocities measured between the UV/optical features in MUSE and CO in ALMA, we need to place both on the same reference frame. The MUSE redshifts are provided in the barycentric reference frame, while the ALMA cube is set to the kinematic local standard of rest (LSRK). When determining detailed velocity offsets we place both on the same reference frame by removing the velocity difference; $\mathrm{BARY} - \mathrm{LSRK} = -16.7\ \mathrm{km\,s^{-1}}$ (accounting for the angle between the LSRK vector and the observation direction toward the HUDF).

The redshift distribution of the MUSE galaxies that fall within $> 40\%$ of the primary beam peak sensitivity of the ASPECS-LP footprint in the HUDF is shown in Figure 3.1, where

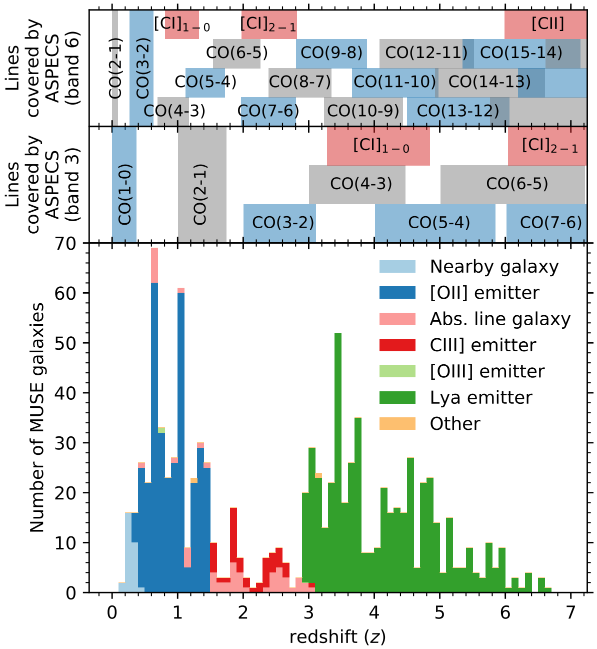

Figure 3.1: Molecular line redshift coverage of the galaxies in the MUSE and ASPECS-LP *Hubble* Ultra Deep Field (HUDF). The histogram shows the galaxies with spectroscopic redshifts from MUSE (*udf10* and *mosaic*; see § 3.2.2) that lie within > 40% of the primary beam sensitivity of the ASPECS-LP mosaic, distinguished by the primary spectral feature used to identify the redshift (Inami et al. 2017; 'Nearby galaxy' summarizes a range of rest-frame optical features). The decrease in the number of redshifts between $1.5 < z < 2.9$ is due to the lack of strong emission line features in the MUSE spectrograph ('redshift desert'). The drop at the lowest redshifts is due to the nature and volume of the HUDF. The top panel shows the specific CO and [C I] transitions covered by the frequency setup of ASPECS Band 3 at different redshifts (Walter et al., 2016; Decarli et al., 2019). ASPECS covers CO(2–1) for [O II] emitters and absorption line galaxies at $1.0 < z < 1.74$. Galaxies with CO(3–2) at $2.0 < z < 3.11$ are identified mostly by UV absorption and weaker emission lines (e.g., C IIII]). For higher-order CO and [C I] transitions above $z > 2.90$, MUSE has coverage of Lyα. *For reference, the band 6 line coverage is also added to this figure, as presented in Boogaard (2020).*

galaxies are color coded by the primary spectral feature(s) used to identify the redshift (see Inami et al. 2017 for details). The redshifts that correspond to the ASPECS band 3 coverage of the different molecular lines are indicated in the top panel. CO(1–0) [115.27 GHz] is observable at the lowest redshifts ($z < 0.3694$), where MUSE still covers a major part of the rest-frame optical spectrum that contains a wealth of spectral features, including absorption and (strong) emission lines (e.g., Hα λ6565, [O III] $\lambda\lambda$4960, 5008 and [O II] $\lambda\lambda$3727, 3730). The strong lines are the main spectral features used to identify star-forming galaxies all the way up to $z < 1.50$, where [O II] $\lambda\lambda$3727, 3730 moves out of the spectral range of MUSE. CO(2–

1) [230.54 GHz] is covered by ASPECS at $1.0059 < z < 1.7387$, mostly overlapping with [O II] in MUSE. At $z > 1.5$, the main features used to identify these galaxies are absorption lines such Mg II λ2796, 2803 and Fe II λ2587, 2600. Over the redshift range of CO(3–2) [345.80 GHz], $2.0088 < z < 3.1080$, MUSE only has coverage of weaker UV emission lines (mainly C III] $\lambda\lambda$1907, 1909), making redshift identifications more challenging (the 'redshift desert'). Here, UV absorption lines are commonly used to identify redshifts, for galaxies where the continuum is strong enough ($m_{\rm F775W} \lesssim 26$ mag). Above $z = 2.9$, MUSE flourishes again, with the coverage of Lyα λ1216 all the way out to $z \approx 6.7$. Here, ASPECS covers CO(4–3) [461.04 GHz] and transitions with $J_{\rm up} \geq 4$, and atomic carbon lines ([C I]$_{1-0}$ 610 μm and [C I]$_{2-1}$ 370 μm).

3.2.3 Multi-wavelength data (UV–radio) and MAGPHYS

In order to construct spectral energy distributions (SEDs) for the ASPECS-LP sources, we utilize the wealth of available photometric data over the HUDF, summarized below.

We use the photometric compilation by Skelton et al. (2014, see references therein), which includes UV, optical and near-IR photometry from the *Hubble* Space Telescope (*HST*) and ground-based facilities, as well as (deblended) *Spitzer*/IRAC 3.6μm, 4.5μm, 5.8μm and 8.0μm. We also include the corresponding deblended *Spitzer*/MIPS 24μm photometry from (Whitaker et al., 2014). We take deblended far-infrared (FIR) data from *Herschel*/PACS 100μm and 160μm from Elbaz et al. (2011), which have a native resolution of 6.″7 and 11.″0, respectively. The PACS 100μm and 160μm have a 3σ depth of 0.8 mJy and 2.4 mJy and are limited by confusion. For the flux uncertainties we use the maximum of the local and simulated noise levels for each source, as recommended by the documentation.[26] We further include the 1.2 mm continuum data from the combination of the available ASPECS-LP data with the ALMA observations by Dunlop et al. (2017), taken over the same region, as detailed in Aravena et al. (2019). We also include the ASPECS-LP 3.0 mm continuum data, as presented in (González-López et al., 2019). For the ASPECS survey we have created a master photometry catalog for the galaxies in the HUDF, adopting the spectroscopic redshifts from MUSE (§ 3.2.2) and literature sources, as detailed in Decarli et al. (2019).

We use the high-z extension of the SED-fitting code MAGPHYS to infer physical parameters from the photometric information of the galaxies in our field (Da Cunha et al., 2008, 2015). The high-z extension of MAGPHYS includes a larger library of spectral emission models that extend to higher dust optical depths, higher SFRs and younger ages compared to what is typically found in the local universe. From the spectral emission models, the code can constrain the stellar mass, sSFR and the dust attenuation (A_V) along the line of sight. An energy balance argument ensures that the amount of absorption at rest-frame UV/optical wavelengths is consistent with the light reradiated in the infrared. The code performs a Bayesian inference of the posterior likelihood distribution of the fitted parameter, to account for uncertainties such as degeneracies in the models, missing data and nondetections.

We run MAGPHYS on all the galaxies in our catalog, using the available photometric information in all the bands (listed in § 3.B). We do not include the *Spitzer*/MIPS and *Herschel*/PACS photometry in the fits of the general sample because the angular resolution of these observations is relatively modest ($> 5''$), thus a delicate de-blending analysis would be required (the average sky density of galaxies in the HUDF is $\gtrsim 1$ galaxy per 3 arcsec^2). For the CO-detected galaxies we repeat the MAGPHYS fits including these bands (§ 3.4.1). In order to take into account systematic errors in the zero point fitting for these sources, we add the zero point errors (Skelton et al., 2014) in quadrature to the flux errors in all filters except *HST*, and include a 5% error-floor to further account for systematic errors in the physical models (following Leja et al. 2019). The filter selection of the general sample provides excellent photometric coverage of the stellar population. Paired with the wealth of spectroscopic redshifts (see Decarli et al. 2019 for a detailed description), this enables robust constraints on properties such as M_*, SFR and A_V. We do note that while the formal uncertainties on the inferred properties are generally small, systematic uncertainties can be of order ~ 0.3 dex (e.g., Conroy, 2013).

---

[26] https://hedam.lam.fr/GOODS-Herschel/data/files/documentation/GOODS-Herschel_release.pdf

3.2.4 X-ray photometry

To identify AGN in the field, we use the *Chandra* X-ray data available over the GOODS-S region from Luo et al. (2017), which reaches the full depth of 7 Ms over the HUDF area. In total, there are 36 X-ray sources within the ASPECS-LP region of the HUDF (i.e., within 40% of the primary beam). We spatially cross-match the X-ray catalog to the closest source within $1''$ in our MUSE and multiwavelength catalog over the ASPECS-LP area, visually inspecting all matches used in this paper to ensure they are accurately identified.

At the depth of the X-ray data, there are multiple physical mechanisms (e.g., AGN and star formation) that may produce the X-ray emission detected at $0.5 - 7$ keV. Luo et al. (2017) adopt the following 6 criteria to distinguish X-ray AGN from other sources of X-ray emission, of which at least one needs to be satisfied to be classified as AGN (we refer the reader to Xue et al. 2011, Luo et al. 2017 and references therein for details): (1) $L_X \geq 3 \times 10^{42}$ erg s^{-1}, identifying luminous X-ray sources; (2) an effective photon index $\Gamma_{\rm eff} \leq 1.0$ indicating hard X-ray sources, identifying obscured AGN; (3) X-ray-to-R-band flux ratio of $\log\left(f_X/f_R\right) > -1$; (4) spectroscopically classified as AGN via, e.g., broad emission lines and/or high excitation lines; (5) X-ray-to-radio flux ratio of $L_X/L_{1.4\rm GHz} \geq 2.4 \times 10^{18}$, indicating an excess of X-ray emission over the level expected from pure star formation; (6) X-ray-to-K-band flux ratio of $\log\left(f_X/f_{K_s}\right) > -1.2$. Note that even with these criteria it is possible that some X-ray sources host low-luminosity or heavily obscured AGN and are currently misclassified.

Overall, there are six X-ray AGN in the ASPECS-LP volume at $1.0 < z < 1.7$, all of which have a MUSE redshift (one being a broad-line AGN). In the ASPECS-LP volume at $2.0 < z < 3.1$, there are seven X-ray AGN, three of which have spectroscopic redshifts from MUSE (including one broad-line AGN), and four with a photometric redshift (we discard one source in the catalog with a photometric redshift in this regime for which we cannot securely identify a counterpart in *HST*). There is one X-ray AGN at a higher redshift, which is also identified by MUSE as a broad-line AGN at $z = 3.188$.

3.3 The ASPECS-LP sample

3.3.1 Identification of the line search sample

An extensive description of the line search is provided in González-López et al. (2019). In summary, three independent methods were combined to search for CO lines in the ASPECS-LP band 3 data without any preselection; LineSeeker (González-López et al., 2017b), FindClump (Decarli et al., 2014; Walter et al., 2016) and MF3D (Pavesi et al., 2018). The fidelity[27] of these line candidates was estimated from the ratio of the number of lines with a negative and positive flux detected at a given S/N. Lastly, the completeness of the sample was estimated by ingesting simulated emission lines into the real data cube.

In total, there are 16 emission line candidates for which the fidelity is ≥ 0.9. Statistical analysis shows that this sample is free from false positives (the sum of their fidelities, based on the ALMA data alone, is 15.9; González-López et al. 2019). These 16 sources form the primary, *line search*-sample and are shown in Figure 3.2. All these candidates have a $\mathrm{S/N} \geq 6.4$.

For all sources in the primary sample, one or multiple potential counterpart galaxies are visible in the deep *HST* imaging shown in Figure 3.2. In order to confidently identify a single CO emission line, an independent redshift measurement of the potential counterpart measurement is needed. Given the wealth of multiwavelength photometry in the HUDF, photometric redshifts can often already provide sufficient constraints to discern between different rotation transitions of CO in the case of isolated galaxies at redshifts $z \lesssim 3$. However, complex systems of several galaxies, or projected superpositions of independent galaxies at distinct redshifts, can make redshift assignments more complicated. Fortunately, the integral-field spectroscopy from MUSE is ideally suited to disentangle spectral features belonging to different galaxies, allowing us to confidently assign redshifts to the CO emission lines. The frequency of a CO line can correspond to different rotational transitions, each with a unique associated redshift. With the potential redshift solutions in hand, we systematically identify the CO line candidates from the line search. We provide a summary of the redshift identifications here. A detailed description of the individual sources and their redshift identifications can be found in § 3.A, where we also show the MUSE spectra for all sources (Figure 3.13 – 3.16).

First, we correlate the spatial position and potential redshifts of the CO lines with known spectroscopic redshifts from MUSE (Inami et al., 2017). From the MUSE redshifts alone, we immediately identify most (11/16) of the CO lines with the highest fidelity. The brightest (ASPECS-LP.3mm.01) is a CO(3–2) emitter at $z = 2.54$, showing a wealth of UV absorption features. The other 10 galaxies are a diverse sample of CO(2–1) emitters spanning the redshift range over which we are sensitive; $1.01 < z < 1.74$. They show a variety of spectra at different levels of S/N, covering a range of UV and optical absorption and emission features. Notably, [O II] $\lambda\lambda3727, 3730$ is detected in all galaxies where it is covered by MUSE, while [Ne III] $\lambda3870$ is detected in some of the higher S/N spectra.

Next, we extract MUSE spectra for the remaining five (5/16) sources without a cataloged

---

[27] The fidelity is defined as $F = 1 - P$, where P is the probability of a line being produced by noise (González-López et al., 2019).

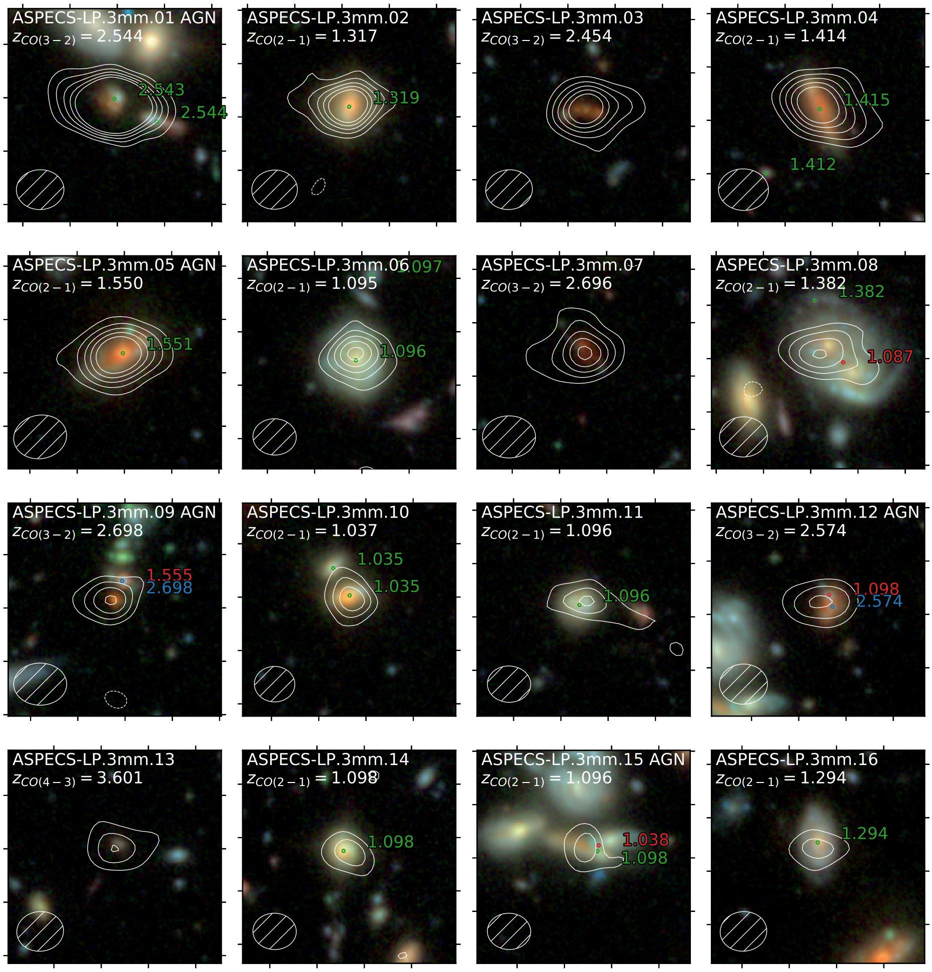
ASPECS-LP.3mm.01 AGN
$z_{CO(3-2)}$ = 2.544
2.543
2.544
ASPECS-LP.3mm.02
$z_{CO(2-1)}$ = 1.317
1.319
ASPECS-LP.3mm.03
$z_{CO(3-2)}$ = 2.454
ASPECS-LP.3mm.04
$z_{CO(2-1)}$ = 1.414
1.415
1.412
ASPECS-LP.3mm.05 AGN
$z_{CO(2-1)}$ = 1.550
1.551
ASPECS-LP.3mm.06
1.097
$z_{CO(2-1)}$ = 1.095
1.096
ASPECS-LP.3mm.07
$z_{CO(3-2)}$ = 2.696
ASPECS-LP.3mm.08
$z_{CO(2-1)}$ = 1.382
1.382
1.087
ASPECS-LP.3mm.09 AGN
$z_{CO(3-2)}$ = 2.698
1.555
2.698
ASPECS-LP.3mm.10
$z_{CO(2-1)}$ = 1.037
1.035
1.035
ASPECS-LP.3mm.11
$z_{CO(2-1)}$ = 1.096
1.096
ASPECS-LP.3mm.12 AGN
$z_{CO(3-2)}$ = 2.574
1.098
2.574
ASPECS-LP.3mm.13
$z_{CO(4-3)}$ = 3.601
ASPECS-LP.3mm.14
$z_{CO(2-1)}$ = 1.098
1.098
ASPECS-LP.3mm.15 AGN
$z_{CO(2-1)}$ = 1.096
1.038
1.098
ASPECS-LP.3mm.16
$z_{CO(2-1)}$ = 1.294
1.294

Figure 3.2: *HST* RGB cutouts (F160W, F125W, and F105W) of the 16 CO line detections from the line search, all revealing an optical/NIR counterpart. Each panel is 8″ × 8″ centered around the CO emission (corrected astrometry; § 3.2.1). The white contours indicate the CO signal from ±[3, .., 11]σ in steps of 2σ. The ALMA beam indicated in the bottom left corner. Galaxies with a spectroscopic redshift from MUSE (Inami et al., 2017) matching the CO signal are labeled in green (and red if not matching); spectroscopic redshifts in blue are newly determined in this paper. Of the 16 galaxies, 12 match closely to a redshift from MUSE (including ASPECS-LP.3mm.08, discussed in § 3.A and Decarli et al. 2016b). ASPECS-LP.3mm.03, 3mm.07 and 3mm.09 have $m_{\mathrm{F775W}} > 27$, which is too faint for a direct absorption line redshift from MUSE (but are independently confirmed). For ASPECS-LP.3mm.09 we do find UV absorption features matching the CO(3–2) in the galaxy slightly to the north. A new absorption line redshift is found for ASPECS-LP.3mm.12 (see Figure 3.18). The photometric redshift and absence of lower-z spectral features indicate ASPECS-LP.3mm.13 being at z = 3.601.

Table 3.1: Sixteen ASPECS-LP CO-detected sources from the line search, with MUSE spectroscopic counterparts, and two ASPECS-LP CO(2–1) detected sources based on a spectroscopic redshift prior from MUSE.

ID (1)	R.A. (J2000) (2)	Dec. (J2000) (3)	$\nu_{\rm CO}$ (GHz) (4)	CO trans. ($J_{\rm up} \rightarrow J_{\rm low}$) (5)	$z_{\rm CO}$ (6)	MUSE ID (7)	$z_{\rm MUSE}$ (8)	Δv km s^{-1} (9)
3mm.01	03:32:38.54	-27:46:34.6	97.584 ± 0.003	3 → 2	2.5436	35	2.5432	−15.5 ± 41.0
3mm.02	03:32:42.38	-27:47:07.9	99.510 ± 0.005	2 → 1	1.3167	996	1.3172*	73.5 ± 42.7
3mm.03	03:32:41.02	-27:46:31.5	100.131 ± 0.005	3 → 2	2.4534	···	···	···
3mm.04	03:32:34.44	-27:46:59.8	95.501 ± 0.006	2 → 1	1.4140	1117	1.4147	102.9 ± 44.2
3mm.05	03:32:39.76	-27:46:11.5	90.393 ± 0.006	2 → 1	1.5504	1001	1.5509	71.7 ± 44.7
3mm.06	03:32:39.90	-27:47:15.1	110.038 ± 0.005	2 → 1	1.0951	8	1.0955	79.2 ± 42.3
3mm.07	03:32:43.53	-27:46:39.4	93.558 ± 0.008	3 → 2	2.6961	···	···	···
3mm.08	03:32:35.58	-27:46:26.1	96.778 ± 0.002	2 → 1	1.3821	6415	1.3820	−0.1 ± 40.5
3mm.09	03:32:44.03	-27:46:36.0	93.517 ± 0.003	3 → 2	2.6977†	···	···	···
3mm.10	03:32:42.98	-27:46:50.4	113.192 ± 0.009	2 → 1	1.0367	1011	1.0362*	−53.7 ± 46.6
3mm.11	03:32:39.80	-27:46:53.7	109.966 ± 0.003	2 → 1	1.0964	16	1.0965	19.8 ± 40.8
3mm.12	03:32:36.21	-27:46:27.7	96.757 ± 0.004	3 → 2	2.5739	1124‡	2.5739*	16.8 ± 41.9
3mm.13	03:32:35.56	-27:47:04.3	100.209 ± 0.006	4 → 3	3.6008	···	···	···
3mm.14	03:32:34.84	-27:46:40.7	109.877 ± 0.009	2 → 1	1.0981	924	1.0981	15.0 ± 46.9
3mm.15	03:32:36.48	-27:46:31.9	109.971 ± 0.005	2 → 1	1.0964	6870	1.0979	240.4 ± 42.3
3mm.16	03:32:39.92	-27:46:07.4	100.503 ± 0.004	2 → 1	1.2938	925	1.2942	66.3 ± 41.7
MP.3mm.01	03:32:37.30	-27:45:57.8	109.978 ± 0.011	2 → 1	1.0962	985	1.0959	−28.2 ± 50.6
MP.3mm.02	03:32:35.48	-27:46:26.5	110.456 ± 0.007	2 → 1	1.0872	879	1.0874	55.8 ± 44.3

Notes. The CO frequencies of the first 16 sources are taken from González-López et al. (2019). (1) ASPECS-LP 3mm ID or MP.3mm (MUSE prior) ID. (2)-(3) Coordinates. (4) CO line Frequency. (5) Identified CO transition (§ 3.3.1). (6) CO redshift. (7) MUSE ID. (8) MUSE redshift. (9) Velocity offset between MUSE and ALMA ($\Delta v = (z_{\rm MUSE} - z_{\rm CO})/(1 + z_{\rm CO})$; after converting both to the same reference frame).

*Updated from Inami et al. (2017), see § 3.A.

†Additionally supported by matching absorption found in MUSE#6941, at $z = 2.695$, 0.″7 to the north.

‡Additional redshift for MUSE#1124, which is cataloged as the foreground [O II]-emitter at $z = 1.098$ (see Figure 3.18).

redshift and investigate their spectra for a redshift solution matching the observed CO line. We discover two new spectroscopic redshifts at $z = 2.54$ (ASPECS-LP.3mm.12) and $z = 2.69$ (associated with ASPECS-LP.3mm.09) confirming detections of CO(3–2), which were both not included in the catalog of Inami et al. (2017) as their spectra are blended with foreground sources. The former in particular demonstrates the key use of MUSE in disentangling a spatially overlapping system comprised of a foreground [O II] emitter and a faint background galaxy, which is detected at $S/N > 4$ both via cross-correlation with a $z \approx 2.5$ spectral template and by stacking absorption features (see Figure 3.18). For ASPECS-LP.3mm.03 and ASPECS-LP.3mm.07 we leverage the absence of spectral features (e.g., [O II], Lyα), consistent with their faint magnitudes ($m_{\rm F775W} > 27$ mag) and a redshift in the MUSE redshift desert, in combination with photometric redshifts in the $z = 2 - 3$ regime from the deep multiwavelength data, to confirm detections of CO(3–2). Lastly, we find ASPECS-LP.3mm.13 being CO(4–3) at $z = 3.601$, based on the photometric redshifts suggesting $z \approx 3.5$ and the absence of a lower redshift solution from the spectrum. Lyα λ1216 is not detected for this source, but we caution that at this redshift Lyα falls very close to the [O I] λ5577 skyline. Furthermore, given that the source potentially contains significant amounts of dust, no Lyα emission may be expected at all.

In summary, we determine a redshift solution for all (16/16) candidates from the line search. Twelve are directly confirmed by MUSE spectroscopy, while the remaining four are supported by their photometric redshifts and indirect spectroscopic evidence. We highlight that some of these counterparts are very faint, even in the reddest *HST* bands, and their identifications would not have been possible without the exquisite depth of both the *HST* and MUSE data over the HUDF. Similar objects would typically not have robust photometric counterparts in areas of the sky with inferior coverage (let alone have independent spectroscopic confirmation).

The identifications of the CO transitions, along with their MUSE counterparts, are presented in Table 3.1. We show the spatial extent of the CO emission on top of the *HST* images in Figure 3.2. The MUSE spectra for the individual sources are shown in Figure 3.13 – 3.16 and discussed in § 3.A.

3.3.2 Additional sources with MUSE redshift priors at $z < 2.9$

The CO-line detections from González-López et al. (2019) are selected to have the highest fidelity and are therefore the highest S/N (≥ 6.4) candidates over the ASPECS-LP area. In Figure 3.3, we plot the stellar mass - SFR relation for all MUSE sources at $1.01 < z < 1.74$, where we indicate all the galaxies that have been detected in CO(2–1) in the line search.[28] There are several galaxies in the field with properties similar to the ASPECS-LP galaxies that are not detected in the line search. This raises the question: Why are these galaxies not detected? Given their physical properties, we may expect some of these galaxies to harbor molecular gas and therefore to have CO signal in the ASPECS-LP cube. The reason that we did not detect these sources in the line search may, therefore, simply be due to the fact that

---

[28] Note that we do not show the MUSE source associated with ASPECS-LP.3mm.08 and the two MUSE sources that are severely blended with ASPECS-LP.3mm.12 and the galaxy north of ASPECS-LP.3mm.09 on the plot.

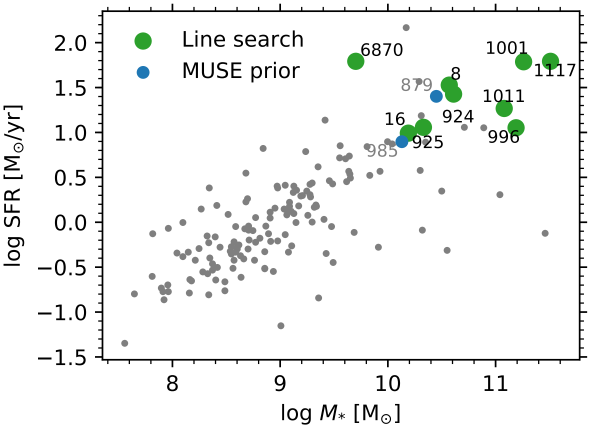

Figure 3.3: Stellar mass vs. SFR (from MAGPHYS) of all galaxies with a MUSE redshift at $1.01 < z < 1.74$ in the ASPECS-LP footprint. Leveraging the MUSE redshift as prior, we find CO(2–1) signal in two additional galaxies (blue). The numbers indicate the MUSE IDs of the sources. The detections from the line search (green; § 3.3.1) are also recovered in the prior-based search. By using the MUSE redshifts to search for CO at lower luminosities, we reveal molecular gas in most of the massive, star-forming galaxies at these redshifts.

they are present at lower S/N, which puts them in the regime where the decreasing fidelity makes it challenging to identify them among the spurious sources.

However, the physical properties of the galaxies themselves provide an extra piece of information that can guide us in detecting CO for these sources. In particular, we can use the spectroscopic redshifts from MUSE to obtain a measurement of the CO flux for each source, either identifying them at lower S/N, or putting an upper limit on their molecular gas mass. We aim at the CO transitions covered at $z < 2.9$, where the features in the MUSE spectrum typically provide a systemic redshift. At higher redshift the main spectral feature used to identify redshifts is often Lyα, which can be offset from the systemic redshift by a few hundred km s^{-1} (e.g., Shapley et al., 2003; Rakic et al., 2011; Verhamme et al., 2018).

We extract a single-pixel spectrum from the 3″ tapered cube at the position of each MUSE source in the redshift range, after correcting for the astrometric offset (§ 3.2.1). We then fit the lines with a Gaussian curve, using a custom-made Bayesian Markov chain Monte Carlo routine with the following priors:

- *line peak velocity*: a Gaussian distribution centered at $\Delta v = 0$ (based on the MUSE redshift) and $\sigma = 100$ km s^{-1} (the MUSE spectral resolution).
- *line width*: a Maxwellian distribution with a width of 100 km s^{-1}.
- *line flux*: a Gaussian distribution centered at zero, with $\sigma = 0.5$ Jy km s^{-1}, allowing both positive and negative line fluxes to be fitted.

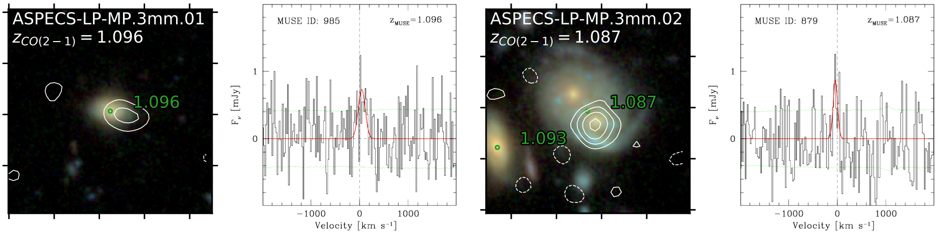

Figure 3.4: *HST* cutouts (F160W, F125W, F105W) and CO(2–1) spectra for two additional CO line candidates, found through a MUSE redshift prior. The CO contours are shown in white starting at $\pm 2\sigma$ in steps of 1σ. All other labeling in the cutouts is the same as in Figure 3.3. In the spectra the velocity is given relative to the MUSE redshift. The spectrum and best-fit Gaussian are shown in black and red, respectively. The local rms noise level is shown in green.

We choose a strong prior on the velocity difference, as we only search for lines at the exact MUSE redshift. The Gaussian prior on the line flux is important to estimate the fidelity of our measurements, allowing an unbiased comparison of positive versus negative line fluxes (see González-López et al. 2019 for details). The Maxwellian prior is chosen because it is bound to produce positive values of the line width, depends on a single scale parameter and has a non-null tail at very large line widths. The uncertainties are computed from the 16th and 84th percentiles of the posterior distributions of each parameter.

As narrow lines are more easily caused by noise in the cube (González-López et al., 2019), we rerun the fit with a broader prior on the line width of 200 km s^{-1}. We also independently fit the spectrum with a uniform prior over ±1 GHz around the MUSE redshift. We select only the sources in which the same feature was recovered with $S/N > 3$ in all three fits. In order to select a sample that is as pure as possible, we select only the objects that have a velocity offset of < 80 km s^{-1} from the MUSE systemic redshift ($\approx \times 2$ the typical uncertainty on the MUSE redshift). In addition, we only keep objects with a line width of > 100 km s^{-1}, to avoid including spurious narrow lines. We note that, while these cuts potentially remove other sources that are detected at lower S/N, we do not attempt to be complete. Rather, we aim to have the prior-based sample as clean as possible.

The prior-based search reveals two additional sources detected in CO(2–1) with a $S/N > 3$. Both sources lie within the area in which the sensitivity is $> 40\%$ of the primary beam peak sensitivity. We show the *HST* cutouts with the CO spectra of these sources in Figure 3.4, ordered by S/N. ASPECS-LP-MP.3mm.02 is the foreground spiral galaxy of ASPECS-LP.3mm.08. This source was already found in the ASPECS-Pilot (Decarli et al., 2016b, see § 3.A).

Because the molecular gas mass is to first order correlated with the SFR, we expect to detect CO in the galaxies with the highest SFRs at a given redshift. Sorting all the galaxies by their SFR indeed reveals a clear correlation between the SFR and the S/N in CO, suggesting there are additional sources in the ASPECS-LP datacube at lower S/N. This can also be clearly seen from Figure 3.3, where our stringent sample of prior-based sources all lie at $\log \mathrm{SFR}[M_\odot\,\mathrm{yr}^{-1}] > 0.5$. Qualitatively, it becomes clear that the ASPECS-LP is sensitive

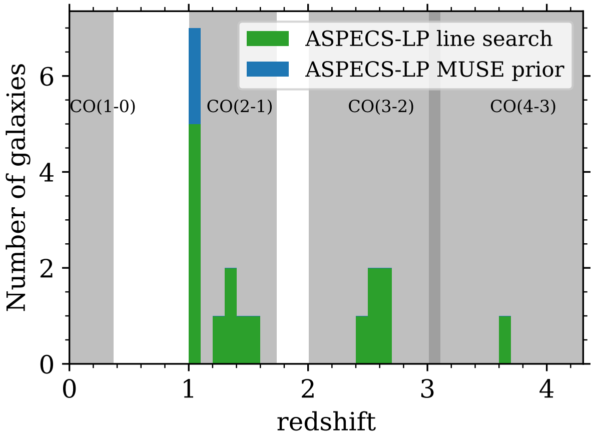

Figure 3.5: Redshift distribution of the ASPECS-LP CO-detected sources, which all have a *HST* counterpart. We show both the detections from the line search (§ 3.3) as well as the MUSE prior-based galaxies (§ 3.3.2). The gray shading indicates the redshift ranges over which we can detect different CO transitions.

enough to detect molecular gas in most massive MS galaxies at $1.01 < z < 1.74$ (a quantitative discussion of the detection fraction for the full sample is provided in § 3.6). For many galaxies, the reason these are not unveiled in the line search may simply be because their lower CO luminosity and/or smaller line width puts them below the conservative S/N threshold we adopt in the line search. Using the MUSE redshifts as prior information, it is possible to unveil their molecular gas reservoirs at lower S/N.

3.3.3 Full sample redshift distribution

The full ASPECS-LP CO line sample consists of 18 galaxies with a CO detection in the HUDF; 16 detections without preselection and 2 MUSE redshift prior-based detections. These galaxies span a range of redshifts between $1 < z < 4$. The lowest redshift galaxy is detected in CO(2–1) at $z = 1.04$, while the highest redshift galaxy is detected (without prior) in CO(4–3) at $z = 3.60$. We show a histogram of the redshifts of the line search and prior-based detections in Figure 3.5.

Twelve sources are detected in CO(2–1) at $1.01 < z < 1.74$, where the combination of molecular line sensitivity and survey volume are optimal. Most prominently, we detect five galaxies at the same redshift of $z \approx 1.1$. These galaxies are all part of an overdensity of galaxies in the HUDF at $z = 1.096$, visible in Figure 3.1.

Five sources are detected in CO(3–2) at $2.01 < z < 3.11$, including the brightest CO emitter in the field at $z = 2.54$ (ASPECS-LP.3mm.01; see also Decarli et al. 2016b) and a pair of galaxies (ASPECS-LP.3mm.07 and #9) at $z \approx 2.697$ (see § 3.3.1). All five CO(3–2) sources are detected in 1 mm dust continuum (Aravena et al., 2016a; Dunlop et al., 2017) with flux

Table 3.2: Physical properties of the ASPECS-LP detected sources from the line search and the MUSE prior-based search, with formal uncertainties.

ID	z	$\log M_{*,\mathrm{SED}}$ ($\mathrm{M}_\odot$)	$\mathrm{SFR}_\mathrm{SED}$ ($\mathrm{M}_\odot\,\mathrm{yr}^{-1}$)	$A_{V,\mathrm{SED}}$ (mag)	X-ray	XID
(1)	(2)	(3)	(4)	(5)	(6)	(7)
ASPECS-LP.3mm.01	2.5436	$10.4^{+0.0}_{-0.0}$	233^{+0}_{-0}	$2.7^{+0.0}_{-0.0}$	AGN	718
ASPECS-LP.3mm.02	1.3167	$11.2^{+0.0}_{-0.0}$	11^{+2}_{-0}	$1.7^{+0.1}_{-0.0}$		
ASPECS-LP.3mm.03	2.4534	$10.7^{+0.1}_{-0.1}$	68^{+19}_{-20}	$3.1^{+0.1}_{-0.3}$		
ASPECS-LP.3mm.04	1.4140	$11.3^{+0.0}_{-0.0}$	61^{+3}_{-12}	$2.9^{+0.1}_{-0.0}$		
ASPECS-LP.3mm.05	1.5504	$11.5^{+0.0}_{-0.0}$	62^{+5}_{-19}	$2.3^{+0.1}_{-0.3}$	AGN	748
ASPECS-LP.3mm.06	1.0951	$10.6^{+0.0}_{-0.0}$	34^{+0}_{-0}	$0.8^{+0.0}_{-0.0}$	X	749
ASPECS-LP.3mm.07	2.6961	$11.1^{+0.1}_{-0.1}$	187^{+35}_{-16}	$3.2^{+0.1}_{-0.1}$		
ASPECS-LP.3mm.08	1.3821	$10.7^{+0.0}_{-0.0}$	35^{+8}_{-5}	$0.9^{+0.1}_{-0.1}$		
ASPECS-LP.3mm.09	2.6977	$11.1^{+0.1}_{-0.0}$	318^{+35}_{-35}	$3.6^{+0.1}_{-0.1}$	AGN	805
ASPECS-LP.3mm.10	1.0367	$11.1^{+0.0}_{-0.1}$	18^{+1}_{-1}	$3.0^{+0.0}_{-0.1}$		
ASPECS-LP.3mm.11	1.0964	$10.2^{+0.0}_{-0.0}$	10^{+0}_{-1}	$0.8^{+0.0}_{-0.1}$		
ASPECS-LP.3mm.12	2.5739	$10.6^{+0.0}_{-0.1}$	31^{+18}_{-3}	$0.8^{+0.2}_{-0.1}$	AGN	680
ASPECS-LP.3mm.13	3.6008	$9.8^{+0.1}_{-0.1}$	41^{+15}_{-9}	$1.4^{+0.3}_{-0.2}$		
ASPECS-LP.3mm.14	1.0981	$10.6^{+0.1}_{-0.1}$	27^{+1}_{-4}	$1.6^{+0.0}_{-0.2}$		
ASPECS-LP.3mm.15	1.0964	$9.7^{+0.3}_{-0.0}$	62^{+0}_{-4}	$2.9^{+0.0}_{-0.0}$	AGN	689
ASPECS-LP.3mm.16	1.2938	$10.3^{+0.1}_{-0.0}$	11^{+1}_{-3}	$0.5^{+0.1}_{-0.2}$		
ASPECS-LP-MP.3mm.01	1.0959	$10.1^{+0.1}_{-0.0}$	8^{+3}_{-2}	$1.3^{+0.2}_{-0.2}$		
ASPECS-LP-MP.3mm.02	1.0874	$10.4^{+0.0}_{-0.0}$	25^{+0}_{-0}	$1.0^{+0.0}_{-0.0}$	X	661

Notes. (1) ASPECS-LP ID number. (2) Source redshift. (3) Stellar mass (M_*). (4) Star formation rate (SFR). (5) Visual attenuation (A_V). (6)–(7) X-ray classification as active galactic nucleus (AGN) or other X-ray source (X) from Luo et al. (2017) and corresponding X-ray ID (XID).

densities below 1 mJy. However, only one of these sources (ASPECS-LP.3mm.01) previously had a spectroscopic redshift (Walter et al., 2016; Inami et al., 2017).

3.4 Physical properties

3.4.1 Star formation rates from MAGPHYS and [O II]

For all the CO-detected sources, we derive the SFR (and M_* and A_V) from the UV-FIR data (including 24μm–160μm and ASPECS-LP 1.2 mm and 3.0 mm) using MAGPHYS (see § 3.2.3), which are provided in Table 3.2. The full SED fits are shown in Figure 3.19.

For the $1 < z < 1.5$ subsample, we have access to the [O II] $\lambda\lambda$3727, 3730-doublet. We derive SFRs from [O II] $\lambda\lambda$3727, 3730 following Kewley et al. (2004), adopting a Chabrier (2003) IMF. The observed [O II] luminosity gives a measurement of the unobscured SFR, which

Table 3.3: Emission line fluxes, unobscured [O ɪɪ] SFRs, and metallicities for the ASPECS-LP line search and prior-based sources at $z < 1.5$ with S/N([O ɪɪ]) > 3.

ID (1)	MUSE ID (2)	$z_{\rm MUSE}$ (3)	$F_{\rm [O\,II]\,\lambda3726+\lambda3729}$ ($\times10^{-20}$erg s^{-1} cm^{-2}) (4)	$F_{\rm [Ne\,III]\,\lambda3870}$ ($\times10^{-20}$erg s^{-1} cm^{-2}) (5)	$\mathrm{SFR}^{\rm no\ dust}_{\rm [O\,II]}$ ($\mathrm{M}_\odot\,\mathrm{yr}^{-1}$) (6)	$Z_{\rm [Ne\,III]/[O\,II],M08}$ (12 + log(O/H)) (7)
3mm.06	8	1.0955	111.4 ± 1.4	1.9 ± 0.4	3.59 ± 0.05	9.05 ± 0.08
3mm.11	16	1.0965	24.4 ± 0.3	0.9 ± 0.1	0.79 ± 0.01	8.78 ± 0.06
3mm.14	924	1.0981	53.6 ± 1.6	2.4 ± 0.4	1.74 ± 0.05	8.70 ± 0.07
3mm.15	6870	1.0979	13.8 ± 0.4	$< 0.2 \pm 0.1$	…	…
3mm.16	925	1.2942	67.0 ± 4.0	$< 1.9 \pm 0.8$	3.26 ± 0.20	$> 8.79 \pm 0.17$
MP.3mm.01	985	1.0959	17.8 ± 1.5	$< 0.6 \pm 0.5$	0.57 ± 0.05	$> 8.56 \pm 0.29$
MP.3mm.02	879	1.0874	245.9 ± 1.1	11.5 ± 0.6	7.78 ± 0.03	8.73 ± 0.02

Notes. We do not compute a SFR([O ɪɪ]) or metallicity for the X-ray detected AGN (3mm.15). (1) ASPECS-LP.3mm ID number. (2) MUSE ID (3) MUSE redshift. (4) [O ɪɪ] $\lambda3726 + \lambda3729$ flux (S/N > 3). (5) [Ne ɪɪɪ] $\lambda3870$ flux (upper limits are reported if S/N < 3). (6) SFR([O ɪɪ] $\lambda\lambda3727, 3730$) without correction for dust attenuation. (7) Metallicity from [Ne ɪɪɪ]/[O ɪɪ] based on Maiolino et al. (2008).

can be compared to the total SFR (including the FIR) to derive the fraction of obscured star formation. For that reason, we not apply a dust correction when calculating the SFR([O ɪɪ]).

The derived SFR([O ɪɪ] $\lambda\lambda 3727, 3730$) is dependent on the oxygen abundance. We have access to the oxygen abundance directly for some of the sources and can also make an estimate through the mass-metallicity relation (e.g., Zahid et al., 2014). However, because of the additional uncertainties in the calibrations for the oxygen abundance, we instead adopt an average [O ɪɪ] $\lambda\lambda 3727, 3730/\mathrm{H}\alpha$ ratio of unity, given that all our sources are massive and hence expected to have high oxygen abundance $12 + \log(\mathrm{O/H}) \sim 8.8$, where $[\mathrm{O\,II}]/\mathrm{H}\alpha = 1.0$ (e.g., Kewley et al., 2004). For all galaxies with S/N([O ɪɪ] $\lambda\lambda 3727, 3730) > 3$, excluding the X-ray AGN, the [O ɪɪ] $\lambda 3726 + \lambda 3729$ line flux measurements and SFRs are presented in Table 3.3.

3.4.2 Metallicities

It is well known that the gas-phase metallicity of galaxies is correlated with their stellar mass, with more massive galaxies having higher metallicities on average (e.g., Tremonti et al., 2004; Maiolino et al., 2008; Mannucci et al., 2010; Zahid et al., 2014). For the $1.0 < z < 1.42$ sub-sample, we have access to [Ne ɪɪɪ] $\lambda 3870$ which allows us to derive a metallicity from [Ne ɪɪɪ] $\lambda 3870$/[O ɪɪ] $\lambda\lambda 3727, 3730$. We follow the relation as presented by Maiolino et al. (2008), who calibrated the [Ne ɪɪɪ]/[O ɪɪ] line ratio against metallicities inferred from the direct T_e method (at low metallicity; $12 + \log(\mathrm{O/H}) < 8.35$) and theoretical models from Kewley & Dopita (2002) (at high metallicity, mainly relevant for this paper; $12 + \log(\mathrm{O/H}) > 8.35$). Since the wavelengths of [Ne ɪɪɪ] $\lambda 3870$ and [O ɪɪ] $\lambda\lambda 3727, 3730$ are close, this ratio is practically insensitive to dust attenuation. The physical underpinning lies in the fact that the ratio of the low-ionization [O ɪɪ] and high-ionization [Ne ɪɪɪ] lines is a solid tracer of the shape of the ionization field, given that neon closely tracks the oxygen abundance (e.g., Ali et al., 1991; Levesque & Richardson, 2014; Feltre et al., 2018). As the ionization parameter decreases with increasing stellar metallicity (Dopita et al., 2006a,b) and the metallicity of the young ionizing stars and their birth clouds is correlated, the ratio of [Ne ɪɪɪ] $\lambda 3870$/[O ɪɪ] $\lambda\lambda 3727, 3730$ is a reasonable gas-phase metallicity diagnostic, albeit indirect, with significant scatter (Nagao et al., 2006; Maiolino et al., 2008) and sensitive to model assumptions (e.g., Levesque & Richardson, 2014). If an AGN contributes significantly to the ionizing spectrum, the emission lines may no longer only trace the properties associated with massive star formation. For this reason, we exclude the sources with an X-ray AGN from the analysis of the metallicity.

We report the [Ne ɪɪɪ] flux measurements and [Ne ɪɪɪ]/[O ɪɪ] metallicities in Table 3.3. The solar metallicity is $12 + \log(\mathrm{O/H}) = 8.76 \pm 0.07$ (Caffau et al., 2011).

3.4.3 Molecular gas properties

The derivation of the molecular gas properties of our sources is detailed in Aravena et al. (2019). For reference, we provide a brief summary here.

We convert the observed CO($J \rightarrow J-1$) flux to a molecular gas mass (M_{H_2}) using the relations from Carilli & Walter (2013). To convert the higher-order CO transitions to CO(1–0), we need to know the excitation dependent intensity ratio between the CO

Table 3.4: Molecular gas properties of the ASPECS-LP line search and prior-based sources, with formal uncertainties.

ID	$z_{\rm CO}$	$J_{\rm up}$	FWHM $({\rm km\,s^{-1}})$	$F_{\rm line}$ $({\rm Jy\,km\,s^{-1}})$	$L'_{\rm line}$ $(\times10^9\,{\rm K\,km\,s^{-1}\,pc^2})$	$L'_{\rm CO(1-0)}$	$M_{\rm H_2}$ $(\times10^{10}\,{\rm M_\odot})$	$M_{\rm H_2}/M_*$	$t_{\rm depl}$ (Gyr)
(1)	(2)	(3)	(4)	(5)	(6)	(7)	(8)	(9)	(10)
3mm.01	2.5436	3	517 ± 21	1.02 ± 0.04	33.9 ± 1.3	80.8 ± 13.8	29.1 ± 5.0	12.1 ± 2.1	1.2 ± 0.2
3mm.02	1.3167	2	277 ± 26	0.47 ± 0.04	10.7 ± 0.9	14.1 ± 2.1	5.1 ± 0.7	0.3 ± 0.1	4.5 ± 0.8
3mm.03	2.4534	3	368 ± 37	0.41 ± 0.04	12.8 ± 1.3	30.5 ± 5.9	11.0 ± 2.1	2.2 ± 0.6	1.6 ± 0.6
3mm.04	1.4140	2	498 ± 47	0.89 ± 0.07	23.2 ± 1.8	30.5 ± 4.3	11.0 ± 1.6	0.6 ± 0.1	1.8 ± 0.3
3mm.05	1.5504	2	617 ± 58	0.66 ± 0.06	20.4 ± 1.9	26.9 ± 4.0	9.7 ± 1.4	0.3 ± 0.1	1.6 ± 0.4
3mm.06	1.0951	2	307 ± 33	0.48 ± 0.06	7.7 ± 1.0	10.1 ± 1.7	3.6 ± 0.6	1.0 ± 0.2	1.1 ± 0.2
3mm.07	2.6961	3	609 ± 73	0.76 ± 0.09	27.9 ± 3.3	66.5 ± 13.6	23.9 ± 4.9	2.0 ± 0.5	1.3 ± 0.3
3mm.08	1.3821	2	50 ± 8	0.16 ± 0.03	4.0 ± 0.7	5.3 ± 1.2	1.9 ± 0.4	0.4 ± 0.1	0.5 ± 0.2
3mm.09	2.6977	3	174 ± 17	0.40 ± 0.04	14.7 ± 1.5	35.0 ± 6.8	12.6 ± 2.5	1.0 ± 0.2	0.4 ± 0.1
3mm.10	1.0367	2	460 ± 49	0.59 ± 0.07	8.5 ± 1.0	11.1 ± 1.9	4.0 ± 0.7	0.3 ± 0.1	2.2 ± 0.4
3mm.11	1.0964	2	40 ± 12	0.16 ± 0.03	2.6 ± 0.5	3.4 ± 0.7	1.2 ± 0.3	0.8 ± 0.2	1.2 ± 0.3
3mm.12	2.5739	3	251 ± 40	0.14 ± 0.02	4.8 ± 0.7	11.3 ± 2.5	4.1 ± 0.9	0.9 ± 0.2	1.3 ± 0.5
3mm.13	3.6008	4	360 ± 49	0.13 ± 0.02	4.3 ± 0.7	13.9 ± 3.4	5.0 ± 1.2	8.8 ± 2.8	1.2 ± 0.5
3mm.14	1.0981	2	355 ± 52	0.35 ± 0.05	5.6 ± 0.8	7.4 ± 1.4	2.7 ± 0.5	0.7 ± 0.1	1.0 ± 0.2
3mm.15	1.0964	2	260 ± 39	0.21 ± 0.03	3.4 ± 0.5	4.4 ± 0.8	1.6 ± 0.3	3.2 ± 1.1	0.3 ± 0.1
3mm.16	1.2938	2	125 ± 28	0.08 ± 0.01	1.8 ± 0.2	2.3 ± 0.4	0.8 ± 0.1	0.4 ± 0.1	0.7 ± 0.2
MP.3mm.01	1.0962	2	169 ± 21	0.13 ± 0.03	2.1 ± 0.5	2.8 ± 0.7	1.0 ± 0.2	0.7 ± 0.2	1.3 ± 0.5
MP.3mm.02	1.0872	2	107 ± 30	0.10 ± 0.03	1.6 ± 0.4	2.0 ± 0.6	0.7 ± 0.2	0.3 ± 0.1	0.3 ± 0.1

Notes. The CO full width at half maximum (FWHM) and line fluxes are taken from González-López et al. (2019). (1) ASPECS-LP ID number. (2) CO redshift. (3) Upper level of CO transition. (4) CO line FWHM. (5) Integrated line flux. (6) Line luminosity (7) CO(1–0) line luminosity assuming Daddi et al. (2015) excitation (§ 3.4.3). (8) Molecular gas mass assuming $\alpha_{\rm CO} = 3.6\,{\rm K\,(km\,s^{-1}\,pc^2)^{-1}}$. (9) Molecular-to-stellar mass ratio, $M_{\rm H_2}/M_*$. (10) Depletion time, $t_{\rm depl} = M_{\rm H_2}/{\rm SFR}$.

lines, r_{J1}. We use the excitation ladder as estimated by Daddi et al. (2015) for galaxies on the MS, where $r_{21} = 0.76 \pm 0.09$, $r_{31} = 0.42 \pm 0.07$ and $r_{41} = 0.31 \pm 0.06$ (see also Decarli et al. 2016b). To subsequently convert the CO(1–0) luminosity to M_{H_2}, we use an $\alpha_{\mathrm{CO}} = 3.6\,\mathrm{M}_\odot\,(\mathrm{K\,km\,s^{-1}\,pc^2})^{-1}$, appropriate for star-forming galaxies (Daddi et al. 2010a; see Bolatto et al. 2013 for a review). This choice of α_{CO} is supported by our finding that the ASPECS-LP sources are mostly on the MS and have (near-)solar metallicity (see § 3.5.4).

With these conversions in mind, the molecular gas mass and derived quantities we report here can easily be rescaled to different assumptions following:

$$M_{\mathrm{H}_2}/\mathrm{M}_\odot = (\alpha_{\mathrm{CO}}/r_{J1})L'_{\mathrm{CO}(J\rightarrow J-1)}/(\mathrm{K\,km\,s^{-1}\,pc^2}). \tag{3.1}$$

The CO line and derived molecular gas properties are all presented in Table 3.4.

3.5 Results: Global sample properties

In this section we discuss the physical properties of all the ASPECS-LP sources that were found in the line search (without preselection) and based on a MUSE redshift prior. Since the sensitivity of ASPECS-LP varies with redshift, we discuss the galaxies detected in different CO transitions separately. In terms of the demographics of the ASPECS-LP detections, we focus on CO(2–1) and CO(3–2), where we have the most detections.

3.5.1 Stellar mass and SFR distributions

The majority of the detections consist of CO(2–1) and CO(3–2), at $1 < z < 2$ and $2 < z < 3$, respectively. A key question is in what part of the galaxy population we detect the largest gas-reservoirs at these redshifts.

We show histograms of the stellar masses and SFRs for the sources detected in CO(2–1) and CO(3–2) in Figure 3.6. We compare these to the distribution of all galaxies in the field that have a spectroscopic redshift from MUSE and our extended (photometric) catalog of all other galaxies. In the top part of each panel we show the percentage of galaxies we detect in ASPECS, compared to the number of galaxies in reference catalogs.

We focus first on the SFRs, shown in the right panels of Figure 3.6. The galaxies in which we detect molecular gas are the galaxies with the highest SFRs and the detection fraction increases with SFR. This is expected as molecular gas is a prerequisite for star formation and the most highly star-forming galaxies are thought to host the most massive gas reservoirs. The detections from the line search at $1.0 < z < 1.7$ alone account for $\approx 40\%$ of the galaxy population at $10 < \mathrm{SFR}[\mathrm{M}_\odot/\mathrm{yr}] < 30$, increasing to $> 75\%$ at $\mathrm{SFR} > 30\mathrm{M}_\odot/\mathrm{yr}$. Including the prior-based detections, we find 60% of the population at $\mathrm{SFR} \approx 20\,\mathrm{M}_\odot\,\mathrm{yr}^{-1}$. Similarly, at $2.0 < z < 3.1$, the detection fraction is highest in the most highly star-forming bin. Notably, however, with ASPECS-LP we probe molecular gas in galaxies down to much lower SFRs as well. The sources span over two orders of magnitude in SFR, from ≈ 5 to $> 500\,\mathrm{M}_\odot\,\mathrm{yr}^{-1}$.

The stellar masses of the ASPECS-LP detections in CO(2–1) and CO(3–2) are shown in the left panels of Figure 3.6. We detect molecular gas in galaxies spanning over two orders of magnitude in stellar mass, down to $\log M_*[\mathrm{M}_\odot] \sim 9.5$. The completeness increases with

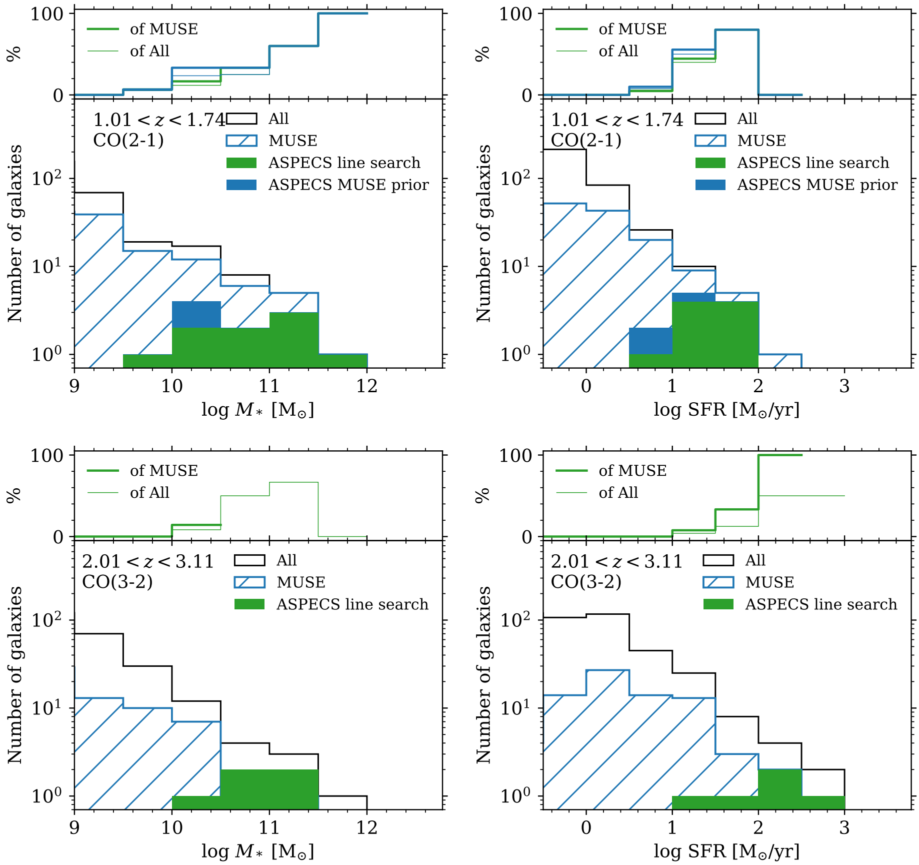

Figure 3.6: Histograms of the stellar mass (M_*, *left*) and star formation rate (SFR, *right*) of the ASPECS-LP detected galaxies, in comparison to all galaxies with MUSE redshifts and our extended photometric redshift catalog, in the indicated redshift range. We only show the range relevant to the ASPECS-LP detections: $M_* > 10^9\,\mathrm{M}_\odot$ and SFR $> 0.3\,\mathrm{M}_\odot$/yr. *Top:* CO(2–1) detected sources at $1.01 < z < 1.74$. *Bottom:* CO(3–2) detected sources at $2.01 < z < 3.11$. In each of the four panels, the detected fraction in both reference catalogs is shown on top (no line is drawn if the catalog does not contain any objects in that bin). With the ASPECS-LP, we detect approximately 40% of (50%) of all galaxies at $M_* > 10^{10}\,\mathrm{M}_\odot (> 10^{10.5}\,\mathrm{M}_\odot)$ at $1.0 < z < 1.7$ $(2.0 < z < 3.1)$, respectively. In the same redshift bins, we detect approximately 60% (30%) of all galaxies with SFR $> 10\,\mathrm{M}_\odot$/yr $(> 30\,\mathrm{M}_\odot$/yr).

stellar mass, which is presumably a consequence of the fact that more massive galaxies star-forming galaxies also have a larger gas fraction and higher SFR. At $M_* > 10^{10}$ M$_\odot$, we are $\approx$ 40% complete at $1.0 < z < 1.7$, while we are $\approx$ 50% complete at $M_* > 10^{10.5}$ M$_\odot$ at $2 < z < 3.1$. The full distribution includes both star-forming and passive galaxies, which would explain why we do not pick-up all galaxies at the highest stellar masses.

3.5.2 AGN fraction

From the deepest X-ray data over the field we identify five AGN in the ASPECS-LP line search sample (see Table 3.2). Two of these are detected in CO(2–1); namely, ASPECS-LP.3mm.05 and ASPECS-LP.3mm.15. The remaining three X-ray AGN are ASPECS-LP.3mm.01, 3mm.09, and 3mm.12, detected in CO(3–2). The AGN fraction among the ASPECS-LP sources is thus $2/10 = 20\%$ at $1.0 < z < 1.7$ and $3/5 = 60\%$ at $2.0 < z < 3.1$ (note that including the MUSE-prior sources decreases the AGN fraction). If we consider the total number of X-ray AGN over the field, we detect $2/6 = 30\%$ of the X-ray AGN at $1.0 < z < 1.7$ and $3/6 = 50\%$ at $2.0 < z < 3.1$, without preselection.

The comoving number density of AGN increases out to $z \approx 2 - 3$ (Hopkins et al., 2007). Using a volume limited sample out to $z \sim 0.7$ based on the Sloan Digital Sky Survey and *Chandra*, Haggard et al. (2010) showed that the AGN fraction increases with both stellar mass and redshift, from a few percent at $M_* \sim 10^{10.7}$ M$_\odot$, up to 20% in their most massive bin ($M_* \sim 10^{11.8}$ M$_\odot$). Closer in redshift to the ASPECS-LP sample, Wang et al. (2017) investigated the fraction of X-ray AGN in the GOODS fields and found that among massive galaxies, $M_* > 10^{10.6}$M$_\odot$, $5 - 15\%$ and $15 - 50\%$ host an X-ray AGN at $0.5 < z < 1.5$ and $1.5 < z < 2.5$, respectively. The AGN fractions found in ASPECS-LP are broadly consistent with these ranges given the limited numbers and considerable Poisson error.

Given the AGN fraction among the ASPECS-LP sources (20% at $z \sim 1.4$ and 60% at $z \sim 2.6$), the question arises whether we detect the galaxies in CO *because* they are AGN (i.e., AGN-powered), or, whether we detect a population of galaxies that hosts a larger fraction of AGN (e.g., because the higher gas content fuels both the AGN and star-formation)? The CO ladders in, e.g., quasar host galaxies can be significantly excited, leading to an increased luminosity in the high-J CO transitions compared to star-forming galaxies at lower excitation (see, e.g., Carilli & Walter, 2013; Rosenberg et al., 2015). With the band 3 data we are sensitive to the lower-J transitions, decreasing the magnitude of such a bias toward AGN. At the same time, the ASPECS-LP is sensitive to the galaxies with the largest molecular gas reservoirs, which are typically the galaxies with the highest stellar masses and/or SFRs. As AGN are more common in massive galaxies, it is natural to find a moderate fraction of AGN in the sample, increasing with redshift. Once the ASPECS-LP is complete with the observations of the band 6 (1 mm) data, we can investigate the higher J CO transitions for these sources and possibly test whether the CO is powered by AGN activity.

3.5.3 Obscured and unobscured star formation rates

We investigate the fraction of dust-obscured star formation by comparing the SFR derived from the [O II] $\lambda\lambda$3727, 3730 emission line, without dust correction, with the (independent)

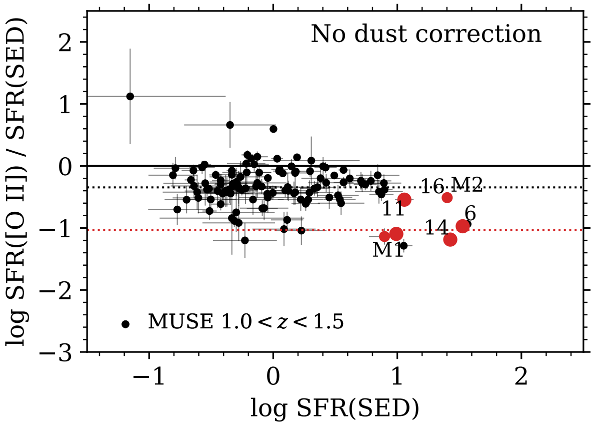

Figure 3.7: Total SFR from the SED fitting versus the ratio between SFR([O II] λλ3727, 3730) and SFR(SED) for the ASPECS-LP detected sources (red) and the MUSE $1.0 < z < 1.5$ reference sample (black). This shows the ratio between the unobscured SFR([O II]) and total SFR. The black and red dotted lines show the median ratio between SFR([O II]) and SFR(SED) for all galaxies and the ASPECS-LP sources only. The median fraction of obscured/unobscured SFR is $10.8^{+2.3}_{-5.1}$ for all the ASPECS-LP sources.

total SFR from modeling the UV-FIR SED with MAGPHYS. We show the ratio between the SFR([O II]) and the total SFR(SED) as a function of the total SFR in Figure 3.7. We use the observed (unobscured) [O II] luminosity, yielding a measurement of the fraction of unobscured SFR. Immediately evident is the fact that more highly star-forming galaxies (which are on average more massive) are more strongly obscured. The median ratio (bootstrapped errors) of obscured/unobscured SFR is $10.8^{+3.0}_{-5.1}$ for the ASPECS-LP sources from the line search, which have a median mass of $10^{10.6}$ $M_{\odot}$ (cf. $2.2^{+0.2}_{-0.1}$ for the complete sample of MUSE galaxies, with a median mass of 10^{9} $M_{\odot}$). Including the objects from the prior-based search does not significantly affect this fraction ($10.8^{+2.3}_{-5.1}$, at a median mass of $M_{*} \sim 10^{10.6}$ $M_{\odot}$).

3.5.4 Metallicities at $1.0 < z < 1.42$

The molecular gas conversion factor is dependent on the metallicity, which is therefore an important quantity to constrain. Specifically, $\alpha_{\rm CO}$ can be higher in galaxies with significantly sub-solar metallicities, where a large fraction of the molecular gas may be CO faint, or lower in (luminous) starburst galaxies, where CO emission originates in a more highly excited molecular medium (e.g., Bolatto et al., 2013).

Given that the majority of the ASPECS-LP sources are reasonably massive, $M_{*} \geq 10^{10}$ $M_{\odot}$, their metallicities are likely to be (super-)solar, based on the mass-metallicity relation (e.g., Zahid et al., 2014).

For the ASPECS-LP sources at $1.0 < z < 1.42$, the MUSE coverage includes [Ne III] λ3870, which can be used as a metallicity indicator (§ 3.4.2). We infer a metallicity for ASPECS-

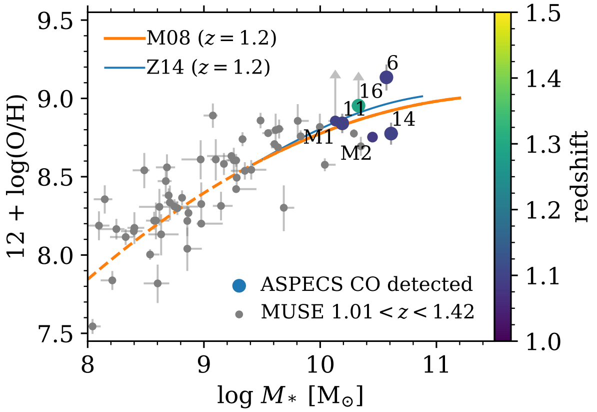

Figure 3.8: Stellar mass (M_*) - metallicity ($12 + \log(\mathrm{O/H})$) relation for the $1 < z < 1.5$ sub-sample. We use the ratio of [Ne III] λ3870 and the [O II] $\lambda\lambda$3727, 3730-doublet, available at $z < 1.42$, to derive the metallicity (Maiolino et al. 2008). The solid lines show the mass-metallicity relations from Zahid et al. (2014) and Maiolino et al. (2008), (converted to the same IMF and metallicity scale, Kewley & Ellison 2008), where the latter was interpolated to the average redshift of the sample (and extrapolated to lower masses, dashed line, for reference). Overall, the ASPECS-LP galaxies are consistent with a (super-)solar metallicity.

LP.3mm.06, 3mm.11, 3mm.14 and ASPECS-LP-MP.3mm.02. In addition, we can provide a lower limit on the metallicity for ASPECS-LP.3mm.16 and ASPECS-LP-MP.3mm.01, based on the upper limit on the flux of [Ne III].

In Figure 3.8, we show the ASPECS-LP sources on the stellar mass - gas-phase metallicity plane. For reference, we show the mass-metallicity relation from Maiolino et al. (2008) (that matches the [Ne III]/[O II] calibration) and Zahid et al. (2014), both converted to the same IMF and metallicity scale (Kewley & Ellison, 2008). The AGN-free ASPECS-LP sources span about half a dex in metallicity. They are all metal-rich and consistent with a solar or super-solar metallicity, in line with the expectations from the mass-metallicity relation.

The (near-)solar metallicity of our targets supports our choice of α_{CO}, which was derived for $z \approx 1.5$ star-forming galaxies (Daddi et al., 2010a) and is similar to the Galactic α_{CO} (cf. Bolatto et al., 2013).

3.6 Discussion

3.6.1 Sensitivity limit to molecular gas reservoirs

Being a flux-limited survey, the limiting molecular gas mass of the ASPECS-LP, $M_{\mathrm{H}_2}(z)$, increases with redshift. Based on the measured flux limit of the survey, we can gain insight into what masses of gas we are sensitive to at different redshifts. The sensitivity of the ASPECS-LP Band 3 data itself is presented and discussed in González-López et al. (2019):

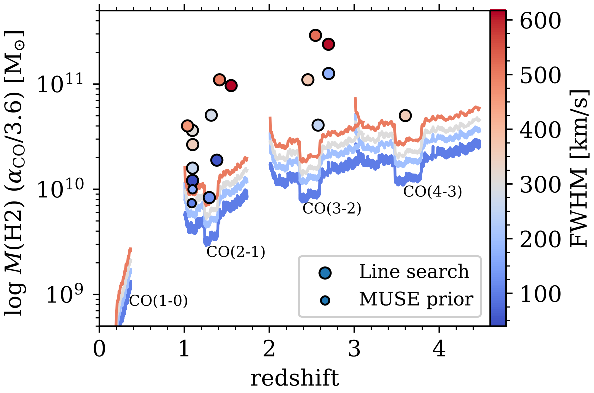

Figure 3.9: The 5σ molecular gas mass detection limit of ASPECS-LP as a function of redshift and CO line full width at half maximum (FWHM), assuming $\alpha_{CO} = 3.6$ and Daddi et al. (2015) excitation (see § 3.4.3). The sensitivity varies with redshift and increases with the square root of the decreasing line width at fixed luminosity, indicated by the color. The points indicate the ASPECS-LP blind and prior-based sources, which are detected both in the deeper and shallower parts of the sensitivity curve.

it is relatively constant across the frequency range, being deepest in the center where the different spectral tunings overlap.

Assuming a CO line full width at half maximum (FWHM) and an α_{CO} and excitation ladder as in § 3.4.3, we can convert the root-mean-square noise level of ASPECS-LP in each channel to a sensitivity limit on $M_{H_2}(z)$. The result of this is shown in Figure 3.9. With increasing luminosity distance, ASPECS-LP is sensitive to more massive reservoirs. This is partially compensated by the fact that the first few higher-order transitions are generally more luminous at the typical excitation conditions in star-forming galaxies. The $M_{H_2}(z)$ function has a strong dependence on the FWHM, as broader lines at the same total flux are harder to detect (see also González-López et al. 2019). As the FWHM is related to the dynamical mass of the system, and we are sensitive to more massive systems at higher redshifts, these effects will conspire in further pushing up the gas-mass limit to more massive reservoirs.

At $1.0 < z < 1.7$, the lowest gas mass we can detect at 5σ (using the above assumptions and a FWHM for CO(2–1) of 100 km s^{-1}) is $M_{H_2} \sim 10^{9.5}$ M$_\odot$, with a median limiting gas mass over the entire redshift range of $M_{H_2} \geq 10^{9.7}$ M$_\odot$ ($M_{H_2} \geq 10^{9.9}$ M$_\odot$ at FWHM = 300 km s^{-1}). At $2.0 < z < 3.1$ the median sensitivity increases to $M_{H_2} \gtrsim 10^{10.3}$ M$_\odot$, assuming a FWHM of 300 km s^{-1} for CO(3–2). In reality the assumptions made above can vary significantly for individual galaxies, depending on the physical conditions of their ISM.

As cold molecular gas precedes star formation, the $M_{H_2}(z)$ selection function of ASPECS-LP can, to first order, be viewed as a SFR(z) selection function. Since more massive star-forming galaxies have higher SFRs (albeit with significant scatter), a weaker correlation with stellar mass may also be expected. These rough, limiting relations will provide useful context to understand what galaxies we detect with ASPECS.

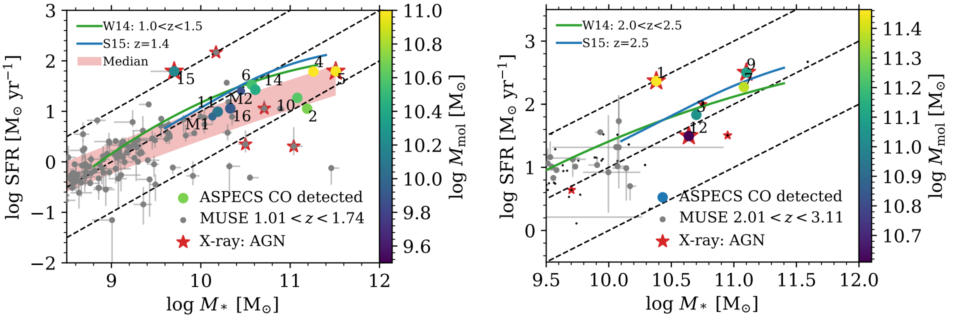

Figure 3.10: Stellar mass (M_*) versus SFR (from MAGPHYS) for the CO(2–1) and CO(3–2) detected galaxies at $1.0 < z < 1.7$ (*left*) and $2.0 < z < 3.1$ (*right*), respectively. The ASPECS-LP line search and MUSE prior-based CO detections are represented by the larger and smaller circles respectively, colored by their molecular gas mass (M_{H_2}). The gray and black points show the MUSE and photometric reference sample of galaxies, respectively. Red stars indicate X-ray sources identified as AGN from Luo et al. (2017). The green and blue solid curves denote the galaxy main sequence relationships from, respectively, Whitaker et al. (2014) and Schreiber et al. (2015). The red band shows ±0.3 dex around a polynomial fit to the running median of all galaxies in the panel. Lines of constant sSFR (0.1, 1 and 10 Gyr^{-1}) are shown black and dashed. At $z \sim 1.4$ ASPECS-LP detects molecular gas in galaxies that span a range of SFRs above, on, and below the galaxy MS.

3.6.2 Molecular gas across the galaxy main sequence

We show the ASPECS-LP sources in the stellar mass - SFR plane at $1.01 < z < 1.74$ and $2.01 < z < 3.11$ in Figure 3.10. On average, star-forming galaxies with a higher stellar mass have a higher star formation rate, with the overall star formation rate increasing with redshift for a given mass, a relation usually denoted as the galaxy main sequence (MS). We show the MS relations from Whitaker et al. (2014, W14) and Schreiber et al. (2015, S15) at the average redshift of the sample. The typical intrinsic scatter in the MS at the more massive end is around 0.3 dex or a factor 2 (Speagle et al., 2014), which we can use to discern whether galaxies are on, above or below the MS at a given mass.

Systematic offsets in the MS

It is interesting to note that the average SFRs we derive with MAGPHYS are lower than what is predicted by the MS relationships from W14 and S15 (Figure 3.10). This offset is seen irrespective of including the FIR photometry to the SED fitting of the ASPECS-LP sources. This illustrates the fact that different methods of deriving SFRs from (almost) the same data can lead to somewhat different results (see, e.g., Davies et al. 2016 for a recent comparison). Both W14 and S15 derive their SFRs by summing the estimated UV and IR flux (UV+IR): W14 obtains the UV flux from integrating the UV part of their best-fit FAST SED (Kriek et al., 2009) and scales the *Spitzer*/MIPS 24 μm flux tot a total IR luminosity using a single template based on the Dale & Helou (2002) models. S15 instead uses (stacked) *Herschel*/PACS and SPIRE data for the IR luminosity, modeling these with Chary & Elbaz (2001) templates.

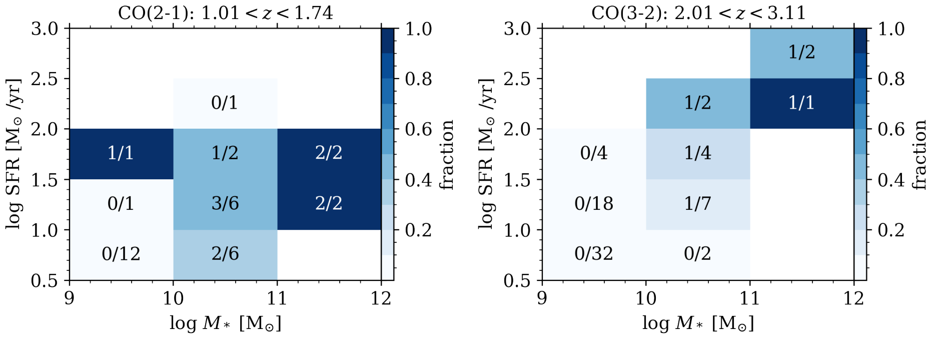

Figure 3.11: Fraction of sources detected by ASPECS-LP in M_*–SFR space at $1.01 < z < 1.74$ (*left*) and $2.01 < z < 3.11$ (*right*). This includes the detections from both the line search and the MUSE prior-based search. We are most complete at the highest SFRs and stellar masses. At a fixed stellar mass (SFR), the completeness fraction increases with SFR (stellar mass).

Recently, Leja et al. (2019) remodeled the UV–24μm photometry for all galaxies from 3D-HST survey (which were used in deriving the W14 result) using the Bayesian SED fitting code Prospector-α (Leja et al., 2017). While Prospector-α also models the broadband SED in a Bayesian framework and shares several similarities with magphys, such as the energy-balance assumption, it is a completely independent code with its own unique features (e.g., the inclusion of emission lines, different stellar models, and nonparametric star formation histories). Interestingly, the SFRs derived by Leja et al. (2019) are $\sim 0.1 - 1$ dex lower than those derived from UV+IR, because of the contribution of old stars to the overall energy output that is neglected in SFR(UV+IR).

While the exact nature of this offset remains to be determined, solving the systematic calibrations between different SFR indicators (or a rederivation of the MS relationship) is beyond the scope of this paper. In the following we show ±0.3 dex scatter around a second order polynomial fit to the rolling median of the SFRs all the galaxies (without any color selection) as a reference in the lower redshift bin. At the massive end where our ASPECS-LP sources lie, we indeed find that this curve lies somewhat below the W14 and S15 relationships. In the higher redshift bin the situation is less clear (given the limited number of sources) and we keep the literature references. With this description of the median SFR at a given stellar mass in hand, we are in the position to compare the SFRs of the individual ASPECS-LP sources to the population average SFR.

Normal galaxies at $1.01 < z < 1.74$

The ASPECS-LP sources at $1.01 < z < 1.74$ are shown in the (M_*, SFR)-plane in left panel of Figure 3.10. For comparison we show all sources in this redshift range with a secure spectroscopic redshift, as MUSE is mostly complete for massive, star-forming galaxies in the regime of the ASPECS-LP detections at these redshifts (see Figure 3.6).

At the depth of the ASPECS-LP, we are sensitive enough to probe molecular gas reservoirs

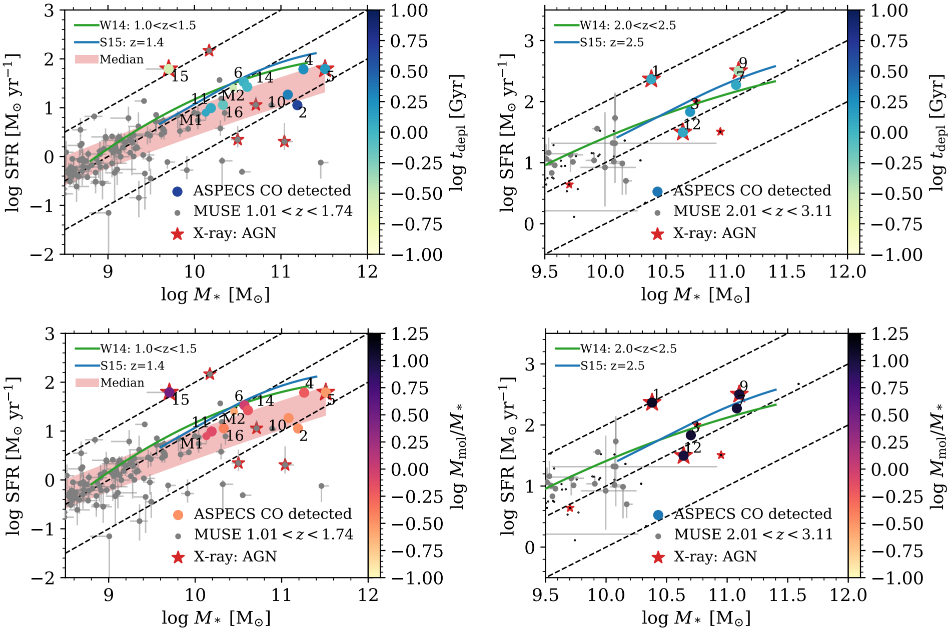

Figure 3.12: Stellar mass (M_*) versus SFR for the galaxies at $1 < z < 1.7$ (*left*) and $2 < z < 3.1$ (*right*). The ASPECS-LP detections from the full and prior-based search are represented by the larger and smaller circles respectively. The gray and black points show the MUSE and photometric reference samples of galaxies, respectively. Red stars indicate X-ray sources identified as AGN from (Luo et al., 2017). The color in the different panels denotes the change in depletion time ($t_{\rm depl} = M_{\rm H_2}/{\rm SFR}$; *top*) and molecular-to-stellar mass ratio ($M_{\rm H_2}/M_*$; *bottom*). The green and blue solid curves denote the MS relationships from, respectively, Whitaker et al. (2014) and Schreiber et al. (2015). The red band shows ±0.3 dex around a polynomial fit to the running median of all galaxies in the panel. Lines of constant sSFR (0.1, 1 and 10 $\rm Gyr^{-1}$) are shown black and dashed. The gas fraction and depletion time vary systematically in galaxies across the main sequence.

in a variety of galaxies that lie on and even below the MS at $z \sim 1.4$. Most of the ASPECS-LP galaxies detected in this redshift range lie on the MS, spanning a mass range of ~ 2 decades at the massive end. These galaxies belong to the population of normal star-forming galaxies at these redshifts.

As expected, with the primary sample alone we detect essentially all massive galaxies that lie above the MS, for $M_* > 10^{9.5}$ $\rm M_\odot$. The lowest mass galaxy we detect is ASPECS-LP.3mm.15, which is elevated significantly above the MS and is also an X-ray classified AGN. One galaxy, with the highest SFR of all, is a notable outlier for not being detected: MUSE#872 ($M_* = 10^{10.2}$ $\rm M_\odot$, SFR ~ 150 $\rm M_\odot\ yr^{-1}$). From the prior-based search we find that no molecular gas emission is seen in this source at lower levels either. While the nondetection of this object is very interesting, we caution that this source is also a broad-line AGN in MUSE and it is possible that its SFR is overestimated.

Notably, we also detect a number of galaxies that lie significantly below the MS (e.g., ASPECS-LP.3mm.02), meaning they have SFRs well below the population average. Despite their low SFR, these sources host a significant gas reservoir and have a gas fraction that is in some cases similar to MS galaxies at their stellar mass. The detection of a significant molecular gas reservoir in these sources is interesting, as these sources would typically not be selected in targeted observations for molecular gas.

Overall, we detect the majority of the galaxies on the massive end of the MS at $1.0 < z < 1.7$ in CO. We show the detection rate in bins of stellar mass and SFR in the left panel of Figure 3.11. At a SFR $> 10\ \mathrm{M_\odot\,yr^{-1}}$, we detect $> 60\%$ of galaxies at all masses at these redshifts. If we focus on galaxies with $M_* > 10^{10}\mathrm{M_\odot}$, we are $> 60\%$ complete down to $\log \mathrm{SFR}[\mathrm{M_\odot\,yr^{-1}}] > 0.5$, where we encompass all MS galaxies.

Massive galaxies at $2.01 < z < 3.11$

At $2.01 < z < 3.11$, we are sensitive to CO(3–2) emission from massive gas reservoirs. We plot the galaxies detected in CO(3–2) on the MS in the right panel of Figure 3.10. For completeness, we have added ASPECS-LP.3mm.12 to the figure as well, but caution that the photometry is blended with a lower redshift foreground source. As the number of spectroscopic redshifts from MUSE is more limited in this regime, we also include galaxies from our extended photometric redshift catalog as small black dots (indicating AGN with red stars).

The detections from ASPECS-LP make up most of the massive and highly star-forming galaxies at these redshifts. Based on their CO flux, the sources all have a molecular gas mass of $\geq 10^{10.5}\ \mathrm{M_\odot}$ and correspondingly high molecular gas fractions $M_{\mathrm{H_2}}/M_* \geq 1.0$. Their SFRs differ by over an order of magnitude. ASPECS-LP.3mm.07 and 09 are both at $z \approx 2.697$ and lie on the MS with SFRs between $150 - 350\ \mathrm{M_\odot\,yr^{-1}}$. In contrast, ASPECS-LP.3mm.03 has a lower SFR of $< 100\mathrm{M_\odot\,yr^{-1}}$. ASPECS-LP.3mm.01 has a very high gas fraction and SFR for its stellar mass and is also detected as an X-ray AGN.

We show the quantitative detection fraction for CO(3–2) at these redshifts in the right panel of Figure 3.11. Note that, as the area of the HUDF and the ASPECS-LP is small, there are relatively few massive galaxies in the field at these redshifts.

3.6.3 Evolution of molecular gas content in galaxies

We now provide a brief discussion of the evolution of the molecular gas properties (and the individual outliers) in the full ASPECS-LP sample of 18 sources, including the muse prior-based sources, in the context of the MUSE derived properties. A more detailed discussion of these results will be provided in Aravena et al. (2019).

From systematic surveys of the galaxy population at $z \approx 0$, we know that the molecular gas properties of galaxies vary across the MS (e.g., Saintonge et al., 2016, 2017). The same trends are unveiled in the ASPECS-LP sample out to $z \approx 3$. To reveal these trends more clearly, we show the MS plot colored by the depletion time ($t_{\mathrm{depl}} = M_{\mathrm{H_2}}/\mathrm{SFR}$) and gas fraction (indicated by $M_{\mathrm{H_2}}/M_*$) in Figure 3.12. The molecular gas mass and depletion time of the ASPECS-LP sources vary systematically across the MS. On average, galaxies above the MS have higher gas fractions and shorter depletion times than galaxies on the MS, while the contrary is true for galaxies below the MS (longer depletion times, smaller gas fractions).

At $z \sim 1.4$, the sources span about an order of magnitude in depletion time, from $0.3 - 5$ Gyr, with a median depletion time of ≈ 1.2 Gyr. This is comparable to the average depletion times found in $z = 1-3$ star-forming galaxies (e.g., Daddi et al., 2010a; Tacconi et al., 2013). ASPECS-LP.3mm.02, which appears to harbor a substantial gas reservoir while its SFR puts it significantly below the MS, has a correspondingly long depletion time of several gigayears. Although the numbers are more limited at higher redshifts, we see a similar variety in depletion times at $z \sim 2.6$, with a median depletion time of ≈ 1.3 Gyr. For galaxies of similar masses we do not find a strong evolution in the depletion time between the $z \sim 1.4$ and $z \sim 2.6$ bins.

The evolution of the gas fraction across the MS is clearly seen for the sources at $z \sim 1.4$. The lowest gas-mass fractions we find are of the order of 30%, while the galaxies with the highest gas fractions have about equal mass in stars and in molecular gas, with a median of $M_{\mathrm{H}_2}/M_* \approx 0.6$. These are comparable to the gas fractions found at similar redshifts (Daddi et al., 2010a; Tacconi et al., 2013). The gas fractions at $z \sim 2.6$ are substantially higher than they are at lower redshift. ASPECS-LP.3mm.09 and 12 have substantial gas fractions close to unity, while both ASPECS-LP.3mm.03 and 07, have a molecular gas mass of about ×2 their mass in stars (median $M_{\mathrm{H}_2}/M_* \approx 2.0$). ASPECS-LP.3mm.1, 3mm.13 and 3mm.15 are outliers in this picture, with a substantially higher gas fraction than the other sources. Both 3mm.01 and 3mm.15 are also starbursts with a high inferred SFR and show an X-ray detected AGN. This high SFR is consistent with the high gas fraction and a picture in which the large gas reservoir fuels a strong starburst, while some gas powers the AGN simultaneously. As may be expected given the flux-limited nature of the observations, the highest redshift source, ASPECS-LP.3mm.13, also has a substantial gas fraction ($M_{\mathrm{H}_2}/M_* = 8.8 \pm 2.8$). As a whole, Figure 3.12 reveals the strength of the ASPECS-LP probing the molecular gas across cosmic time without preselection.

3.7 Summary

In this paper we use two spectroscopic integral-field observations of the *Hubble* Ultra Deep Field, ALMA in the millimeter, and MUSE in the optical regime, to further our understanding of the properties of the galaxy population at the peak of cosmic star formation ($1 < z < 3$). We start with the line emitters identified from the ASPECS-LP Band 3 (3 mm) data without any preselection (González-López et al., 2019). By using the MUSE data, as well as the deep multiwavelength data that is available for the HUDF, we find that all ALMA-selected sources are associated with a counterpart in the optical/near-IR imaging. The spectroscopic information from MUSE enables us to associate all ALMA line emitters with emission coming from rotational transitions of carbon monoxide (CO) that result in unique redshift identifications: We identify 10 line emitters as CO(2–1) at $1 < z < 2$, five as CO(3–2) at $2 < z < 3$ and one as CO(4–3) at $z = 3.6$. The line search done using the ALMA data is conservative, to avoid contamination by spurious sources in the very large 3 mm data cube (González-López et al., 2019). We therefore also use the MUSE data as a positional and redshift prior to push the detection limit of the ALMA data to greater depth and identify additional CO emitters at $z < 2.9$, increasing the total number of ALMA line detections in the field to 18.

We present MUSE spectra of all CO-selected galaxies, and use the diagnostic emission lines covered by MUSE to constrain the physical properties of the ALMA line emitters. In particular, for galaxies with coverage of [O II] $\lambda3727$/[Ne III] $\lambda3870$ at $z \leq 1.5$ in the MUSE data, we infer metallicities consistent with being (super-)solar, which motivates our choice of a Galactic conversion factor to transform CO luminosities to molecular (H_2) gas masses for these galaxies in this series of ASPECS-LP papers (Decarli et al., 2019; González-López et al., 2019; Aravena et al., 2019; Popping et al., 2019). We also compare the unobscured [O II] $\lambda3727$-derived SFRs of the galaxies to the total SFR derived from their spectral energy distributions with MAGPHYS and confirm that a number of them have high extinction in the rest-frame UV/optical regime.

Using the very deep *Chandra* imaging available for the HUDF, we determine an X-ray AGN fraction of 20% and 60% among the CO(2–1) and CO(3–2) emitters at $z \sim 1.4$ and $z \sim 2.6$, respectively, suggesting that we do not preferentially detect AGN at $z < 2$. A future analysis of the band 6 data from the ASPECS-LP will reveal if those sources hosting an AGN show higher CO excitation compared to those that do not.

We use the exquisite multiwavelength data available for the HUDF to derive basic physical parameters (such as stellar masses and SFRs) for all galaxies in the HUDF. We recover the MS of galaxies and show that most of our CO detections are located toward higher stellar masses and SFRs, consistent with expectations from earlier studies. However, being a CO-flux-limited survey, besides galaxies on or above the MS our ALMA data also reveal molecular gas reservoirs in galaxies below the MS at $z \sim 1.4$, down to SFRs of $\approx 5\ \mathrm{M_\odot\,yr^{-1}}$ and stellar masses of $M_* \approx 10^{10}\ \mathrm{M_\odot}$. At higher redshift, we detect massive and highly star-forming galaxies in molecular gas emission on and above the MS. With our ALMA spectral scan, for stellar masses $M_* \geq 10^{10}(10^{10.5})\ \mathrm{M_\odot}$, we detect about 40% (50%) of all galaxies in the HUDF at $1 < z < 2$ $(2 < z < 3)$. The ASPECS-LP galaxies span a wide range of gas fractions and depletion times, which vary with their location above, on, and below the galaxy main-sequence.

The cross-matching of the integral-field spectroscopy from ALMA and MUSE has enabled us to perform an unparalleled study of the galaxy population at the peak of galaxy formation in the HUDF. Given the large range of redshifts covered by the ALMA spectral lines, key diagnostic lines in the UV/optical are only covered by the MUSE observations in specific redshift ranges. The launch of the *James Webb Space Telescope* will greatly expand the coverage of spectral lines that will help to further constrain the physical properties of ALMA-detected galaxies in the HUDF.

Acknowledgements

We are grateful to the referee for providing a constructive report. L.A.B. wants to thank Madusha L.P. Gunawardhana for her help with PLATEFIT. Based on observations collected at the European Southern Observatory under ESO programme(s): 094.A-2089(B), 095.A-

0010(A), 096.A-0045(A), and 096.A-0045(B). This paper makes use of the following ALMA data: ADS/JAO.ALMA#2016.1.00324.L. ALMA is a partnership of ESO (representing its member states), NSF (USA) and NINS (Japan), together with NRC (Canada), NSC and ASIAA (Taiwan), and KASI (Republic of Korea), in cooperation with the Republic of Chile. The Joint ALMA Observatory is operated by ESO, AUI/NRAO, and NAOJ. The National Radio Astronomy Observatory is a facility of the National Science Foundation operated under cooperative agreement by Associated Universities, Inc. "Este trabajo contó con el apoyo de CONICYT + Programa de Astronomía+ Fondo CHINA-CONICYT" J.G-L. acknowledges partial support from ALMA-CONICYT project 31160033. F.E.B. acknowledges support from CONICYT grant Basal AFB-170002 (FEB), and the Ministry of Economy, Development, and Tourism's Millennium Science Initiative through grant IC120009, awarded to The Millennium Institute of Astrophysics, MAS (FEB). J.B. acknowledges support by Fundação para a Ciência e a Tecnologia (FCT) through national funds (UID/FIS/04434/2013) and Investigador FCT contract IF/01654/2014/CP1215/CT0003., and by FEDER through COMPETE2020 (POCI-01-0145-FEDER-007672). T.D-S. acknowledges support from ALMA-CONYCIT project 31130005 and FONDECYT project 1151239. J.H. acknowledges support of the VIDI research programme with project No. 639.042.611, which is (partly) financed by the Netherlands Organization for Scientific Research (NWO). D.R. acknowledges support from the National Science Foundation under grant No. AST-1614213. I.R.S. acknowledges support from the ERC Advanced Grant DUSTYGAL (321334) and STFC (ST/P000541/1). Work on GNUASTRO has been funded by the Japanese MEXT scholarship and its Grant-in-Aid for Scientific Research (21244012, 24253003), the ERC advanced grant 339659-MUSICOS, European Union's Horizon 2020 research and innovation programme under Marie Sklodowska-Curie grant agreement No 721463 to the SUNDIAL ITN, and from the Spanish MINECO under grant No. AYA2016-76219-P.

Facilities: ALMA, VLT: Yepun. *Software:* TOPCAT (Taylor, 2005), GNUASTRO (Akhlaghi & Ichikawa, 2015), IPYTHON (Perez & Granger, 2007), NUMPY (van der Walt et al., 2011), MATPLOTLIB (Hunter, 2007), ASTROPY (The Astropy Collaboration et al., 2013, 2018).

Appendix 3.A Source description and redshift identifications

ASPECS-LP.3mm.01: CO(3–2) at $z = 2.543$. The brightest CO line emitter in the field. It is a *Chandra*/X-ray detected AGN (Luo et al., 2017, #718) and was already found in the line search at 3 mm and 1 mm in CO(3–2), CO(7–6), and CO(8–7) and continuum in the ASPECS-Pilot (Walter et al. 2016; Decarli et al. 2016b, 3mm.1, 1mm.1, 1mm.2; Aravena et al. 2016a, C1) as well as at 1 mm and 5 cm continuum (Dunlop et al., 2017; Rujopakarn et al., 2016, UDF3). The MUSE spectrum (MUSE#35) reveals a high S/N continuum with a wealth of UV absorption features and C III] $\lambda\lambda$1907, 1909 emission, confirming the redshift (Figure 3.13). The source is a (likely interacting) pair with the source $\sim 1\farcs5$ to the west, MUSE#24, at the same redshift ($\Delta v \approx 76\,\mathrm{km\,s^{-1}}$).

ASPECS-LP.3mm.02: CO(2–1) at $z = 1.317$. Detected in both [O II] and continuum in

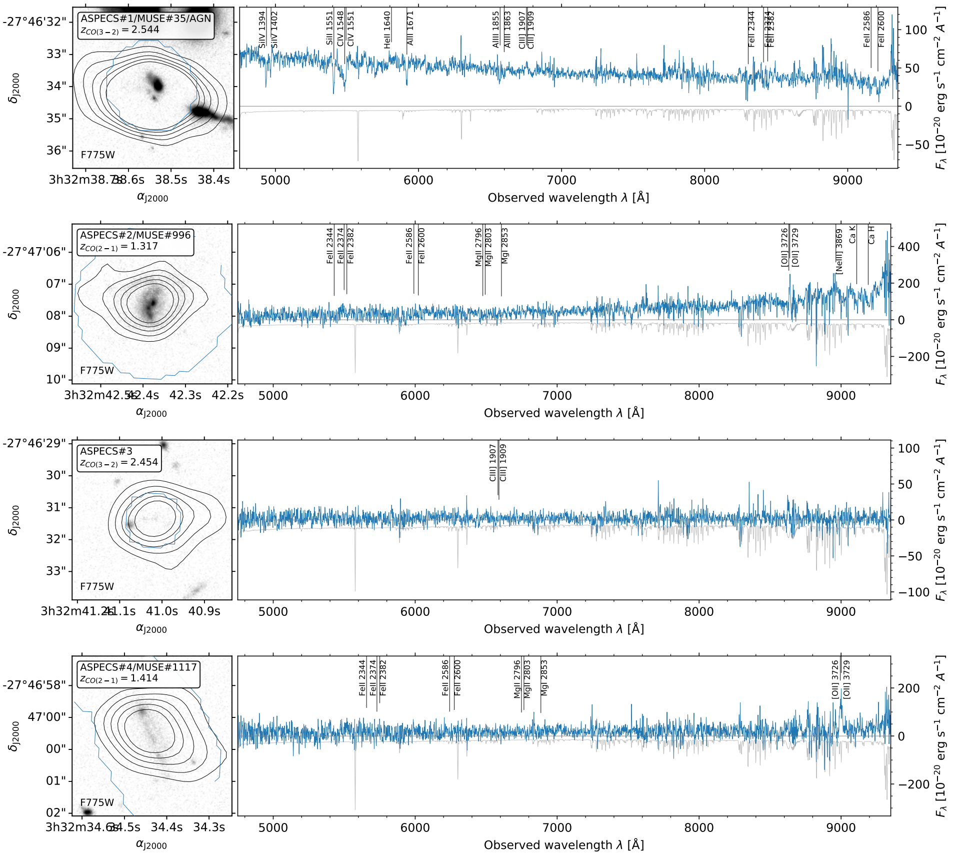

Figure 3.13: MUSE spectroscopy of the ASPECS-LP sources. *Left: HST*/F775W cutout. The colored contour(s) mark the region of the spectral extraction(s), defined by convolving the MUSE PSF with the *HST* segmentation map (see Inami et al. 2017 for details), or a fixed 0.8″ aperture (in the case of a new extraction; #3, #7, #9, #13). The black contours indicate the CO emission from $\pm[3, .., 11]\sigma$ in steps of 2σ. *Right:* MUSE spectrum (1.5 Å Gaussian smoothing) extracted over the marked region. The 1σ uncertainty on the spectrum is shown by the gray line in the direction of negative flux (for clarity), and is largest around skylines. The (expected) positions of different spectral features are annotated; this does not indicate that the feature is also detected. Spectra and lines of nearby or blended sources are shown in red.

MUSE. This source is also detected in continuum at 1 mm and 5 cm (Dunlop et al., 2017; Rujopakarn et al., 2016, UDF16). [O II] λ3727 is severely affected by a sky-line complicating the redshift and line flux measurement. We remeasure the cataloged redshift for this source, which is used to compute the velocity offset with CO(2–1) (Table 3.1). Since we cannot confidently recover the full [O II] flux, we do not include this source in the analyses of § 3.5.3 and § 3.5.4.

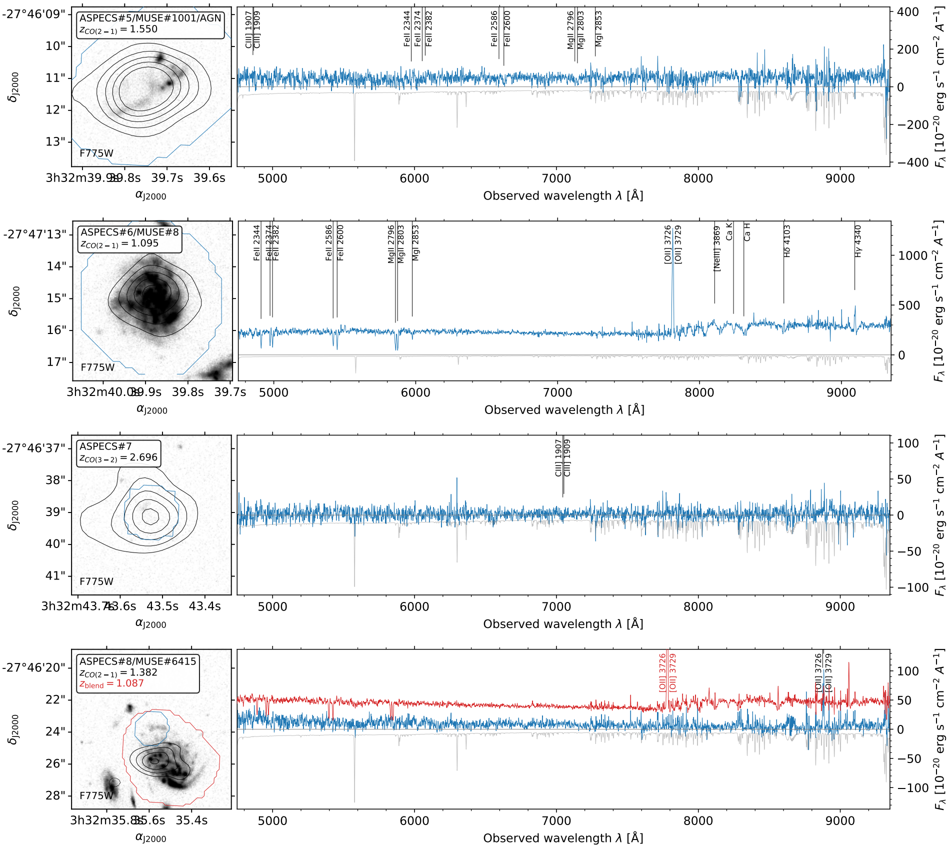

Figure 3.14: Continuation of Figure 3.13. We show spectrum of the complete system of spiral galaxies at ASPECS-LP.3mm.08 in red (scaled down by a factor of 10), to make the faint [O II] $\lambda\lambda$3727, 3730 line matching the CO(2–1) redshift visible. The spectrum for ASPECS-LP.3mm.08 itself is shown in blue (extracted only over a part of the spiral arm). Note the foreground source is independently detected in CO(2–1) as ASPECS-LP-MP.3mm.02 and the fully annotated spectrum for this source is show in Figure 3.15.

ASPECS-LP.3mm.03: CO(3–2) at $z = 2.454$. Photometric redshift indicates $z = 2 - 3$ (Skelton et al., 2014; Rafelski et al., 2015), perfectly in agreement with the detection of CO(3–2) at $z = 2.45$. The source is faint ($m_{\rm F775W} > 27$ mag) and an extraction of the MUSE spectrum yields essentially no continuum signal (see Figure 3.13). This supports a redshift solution between $z = 2 - 3$, where no bright emission lines lie in the MUSE spectral range (see § 3.2.2). Beside there being little continuum in the spectrum, there are no spectral features (in particular emission lines) indicative of a lower redshift ([O II] at $z = 1.30$) or higher redshift (Lyα at $z = 3.60$) solution. Detected in continuum at 1 mm and 5 cm (Dunlop et al., 2017; Rujopakarn et al., 2016, UDF4).

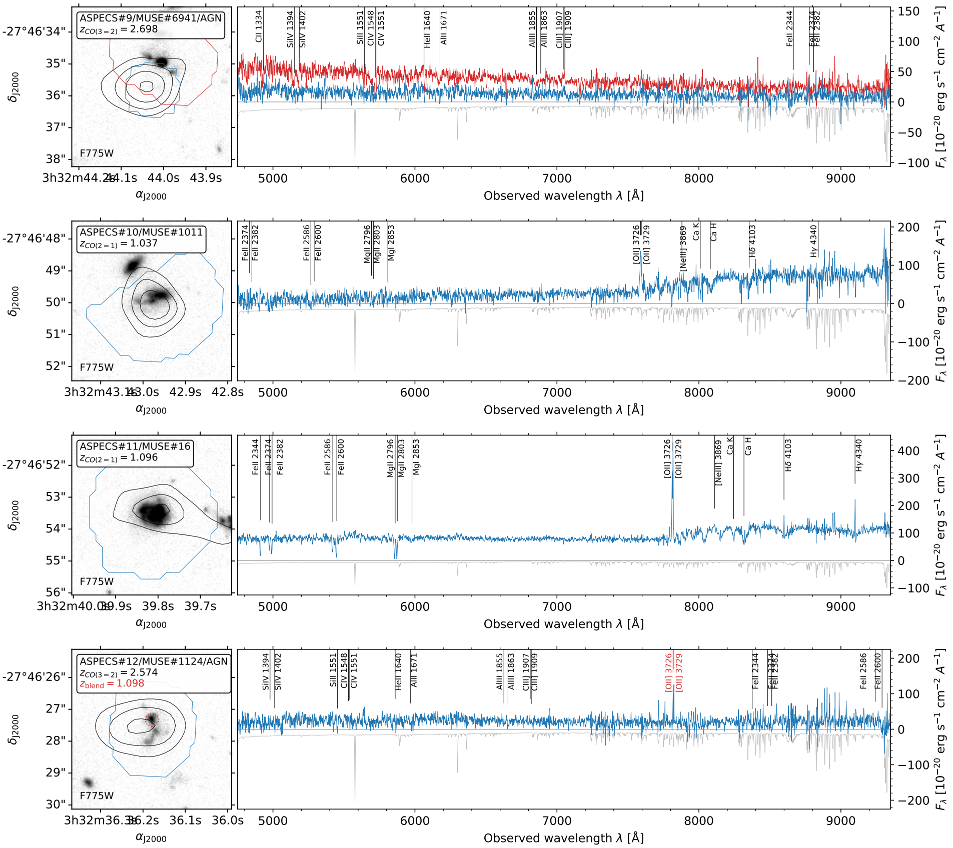

Figure 3.15: Continuation of Figure 3.13. For ASPECS-LP.3mm.09 the UV absorption features matching the CO(3–2) redshift are seen in the source to the north (red spectrum). ASPECS-LP.3mm.12 is blended with a foreground [O II]-emitter (see Figure 3.18).

ASPECS-LP.3mm.04: CO(2–1) at $z = 1.414$. MUSE spectrum shows [O II] and (weak) continuum. Detected in continuum at 1 mm and 5 cm (Dunlop et al., 2017; Rujopakarn et al., 2016, UDF6).

ASPECS-LP.3mm.05: CO(2–1) at $z = 1.550$. A massive ($M_* \approx 10^{11.5}$ M$_\odot$) galaxy and an X-ray classified AGN (Luo et al., 2017, #748). It was also detected by the ASPECS-Pilot in 1 mm continuum (C2, Aravena et al. 2016a; cf. Dunlop et al. 2017), in CO(2–1) and also CO(5–4) and CO(6–5) (ID.3, Decarli et al., 2016b), and in 5 cm continuum (Rujopakarn et al., 2016, UDF8). NIR spectroscopy from the SINS survey (Förster Schreiber et al., 2009) reveals Hα λ6565, confirming the redshift we also find from MUSE, based on the Fe II and Mg II absorption features.

ASPECS-LP.3mm.06: CO(2–1) at $z = 1.095$. Part of an overdensity in the HUDF at the same redshift. Rich star-forming spectrum in MUSE with a wealth of continuum and

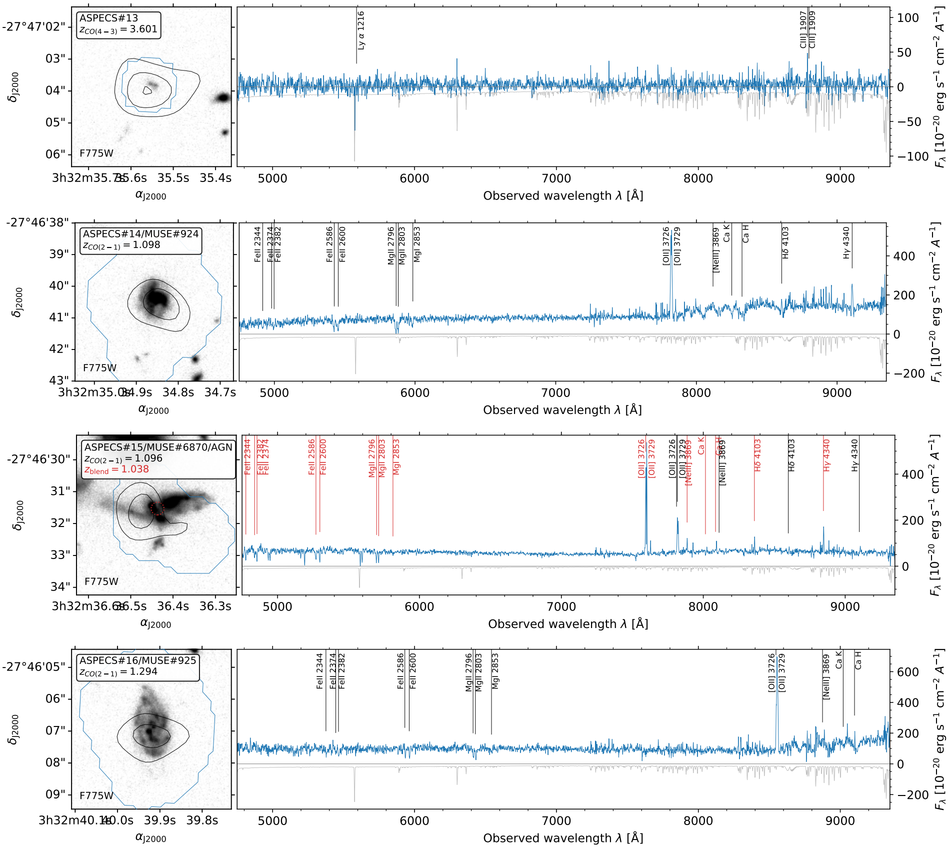

Figure 3.16: Continuation of Figure 3.13. The spectrum of ASPECS-LP.3mm.15 is severely blended. We have highlighted the strongest blended features (from a foreground source at $z = 1.038$) in red.

emission features. Detected in X-ray, but not classified as an AGN (Luo et al., 2017, #749).

ASPECS-LP.3mm.07: CO(3–2) at $z = 2.696$. Photometric redshift indicates $z = 2 - 3$ (Skelton et al., 2014; Rafelski et al., 2015), perfectly in agreement with the detection of CO(3–2) at $z = 2.69$. The source is faint ($m_{\mathrm{F775W}} > 27$ mag) and a reextraction of the MUSE spectrum yields essentially no continuum signal (see Figure 3.14). This supports a redshift solution between $z = 2 - 3$, where no bright emission lines lie in the MUSE spectral range (see § 3.2.2). Beside there being little continuum in the spectrum, there are no spectral features indicative of a lower redshift or higher redshift solution (cf. ASPECS-LP.3mm.03). There is reasonably close proximity between ASPECS-LP.3mm.07 and 09 at $z = 2.69$, which are separated by only $\sim 7''.5$ (60 kpc at that redshift). This object is one of the brightest sources in the HUDF at 1 mm (UDF2; Dunlop et al. 2017) and also detected at 5 cm (Rujopakarn et al., 2016).

ASPECS-LP.3mm.08: CO(2–1) at $z = 1.382$. The source has a more complex morphology which was already discussed in the ASPECS-Pilot program (Decarli et al. 2016b, see their

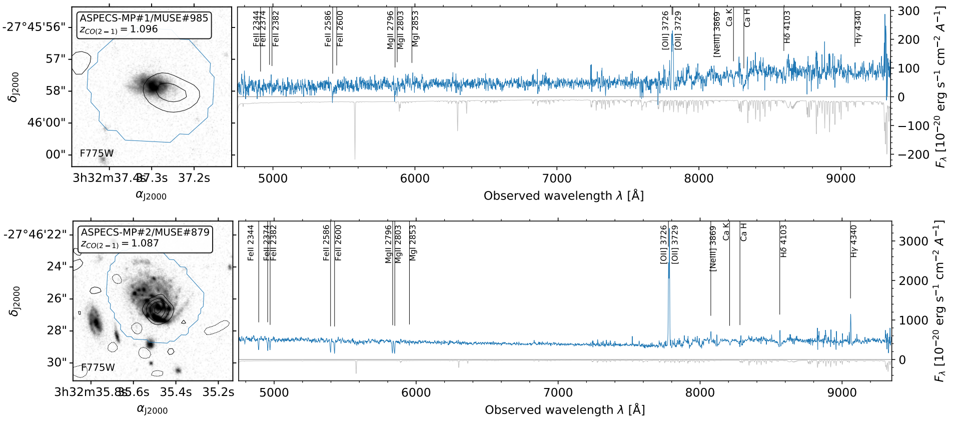

Figure 3.17: Continuation of Figure 3.13, showing the MUSE-prior based sources.

Fig. 3). The CO emission is spatially consistent with a system of spiral galaxies. MUSE reveals that the south-west spiral is in the foreground at $z = 1.087$. Careful examination of the MUSE cube reveals [O II] emission matching the CO redshift in an arc north of the galaxies and possibly toward the south-west, which is $\sim 1''.8$ away of peak of the CO emission ($\sim$ 15 kpc at the redshift of the source). A potential scenario is that the north-east spiral galaxies is the background source, in which case the ionized gas emission of the spiral is completely obscured by the disk of the (south-west) foreground spiral. This is consistent with the spatial position of the CO emission. An alternative scenario is that of a third disk galaxy harboring the CO reservoir, which is completely hidden from sight by the spiral galaxies in the foreground, except for the structures seen in the north and east. We note that resolved SED fitting of this source was recently performed by Sorba & Sawicki (2018), assuming the foreground redshift for the entire system. A clear break can be seen in the sSFR (their Figure 1.) for the northern-arm and possibly also a south-west arm; consistent with locations where [O II]-emission is seen. For the purpose of this paper, we associate the north-east spiral with ASPECS-LP.3mm.08 and the south-west spiral with ASPECS-LP-MP.3mm.02, but we note that this is uncertain in the case of ASPECS-LP.3mm.08. Given the limited flux we observe from the ionized gas, we do not discuss this source in that context.

ASPECS-LP.3mm.09: CO(3–2) at $z = 2.698$. Photometric redshift indicates $z = 2 - 3$ (Skelton et al., 2014; Rafelski et al., 2015), perfectly in agreement with the detection of CO(3–2) at $z = 2.69$. The source is faint ($m_{\mathrm{F775W}} > 27$ mag), yet, UV absorption features at $z = 2.695$, matching the expected redshift of CO(3–2) at $z = 2.698$, are found in the MUSE spectrum at the position of the source (see Figure 3.15). The features arise in a source (MUSE#6941) $\sim 0''.8$ to the north ($\sim$ 6.5 kpc at $z \sim 2.7$). The spectrum of the northern source reveals a superposition of the $z = 2.695$ source with a foreground galaxy at $z = 1.555$. This is also suggestive from the morphology in *HST*, which shows a redder central clump for the northern source. Given the potential proximity of the two sources, both spatially and spectrally, ASPECS-LP.3mm.09 could be part of a pair of galaxies with the source to the north.

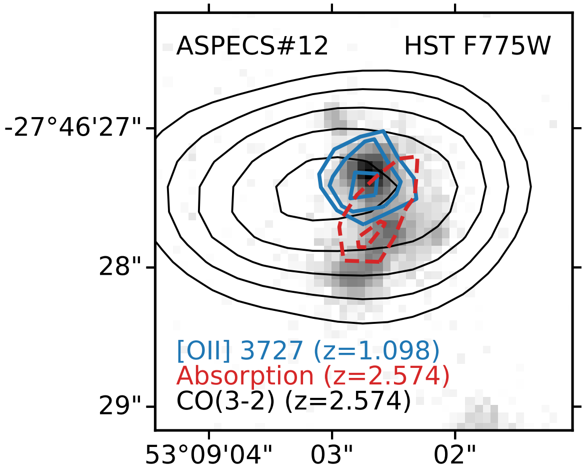

Figure 3.18: *HST*/F775W cutout of ASPECS-LP.3mm.12, with CO(3–2) emission at $z = 2.5738$. The MUSE spectrum of this source reveals two redshifts. There is [O II] emission at z=1.098, spatially consistent with a foreground galaxy to the north. While the continuum is faint, cross-correlating the spectrum with an absorption line template reveals a peak at $z = 2.5738$ with S/N > 4. Subsequent stacking of the UV absorption lines (C II λ1335, Si IV $\lambda\lambda$1394, 1403, C IV $\lambda\lambda$1548, 1551, Al II λ1671, Al II $\lambda\lambda$1854, 1862) reveals that the absorption is co-spatial with the background galaxy and consistent with the redshift of CO(3–2). All contours start at $\pm 3\sigma$, increasing by 1σ (where solid and dashed indicate emission and absorption respectively).

Notably, ASPECS-LP.3mm.09 is also detected as an X-ray AGN; Luo et al. 2017, #865. Note there is also reasonably close proximity between ASPECS-LP.3mm.07 and 09 at $z = 2.69$, which are separated by only $\sim 7.''5$ (60 kpc at that redshift). One of the brightest sources in the HUDF at 1 mm (UDF1; Dunlop et al. 2017), also detected at 5 cm (Rujopakarn et al., 2016).

ASPECS-LP.3mm.10: CO(2–1) at $z = 1.037$. The lowest redshift detection. Features a close star-forming companion at the same redshift. The MUSE spectrum shows continuum with both absorption and emission line features ([O II]). We reextract the spectrum with a new segmentation map to recompute the redshift and to minimize blending of the [O II] flux from the close companion at slightly different redshift. The [O II] line is detected in the source, but given the residual deblending uncertainties we do not take into it into account in the analyses of § 3.5.3 and § 3.5.4.

ASPECS-LP.3mm.11: CO(2–1) at $z = 1.096$. Part of the overdensity in the HUDF at the same redshift. MUSE reveals a rich star-forming spectrum with stellar continuum and both absorption and emission ([O II], [Ne III]) features.

ASPECS-LP.3mm.12: CO(3–2) at $z = 2.574$. Detected in 1 mm continuum (C4; (Aravena et al., 2016a)) and an X-ray AGN (Luo et al., 2017, #680). The source contains a CO line at 96.76 GHz. The optical counterpart shows red colors in *HST* and features a blue component toward the north. The source is considered to be a single galaxy in most photometric catalogs (e.g., Skelton et al., 2014; Rafelski et al., 2015). However, the redshift from the MUSE catalog for this source, $z = 1.098$ (based on a confident [O II] detection, see Figure 3.15), is incompatible with being CO(2–1), which would be at $z = 1.383$. Closer inspection of the source in the MUSE IFU data reveals that the [O II] emission is only originating from the blue clump to the north of the source (see Figure 3.18). A reanalysis of the MUSE spectrum revealed weak absorption features that, when cross correlated with an absorption line template, correspond a redshift $z = 2.5738$. Assuming that the CO line is CO(3–2) instead, this independently matches the redshift from ASPECS-LP exactly ($z = 2.5738$). To further confirm that the absorption features are associated with ASPECS-LP.3mm.12, we spatially stacked narrow-bands over all strong UV absorption features (without any preselection). To construct the narrow-band, we sum the flux over each absorption feature (assuming a fixed 7Å line width) and subtract the continuum measured in two side bands offset by ±10Å (same width in total). We then stacked the individual narrow-bands by summing the flux in each spatial pixel (note, the same result is found when taking the mean or median). The stacked absorption features have $S/N > 4$ and are co-spatial with the background galaxies and the CO, confirming the detection of CO(3–2) at $z = 2.5738$ (see Figure 3.18).

ASPECS-LP.3mm.13: CO(4–3) at $z = 3.601$. Highest redshift CO detection. It is an F435W dropout and the photometric redshifts for this source consistently suggest that it lies in the $z = 3 - 4$ range (Skelton et al., 2014; Straatman et al., 2016), with $z_{\rm BPZ} = 3.67^{+0.74}_{-0.24}$ (Rafelski et al., 2015). These all suggest a detection of CO(4–3) at $z = 3.601$. In order the spectroscopically confirm this redshift, we extract a MUSE spectrum at the position of the source. The strongest UV emission line observed by MUSE at these redshifts is Lyα, while it also covers the much weaker C IIII] line. Both are not detected in the spectrum of ASPECS-LP.3mm.13. The nondetection of C IIII] at the 10 h depth of the mosaic is understandable, as robustly detecting C IIII] at these redshifts is challenging (see Maseda et al. 2017 for a in-depth discussion, which finds the highest redshift detection of C IIII] in the deep 30 h MUSE data to be at $z \sim 2.9$). Unfortunately, at $z = 3.601$ the expected position of Lyα in MUSE falls close to the [O I] $\lambda5577$ skyline (Figure 3.16), which could explain why it is not detected. Furthermore, the source is likely to have a significant dust content in which case no Lyα emission may be expected at all. Nevertheless, while at $m_{\rm F775W} = 26.4$, the spectrum does not reveal emission or absorption lines compatible with a solution for CO(2–1) at $z = 1.30$ or CO(3–2) at $z = 2.45$, which suggests a higher redshift solution is appropriate for ASPECS-LP.3mm.13 (in agreement with the photo-z). In summary, the combined evidence of the photometric redshifts indicating $z \sim 3.5$ and the lack of a lower redshift solution from MUSE makes the case for the detection of CO(4–3) at $z = 3.601$ in ASPECS-LP.3mm.13.

ASPECS-LP.3mm.14: CO(2–1) at $z = 1.098$. Part of an overdensity in the HUDF. MUSE reveals a rich spectrum with continuum, absorption and a range of emission lines (among which [O II], [Ne III] and Balmer lines).

ASPECS-LP.3mm.15: CO(2–1) at $z = 1.096$. Part of an overdensity in the HUDF at the same redshift. The source lies in a very crowded part of the sky with multiple galaxies at different redshifts overlapping in projection. Detected in X-rays, classified as AGN (Luo et al., 2017, #689). Source was also covered by the ASPECS-Pilot program and detected in CO(2–1) and CO(4–3) (Decarli et al., 2016b, ID.5).

ASPECS-LP.3mm.16: CO(2–1) at $z = 1.294$. Shows a disk-like morphology. MUSE

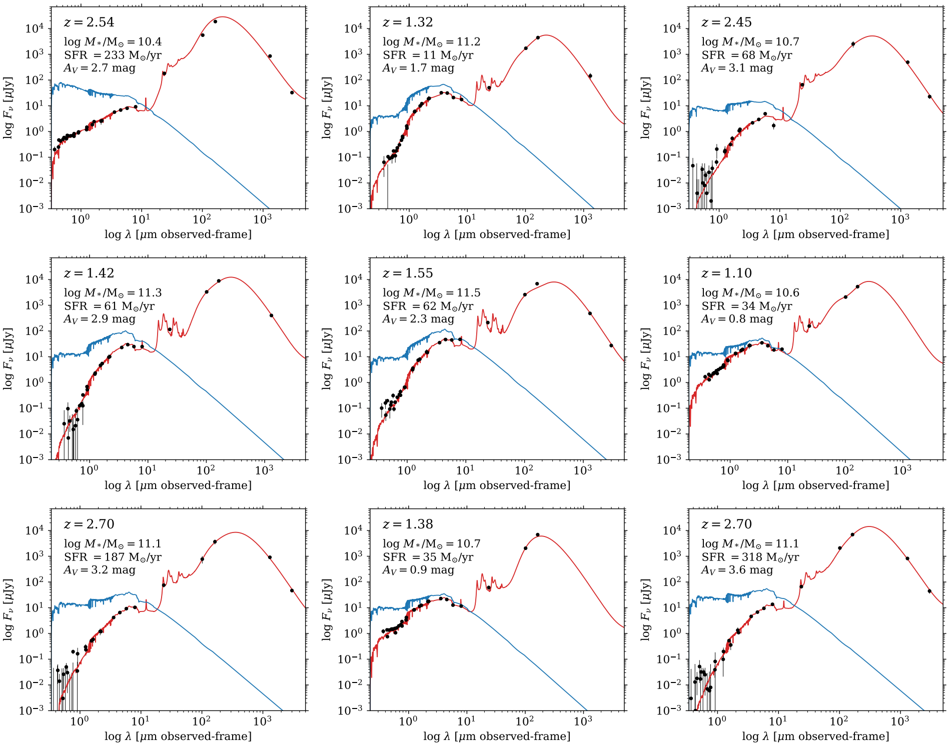

Figure 3.19: Spectral energy distributions (SEDs) for all the ASPECS-LP CO-detected sources from the line search (first sixteen) and MUSE redshift prior-based search (last two). The black points are the observed photometry. The overall best fit SED from MAGPHYS is shown by the red line, while the the model of the unattenuated stellar emission is shown in blue. The redshift and median values of the posterior likelihood distribution of the stellar mass (M_*), star formation rate (SFR) and visual attenuation (A_V) are indicated in each panel.

spectrum reveals a stellar continuum with absorption, as well as emission lines ([O II] and [Ne III]).

ASPECS-LP-MP.3mm.01: CO(2–1) at $z = 1.096$. Part of an overdensity in the HUDF at the same redshift. MUSE spectrum shows stellar continuum with absorption, as well as emission lines ([O II]; Figure 3.17).

ASPECS-LP-MP.3mm.02: CO(2–1) at $z = 1.087$. Foreground galaxy to ASPECS-LP.3mm.08, also described in Decarli et al. (2016b). See ASPECS-LP.3mm.08 for a further description.

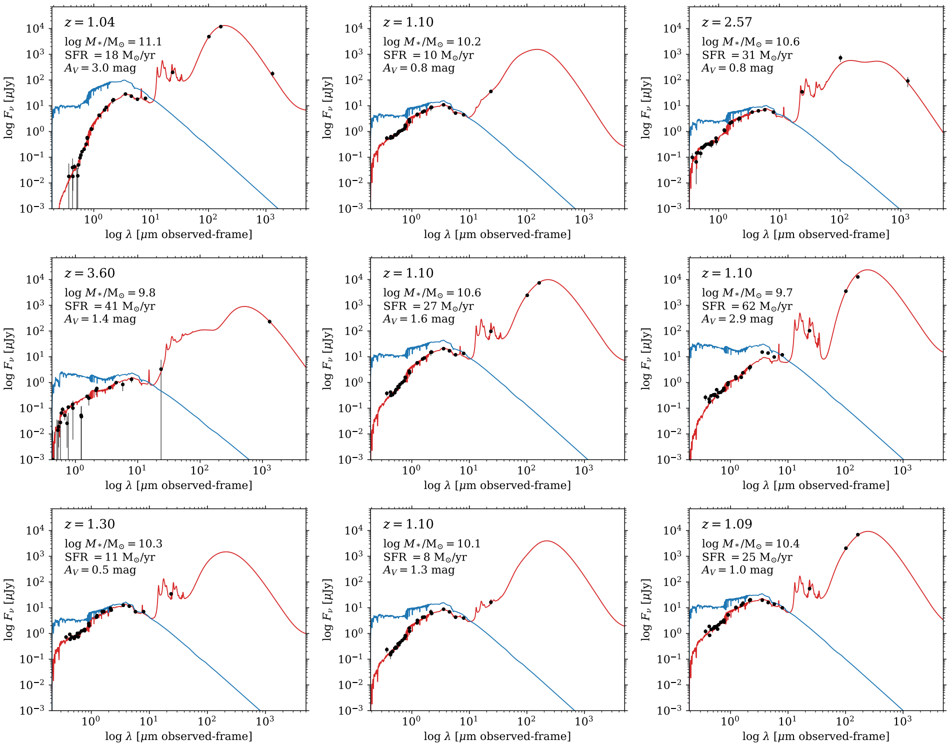

Figure 3.19: *(continued)*

Appendix 3.B MAGPHYS fits for all CO-detected galaxies

We performing SED fitting with MAGPHYS for all ASPECS-LP galaxies, as described in detail in § 3.2.3. The following bands are considered in the SED fitting of the ASPECS-LP galaxies: U_{38} (0.37μm), IA_{427} (0.43μm), F435W (0.43μm), B (0.46μm), IA_{505} (0.51μm), IA_{527} (0.53μm), V (0.54μm), IA_{574} (0.58μm), F606W (0.60μm), IA_{624} (0.62μm), IA_{679} (0.68μm), IA_{738} (0.74μm), IA_{767} (0.77μm), F775W (0.77μm), I (0.91μm), F850LP (0.90μm), J (1.24μm), tJ (1.25μm), F160W (1.54μm), H (1.65μm), tK_s (2.15μm), K (2.21μm), IRAC (3.6μm, 4.5μm, 5.8μm, 8.0μm), MIPS (24μm), PACS (100μm and 160μm) and ALMA Band 6 (1.2 mm) and Band 3 (3.0 mm). The resulting SEDs are shown in Figure 3.19.

4 The ALMA Spectroscopic Survey in the HUDF: CO excitation and atomic carbon in star-forming galaxies at $z = 1 - 3$

Abstract

We investigate the CO excitation and interstellar medium (ISM) conditions in a cold gas mass-selected sample of 22 star-forming galaxies at $z = 0.46 - 3.60$, observed as part of the ALMA Spectroscopic Survey in the *Hubble* Ultra Deep Field (ASPECS). Combined with Very Large Array follow-up observations, we detect a total of 34 CO $J \rightarrow J - 1$ transitions with $J = 1$ up to 8 (and an additional 21 upper limits, up to $J = 10$) and 6 [C I] $^3P_1 \rightarrow {}^3P_0$ and $^3P_2 \rightarrow {}^3P_1$ transitions (and 12 upper limits). The CO(2–1) and CO(3–2)-selected galaxies, at $\langle z \rangle = 1.2$ and 2.5, respectively, exhibit a range in excitation in their mid-$J = 4, 5$ and high-$J = 7, 8$ lines, on average lower than (L_{IR}-brighter) BzK-color- and submillimeter-selected galaxies at similar redshifts. The former implies that a warm ISM component is not necessarily prevalent in gas mass-selected galaxies at $\langle z \rangle = 1.2$. We use stacking and Large Velocity Gradient models to measure and predict the average CO ladders at $z < 2$ and $z \geq 2$, finding $r_{21} = 0.75 \pm 0.11$ and $r_{31} = 0.77 \pm 0.14$, respectively. From the models, we infer that the galaxies at $z \geq 2$ have intrinsically higher excitation than those at $z < 2$. This fits a picture in which the global excitation is driven by an increase in the star formation rate surface density of galaxies with redshift. We derive a neutral atomic carbon abundance of $(1.9 \pm 0.4) \times 10^{-5}$, comparable to the Milky Way and main-sequence galaxies at similar redshifts, and fairly high densities ($\geq 10^4$ cm^{-3}), consistent with the low-J CO excitation. Our results imply a decrease in the cosmic molecular gas mass density at $z \geq 2$ compared to previous ASPECS measurements.

L. A. Boogaard, P. van der Werf, A. Weiss, G. Popping, R. Decarli, F. Walter, *et al.*
The Astrophysical Journal, 902, 109 (2020)

4.1 Introduction

Cold molecular gas is the fuel for star formation. Characterizing the mass of the cold interstellar medium (ISM) and the internal physical conditions (temperature, density and radiation field) is therefore fundamental to our understanding of the process of star formation (see the reviews by McKee & Ostriker 2007; Kennicutt & Evans 2012; and Carilli & Walter 2013). The majority of the star formation at intermediate redshifts ($z = 1 - 3$) takes place in galaxies which have an average star formation rate (SFR) for their stellar mass. These galaxies lie on the 'main sequence of star-forming galaxies'—the empirical correlation between the stellar mass and star formation rate of galaxies across cosmic time (e.g., Noeske et al., 2007a; Elbaz et al., 2011; Whitaker et al., 2014; Schreiber et al., 2015; Boogaard et al., 2018). Although measurements of the molecular gas mass in these galaxies are now more frequently conducted, the physical conditions in the cold ISM of star-forming galaxies (SFGs) at $z > 1$ are still poorly constrained.

The mass of the molecular ISM is dominated by H_2, which does not radiate under typical conditions, and must therefore be traced by other species. The most common and direct tracer of the molecular gas mass is the first rotational transition of carbon monoxide $^{12}C^{16}O$ $J = 1 \rightarrow 0$, hereafter CO(1–0) (e.g., Dickman et al., 1986; Solomon et al., 1987; Bolatto et al., 2008). Alternative tracers of the molecular gas mass include the dust emission (e.g., Hildebrand, 1983; Magdis et al., 2012; Scoville et al., 2014, 2016; Magnelli et al., 2020) and lines from fainter optically thin species, such as neutral atomic carbon ([C I]; Papadopoulos et al., 2004; Weiß et al., 2005; Walter et al., 2011), now more frequently observed in SFGs at $z > 1$ (e.g., Popping et al., 2017b; Valentino et al., 2018; Bourne et al., 2019).

Measurements of the molecular gas mass via CO at $z > 1$ are limited to the specific transitions that can be observed through the atmospheric windows from Earth. Constraints on the CO excitation are therefore crucial to convert observations from higher-J lines back to CO(1–0). The higher rotational levels of CO (with quantum number $J > 1$) are populated both radiatively and collisionally and the rotational ladder of CO is therefore a key probe of the density, n_{H_2}, and kinetic temperature, T_{kin}, of the emitting medium. The excitation of CO can be driven by a number of processes, related to star formation, (galactic) dynamics (including shocks/mechanical heating) and potential activity from an active galactic nucleus (AGN). In the local universe, observations with the *Herschel* satellite have shown that the CO excitation in (U)LIRGS, (Ultra) Luminous Infrared Galaxies with $L_{IR} \geq 10^{11}$ (10^{12}) (Sanders & Mirabel, 1996), can often be well modeled by the combination of a cold component (containing most of the mass) and a warm component, dominating the emission below and above $J \approx 4$ respectively, while heating from an AGN is the dominant contributor to the line emission only for the levels above $J \approx 10$ (e.g., van der Werf et al., 2010; Greve et al., 2014; Kamenetzky et al., 2014, 2017; Rosenberg et al., 2015; Lu et al., 2017). The CO excitation in sources at higher redshift has been a field of intense study, yet, to date, only limited constraints exist regarding the CO ladder in SFGs at $z > 1$.

At the time of the review by Carilli & Walter (2013), the main sources studied in multiple CO transitions at $z > 1$ were quasars (QSOs), radio galaxies, and submillimeter-selected galaxies (SMGs), with high $L_{IR} \gg 10^{12}$ $L_\odot$. Overall, these early results were indicative of decreasing excitation (i.e., a lower n_{H_2} and T_{kin}) going from quasars to SMGs. Since then, the average CO excitation of SMGs has been studied by Bothwell et al. (2013), who characterized a sample of mostly unlensed SMGs at $z = 2-4$, up to CO(7–6) (including CO(1–0) observations from Carilli et al. 2010; Riechers et al. 2010, 2011a; Ivison et al. 2011). Spilker et al. (2014) used Atacama Large Millimeter Array (ALMA) spectral scan observations of 22 lensed SMGs detected with the South Pole Telescope (SPT) at $z = 2 - 6$ (Weiß et al., 2013) to stack CO(3–2) up to CO(6–5). More recently, Yang et al. (2017a) studied *Herschel*-selected, strongly lensed SMGs at $z = 2 - 4$ up to CO(8–7). These studies find that the CO ladders of SMGs can continue to rise up to $J \sim 7$, testifying to a warm and dense ($n \geq 10^{5.5}\,\mathrm{cm}^{-3}$) ISM. The differences between the (low-J) CO excitation in SMGs and (mid-IR selected) AGN have not been found to be statistically significant (Sharon et al., 2016; Kirkpatrick et al., 2019).

In contrast, observations of CO excitation in main-sequence SFGs at $z > 1$ have only recently become possible, with the advent of the Northern Extended Millimeter Array (NOEMA) and ALMA. The Plateau de Bure Interferometer HIgh-z Blue Sequence Survey (PHIBSS) has observed CO(3–2) in a sample of massive, main-sequence-selected galaxies between $z = 1 - 3$ (Genzel et al., 2010, 2015; Tacconi et al., 2010, 2013, 2018), with multi-line CO excitation follow-up of only a few sources (Bolatto et al., 2015; Brisbin et al., 2019). A number of SFGs, selected by their BzK-color (Daddi et al., 2004) and having a detection at 24 μm and 1.4 GHz (Daddi et al., 2010a), have been observed in more than one CO transition from CO(1–0) to CO(3–2) (Dannerbauer et al., 2009; Daddi et al., 2010a; Aravena et al., 2010, 2014). The CO ladder of four of these 'BzK-selected' galaxies at $z \approx 1.5$ was characterized comprehensively by Daddi et al. (2015). They found all sources were significantly excited in their CO(5–4) transition, compared to the lower-J transitions, indicating the presence of both a cold and a denser, possibly warmer gas component. Very recently, Valentino et al. (2020a) expanded these results with observations of a larger sample of similarly IR-bright SFGs at $z = 1.25$. However, all these samples were preselected based on their SFR, and are still among the most massive and IR luminous main-sequence galaxies at these redshifts, with only specific sources selected for multi-line follow-up. Therefore, it remains unclear whether the excitation conditions found in these sources are representative of the general population of SFGs at these redshifts, in particular at lower masses and SFRs.

The ALMA Spectroscopic Survey in the *Hubble* Ultra Deep Field (ASPECS; Walter et al. 2016) provides a unique avenue to study the CO excitation, molecular gas content and physical conditions of the cold ISM of SFGs at high redshift. ASPECS is a flux-limited survey, designed to detect CO in galaxies without preselection. It thereby provides the most complete inventory of the cosmic molecular gas density, $\rho_{\mathrm{H}_2}(z)$, to date (Decarli et al., 2016a, 2019, 2020). The galaxies detected in CO by ASPECS are found to lie on, above, and below the main sequence at $z = 1 - 3$, with near-solar metallicities (Aravena et al., 2019; Boogaard et al., 2019). The coverage of ASPECS (Band 3 and Band 6) provides simultaneous constraints on multiple lines from CO, [C I] for most sources, depending on the redshift (as well as any other species in the frequency range). Furthermore, the multiple tunings scanning through the entire ALMA frequency bands give a high continuum sensitivity, providing a deep (9.3 μJy beam^{-1}, § 4.2.1), contiguous continuum map at 1.2 mm in the *Hubble* Ultra Deep Field (HUDF; Aravena et al., 2020; González-López et al., 2020). Using earlier data from the ASPECS-Pilot program on a smaller area of the sky, Decarli et al. (2016b) studied a sample of seven galaxies at $z = 1 - 3$ (a subset of the sources studied in this paper), finding that the CO excitation conditions were overall lower than those typically found in starbursts, SMGs, and QSO environments.

This paper studies the CO excitation, atomic carbon emission and ISM conditions in a flux-limited sample of 22 CO and/or dust-continuum detected galaxies at $z = 1 - 3$ from the ASPECS Large Program (LP), supplemented by follow-up CO(1–0) observations from VLASPECS (Riechers et al., 2020). The paper is organized as follows. We first present the ALMA and Very Large Array (VLA) observations and the physical properties of the galaxies in the sample (§ 4.2). All line fluxes are measured homogeneously through simultaneous Gaussian fitting (§ 4.3) and presented in § 4.4. We discuss the mid- and high-J CO excitation in the individual CO(2–1)- and CO(3–2)-selected sources at $\langle z \rangle = 1.2$ and $\langle z \rangle = 2.5$, respectively, in § 4.5.1 and compute the average CO ladders through stacking (including individually undetected lines; § 4.5.2). We then use Large Velocity Gradient (LVG) models to characterize the average ladders at $z \leq 2$ and $z > 2$ (§ 4.5.3). We further analyze the low-J CO excitation by placing our galaxies on empirical relations with the rest-frame 850 μm dust luminosity (§ 4.5.4). We next turn to the neutral atomic carbon, discuss its mass and abundance, and use photodissociation (PDR) models to analyze the average ISM conditions in our galaxies (§ 4.6). The implications of our measurements on the average low-, mid-, and high-J CO excitation in SFGs at $z \geq 1$ are discussed in § 4.7. Finally, we conclude with the implications of our results for the inference of the cosmic molecular gas density from ASPECS, as these are the galaxies that directly inform that measurement (§ 4.7.5). Throughout this paper, we use a Chabrier (2003) initial mass function and a concordance flat ΛCDM cosmology with $H_0 = 70\,\mathrm{km\,s^{-1}\,Mpc^{-1}}$, $\Omega_m = 0.3$, and $\Omega_\Lambda = 0.7$, in good agreement with the results from Planck Collaboration et al. (2016).

4.2 Observations and ancillary data

4.2.1 ALMA Spectroscopic Survey Data Reduction

The ASPECS data consists of two spectral scan mosaics over the deepest part of the HUDF (Illingworth et al., 2013; Koekemoer et al., 2013). The raw ASPECS data were processed with CASA (McMullin et al., 2007) as described in González-López et al. (2019) for Band 3 and Decarli et al. (2020) for Band 6. The visibilities were imaged using the task `tclean`, adopting natural weighting. The complete mosaics cover an area of 4.6 arcmin^2 (Band 3) and 2.9 arcmin^2 (Band 6), measured as the region in which the primary beam sensitivity is ≥ 50% of the peak sensitivity (6.1 and 3.7 arcmin^2 when measured down to 20%).

The Band 3 data cube ranges from 84 to 115 GHz, with a channel width of 7.813 MHz, corresponding to velocity resolution of $\Delta v \approx 23.5\,\mathrm{km\,s^{-1}}$ at 99.5 GHz. The spatial resolution of the naturally weighted cube is $\approx 1\farcs8 \times 1\farcs5$ (at 99.5 GHz). The sensitivity varies across the frequency range, reaching an average root-mean-square (rms) sensitivity per channel of $\approx 0.2\,\mathrm{mJy\,beam^{-1}}$, varying across the frequency range (see González-López et al., 2019, Fig. 3). The Band 6 data cube spans from 212–272 GHz, and was resampled at a channel width of 15.627 MHz, corresponding to $\Delta v \approx 19.4\,\mathrm{km\,s^{-1}}$ at 242 GHz. The naturally weighted cube has a beam size of $\approx 1\farcs5 \times 1\farcs1$ and reaches an average rms depth of $\approx 0.5\,\mathrm{mJy\,beam^{-1}}$ per

Table 4.1: Physical properties of the ASPECS-LP sample considered in this paper.

ID 1mm (1)	ID 3mm (2)	ID 9mm (3)	z (4)	$\log M_*$ ($M_\odot$) (5)	$\log$ SFR ($M_\odot$ yr^{-1}) (6)	$\log L_{IR}$ ($L_\odot$) (7)	$\log \Sigma_{SFR}$ ($M_\odot$ yr^{-1} kpc^{-2}) (8)	r_e (arcsec) (9)	X-ray (10)
1mm.C01	3mm.01	9mm.1	2.543	10.4 ± 0.1	2.37 ± 0.10	12.9 ± 0.1	1.07 ± 0.19	0.21 ± 0.04	AGN
1mm.C03	3mm.04	· · ·	1.414	11.3 ± 0.1	1.72 ± 0.13	12.0 ± 0.1	-0.82 ± 0.14	0.88 ± 0.04	· · ·
1mm.C04	3mm.03	9mm.6	2.454	10.7 ± 0.2	1.78 ± 0.21	11.9 ± 0.2	-0.46 ± 0.22	0.63 ± 0.04	· · ·
1mm.C05	3mm.05	· · ·	1.551	11.5 ± 0.1	1.79 ± 0.17	12.0 ± 0.2	-0.83 ± 0.18	0.98 ± 0.04	AGN
1mm.C06	3mm.07	9mm.3	2.696	11.1 ± 0.1	2.32 ± 0.14	12.4 ± 0.1	0.10 ± 0.15	0.61 ± 0.04	· · ·
1mm.C07	· · ·	9mm.7	2.580	11.0 ± 0.1	1.65 ± 0.14	11.9 ± 0.1	0.48 ± 0.24	0.18 ± 0.04	AGN
1mm.C09	3mm.13	· · ·	3.601	9.8 ± 0.2	1.58 ± 0.21	11.6 ± 0.2	0.06 ± 0.25	0.27 ± 0.04	· · ·
1mm.C10	· · ·	· · ·	1.997	11.1 ± 0.1	2.04 ± 0.10	12.4 ± 0.1	-0.16 ± 0.12	0.60 ± 0.04	X
1mm.C12	3mm.15	· · ·	1.096	9.5 ± 0.1	1.55 ± 0.10	11.7 ± 0.1	-0.82 ± 0.11	0.73 ± 0.04	AGN
1mm.C13	3mm.10	· · ·	1.037	11.1 ± 0.1	1.27 ± 0.10	11.6 ± 0.1	-0.36 ± 0.15	0.31 ± 0.04	· · ·
1mm.C14a	· · ·	9mm.5	1.999	10.8 ± 0.1	1.70 ± 0.17	11.9 ± 0.2	0.20 ± 0.22	0.27 ± 0.04	· · ·
1mm.C16	3mm.06	· · ·	1.095	10.6 ± 0.1	1.52 ± 0.10	11.5 ± 0.1	-0.76 ± 0.11	0.66 ± 0.04	X
1mm.C15	3mm.02	· · ·	1.317	11.2 ± 0.1	1.05 ± 0.12	11.5 ± 0.1	-0.95 ± 0.14	0.48 ± 0.04	· · ·
1mm.C19	3mm.12	9mm.4	2.574	10.6 ± 0.1	1.54 ± 0.20	11.6 ± 0.2	-0.43 ± 0.21	0.46 ± 0.04	AGN
1mm.C20	· · ·	· · ·	1.093	10.9 ± 0.1	0.97 ± 0.14	11.2 ± 0.1	-1.01 ± 0.16	0.46 ± 0.04	· · ·
1mm.C25	3mm.14	· · ·	1.098	10.6 ± 0.1	1.35 ± 0.11	11.4 ± 0.1	-0.00 ± 0.19	0.22 ± 0.04	· · ·
1mm.C23	3mm.08	· · ·	1.382	10.7 ± 0.1	1.60 ± 0.12	11.7 ± 0.1	-1.03 ± 0.12	0.99 ± 0.04	· · ·
1mm.C30	· · ·	· · ·	0.458	10.0 ± 0.1	1.12 ± 0.10	11.0 ± 0.1	-0.01 ± 0.22	0.17 ± 0.04	X
· · ·	3mm.11	· · ·	1.096	10.2 ± 0.1	0.99 ± 0.11	11.0 ± 0.1	-0.70 ± 0.15	0.33 ± 0.04	· · ·
· · · †	3mm.09	9mm.2	2.698	11.1 ± 0.1	2.54 ± 0.10	12.6 ± 0.1	2.05 ± 0.42	0.08 ± 0.04	AGN
Faint.1mm.C20	3mm.16	· · ·	1.294	10.3 ± 0.1	1.06 ± 0.14	11.0 ± 0.2	-1.10 ± 0.15	0.57 ± 0.04	· · ·
· · ·	MP.3mm.2	· · ·	1.087	10.4 ± 0.1	1.40 ± 0.10	11.5 ± 0.1	-0.95 ± 0.11	0.71 ± 0.04	X

Notes. (1) ASPECS-LP continuum ID (Aravena et al., 2020; González-López et al., 2020). (2) ASPECS-LP line ID (Boogaard et al., 2019). (3) VLASPECS ID (Riechers et al., 2020) (4) Spectroscopic redshift. (5) Stellar mass. (6) Star formation rate (SFR). (7) Infrared luminosity; $L_{IR}(3 - 1000\,\mu m)$. (8) SFR surface density; $\Sigma_{SFR} = SFR/2\pi r_e^2$. (9) *HST*/F160W effective radius from van der Wel et al. (2012), for which we adopt an 0.″04 error floor. (10) X-ray classification as either hosting an active galactic nucleus or another source of X-ray emission (X) (Luo et al., 2017). Columns (5)–(7) were derived with MAGPHYS (Da Cunha et al., 2008, 2015). We conservatively fold in a 0.1 dex error to the MAGPHYS uncertainties, to account for underestimated and systematic uncertainties, and report the values as $p_{50} \pm \sqrt{(0.5(p_{84} - p_{16}))^2 + 0.1^2}$, where p_i is the i^{th} percentile.

† Object falls outside of the Band 6 mosaic, but is the brightest 1 mm continuum source in the ASPECS field (see Dunlop et al., 2017).

channel (see Decarli et al., 2020, Fig. 1).

To create continuum maps, we collapse both the Band 6 (1.2 mm) and Band 3 (3.0 mm) data cubes over their full frequency range. The deepest parts of the continuum reach 3.8 μJy beam^{-1} in Band 3, with a beam size of $2\farcs8 \times 1\farcs7$, and 9.3 μJy beam^{-1} in Band 6, with a beam size of $1\farcs5 \times 1\farcs1$ (González-López et al., 2019, 2020). The absolute flux calibration is expected to be reliable at the $\sim$ 10% level.

4.2.2 ASPECS Sample

We search for line and continuum sources in the ASPECS data cubes, which are described in González-López et al. (2019) and González-López et al. (2020). In the Band 3 data we detect 16 CO emitters at high significance from the line search, plus 2 additional CO emitters based on a MUSE redshift prior (Boogaard et al., 2019). For five of these sources we also detect the continuum at 3 mm (González-López et al., 2019). From the Band 6 data we detect 35 sources in 1.2 mm dust-continuum at high significance, 32 of which show counterparts in the optical/near-IR imaging (Aravena et al., 2020; González-López et al., 2020). We conduct a search for emission lines in the Band 6 cube following the same approach as for the Band 3 data. This reveals several CO (and [C I]) emitters, all coinciding with sources detected in the Band 6 continuum image, with one exception: a narrow CO line in one of the CO emitters also found in Band 3 (3mm.11; not detected in continuum at all). Notably, we did not find any high-significance lines in sources not already detected in the dust-continuum. The Band 6 continuum sources furthermore encompass all Band 3 CO emitters (Aravena et al., 2020), with four exceptions: the first two are the lowest mass and SFR source of the main sample (3mm.11) and the faintest source in CO (ASPECS-LP-MP.3mm.02). The third is 3mm.16, which does however have a dust-continuum counterpart in the supplementary catalog of 26 sources at lower significance (the 'Faint' sample), which were selected based on the presence of a optical/near-IR counterpart (González-López et al., 2020). The fourth is 3mm.09, which is the brightest source at 1.3 mm in the field (UDF1; Dunlop et al., 2017). This source was detected toward the edge of the Band 3 mosaic (at 40% of the primary beam peak sensitivity; hereafter PB response) and is at the extreme edge of the Band 6 mosaic. The CO(7–6) and [C I](2–1) lines lie at 6% of the PB response at 218 GHz and the source falls outside the continuum map (below 10% PB response). We do include this source in this paper, but note that the upper limits on the lines in Band 6 are essentially unconstraining. For the SED fitting (§ 4.2.4) we use the continuum measurement at 1.3 mm.

We therefore consider all of the Band 3 and Band 6 continuum and line sources that are detected in at least one line. In total, the sample consists of 22 sources. The majority of the sample is low-J CO-selected in Band 3 (17/22). There are five exceptions, i.e., sources which are added based on the Band 6 data. Three sources lack coverage of any CO lines in Band 3. These include (1mm.C10 and C14a) at $z \approx 1.99$ and 1mm.C30 at $z = 0.46$. One source, 1mm.C20, does not show CO lines in Band 3 nor 6, but is detected in [C I] in Band 6. Lastly, we report a new CO(3–2) detection for 1mm.C07 in Band 3. This source was not included in the original sample from González-López et al. (2019) because the line is below their single-line fidelity threshold and the source lacks a MUSE redshift. However, this source is now confirmed through the detection of the high-J CO and [C I] lines in Band 6. One Band

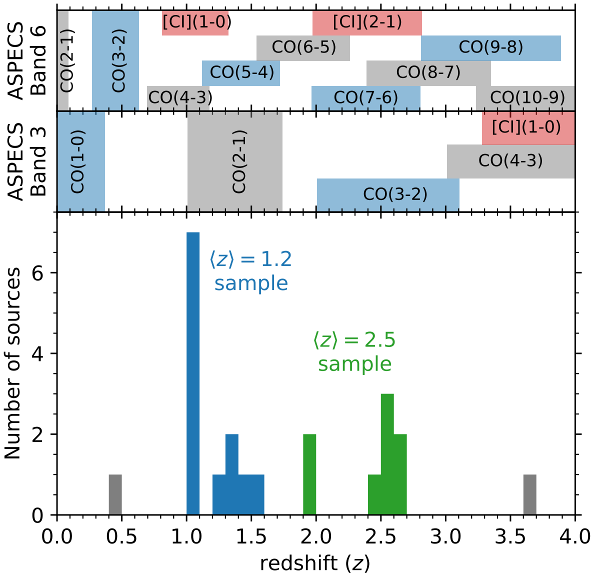

Figure 4.1: Redshift distribution of the ASPECS sources discussed in this paper (bottom panel). The top panels indicate the lines covered by ASPECS in Band 3 and Band 6 at different redshift ranges (colored just to make them more easily distinguishable). We highlight the samples at $z = 1.0 - 1.6$ (blue) and $z = 2.0 - 2.7$ (green), for which we have coverage of both a low-J and a mid/high-J CO line. Additional VLA CO(1–0) follow-up is available for all but one source in the $\langle z \rangle = 2.5$ sample (§ 4.2.3; Riechers et al. 2020).

3 CO(2–1) emitter (MP.3mm.1; based on a MUSE prior) is not included in this paper, because we re-measure the integrated flux to be slightly below 3σ. This is likely because we convolve both cubes to a slightly larger beam size, in order to consistently measure the line ratios, at the cost of signal-to-noise (S/N; see § 4.3.1).

The full sample is listed in Table 4.1. It spans redshifts from $z = 0.46 - 3.60$, with the majority of the sample being at $z = 1 - 3$. We show the redshift distribution in Figure 4.1, highlighting the spectral lines covered by ASPECS in the top panels. The final redshifts are determined from our fits of the CO and/or [C I] line(s), using the redshifts from the MUSE HUDF survey and our literature compilation (see Boogaard et al., 2019; Decarli et al., 2019) as prior information (§ 4.3.1).

4.2.3 Very Large Array Observations (VLASPECS)

The CO(1–0) transition in the ASPECS galaxies between $z = 1.99 - 2.70$ was observed with the Karl G. Jansky VLA as part of the VLASPECS survey (Riechers et al. 2020; VLA program ID: 19B-131; PI: Riechers). Two pointings were conducted with the D array in the Ka band, over a continuous bandwidth of 30.593–38.662 GHz at 2 MHz spectral resolution, resulting in a 17 km s^{-1} resolution (at 35 GHz). The naturally weighted cube has an average rms noise level of ≈ 0.1 mJy beam^{-1} $\mathrm{channel}^{-1}$ (increasing by about a factor of two from the low- to the high-frequency edge of the bandpass, as expected) and a beam size of $4\farcs99 \times 1\farcs96$. Given the recent flaring activity in the calibrator, the absolute flux is conservatively considered to be reliable at the $\sim$ 15% level. The full data reduction and presentation is part of Riechers et al. (2020). In this paper, we focus primarily on the CO excitation and analyze the data in concert with the higher-J CO lines.

4.2.4 Multi-wavelength data and SED fitting

The wealth of multi-wavelength photometry available over the HUDF provides good constraints on the spectral energy distribution (SED) of each of the ASPECS galaxies. By modeling the SEDs using the MAGPHYS (Da Cunha et al., 2008, 2015), we derive stellar masses, SFRs, and IR luminosities (L_{IR}; $3 - 1000\,\mu$m). We follow the same procedure as described in Boogaard et al. (2019), utilizing the UV – 24 μm photometry from 3D-HST (Skelton et al., 2014; Whitaker et al., 2014), in combination with the *Herschel* $70 - 160\,\mu$m data from Elbaz et al. (2011) and the 3 mm continuum from González-López et al. (2019). Superseding the earlier fits, we now include the updated 1.2 mm flux measurements from González-López et al. (2020). Furthermore, we include 5σ upper limits of 50 μJy and 20 μJy in the case of a non-detection at 1.2 mm and 3 mm, respectively. The fits for the full dust-continuum sample (including the sources not detected in CO) are presented in Aravena et al. (2020). Following Aravena et al. (2020), we conservatively fold in an additional 0.1 dex to the errorbars to account for underestimated and systematic uncertainties. We derive average SFR surface densities, $\Sigma_{\mathrm{SFR}} = \mathrm{SFR}/2\pi r_e^2$, using the *HST*/F160W half-light radii (r_e) from van der Wel et al. (2012). This is a reasonable approximation for sources in which the radial extent of the star formation follows the stellar disk, but should be considered as a lower limit in the case of a more nuclear starburst. The formal errors on the radii are of order a few percent of the point spread function (PSF $\sim 0\farcs16$), which we find to be very small. Hence, we conservatively adopt a floor on the errorbar of PSF/4 = $0\farcs04$. Lastly, the X-ray sources in the ASPECS sample are identified and classified using the deep *Chandra* 7 Ms data from Luo et al. (2017) as described in Boogaard et al. (2019).

4.3 Methods

4.3.1 Spectral line analysis

We extract single pixel spectra from the naturally weighted Band 3 and Band 6 cubes, convolved to a common beam size of $2\farcs2$. In this way, we ensure that the line fluxes are extracted over the same region of the galaxy, whilst minimizing the impact of flux loss for sources that are more slightly extended than the beam size of the naturally weighted cube. We use the cubes at their native spectral resolution in order to resolve even the narrowest lines ($\sim$ 50 km s^{-1}) into several resolution elements. We adopt the position of the dust-continuum detection (Aravena et al., 2020; González-López et al., 2020), or, in the case of no dust-continuum

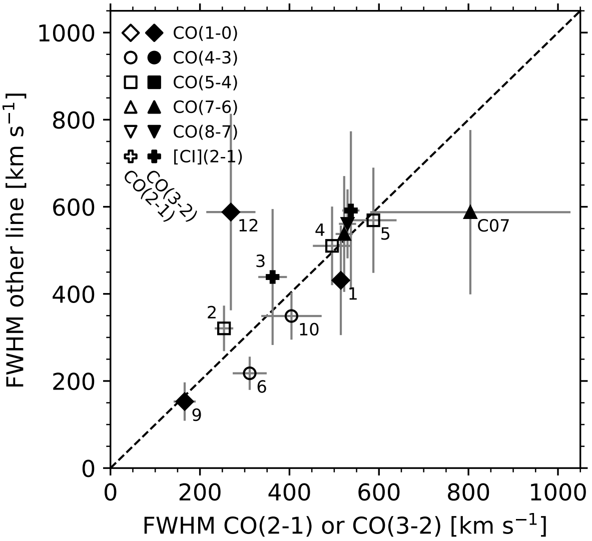

Figure 4.2: Comparison of the line width (full-width at half-maximum; FWHM) between the CO(2–1) and CO(3–2) lines (by which the sample was selected) and the higher-J CO ($J > 4$) or [C I] lines in individual ASPECS galaxies (extracted over the same 2.″2 aperture), as well as CO(1–0) from the VLA. The sources were fit with a single redshift but allowing, *for this figure only,* a varying line width for each transition. Sources are identified by the 3mm.ID or else their 1mm.CID. We only show sources where the relevant lines are detected with a S/N > 3 in these fits. We add a small positive offset to the multiple lines of 3mm.1, for readability. Overall, we find consistent line widths between the low-J CO and higher-J CO/[C I] lines. Throughout the analysis presented in this work, we will therefore use a fixed line width to model the different transitions of a particular source, which is determined by fitting all the lines simultaneously (see § 4.3.1).

detection, the CO line positions (González-López et al., 2019; Boogaard et al., 2019). The beam size of the VLA data is already larger than that of ASPECS (≈ 5.″0 × 2.″0) and only the brightest two sources are slightly resolved along the minor axis by the VLA (similar to what is seen in ASPECS, which motivated the convolution to 2.″2). We therefore use the spectra extracted by Riechers et al. (2020) in order to measure the flux over as-similar regions as possible.

For each source, we simultaneously fit all CO and [C I] lines that are expected to fall in Band 3, Band 6, and the VLA *Ka* band, based on the redshift from the line search, using the nonlinear least square fitting code LMFIT[29] (Newville et al., 2019a). We first subtract the continuum in Band 6, which is determined by fitting a first order polynomial to the median filtered spectrum. All the lines in the continuum-free spectrum are modeled by Gaussian line shapes, whose central frequencies are tied together by a single redshift.

Fitting the sources with the highest S/N spectra, we find that the widths of the different

---

[29] https://lmfit.github.io/lmfit-py/

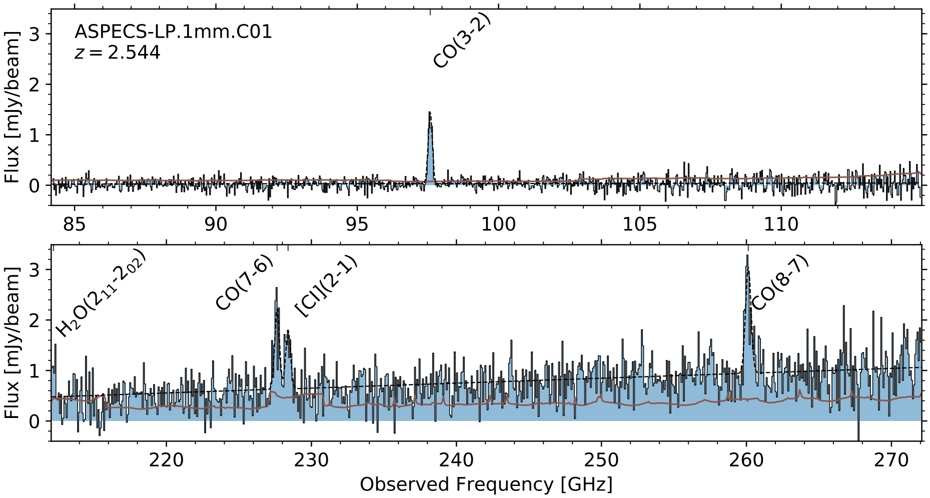

Figure 4.3: Full spectrum in Band 3 (*top*) and Band 6 (*bottom*) of ASPECS-LP.1mm.C01, shown as an example of the ASPECS frequency coverage. The brown line shows the root-mean-square noise in each of the channels. For visualization purposes, the spectra are averaged to a similar resolution of 95 km s^{-1}. The black dashed line shows the best-fit model, which includes Gaussian line fits to the ^{12}CO and atomic carbon ([C I]) lines (constrained in redshift and line width by all the lines simultaneously) and a linear continuum (§ 4.3.1). Note that in this particular source we also detect a water line at the edge of the Band 6, para $H_2O(2_{11} \rightarrow 2_{02})$, which is not included in the fitting (and not further discussed in the paper).

transitions are consistent in most cases. This is illustrated in Figure 4.2, where we show the line width measured in the CO(2–1) and CO(3–2) lines in Band 3 against the line width of the other CO and [C I] lines. Here we only include sources with $S/N > 3$ in all the relevant lines in the free fit (which is more conservative than for the fits where the line widths are tied together, because of the additional degrees of freedom). We therefore model all the lines with a single line width. Although this assumption is not strictly necessary, this often improves the fitting of lines with lower S/N, where the line width can be better constrained by the strongest lines. The integrated line fluxes are consistent within the uncertainties regardless of whether we force the widths of the lines to match. Furthermore, fitting the non-detected lines simultaneously does not influence the fit of the detected lines within the error (even in the most extreme case of a single detection and multiple upper limits). The observed line widths are likely governed by the global kinematics of the source. As such, the consistent line widths between the different transitions suggest that the gas is not much more compact or extended in some transitions compared to others, which supports our analysis of the global CO excitation (see § 4.A for further discussion).

As an illustration of the fitting procedure, we show the complete Band 3 and 6 spectrum of the brightest source, 1mm.C01, in Figure 4.3, together with the best-fit model (lines and continuum). This particular source is detected in multiple lines as well as the dust-continuum.

4.3.2 Deriving line luminosities and molecular gas masses

The line luminosities are commonly expressed in different units, useful for different purposes, and we briefly review the relevant equations below (see Solomon & Vanden Bout, 2005; Obreschkow et al., 2009; Carilli & Walter, 2013). When expressed in solar luminosities, the line luminosities indicate the total power emitted,

$$L = 1.040 \times 10^{-3}\, S^V d_L^2\, \nu_{\rm obs}\, {\rm L}_\odot. \tag{4.1}$$

Units of integrated brightness temperature are convenient to derive the line excitation (notably, if the CO line emission originates in thermalized, optically thick regions, $L'_{\rm CO}$ is constant for all J levels),

$$L' = 3.255 \times 10^7\, S^V d_L^2\, \nu_{\rm obs}^{-2} (1+z)^{-3}\, {\rm K\,km\,s^{-1}\,pc^2}. \tag{4.2}$$

In both equations, $S^V = \int S_\nu dv$ is the integrated line flux ($[S^V] = {\rm Jy\,km\,s^{-1}}$), d_L is the luminosity distance ($[d_L] = {\rm Mpc}$) and $\nu_{\rm obs}$ is the observed line frequency ($[\nu_{\rm obs}] = {\rm GHz}$) (Solomon et al., 1992b). Note that the two definitions are proportional, with $L' = 3.130 \times 10^{10}\, \nu_{\rm rest}^{-3} L$.

The CO excitation is typically reported as a brightness temperature ratio between two transitions, which is computed from $L'_{\rm CO}$ or S^V as

$$r_{J_2 J_1} = \frac{L'_{{\rm CO}\, J_2 \to J_2 - 1}}{L'_{{\rm CO}\, J_1 \to J_1 - 1}} = \frac{S^V_{{\rm CO}\, J_2 \to J_2 - 1}}{S^V_{{\rm CO}\, J_1 \to J_1 - 1}} \left(\frac{J_1}{J_2}\right)^2 \tag{4.3}$$

The relationship between the molecular gas mass ($M_{\rm mol}$) and the CO luminosity ($L'_{\rm CO}$) is expressed as

$$M_{\rm mol} = \alpha_{\rm CO} \frac{L'_{{\rm CO}\, J \to J-1}}{r_{J1}}, \tag{4.4}$$

where $\alpha_{\rm CO}$ is the conversion factor between CO luminosity and the total molecular gas mass (including a factor of 1.36 to account for heavy elements, primarily Helium; see Bolatto et al. 2013 for a recent review). We adopt an $\alpha_{\rm CO} = 3.6\, {\rm M}_\odot ({\rm K\,km\,s^{-1}\,pc^2})^{-1}$ (Daddi et al., 2010a) where needed (following the discussion in Boogaard et al. 2019 and consistent with the other ASPECS studies, as well as COLDz; Riechers et al. 2019).

4.4 Results

4.4.1 Observed emission lines from CO and [C I]

We detect emission lines from CO and/or [C I] in 22 distinct galaxies in the ASPECS field, between redshifts $z = 0.46 - 3.60$. For the CO $J \to J - 1$ lines we measure 34 detections plus 21 upper limits, with rotational quantum numbers between $J = 1$ and 10. We only probe the frequency range for the CO(9–8) and CO(10–9) transitions in a single source at $z = 3.60$

but neither is detected. Therefore, we focus on the transitions up to CO(8–7). For atomic carbon we report six line detections plus 12 upper limits in the $^3P_1 \rightarrow {}^3P_0$ and $^3P_2 \rightarrow {}^3P_1$ transitions, hereafter [C I](1–0) and [C I](2–1).

We measure the integrated line fluxes as described in § 4.3.1 and show the individual line fits for all sources in Figure 4.15 in § 4.B. The resulting redshifts, line widths (full width at half maximum; FWHM), central frequencies, and line fluxes for all sources can be found in Table 4.6. In the remainder of this paper, we will treat tentative lines with an integrated line flux smaller than 3σ in the VLA and ALMA data as upper limits. Here, σ is the uncertainty on the Gaussian fit, measured over the same line width as the detected lines that they are tied to. As not all lines are perfectly described by single Gaussians, we also compute the line fluxes by integrating the channels within 1.4× the FWHM and confirm these are consistent with the Gaussian fits to within error.

Our method forces all lines for a source to a common line width, which may result in different errorbars for some lines than found based on an S/N optimized extraction of each individual line (González-López et al., 2019; Riechers et al., 2020). This more conservative treatment, which is chosen to minimize biases for the specific analysis carried out in this work, differs from the way they are used in other works in ASPECS focused on studies of the global gas density evolution (Decarli et al., 2019, 2020; Riechers et al., 2020). Compared to the previous ASPECS papers, we find that our fluxes in Band 3 are on average 20% lower than those from González-López et al. (2019), but consistent with Decarli et al. (2016b, for a small subset of the sources).

The CO(1–0) observations cover all ASPECS sources between $z = 1.99 - 2.70$, except 1mm.C10, which lies outside of the VLA pointings (§ 4.2.3). The CO(1–0) fluxes measured here are consistent with Riechers et al. (2020), who measured the flux from the moment 0 maps collapsed over the channels in which emission was seen, while we obtain larger uncertainties compared to the optimized extractions. As all the lines are relatively faint (due to the apparently high r_{31}, see § 4.5), this pushes the significance of some lines from $> 3\sigma$ into the $2.5 - 3\sigma$ range (and are therefore not shown in Figure 4.2). For 3mm.7, the CO(1–0) line-shape is consistent with the CO(3–2), although the line is formally at 2.97σ in our fit. In other cases, the line width of the feature at the frequency of CO(1–0) appears different from the higher-J lines (e.g., 3mm.3, 3mm.12), which could be driven by the low S/N (see Riechers et al., 2020). An interesting case is 1mm.C14a, where the apparent CO(1–0) line appears offset both spatially and in velocity by $\sim 200\,\mathrm{km\,s^{-1}}$, compared to the combined CO(6–5), CO(7–6) and [C I](2–1) lines. For this source we will use the fit results tied to the (formally undetected) CO(1–0) line for consistency, but note that if we only fit the other lines we find a slightly lower redshift solution ($z = 1.9963$) and higher S/N, such that the [C I](2–1) line is also at $> 3\sigma$.

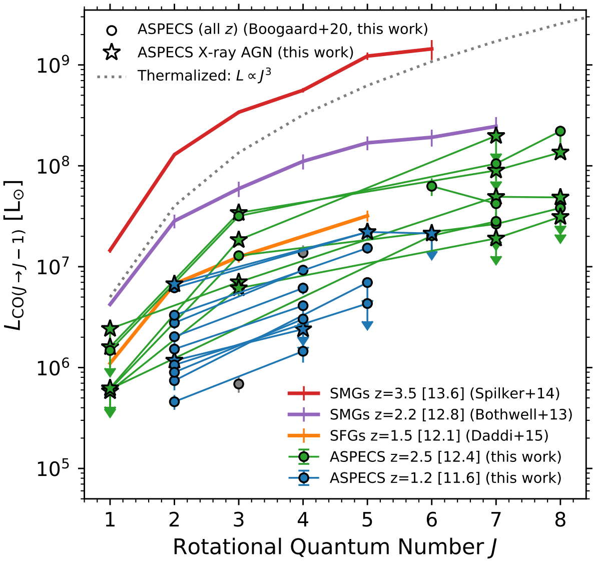

Figure 4.4: CO line luminosities (in units of L$_\odot$) of the ASPECS galaxies (colored circles). Downward pointing arrows indicate 3σ upper limits. Stars indicate X-ray sources classified as AGN (Luo et al., 2017). For comparison, we show the average CO ladders of $\langle z \rangle = 1.5$ star-forming galaxies (Daddi et al., 2015) and submillimeter galaxies at $\langle z \rangle = 2.2$ (Bothwell et al., 2013) and $\langle z \rangle = 3.5$ (Spilker et al., 2014), and a thermalized ladder (arbitrarily scaled to 5×10^6 L$_\odot$). The average infrared luminosity ($\log L_{\mathrm{IR}}$[L$_\odot$]) of the different samples is indicated between brackets in the legend. Overall, the ASPECS galaxies probe lower infrared luminosities than typical samples at their respective redshifts.

4.5 CO excitation

4.5.1 Individual sources

The CO line luminosities of all sources are shown in Figure 4.4 (in units of L$_\odot$) including both detections and 3σ upper limits. The ASPECS observations naturally divide the sample into different redshift bins, through the different low-, mid-, and high-J CO lines that are covered in Band 3 and Band 6 at different redshifts (Figure 4.1). For the galaxies from $z = 1.0 - 1.6$ ($\langle z \rangle = 1.2$), we measure the CO(2–1) line in Band 3 and either CO(4–3), CO(5–4), CO(6–5) and/or [C I](1–0) in Band 6, depending on the exact redshift. We cover both the CO(6–5) and CO(7–6) lines in the two sources at $z \approx 1.997$, but just miss the low-J CO(3–2) line in Band 3. For the higher redshift galaxies at $z = 2.4 - 2.7$, we cover CO(3–2) as well as CO(7–6), CO(8–7) and [C I](2–1). The VLA observations add constraints on CO(1–0) for all but one source at $z \geq 2$. Outside of these redshift bins we only have 1mm.C30 at $z = 0.46$ observed CO(3–2) in Band 6, for which we do not cover any other CO transition with ASPECS, and 3mm.13 at $z = 3.60$ for which we cover, but do not detect, CO(9–8) or CO(10–9).

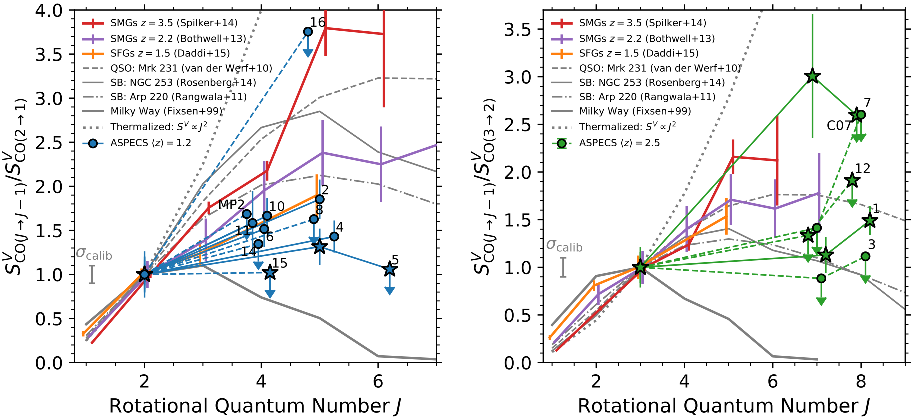

Figure 4.5: CO ladders for the ASPECS galaxies at $\langle z \rangle = 1.2$ (*left*) and $\langle z \rangle = 2.5$ (*right*), normalized to CO(2–1) and CO(3–2) respectively, in units of integrated line flux ($[S^V] = {\rm Jy\,km\,s^{-1}}$). We include all sources with coverage of at least two lines and a detection in the low-J line (except 3mm.09, which has a weakly constraining upper limit putting CO(7–6) just below the thermalized value). Downward pointing arrows indicate 3σ upper limits on the mid/high-J transition(s) and are connected to the lower-J transition with a dotted line. Stars indicate X-ray sources classified as AGN (Luo et al., 2017). The gray errorbar indicates the calibration uncertainty. The galaxies at $\langle z \rangle = 1.2$, show excitation in their mid-J lines, CO(4–3) and CO(5–4), that is consistent with, or lower than, what is found in the BzK-selected star-forming galaxies (Daddi et al., 2015). The range in excitation suggests that an additional, warmer, component is present in some, but not all, sources. At $\langle z \rangle = 2.5$, the excitation in the high-J lines, CO(7–6) and CO(8–7), is comparable to what is found in local starbursts (e.g., Rangwala et al., 2011; Rosenberg et al., 2014), but appears lower than the average sub-mm galaxy (Bothwell et al., 2013).

We compare our observations to the average CO ladders from different samples in the literature: The BzK-selected SFGs at $\langle z \rangle = 1.5$ from Daddi et al. (2015); the SMGs at $\langle z \rangle = 2.2$ from Bothwell et al. (2013); and the stacked CO ladder for SPT-selected (lensed) SMGs at $\langle z \rangle = 3.5$ from Spilker et al. (2014). The ASPECS galaxies at $\langle z \rangle = 1.2$ are less massive and have a lower average infrared luminosity, $\langle L_{\rm IR} \rangle = 10^{11.6}\,{\rm L_\odot}$, than the BzK galaxies at $\langle z \rangle = 1.5$ ($10^{12.1}\,{\rm L_\odot}$). This is also clearly reflected in their overall lower CO luminosity. The ASPECS galaxies at $\langle z \rangle = 2.5$ also have a lower $\langle L_{\rm IR} \rangle = 10^{12.4}\,{\rm L_\odot}$ compared to the SMGs at similar redshifts.

We show the CO excitation ladders for the ASPECS galaxies at $\langle z \rangle = 1.2$ (left) and $\langle z \rangle = 2.5$ (right), relative to the low-J CO(2–1) and CO(3–2) transitions by which they were selected, respectively, in Figure 4.5 (now as line flux ratios). In addition to the $z > 1$ samples mentioned earlier, we also add the observed CO ladders for several local sources: the Milky Way (MW; Fixsen et al., 1999, Inner Disk) and starburst NGC 253 (Rosenberg et al., 2014), as well as the CO ladders for Arp 220 (Rangwala et al., 2011) and the nearest known quasar, Mrk 231 (van der Werf et al., 2010), as modeled by the LVG models of Weiss et al. (2007b).

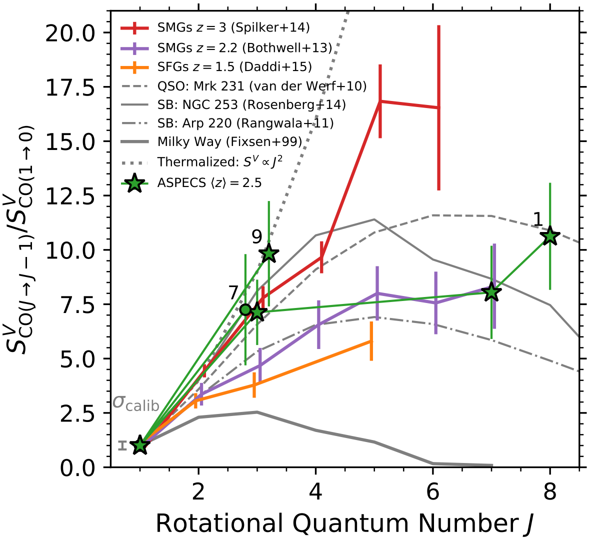

Figure 4.6: CO ladders of the ASPECS galaxies detected in CO(1–0) (green markers and lines), in units of integrated line flux ($[S^V] = \mathrm{Jy\,km\,s^{-1}}$), normalized to CO(1–0). Stars indicate X-ray sources classified as AGN (Luo et al., 2017). The gray errorbar indicates the combined calibration uncertainty on the ALMA and VLA data. The literature sample shown here is the same as in Figure 4.5. For all ladders, we propagate the uncertainty on the transition to which the ladders are normalized to the higher-J lines. We add slight offsets in the horizontal direction for clarity.

The dotted line indicates a thermalized CO ladder (i.e., $S^V \propto J^2$).

The eleven CO(2–1)-selected galaxies at $\langle z \rangle = 1.2$ (left panel) span a range in excitation in their CO(4–3) and CO(5–4) lines. Only one source (and one weak upper limit) show excitation in the CO(5–4) line that is comparable to the average of the BzK-selected SFGs (Daddi et al., 2015), while the other measurements and limits are consistent with lower excitation. We also add direct measurements of the CO(4–3) transition to this picture (which was not directly measured for the BzK galaxies). This ratio is similar to the (interpolated) value in the BzK galaxies for the three detected sources. At the same time we also infer upper limits consistent with lower excitation, although none of the sources have limits strong enough to put them confidently in the low-excitation regime of the MW. In all cases, the excitation is significantly lower compared to SMGs at higher redshift and clearly not as high as seen in the centers of the prototypical local starbursts Arp 220 and NGC 253, nor Mrk 231.

For the five CO(3–2) selected galaxies at $\langle z \rangle = 2.5$ (right panel), we probe the CO(7–6) and CO(8–7) lines. Here, we find the brightest galaxy of the survey (1mm.C01), which is an X-ray identified AGN with detections in all three lines (see Figure 4.3). This source exhibits significant excitation, out to $J = 8$, at the level comparable to the local starbursts and Mrk 231, though still somewhat below the $\langle z \rangle = 2.2$ SMGs at CO(7–6). There is one other source detected in CO(7–6), 1mm.C07, which is also an X-ray AGN. This source shows the highest

r_{73} ratio of all sources, although we caution that the line flux is uncertain for both lines (see Figure 4.2) and the CO(8–7) transition is undetected. The remaining sources at these redshifts are not detected in their high-J lines. At the sensitivity limit of ASPECS, this constrains their high-J excitation to be well below thermalized and comparable to the level of the local starburst and somewhat below the Bothwell et al. (2013) SMGs.

We show the CO ladder normalized to CO(1–0) in Figure 4.6, for the sources with $S/N > 3$ in CO(1–0) in our joint fit. In contrast to the r_{73} ratio, the r_{31} ratio is typically higher than that of the Bothwell et al. (2013) SMGs.

The X-ray radiation from an AGN can drive the emission of the high-J CO lines (e.g., Meijerink et al., 2007; van der Werf et al., 2010; Vallini et al., 2019). The stars in Figure 4.5 and Figure 4.6 indicate X-ray identified AGN (1mm.C05, C12 at $\langle z \rangle = 1.2$ and 1mm.C01, C07, C19, and 3mm.09 at $\langle z \rangle = 2.5$). It is interesting to note that both sources detected in the high-J CO(7–6) line are X-ray AGN. However, the upper limits on the remaining galaxies do not distinguish them clearly from the detected sources. At $\langle z \rangle = 1.2$, the X-ray AGN lie at the low-excitation end of the sample, which is consistent with the AGN not strongly driving the mid-J lines. Based on the low number of sources, we are unable to draw strong conclusions here. However, the results are consistent with recent work that did not find statistically different excitation, up to CO(7–6), between galaxies with and without an active nucleus (e.g., Sharon et al., 2016; Kirkpatrick et al., 2019).

4.5.2 Stacked line fluxes

We construct an average CO ladder in each of the two redshift bins by stacking the CO lines in each transition. The advantage of stacking (compared to taking the average of the measured line fluxes) is that we can straightforwardly take all sources into account in a non-parametric way, regardless of whether they are detected in a specific transition or not. Before stacking, we first take out the intrinsic brightness variations in the sample by dividing their spectra by the integrated flux in the CO(2–1) or CO(3–2) transition (by which they were selected, depending on the redshift), as measured from the Gaussian fits. In this way we determine the average excitation of the other lines in the sample relative to CO(2–1) or CO(3–2) (including CO(1–0) and [C I]).

Because we are stacking sources with different line widths, care must be taken not to lose flux, while keeping an optimal S/N in the stack. Therefore, we stack each transition individually in velocity space, such that all the flux ends up in a single channel in the final stack (see Spilker et al., 2014). We first create a grid of velocities centered around zero. We take a channel width of 700 $\mathrm{km\,s^{-1}}$ for the sources at $\langle z \rangle = 1.2$ and 800 $\mathrm{km\,s^{-1}}$ for the sources at $\langle z \rangle = 2.5$, motivated by the width of the broadest lines in our sample (FWHM $\approx$ 590 and 660 $\mathrm{km\,s^{-1}}$ in each redshift bin, respectively). The average line width of the sample is $\langle \mathrm{FWHM} \rangle = 330\,\mathrm{km\,s^{-1}}$. At this channel width the CO(7–6) and [C I](2–1) lines, with a peak separation of 1000 $\mathrm{km\,s^{-1}}$, are not blended in the stack. We find the results are robust to modifying the channel width by $\pm 100\,\mathrm{km\,s^{-1}}$. After subtracting the continuum from the Band 6 spectra (as in § 4.3.1), we convert each spectrum to velocity-space, centered around the line. We then bin the spectra onto the velocity grid and stack them by taking the $1/\sigma$-weighted mean flux in each velocity bin (where σ is the rms error on the spectrum). Likewise, we

Table 4.2: Average line fluxes from stacking

Line (1)	N (2)	$S^V/S^V_{J=J_{\rm ref}}$ (3)	r_{JJ_l} (4)
$\langle z \rangle = 1.2; J_{\rm ref} = J_l = 2$			
CO(2–1)	11	1.00 ± 0.04	···
CO(4–3)	6	1.33 ± 0.18	0.33 ± 0.04
[C i](1–0)	8	0.33 ± 0.18	···
CO(5–4)	5	1.41 ± 0.15	0.23 ± 0.02
$\langle z \rangle = 2.5; J_{\rm ref} = 3; J_l = 1$			
CO(1–0)	6	0.14 ± 0.03	···
CO(3–2)	6	1.00 ± 0.03	0.77 ± 0.14
CO(7–6)	5	1.32 ± 0.18	0.19 ± 0.04
[C i](2–1)	5	0.93 ± 0.18	···
CO(8–7)	5	1.10 ± 0.20	0.12 ± 0.03

Notes. The lines fluxes are obtained through $1/\sigma$-weighted stacking, scaled to the reference transition in the stack, with propagated errors. (1) Stacked transition (2) Number of objects in the stack of each transition. (3) Mean integrated line flux, normalized to the reference CO($J \rightarrow J - 1$) transition in the stack, with $J = J_{\rm ref}$. (4) CO brightness temperature ratio with the lowest transition in the stack, $r_{JJ_l} = L'_{{\rm CO}(J \rightarrow J-1)}/L'_{{\rm CO}(J_l - J_l - 1)}$.

determine the error spectrum of the stack by propagating the errors from individual spectra. We then measure the flux and error in the zero-velocity bin, which is centered on the line. We use a $1/\sigma$-weighting to avoid strongly weighting toward the detected lines, while at the same time not sacrificing too much S/N by not down-weighting very noisy spectra (as in an unweighted stack). Note this is different from Spilker et al. (2014), who use a $1/\sigma^2$-weighted stack to obtain the highest possible S/N ratio.

The resulting line fluxes, normalized to the reference transition in the stack ($J_{\rm ref}$), are provided in Table 4.2, where we also report the line brightness temperature ratios (Equation 4.3) to the lowest-J transition (J_l; note for the individual galaxies these are reported in Table 4.6). We show the average ladders, normalized to J_l, in Figure 4.7.

The stacks in the two redshift bins reinforce our results from § 4.5.1. For the galaxies at $\langle z \rangle = 1.2$, excitation in the mid-J lines, compared to CO(2–1) is $r_{42} = 0.33 \pm 0.04$ and $r_{52} = 0.23 \pm 0.02$. This is on average lower than BzK-selected galaxies, in particular in CO(5–4) transition ($r_{52} = 0.30 \pm 0.06$; Daddi et al. 2015).[30] We now also add the recently published CO ladders for SFGs at $z = 1.25$ from Valentino et al. (2020a), who separate their sample in main-sequence galaxies and (extreme) starbursts (the latter being defined as lying a factor SFR/SFR$_{\rm MS} \geq 3.5\times$ and $\geq 7\times$ above the main sequence of Sargent et al. 2014). Their main-sequence galaxies show excitation intermediate between the BzK galaxies and ASPECS, with $r_{42} = 0.36 \pm 0.06$ and $r_{52} = 0.28 \pm 0.05$.

---

[30] Daddi et al. (2015) did not measure the excitation in CO(4–3), but interpolating their CO ladder yields $r_{42} = 0.41 \pm 0.09$ (see Decarli et al., 2016b, for details).

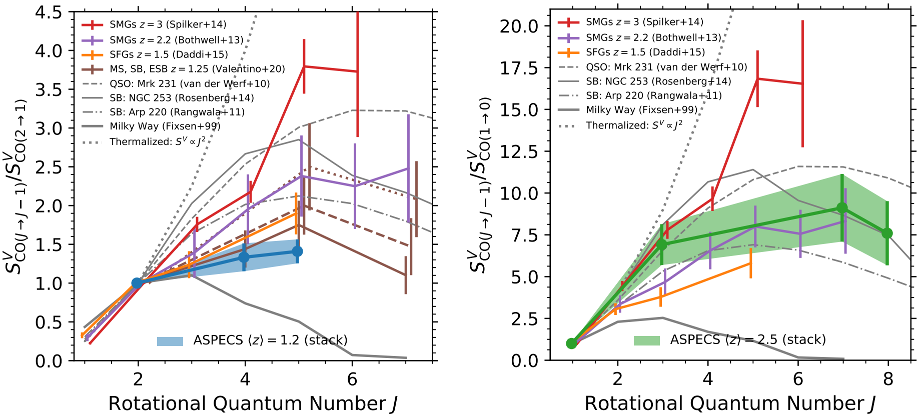

Figure 4.7: Average CO ladders for the ASPECS galaxies at $\langle z \rangle = 1.2$ (*left*) and $\langle z \rangle = 2.5$ (*right*), in units of integrated line flux ($[S^V] = \mathrm{Jy\,km\,s^{-1}}$), obtained through $(1/\sigma)$-weighted mean stacking after scaling to a common CO(2–1) and CO(3–2) flux, respectively. The solid line (and shaded region) show the mean stack of all sources. The literature sample shown here is the same as in Figure 4.5, with the addition of the recently observed main sequence and (extreme) starburst galaxies from Valentino et al. (2020a), shown by the brown, solid, and (dotted) dashed lines. For all ladders, we propagate the uncertainty on the transition to which the ladders are normalized to the higher-J lines. We add slight offsets in the horizontal direction for clarity.

At $\langle z \rangle = 2.5$, we measure an average $r_{31} = 0.77 \pm 0.14$ from the stack of all sources. For comparison, when considering the non-detections as lower limits, the median of the individual measurements is 0.79 ± 0.17 (for 1mm.C01—fully consistent with 0.84 ± 0.18 as measured by Riechers et al. 2020). The stacked r_{31} value is higher than that found for SMGs by Bothwell et al. (2013, $r_{31} = 0.52 \pm 0.09$). At the same time, the high-J excitation, compared to $J = 3$ (r_{73}), is lower in our sample compared to Bothwell et al. (2013), as also seen in Figure 4.5. The mean $r_{71} = 0.19 \pm 0.04$ is similar to that of 1mm.C01 alone, and comparable to the SMGs ($r_{71} = 0.18 \pm 0.04$; Bothwell et al. 2013) and the local starburst NGC 253, while it lies below the local quasar Mrk 231 (see § 4.5.1). Overall, the average ladder appears similar to that found in local starburst galaxies, such as NGC 253.

In addition to stacking all sources selected in a certain transition, we also explored splitting the sample based on the presence of an AGN, or whether a line was individually (un)detected. We find marginal evidence of an overall lower excitation in the galaxies without an X-ray detected AGN at $\langle z \rangle = 2.5$ (in particular for the high-J lines), but the limited numbers in the stack prohibit firm conclusions.

4.5.3 LVG modeling

To further investigate the CO excitation, we study the CO ladder of all sources at $z = 1.0-1.6$ and $z = 2.0-2.7$ in more detail by using a spherical, isothermal LVG model, following Weiss

Table 4.3: LVG modeling results

	1-component		2-component[†]	
J (1)	$S^V/S^V_{J=1}$ (2)	r_{J1} (3)	$S^V/S^V_{J=1}$ (4)	r_{J1} (5)
		$z = 1.0 - 1.6$ (12 galaxies)		
1	1.00 ± 0.00	1.00 ± 0.00	1.00 ± 0.00	1.00 ± 0.00
2	3.33 ± 0.48	0.83 ± 0.12	3.01 ± 0.43	0.75 ± 0.11
3	5.20 ± 0.91	0.58 ± 0.10	4.12 ± 0.80	0.46 ± 0.09
4	4.76 ± 1.26	0.30 ± 0.08	4.01 ± 1.14	0.25 ± 0.07
5	2.70 ± 1.33	0.11 ± 0.05	2.99 ± 1.41	0.12 ± 0.06
6	0.53 ± 1.27	0.01 ± 0.04	1.37 ± 1.69	0.04 ± 0.05
		$z = 2.0 - 2.7$ (8 galaxies)		
1	1.00 ± 0.00	1.00 ± 0.00	1.00 ± 0.00	1.00 ± 0.00
2	4.09 ± 0.72	1.02 ± 0.18	3.88 ± 0.62	0.97 ± 0.15
3	8.24 ± 1.50	0.92 ± 0.17	7.17 ± 1.24	0.80 ± 0.14
4	12.21 ± 2.49	0.76 ± 0.16	9.80 ± 2.01	0.61 ± 0.13
5	14.68 ± 3.62	0.59 ± 0.14	10.95 ± 2.84	0.44 ± 0.11
6	13.86 ± 4.48	0.39 ± 0.12	10.17 ± 3.39	0.28 ± 0.09
7	9.33 ± 4.57	0.19 ± 0.09	8.28 ± 3.67	0.17 ± 0.07
8	4.26 ± 4.13	0.07 ± 0.06	5.55 ± 3.87	0.09 ± 0.06

Notes. The average line ratios are computed by taking the $1/\sigma$-weighted mean of the LVG models of the individual sources in each redshift bin. (1) CO($J \rightarrow J-1$) rotational quantum number J. (2) Single-component LVG model line flux, normalized to $J = 1$. (3) Single-component LVG model CO brightness temperature ratio, $r_{J1} = L'_{\mathrm{CO}(J\rightarrow J-1)}/L'_{\mathrm{CO}(1-0)}$. (4) Two-component LVG model line flux, normalized to $J = 1$. (5) Two-component LVG model CO brightness temperature ratio.

[†] We adopt the two-component models throughout this paper.

et al. (2007b). Because we only observe up to four CO lines, we cannot accurately constrain the model parameters for individual sources. Rather, we use the model to predict the CO line luminosity of the neighboring, unobserved CO lines. The background to this approach is, that CO ladders cannot have arbitrary shapes and in this sense our procedure can be viewed as the molecular line correspondence of interpolating a sparsely sampled dust-continuum SED.

In practice, we fit the observed CO line luminosities using a one- and a two-component LVG model employing a Monte Carlo Bee algorithm (Pham & Castellani, 2009) which samples randomly the parameter space and gives finer sampling for good solutions (evaluated from a χ^2 analysis for each model). The model-predicted CO line luminosities, $L'_{\mathrm{CO}(J\rightarrow J-1)}$, and their uncertainties are calculated using the probability-weighted mean of all solutions and their standard deviations. For the redshift $z = 1.0 - 1.6$ sample, where we detect transitions up to $J = 5$, we report the model-predicted CO ladders up to $J = 6$. For the $z = 2.0 - 2.7$ sample we report transitions up to $J = 8$, because the observations also cover higher transitions.

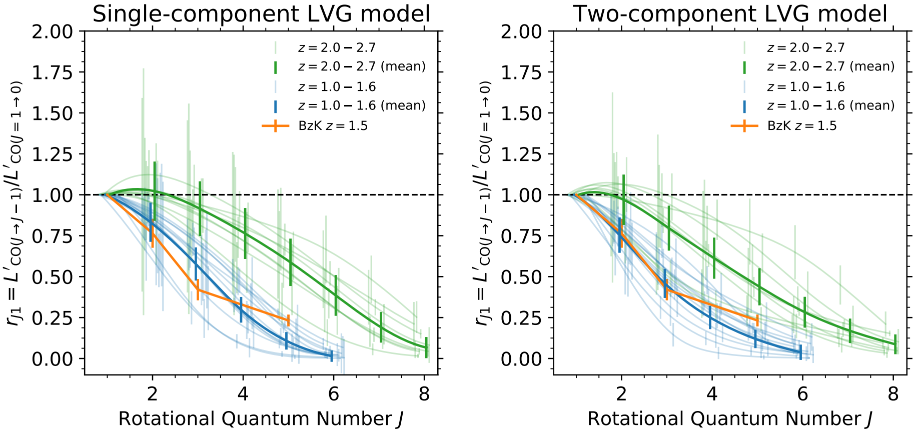

Figure 4.8: Predicted CO line luminosities ($L'_{\mathrm{CO}(J\rightarrow J-1)}$) for the ASPECS galaxies at $z = 1.0 - 1.6$ and $z = 2.0 - 2.7$, normalized to $L'_{\mathrm{CO}(1\rightarrow 0)}$ (so the values on the ordinate are equivalent to r_{J1}). The CO line luminosities for the individual sources are predicted from the best-fit LVG model, assuming a single density and temperature component (left panel) as well as a two-component model (right panel). The light-colored lines show the individual fits, while the strong-colored line shows the $1/\sigma$-weighted mean of the individual ladders. While the temperature and density are degenerate in the fit, the emerging line luminosities are reasonably well constrained. We show the *BzK*-selected galaxies from Daddi et al. (2015) for comparison and add horizontal offsets for clarity. In both the single- and two-component models the CO(3–2) selected galaxies at $z = 2.0 - 2.7$ show on average higher excitation than the CO(2–1) selected galaxies at $z = 1.0 - 1.6$.

Typically, we investigate on the order of 10^6 models per galaxy. The free parameters are the H_2 volume density, the kinetic temperature, the CO abundance per velocity gradient, and the source solid angle (expressed as the equivalent radius of the emitting region, see Weiss et al. 2007b). We include an additional prior that discards solutions where the peak of the CO ladder lies beyond the CO(7–6) line. This is motivated by our average ladder and there being only very few extreme local ULIRGs and $z = 2 - 3$ QSOs/SMGs where this is the case (see Weiss et al., 2007a; Carilli & Walter, 2013). Limits to the parameter space are: $\log_{10}(n_{\mathrm{H}_2}) = 1.0 - 7.0\,\mathrm{cm}^{-3}$, $T_{\mathrm{kin}} = 10 - 200\,\mathrm{K}$, $[\mathrm{CO}]/[\mathrm{H}_2]\,(\Delta v/\Delta r)^{-1} = 10^{-3} - 10^{-7}\,(\mathrm{km\,s^{-1}\,pc^{-1}})^{-1}$ and $r_{\mathrm{eff}} = 1 - 10\,000\,\mathrm{pc}$.

The CO ladders of the individual objects, derived from our single- and two-component LVG fitting, are shown in Figure 4.8, normalized to the predicted CO(1–0) line luminosity. We split the sample in two redshift bins, based on the observed lines (similar to § 4.5.1). We also compute the average ladder in each redshift bin by computing the $1/\sigma$-weighted mean of the L'_{CO} for each of the lines, after first rescaling to a common $L'_{\mathrm{CO}(1-0)}$ (to take out intrinsic variations in the luminosity). The resulting average ladders are provided in Table 4.3.

In general, the galaxies at $z \geq 2$ show more excited CO ladders than the galaxies at $z < 2$. This could partially be a selection effect in the case of the single-component models, if the fit overpredicts the $J = 3$ line luminosity in an attempt to fit $J > 6$, as suggested by the $r_{31} = 0.92 \pm 0.17$ being slightly higher than the stacked value ($r_{31} = 0.77 \pm 0.14$). However, the two-component model at $z \geq 2$ is still higher in $J = 2$ and 3, compared to the single-component fit at $z < 2$ (i.e., the 'maximal' value at $z < 2$), whereas the average $r_{31} = 0.80 \pm 0.14$ is fully consistent with the stacked value. This strongly suggests that there is a true, intrinsic difference in excitation in the CO(2–1)-selected sample at $z < 2$ compared to the CO(3–2)-selected sample at $z \geq 2$. As we constrain two low/mid-J lines at both redshifts ($J = 1$ and 3 at $z \geq 2$, and $J = 2$ and 4 at $z < 2$), these conclusions appears robust against the fact that we also probe higher-J lines at $z \geq 2$.

At $z = 1.0 - 1.6$, the single- and two-component models give formally consistent results, whereas the mean of the low-J lines is slightly higher for the single-component models ($r_{21} = 0.83 \pm 0.12$). The mean ladder of the two-component model is similar to the result from Daddi et al. (2015) for $J = 2$ and $J = 3$ ($r_{21} = 0.75 \pm 0.11$), while yielding a lower $J = 4$ and 5 (consistent with the stack). Although some individual sources show ladders consistent with thermalized $r_{21} = 1.0$ at these redshifts, the average is subthermal.

In general, we note that the single-component fits would overpredict the low-J excitation if the low-J CO line luminosities have a significant contribution from strongly subthermally excited gas. This is particularly significant at $z = 2.0 - 2.7$, as the $J > 6$ and $J \leq 3$ may not stem from the same component. However, this can also be important at $z = 1.0 - 1.6$, if the CO excitation is similar to the sources in Daddi et al. (2015) where the elevated $J = 5$ line luminosity is best described by a second, higher excitation component. This motivates the use of the two-component fit. In contrast, the observed CO transitions have little weight to constrain a two-component fit, in particular at $z = 1.0 - 1.6$, where we mostly only observe two CO transitions.

4.5.4 Dust-continuum versus low-J CO

The 1.2 mm dust-continuum emission provides an alternative way of measuring the molecular gas mass, which is typically traced by the CO(1–0) emission (see Hildebrand, 1983, for an early reference). Because the Rayleigh Jeans tail of the dust emission is nearly always optically thin, the dust emission at long wavelengths is a direct probe of the total dust mass and therefore the molecular gas mass, under the assumption that the dust emissivity per unit dust mass and dust-to-gas ratio can be constrained (Scoville et al., 2014, 2016). Motivating a mass-weighted cold dust temperature $T_{\rm dust} = 25$ K (which, in contrast to the light-weighted $T_{\rm dust}$, is much less sensitive to the radiation field) and a dust emissivity index $\beta = 1.8$, Scoville et al. (2016) show that the observed ratio between the (inferred) dust luminosity at rest frame 850 μm, $L_\nu(850\,\mu{\rm m})$, and $L'_{\rm CO(1-0)}$ is relatively constant under the wide range of conditions found in local SFGs, (U)LIRGS, and (mostly lensed) SMGs. Recently, this has been further confirmed for a sample of $z \sim 2$ SFGs (Kaasinen et al., 2019) as well as simulations (Liang et al., 2018; Privon et al., 2018).[31]

We can thus investigate whether our galaxies (that are observed in $L'_{\rm CO(1-0)}$) follow the empirical relation with $L_\nu(850\,\mu{\rm m})$ by Scoville et al. (2016), by directly comparing to their

---

[31] Motivated by their observed correlation between $L_\nu(850\,\mu{\rm m})$ and $L'_{\rm CO(1-0)}$, Scoville et al. (2016) then empirically calibrate the $L_{\rm dust}$-to-$M_{\rm mol}$ ratio, assuming a CO-to-H$_2$ mass conversion factor of $\alpha_{\rm CO} = 6.5\,{\rm M}_\odot({\rm K\,km\,s^{-1}\,pc^2})^{-1}$ (incl. He). Note that, therefore, this estimate cannot be used to derive $\alpha_{\rm CO}$ independently.

Table 4.4: ASPECS-LP dust-continuum data

ID 1mm (1)	ID 3mm (2)	z (3)	S_ν(1.2 mm) (μJy) (4)	S_ν(3 mm) (μJy) (5)	L_ν(850 μm, rest)[a] (10^{29} erg s^{-1} Hz^{-1}) (6)	L_ν(850 μm, rest)[b] (10^{29} erg s^{-1} Hz^{-1}) (7)
1mm.C01	3mm.01	2.543	752 ± 24	32.5 ± 3.8	66.6 ± 2.1	47.4 ± 5.5
1mm.C03	3mm.04	1.414	429 ± 23	$\leq$ 20	41.3 ± 2.2	· · ·
1mm.C04	3mm.03	2.454	316 ± 12	22.7 ± 4.2	28.3 ± 1.1	34.0 ± 6.3
1mm.C05	3mm.05	1.551	461 ± 28	27.4 ± 4.6	44.4 ± 2.7	52.0 ± 8.7
1mm.C06	3mm.07	2.696	1071 ± 47	46.5 ± 7.1	93.3 ± 4.1	64.8 ± 9.9
1mm.C07	· · ·	2.58	233 ± 12	$\leq$ 20	20.5 ± 1.0	· · ·
1mm.C09	3mm.13	3.601	155 ± 10	$\leq$ 20	12.4 ± 0.8	· · ·
1mm.C10	· · ·	1.997	342 ± 34	$\leq$ 20	32.1 ± 3.2	· · ·
1mm.C12	3mm.15	1.096	114 ± 11	$\leq$ 20	10.5 ± 1.0	· · ·
1mm.C13	3mm.10	1.037	116 ± 16	$\leq$ 20	10.6 ± 1.4	· · ·
1mm.C14a	· · ·	1.999	96 ± 10	$\leq$ 20	9.0 ± 0.9	· · ·
1mm.C16	3mm.06	1.095	143 ± 18	$\leq$ 20	13.2 ± 1.6	· · ·
1mm.C15	3mm.02	1.317	118 ± 13	$\leq$ 20	11.3 ± 1.3	· · ·
1mm.C19	3mm.12	2.574	85 ± 12	$\leq$ 20	7.5 ± 1.1	· · ·
1mm.C20	· · ·	1.093	94 ± 16	$\leq$ 20	8.7 ± 1.5	· · ·
1mm.C25	3mm.14	1.098	90 ± 17	$\leq$ 20	8.3 ± 1.6	· · ·
1mm.C23	3mm.08	1.382	148 ± 30	$\leq$ 20	14.2 ± 2.9	· · ·
1mm.C30	· · ·	0.458	34 ± 10	$\leq$ 20	1.8 ± 0.5	· · ·
· · ·	3mm.11	1.096	$\leq$ 50	$\leq$ 20	· · ·	· · ·
· · ·[†]	3mm.09	2.698	924 ± 76	44.5 ± 9.7	80.5 ± 6.6	62.0 ± 13.5
Faint.1mm.C20	3mm.16	1.294	86 ± 24	$\leq$ 20	8.2 ± 2.3	· · ·
· · ·	MP.3mm.2	1.087	$\leq$ 50	$\leq$ 20	· · ·	· · ·

Notes. (1) ASPECS-LP continuum ID (Aravena et al., 2020; González-López et al., 2020). (2) ASPECS-LP line ID (Boogaard et al., 2019). (3) Redshift. (4) Flux density at 1.2 mm (Aravena et al., 2020; González-López et al., 2020). (5) Flux density at 3 mm (González-López et al., 2019). (6) Rest-frame 850 μm luminosity density inferred from S_ν(1.2 mm), assuming $T_{\rm dust} = 25$ K and $\beta = 1.8$. (7) Rest-frame 850 μm luminosity density inferred from S_ν(3 mm), assuming $T_{\rm dust} = 25$ K and $\beta = 1.8$.

[a] Derived from S_ν(1.2 mm).

[b] Derived from S_ν(3 mm).

[†] Object falls outside of the Band 6 mosaic, but is the brightest 1 mm continuum source in the ASPECS field. We adopt the S_ν(1.3 mm) from Dunlop et al. (2017).

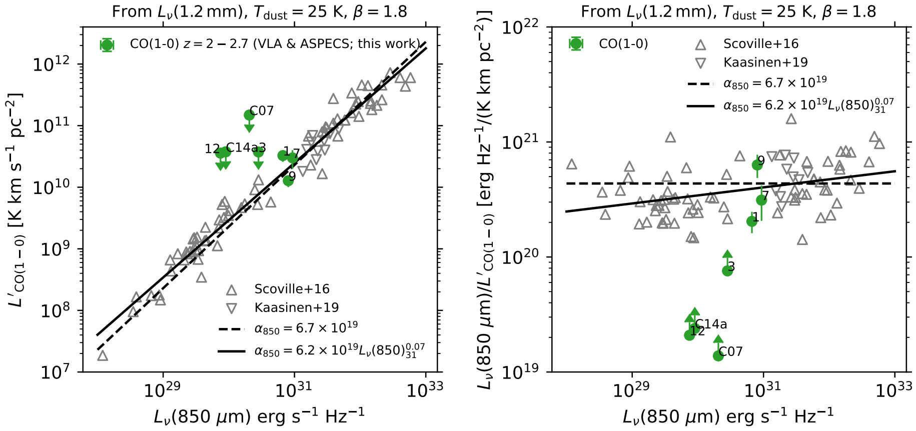

Figure 4.9: Rest frame luminosity at 850 μm compared to the CO(1–0) luminosity (*left*) and the ratio of $L_\nu(850\mu\text{m})/L'_{\text{CO(1-0)}}$ (*right*). The CO(1–0) observations were taken with the VLA (Riechers et al., 2020) and are re-analyzed in this paper. Sources are indicated by the 3mm.ID (except 1mm.C07 and 1mm.C14a). The black lines show the best fit empirical relations from Scoville et al. (2016, assuming both a constant and dust-luminosity dependent dust-to-gas conversion factor), while the gray triangles show their calibration sample as well as more recent observations from Kaasinen et al. (2019).

calibration sample. We then use it to place constraints on the excitation for the sources only observed in higher low-J lines. The advantage of this approach (rather than comparing inferred gas masses) is that it is independent of $\alpha_{\rm CO}$ and only depends on the assumed excitation correction (Equation 4.3). Furthermore, we need not assume a gas-to-dust ratio, as this is implicit in the empirical correlation (but it does depend on the assumptions for $T_{\rm dust}$ and β, mentioned above). We stress that we cannot infer individual excitation corrections in this manner, since the calibration only holds on average and has a certain degree of intrinsic scatter.[32]

We estimate the rest frame $L_\nu(850\,\mu\text{m})$ for our sources from the 1.2 mm continuum emission, assuming $T_{\rm dust} = 25$ K and $\beta = 1.8$ (Table 4.4). While a $T_{\rm dust} = 25$ K is arguably a good assumption for the cold dust that traces the cold gas mass (Scoville et al., 2016), we note that the observed SED, which should be used to scale the flux density to rest-frame 850 μm, is dominated by the luminosity-weighted dust temperature, which is likely higher. However, we adopt $T_{\rm dust} = 25$ K in order to remain consistent with the calibration sample of Scoville et al. (2016). We show the $L_\nu(850\,\mu\text{m})$ against the CO(1–0) luminosity in Figure 4.9. The ASPECS galaxies probe fainter dust luminosities than the calibration sample(s) at high-z. For the sources observed in CO(1–0), we find that the three detections (including 3mm.07) and the upper limits are consistent with the (Scoville et al., 2016) relation. In Figure 4.10

---

[32] Using the data from Scoville et al. (2016), we measure a scatter around the relation of about 0.2 dex. However, this includes the scatter due to measurement and extrapolation errors (which are not provided in the paper), therefore the intrinsic scatter is potentially smaller.

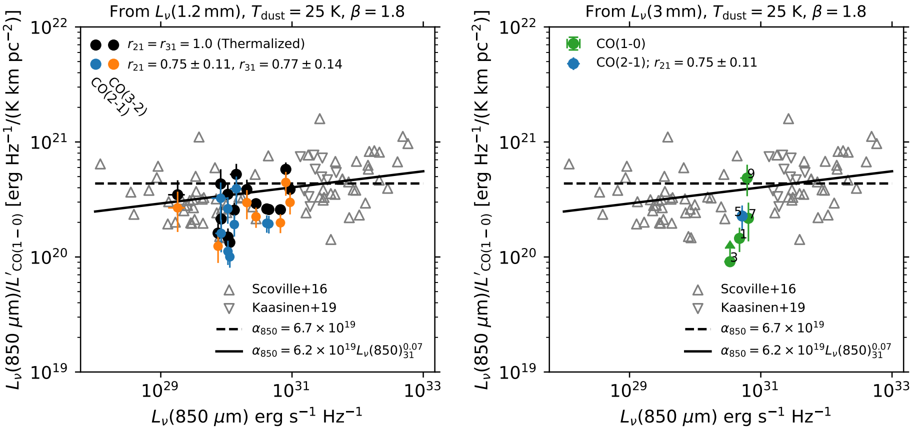

Figure 4.10: *Left:* The same as Figure 4.9 (right), but now using the inferred measurements of CO(1–0) from the low-J CO(2–1) and CO(3–2) lines, using the excitation corrections from § 4.5.2. *Right:* The same as Figure 4.9 (right), but now the $L_\nu(850\mu\text{m})$ is inferred from the observed 3.0 mm continuum instead (when detected). The 3.0 mm continuum probes further down the Rayleigh-Jeans tail and is therefore less sensitive to the extrapolation to rest-frame 850 μm. The latter yields a slightly lower $L_\nu(850\mu\text{m})$, but overall both methods give very consistent results.

(left panel), we show the same ratio, but with the L'_{CO} inferred from the low-J CO lines. Using $r_{21} = 0.75 \pm 0.11$ (§ 4.5.3), we find that the sources detected in CO(2–1) at $\langle z \rangle = 1.2$ on average lie relatively low compared to the Scoville relation, although several individual sources follow it well. Using the mean $r_{31} = 0.77 \pm 0.14$ (measured from stacking, § 4.5.2) for the galaxies at $z = 2.0 - 2.7$, we find that most sources are consistent with the relation, including the galaxies not individually detected in CO(1–0), although the sample average is slightly below the relation. Assuming that the rest-frame 850 μm and CO luminosities are tightly correlated, this would suggest that the excitation values we adopt are too low on average, in particular for CO(2–1). For comparison, we also show the case in which the low-J lines are thermalized on average ($r_{21} = r_{31} = 1.0$; black points). We find an overall better agreement assuming the lines are thermalized on average. Although we cannot constrain the $L'_{\text{CO(1-0)}}$ for individual sources via the $L_\nu(850\ \mu\text{m})$ calibration, the comparison implies that, on average, the r_{21} and r_{31} may not be much lower than ~ 0.75, on average, at $\langle z \rangle = 1.2$ and 2.5, respectively (consistent with the stacking and LVG modeling). Note that to make the CO and dust fully consistent with the empirical relation, based on CO excitation alone, would imply suprathermalized CO in some cases, which is not expected to occur under normal conditions in the ISM, where the CO is optically thick (but $r_{J1} > 1$ is possible if the CO is optically thin).

An alternative explanation for the low $L_\nu(850\mu\text{m})/L'_{\text{CO}}$ ratios is a bias due to the CO-selection. Comparing the primary, flux-limited samples (see § 4.2.2) of both the CO and dust-continuum-selected sources with a redshift at which we can detect CO, we find that there are two CO(2–1)-selected sources without dust-continuum and potentially[33] two vice versa. At the same time, all CO(3–2) emitters are detected in dust-continuum, while there are potentially four dust-selected sources at $z = 2 - 3$ without CO(3–2). While the number of galaxies under consideration is modest, this argues against a strong selection effect, at least for the CO(2–1)-selected sources, in which case we would expect a larger number of dust-selected sources with CO emission (filling in the scatter above the relation). Because the CO detection limit increases relative to that of the dust-continuum (as the latter experiences a strong negative k-correction, e.g., Blain et al. 2002), a selection effect is expected to be stronger for the CO(3–2)-selected sources, as is indeed suggested by the above comparison. However, the latter galaxies do not show systematically lower ratios, compared to the CO(2–1) selected sources, and direct observations of CO(1–0) for a few of the sources do not suggest a strong systematic offset. Overall, we therefore conclude that, while we cannot fully exclude the impact of selection, it does not appear to play a dominant role at least for the CO(2–1)-selected sources.

Finally, to investigate the influence of the Rayleigh Jeans correction on the results (in particular for the higher redshift sources), we also infer $L_\nu(850\mu\mathrm{m})$ from the 3.0 mm continuum data, that has been detected in four of the galaxies at $z \approx 2.6$ and 3mm.05 at $z = 1.55$ (Figure 4.9, right panel). The rest-frame $L_\nu(850\mu\mathrm{m})$ luminosities inferred from 3.0 mm are on average $\approx$ 10% lower than those from the 1.2 mm, but overall we come to the same conclusions.

4.6 Atomic carbon

4.6.1 Atomic carbon abundances

Atomic carbon has been suggested as a good alternative tracer of the molecular gas mass. This is motivated by the fact that the emission from atomic carbon ([C I]) has been found to be closely associated with CO emission in a range of different environments in the MW (Stutzki et al., 1997; Ojha et al., 2001; Ikeda et al., 2002; Schneider et al., 2003) and in local galaxies (e.g., Gerin & Phillips, 2000; Israel et al., 2015; Jiao et al., 2019). There has been some debate to whether [C I] can be used to trace the total molecular gas mass, because the [C I] emission was originally predicted to arise only from a narrow [C II]/[C I]/CO transition zone in molecular clouds on the basis of early theoretical work (Tielens & Hollenbach 1985a,b; see Israel et al. 2015). However, more recent models have supported the picture in which CO and [C I] coexist over a wide range of conditions (see, e.g., Papadopoulos et al., 2004; Bisbas et al., 2015, 2017; Glover et al., 2015).

The [C I] lines are typically found to be optically thin (Ojha et al., 2001; Ikeda et al., 2002; Weiß et al., 2003). As a result, the [C I] column density in the upper levels of the $^3P_2 \rightarrow {}^3P_1$ ($\nu_\mathrm{rest} = 809.342$ GHz) and $^3P_1 \rightarrow {}^3P_0$ ($\nu_\mathrm{rest} = 492.161$ GHz) transitions is directly related to the line intensity, and depends only on the excitation temperature, T_ex (e.g., Frerking et al., 1989; Stutzki et al., 1997; Weiß et al., 2003, given their low critical densities, $< 10^3$ cm^{-3}). This

---

[33] The precise number is dependent on the accuracy of the redshift measurement available for the dust continuum sources.

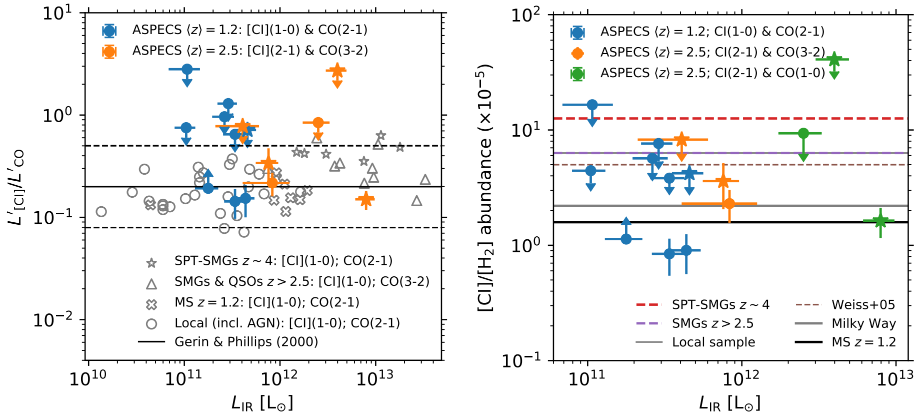

Figure 4.11: *Left:* $L_{[\mathrm{C\,I}]}/L'_{\mathrm{CO}}$ ratio for $[\mathrm{C\,I}](^3P_1 \rightarrow {}^3P_0)$ over CO(2–1) (blue) and $[\mathrm{C\,I}](^3P_2 \rightarrow {}^3P_1)$ over CO(3–2) (orange), where stars indicate X-ray AGN. We compare the observed ratios to SPT-SMGs at $z = 4$ (Bothwell et al., 2017), SMGs at $z \geq 2.5$ (Walter et al., 2011; Alaghband-Zadeh et al., 2013), main-sequence galaxies at $z = 1.2$ and local galaxies, as compiled by Valentino et al. (2018), and the average ratio and scatter in the local sample from Gerin & Phillips (2000). Overall, the ratios broadly agree with the spread found for previous samples of star-forming galaxies. *Right:* atomic carbon abundance in the ASPECS galaxies. The H_2 mass was derived from CO(2–1) (assuming $r_{21} = 0.75 \pm 0.11$) and CO(1–0) or CO(3–2) (assuming $r_{31} = 0.77 \pm 0.14$), with $\alpha_{\mathrm{CO}} = 3.6\,\mathrm{M}_\odot(\mathrm{K\,km\,s^{-1}\,pc^2})^{-1}$, for the galaxies detected in [C I](1–0) and [C I](2–1) respectively. We compare our measurements to the abundances for different galaxy types (excluding active galaxies), converted to a common α_{CO} by Valentino et al. (2018). On average we find [C I] abundances similar to the Milky Way (Frerking et al., 1989) and the star-forming galaxies from Valentino et al. (2018) (who assumes a galaxy-specific α_{CO}, which is 3.0 on average, and $r_{21} = 0.84$), with higher abundances at $\langle z \rangle = 2.5$ compared to $\langle z \rangle = 1.2$. Note that the higher abundances in the submillimeter galaxies from literature are partly driven by the assumed lower α_{CO} in these systems.

means that the atomic carbon mass ($M_{[\mathrm{CI}]}$) can be directly inferred from the line luminosity:

$$M_{[\mathrm{CI}]} = 5.706 \times 10^{-4} Q(T_{\mathrm{ex}}) \frac{e^{T_1/T_{\mathrm{ex}}}}{3} L'_{[\mathrm{C\,I}](1-0)}\,\mathrm{M}_\odot \tag{4.5}$$

$$M_{[\mathrm{CI}]} = 4.556 \times 10^{-4} Q(T_{\mathrm{ex}}) \frac{e^{T_2/T_{\mathrm{ex}}}}{5} L'_{[\mathrm{C\,I}](2-1)}\,\mathrm{M}_\odot. \tag{4.6}$$

Here, $T_1 = 23.6$ K and $T_2 = 62.5$ K are the energies of the $^3P_2$ and $^3P_1$ levels and $Q(T_{\mathrm{ex}}) = 1 + 3e^{-T_1/T_{\mathrm{ex}}} + 5e^{-T_2/T_{\mathrm{ex}}}$ is the partition function in the three-level system approximation (Weiß et al., 2003, 2005).

The excitation temperature itself can be measured directly from the ratio of the integrated line intensities,

$$T_{\mathrm{ex}} = \frac{38.8\,\mathrm{K}}{\ln(2.11/R)}, \tag{4.7}$$

Table 4.5: Masses from different tracers and neutral atomic carbon abundances for the [C I] detected galaxies.

ID	z	$M_{\mathrm{mol,\,RJ}}$ ($\times 10^{10}\,\mathrm{M_\odot}$)	$M_{\mathrm{mol,\,CO}}$ ($\times 10^{10}\,\mathrm{M_\odot}$)	$M_{[\mathrm{C\,I}]}$ ($\times 10^{6}\,\mathrm{M_\odot}$)	([C I]/[H$_2$])$_{\mathrm{RJ}}$ ($\times 10^{-5}$)	([C I]/[H$_2$])$_{\mathrm{CO}}$ ($\times 10^{-5}$)
(1)	(2)	(3)	(4)	(5)	(6)	(7)
1mm.C12	1.09	1.6 ± 0.2	1.4 ± 0.3	≤ 2.7	≤ 3.8	≤ 4.2
1mm.C13	1.03	1.6 ± 0.2	3.4 ± 0.7	1.4 ± 0.4	1.9 ± 0.7	0.9 ± 0.3
1mm.C16	1.09	2.0 ± 0.2	2.5 ± 0.4	0.9 ± 0.3	1.1 ± 0.4	0.8 ± 0.3
1mm.C15	1.31	1.7 ± 0.2	4.0 ± 0.7	≤ 6.8	≤ 9.1	≤ 3.8
1mm.C20	1.09	1.3 ± 0.2	≤ 3.3	1.6 ± 0.5	2.9 ± 1.0	≥ 1.1
1mm.C25	1.09	1.3 ± 0.2	1.9 ± 0.5	≤ 4.7	≤ 8.5	≤ 5.7
3mm.11	1.09	≤ 0.4	0.6 ± 0.1	≤ 1.1	$\cdots$	≤ 4.4
3mm.16	1.29	1.2 ± 0.3	0.9 ± 0.2	≤ 6.6	≤ 12.3	≤ 16.5
MP.3mm.2	1.09	≤ 0.4	1.1 ± 0.3	≤ 3.7	≤ 20.2	≤ 7.6
1mm.C01	2.54	10.0 ± 0.3	11.7 ± 2.4	8.5 ± 1.8	1.9 ± 0.4	1.6 ± 0.5
1mm.C04†	2.45	4.2 ± 0.2	4.5 ± 0.9	4.6 ± 1.1	2.5 ± 0.6	2.3 ± 0.7
1mm.C06	2.69	14.0 ± 0.6	10.7 ± 3.6	≤ 44.3	≤ 7.2	≤ 9.4
1mm.C07†	2.58	3.1 ± 0.2	2.5 ± 0.7	3.9 ± 1.3	2.9 ± 1.0	3.6 ± 1.6
1mm.C19†	2.57	1.1 ± 0.2	2.2 ± 0.5	≤ 7.3	≤ 16.0	≤ 8.2
3mm.9	2.70	12.0 ± 1.0	4.6 ± 1.0	≤ 83.1	≤ 15.6	≤ 40.9

Notes. Properties derived for [C I](1–0) and CO(2–1) at $1 \leq z < 2$, assuming $r_{21} = 0.75 \pm 0.11$ (*top rows*) and from [C I](2–1) and CO(1–0), or CO(3–2) assuming $r_{31} = 0.77 \pm 0.14$, at $2 \leq z < 3$ (*bottom rows*). In the case of a non-detection we report a 3σ upper limit. (1) ASPECS-LP ID (see Table 4.1). (2) Redshift. (3) Molecular gas mass determined via the 1.2 mm dust-continuum emission on the Rayleigh Jeans tail (§ 4.5.4; see Table 4.4). (4) Molecular gas emission determined from the CO line luminosity emission assuming $\alpha_{\mathrm{CO}} = 3.6\,\mathrm{M_\odot}\,(\mathrm{K\,km\,s^{-1}\,pc^2})^{-1}$ (Equation 4.4). (5) Atomic carbon mass derived from [C I](1–0) and [C I](2–1) via Equation 4.5 and Equation 4.6. (6) Neutral atomic carbon abundance computed with $M_{\mathrm{mol,RJ}}$ (Equation 4.8). (7) Neutral atomic carbon abundance, computed with $M_{\mathrm{mol,CO}}$. † CO related properties derived from CO(3–2) assuming $r_{31} = 0.77 \pm 0.14$.

where $R = L'_{[\mathrm{C\,I}](2-1)}/L'_{[\mathrm{C\,I}](1-0)}$ (Stutzki et al., 1997). Walter et al. (2011) measured an excitation temperature of $\langle T_{\mathrm{ex}} \rangle = 29.1 \pm 6.3$ K in a sample of $\langle z \rangle = 2.5$ SMGs. As we never observe both [C I] transitions in the same source, we assume a typical value of $T_{\mathrm{ex}} = 30$ K (see Weiß et al., 2005; Bothwell et al., 2017; Popping et al., 2017b; Valentino et al., 2018; Brisbin et al., 2019, corresponding to $R = 0.58$). Note from Equation 4.5 and Equation 4.6 that the neutral atomic carbon mass is not a strong function of the assumed excitation temperatures above ≈ 20 K for [C I](1–0) and ≈ 40 K for [C I](2–1) (as pointed out by Weiß et al., 2005).

Before turning to the masses inferred from [C I] and CO, we compare the line luminosities directly, as a function of L_{IR}, in the left panel of Figure 4.11. In particular at $\langle z \rangle = 1.2$, we probe [C I] in galaxies at lower L_{IR} than previous studies of similar sources. Overall, the ratios are comparable to those in the main-sequence galaxies from Valentino et al. (2018) and the average ratio in a variety of local galaxies from Gerin & Phillips (2000).

We derive [C i] masses of a few $\times 10^6$ $\mathrm{M_\odot}$(Table 4.5). From the [C i] masses, we derive the galaxy average, luminosity-weighted, neutral atomic carbon abundances,

$$\frac{[\mathrm{C\,I}]}{[\mathrm{H_2}]} = \frac{M_{[\mathrm{CI}]}}{6M_{\mathrm{H_2}}}, \tag{4.8}$$

where $M_{\mathrm{H_2}} = M_{\mathrm{mol}}/1.36$, not including He. We use the CO-derived $\mathrm{H_2}$ masses, adopting $r_{21} = 0.75 \pm 0.11$ and $r_{31} = 0.77 \pm 0.14$ for the sources without CO(1–0), and $\alpha_{\mathrm{CO}} = 3.6\,\mathrm{M_\odot}(\mathrm{K\,km\,s^{-1}\,pc^2})^{-1}$. The abundances are shown as a function L_{IR} in Figure 4.11. We find an average abundance of $([\mathrm{C\,I}]/[\mathrm{H_2}])_{\mathrm{CO}} = (1.9 \pm 0.4) \times 10^{-5}$ (ignoring limits).[34] Overall, the abundances are broadly similar to those in the MW (2.2×10^{-5}, Frerking et al., 1989) and in $z \approx 1.2$ main-sequence galaxies ($(1.6 \pm 0.8) \times 10^{-5}$, Valentino et al., 2018), but lower than in high-redshift SMGs (Walter et al., 2011; Alaghband-Zadeh et al., 2013; Bothwell et al., 2017). However, as pointed out by Valentino et al. (2018), these differences could also be driven by the difference in adopted α_{CO}, as their derived abundances assume an $\alpha_{\mathrm{CO}} = 0.8\,\mathrm{M_\odot}(\mathrm{K\,km\,s^{-1}\,pc^2})^{-1}$, which is the typical value assumed for these systems. Finally, we come to similar conclusions if we use the dust-continuum based molecular gas masses instead, $([\mathrm{C\,I}]/[\mathrm{H_2}])_{\mathrm{RJ}} = (2.2 \pm 0.3) \times 10^{-5}$, assuming the luminosity independent calibration from Scoville et al. (2016) (§ 4.5.4).

4.6.2 PDR modeling

We use the combination of [C i], CO and far-infrared dust emission (L_{IR}) to explore the ISM properties of the galaxies in our sample using PDR models. To this end, we use the results from the PDRToolbox (Kaufman et al., 2006; Pound & Wolfire, 2008). The PDRToolbox is based on the one-dimensional models from Kaufman et al. (2006) and solves for the chemistry, thermal balance, and radiative transfer, assuming metal, dust, and polycyclic aromatic hydrocarbon (PAH) abundances and a gas microturbulent velocity. Every PDR is described by a fixed number density of H nuclei and intensity of the impinging UV radiation field, G_{UV}, in units of the local galactic interstellar radiation field, G_0 (Habing, 1968). The PDRToolbox then provides the line ratio of [C i], CO and L_{IR} as a function of the density and UV radiation field of a PDR.

We estimate the ISM density and UV radiation field by using a combination of the [C i] and CO emission lines for each galaxy. We specifically focus on CO emission from rotational transitions equal to or lower than CO(4–3), unless these are not available, as higher order CO emission originates from significantly denser ISM than [C i] (see Valentino et al., 2020b). We adopt a numerical approach where we bootstrap the observed flux ratios within their error a 1000 times and solve for the ISM density and UV radiation field for each instance. As the final density and radiation field we take the median of these values. The 68% confidence interval is taken as the error on the derived values. For the non-detected lines we run the models using 3σ upper limits on the line fluxes and interpret the results as lower or upper limits accordingly. Similar analyses have been performed in, for instance, Alaghband-Zadeh

---

[34] Instead assuming thermalized CO for all sources without CO(1–0), we derive $([\mathrm{C\,I}]/[\mathrm{H_2}])_{\mathrm{CO}} = (2.2 \pm 0.4) \times 10^{-5}$.

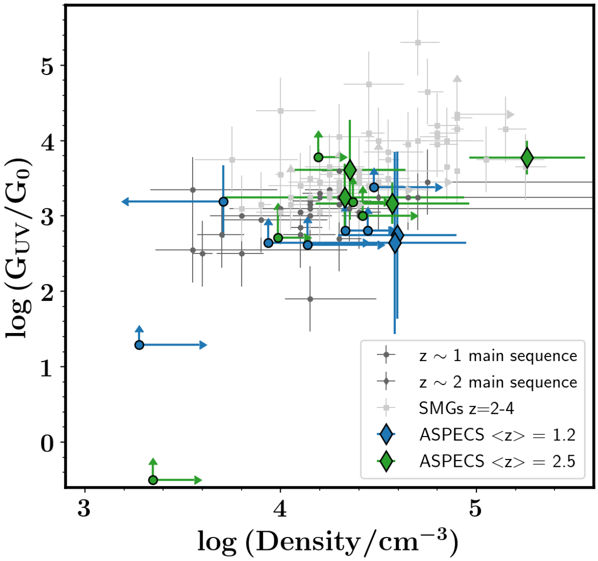

Figure 4.12: The ISM density and UV radiation field strength ($G_{\rm UV}$, relative to the local galactic interstellar radiation field, G_0, Habing 1968) as inferred from PDR modeling. The ASPECS galaxies are shown as diamonds or, in the case of a limit on either parameter, circles. These galaxies are compared to main-sequence galaxies at $z \sim 1$ (Valentino et al., 2018; Bourne et al., 2019; Valentino et al., 2020b) and $z \sim 2$ (Popping et al., 2017b; Talia et al., 2018) and $z = 2 - 4$ SMGs (Walter et al., 2011; Alaghband-Zadeh et al., 2013; Bothwell et al., 2017; Yang et al., 2017a; Andreani et al., 2018; Cañameras et al., 2018; Harrington et al., 2018; Dannerbauer et al., 2019; Jin et al., 2019; Nesvadba et al., 2019) for which Valentino et al. (2020b) re-derived the density and UV radiation field (using similar lines and model assumptions as in this paper).

et al. (2013); Bothwell et al. (2017); Popping et al. (2017b); Cañameras et al. (2018); Brisbin et al. (2019); and Valentino et al. (2020b).

The results of the PDR modeling are shown in Figure 4.12. In general, we find that the PDR models predict fairly high densities, $\geq 10^4$ cm^{-3}, for all sources. In the PDR model, this is constrained by the ratio of [C I] (with low critical density) over CO. The UV radiation field strength is primarily determined by the ratio of the lines over the dust-continuum and found to be $\geq 3 \times 10^2$ G_0 in most cases. The median $G_{\rm UV}$ of the detections appears to be larger at $\langle z \rangle = 2.5$ compared to $\langle z \rangle = 1.2$ in our sample, though this difference is not statistically significant. Overall, the galaxies occupy the same parameter space as the main-sequence galaxies from Valentino et al. (2018); Valentino et al. (2020b), who also modeled the CO and [C I] lines.

We note that the PDR model adopted in this analysis (and other works) assumes that the ISM of a galaxy can be described by a single PDR with a fixed input abundance. In reality, the ISM consists of a range of molecular clouds that all have different properties (density, impinging UV radiation field, abundances). Furthermore, the PDR models assume a fixed density throughout the medium, whereas in reality the density distribution of PDRs is more complex. Following Valentino et al. (2018), we also do not correct the models for the difference in optical depth between CO, [C I] and $L_{\rm IR}$, and therefore restrict our relative comparison with the literature to these data, which are consistently analyzed. Our results should therefore be treated as qualitative measures of the ISM density and UV radiation field. Alaghband-Zadeh et al. (2013), Bothwell et al. (2017), Cañameras et al. (2018), and Valentino et al. (2020b) discuss in more detail that the PDR modeling likely does not capture the full complexity of the ISM in galaxies and should be taken as an order of magnitude indication of the ISM properties. Future work attempting to model the ISM properties of galaxies should thus focus on spatially resolved observations and multi-phase modeling of the ISM.

4.7 Discussion

4.7.1 Modest excitation in mid-J lines at $z = 1.0 - 1.6$

The ASPECS galaxies significantly expand the sample of SFGs with CO excitation measurements at $z = 1.0 - 1.6$. In particular, our observations increase the number of detections of the CO(4–3) and CO(5–4) lines in sources at these redshifts. A key result of our study is that the $\langle z \rangle = 1.2$ galaxies, selected by their CO(2–1) emission, show a range in excitation of their $J \geq 2$ lines up to CO(5–4). In half of the sample we find that the mid-J CO lines are excited to similar (interpolated) levels as the BzK galaxies at $\langle z \rangle = 1.5$, suggesting the presence of a dense, warm component in the ISM of these galaxies (Daddi et al., 2015). However, the remaining galaxies are consistent with lower excitation, as shown by the average stacked ladder including the individually non-detected transitions as well (see Figure 4.5). This indicates that such a warm, dense component is not as dominantly present in all galaxies. On average, the ASPECS galaxies at $\langle z \rangle = 1.2$ are less excited in their mid-J lines compared to the BzK galaxies from Daddi et al. (2015), but, the average mid-J excitation is above that observed in, e.g., the Milky Way.

The lower excitation of the ASPECS galaxies can be naturally explained by their lower surface density of star formation, as the excitation correlates with the radiative energy input into the gas. The CO excitation is sensitive to the gas density and temperature and is known to correlate with the dust temperature (Rosenberg et al., 2015) and radiation field strength, star formation efficiency and star formation rate surface density (Daddi et al., 2015; Valentino et al., 2020a). The excitation has also been shown to correlate, to a lesser extent, with the $L_{\rm IR}$ (e.g., Rosenberg et al., 2015). The connection between $L_{\rm IR}$ and excitation is less direct, however, because the total SFR does not correlate with the density and temperature of the clouds as $\Sigma_{\rm SFR}$ does (see Narayanan & Krumholz, 2014). This conclusion is also reached by Valentino et al. (2020a), who show that the intrinsic scatter in the $r_{52} - L_{\rm IR}$ relation is greater than that in the $r_{52} - \Sigma_{\rm SFR}$ relation. Note that in the case of equally-sloped $L'_{\rm CO} - L_{\rm IR}$ relations for different J (for example, the linear relations found by Liu et al., 2015), a correlation between $L_{\rm IR}$ and excitation would also not be expected.

In Figure 4.13, we show the flux ratios of CO(4–3) and CO(5–4) over CO(2–1), a proxy of the excitation in the CO ladder, as a function of $\Sigma_{\rm SFR}$. As anticipated, our galaxies at $\langle z \rangle = 1.2$

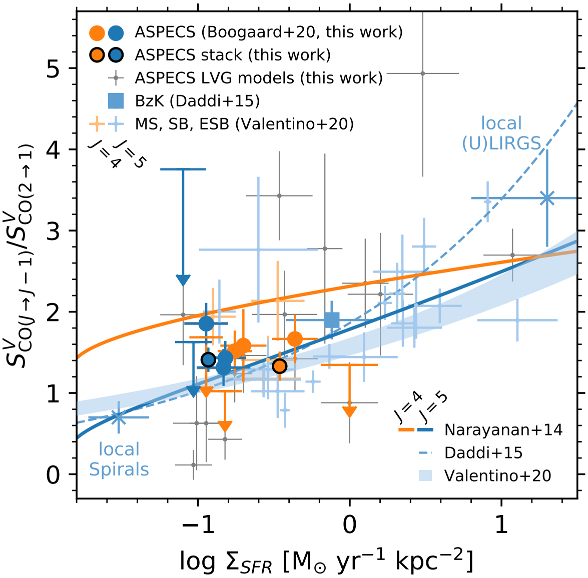

Figure 4.13: Star formation rate surface density ($\Sigma_{\rm SFR}$) versus CO line flux ratio (in units of S^V), for both CO(4–3)/CO(2–1) (orange) and CO(5–4)/CO(2–1) (blue). The colored points (and limits) show the observed line flux ratios of the ASPECS galaxies, while the gray points show the predicted ratios from the LVG model fits for all galaxies (for CO(5–4)/CO(2–1) only; note the points are not visible for the galaxies in which we directly measure the ratio). We also show the values from the stacks (§ 4.5.2) at the mean $\Sigma_{\rm SFR}$. The blue square shows the average of the *BzK*-selected SFGs from Daddi et al. (2015) and the blue crosses show averages for local spirals and (U)LIRGS as reported by Daddi et al. (2015). The light shaded points show the recent data for main-sequence and (extreme) starburst galaxies from Valentino et al. (2020a). The solid lines show the predictions from the Narayanan & Krumholz (2014) models for unresolved observations, the dashed blue line shows the best-fit from Daddi et al. (2015) and the shaded region shows that from Valentino et al. (2020a) (for CO(5–4) only).

probe the low $\Sigma_{\rm SFR}$ regime at this redshift, compared to the sources studied in Daddi et al. (2015) and the recent work by Valentino et al. (2020a). Overall, the modest mid-J excitation of the ASPECS sources appears to naturally follow from the fact that we are probing galaxies with, on average, more moderate surface densities of star formation. We also compare to the models from Narayanan & Krumholz (2014), who have computed theoretical CO ladders for unresolved observations of galaxies, parameterized by $\Sigma_{\rm SFR}$. While the models qualitatively agree and appear to work reasonably well for r_{52}-ratio transition, they seem to overpredict the r_{42}-ratio for the galaxies in our sample.

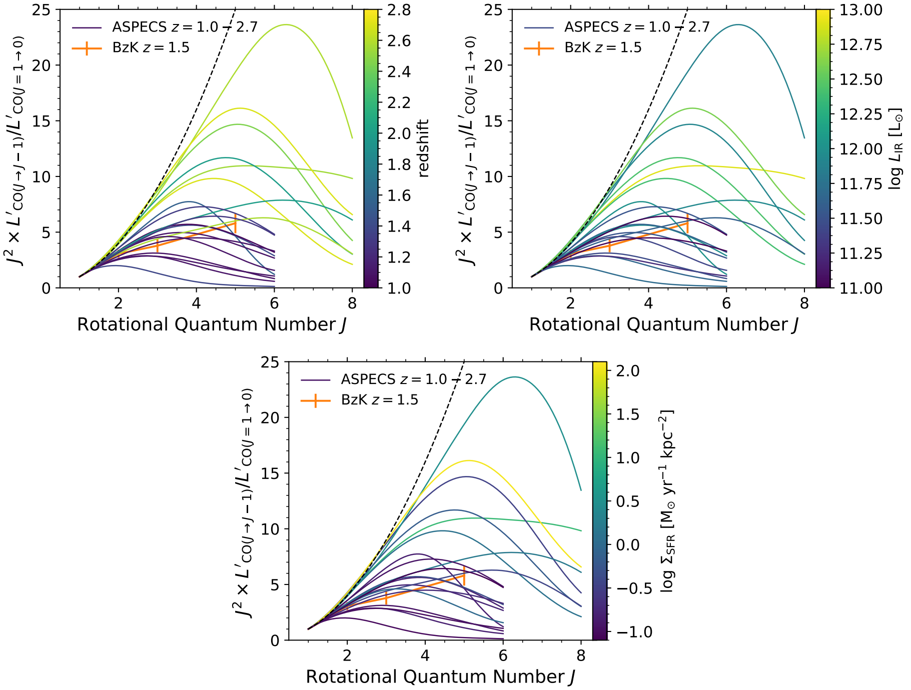

Figure 4.14: ASPECS CO ladders from the two-component LVG models (see Figure 4.8) colored by redshift (*top left*), $L_{\rm IR}$ (*top right*) and $\Sigma_{\rm SFR}$ (*bottom*). The ladders are now shown in units of $J^2 \times L'_{\rm CO}$, normalized to $L'_{\rm CO(1-0)}$, for an easy comparison with the figures in units of line flux shown throughout the paper. While the overall excitation increases with redshift, we also observe a range in excitation at fixed redshift. The increase in excitation is correlated with an increase in both $L_{\rm IR}$ and $\Sigma_{\rm SFR}$.

4.7.2 Increasing excitation with redshift

The CO(3–2) selected galaxies at $z \geq 2$ appear to have intrinsically higher excitation, on average, than the CO(2–1) selected galaxies at $z < 2$. This applies not only to the high-J lines, but also for the excitation in CO(3–2). This observation is robust against the sample being CO flux-selected; because the volume probed in CO(2–1) at $z < 2$ is merely a factor 1.75× smaller, at least some sources with a similarly high r_{31} should have been found at $z < 2$, if they are equally common at both redshifts (such a high r_{31} would be indicated by an as high r_{21}, which is not suggested by the LVG modeling).

The increased excitation at $z \geq 2$ compared to $z < 2$ suggests an intrinsic evolution between the ISM conditions in massive main-sequence galaxies at these redshifts. There are several reasons why more excited CO gas may be anticipated in SFGs going out to higher redshift. SFGs at fixed stellar mass are known to decrease in size (as measured in the rest-frame optical; van der Wel et al., 2014), while they increase in average star formation rate (e.g., Whitaker et al., 2014; Schreiber et al., 2015). This means that the SFR surface density increases with redshift for main-sequence galaxies at fixed mass (e.g., Wuyts et al., 2013), which drives the ambient radiation field. Indeed, there are indications that the dust temperature increases with redshift (e.g., Magdis et al. 2012; Béthermin et al. 2015; Schreiber et al. 2018, but see Dudzevičiūtė et al. 2020), which is linked to the main radiation field intensity. As discussed in § 4.7.1, the CO excitation is expected to increase with these quantities, as they can drive the density and temperature in the clouds.[35]

We compare the excitation to a range of properties, finding that the galaxies with greater excitation at higher redshift indeed have both higher $L_{\rm IR}$ and, more importantly, $\Sigma_{\rm SFR}$. This behavior is illustrated in Figure 4.14. To quantify the increase with $\Sigma_{\rm SFR}$, we add the LVG model predictions for the r_{52} ratio to Figure 4.13, now also including galaxies at $z = 2 - 3$ for which we do not directly measure this line ratio. While there is substantial scatter for the individual models, they broadly support the scenario of increasing excitation with $\Sigma_{\rm SFR}$.

The trend in Figure 4.13 can also be understood more fundamentally as a trend with molecular gas surface density, as a high surface density of gas would also drive the CO excitation upwards.[36] In that context, it is interesting to note that several of the galaxies at $z \approx 2.5$ are found to have a more compact dust distribution, compared to some of the sources at $z \approx 1.5$ (Rujopakarn et al., 2019; Kaasinen et al., 2020).

The difference in excitation between the CO(2–1) and CO(3–2)-selected samples at $z \geq 2$ and $z < 2$ raises the question to what extent our r_{21} and r_{31} are representative of the broader population of galaxies at these redshifts. Whereas the higher r_{31} at $z \geq 2$ could in principle be the result of the CO-flux selection (see § 4.7.4), it appears that at the current sensitivity ASPECS can pick up sources with similar gas masses but with, for example, a factor $\sim 2\times$ lower excitation in r_{31} (see Fig. 9 in Boogaard et al. 2019). The conclusions here are limited by the fact we are limited by the low number of massive sources in the volume in the first place (see Fig. 5 in Boogaard et al. 2019).[37] At $z < 2$, we probe well below the knee of the CO LF, while at $z \geq 2$, we are on or slightly above the knee (Decarli et al., 2019). The same appears true in the context of the IR LF (e.g., Gruppioni et al., 2013). This suggests we are probing the representative part in terms of the cosmic $\rho_{\rm H_2}$, in particular at $z < 2$. Indeed, the individual detections are the dominant contributors to the total $\rho_{\rm H_2}(z = 2.0 - 3.1)$ (Decarli et al., 2019) and not the corrections for sources that fall below the detection limit.

---

[35] Bolatto et al. (2015) point out that a stronger ambient radiation field only drives the low-J excitation upwards if this emission does not arise in a colder, more extended molecular gas reservoir, but is well mixed with the star formation. This is consistent with our data (see § 4.A), but needs to be verified with higher resolution observations.

[36] From a radiative transfer perspective the line ratio will increase with an increasing CO density per velocity gradient (i.e., $N_{\rm H_2}/dv$ for a constant CO abundance), because this drives the line opacity and increases the line trapping and thereby the excitation. Therefore, unless the high column density (gas surface density) is compensated by a linearly increasing turbulence (dv) one naturally expects an increasing excitation with increasing gas surface density. In addition, it is plausible that higher column densities correlate with higher volume densities which will again drive the excitation upwards

[37] Note that while we would, in principle, pick up sources with larger gas masses but lower excitation, this would require ASPECS to probe a larger volume at similar depth. Initial efforts are made in this direction through WIDE ASPECS (R. Decarli et al., in prep.), a survey that covers approximately seven times the area of the ASPECS-LP, albeit at a depth that is more shallow.

4.7.3 The low-J excitation

Constraints on r_{21} at $z = 1.0 - 1.6$

From our two-component LVG model we find $r_{21} = 0.75 \pm 0.11$ for the CO(2–1) selected galaxies at $z = 1.0 - 1.6$. This is in good agreement with the average value of $r_{21} = 0.76 \pm 0.09$ for the three massive SFGs at $z = 1.5$ (Daddi et al., 2015, which are well described by a two-component model).

On the other hand, comparing the dust luminosity at rest-frame 850 μm to the CO(1–0) luminosity—which is inferred from the CO(2–1) line using this value of r_{21}, because we do not have direct observations of CO(1–0) at this redshift range—we find that the dust luminosity under-predicts that of the gas. If such a relation holds (Scoville et al., 2016), this may suggest that the average excitation in CO(2–1) is higher (Figure 4.10). Looking in detail at the galaxies from Daddi et al. (2015), two out of three galaxies have an r_{21} consistent with unity (0.92 ± 0.23 and 1.02 ± 0.20), while the average subthermal excitation is driven by the third source ($r_{21} = 0.48 \pm 0.08$). For comparison, in SMGs at higher redshift, the average r_{21} is often found to be close to, or consistent with unity: $r_{21} = 0.84 \pm 0.13$ (Bothwell et al., 2013) and $r_{21} = 1.11 \pm 0.08$ (Spilker et al., 2014, i.e., suprathermal, though we caution this sample potentially suffers from line-dependent differences in the lensing amplification), though the number of SMGs with direct constraints on r_{21} is still small and significantly spread in redshift (Carilli et al., 2010; Riechers et al., 2013; Aravena et al., 2016a). If we would assume that our sources are on average better described by a single-component model we find a higher value of $r_{21} = 0.83 \pm 0.12$. However, given that both the mid-J excitation and $L_{\rm IR}$ are lower than the BzK galaxies, this appears less likely. The fact that the single-component model is formally consistent with the two-component solution, as well as thermalized CO, highlights that we are considering relatively small differences in excitation in the first place, compared to the observational uncertainties. In any case, as observations of CO(1–0) around $z \approx 1.2$ are impossible given the atmospheric opacity, detailed characterizations of the multi-line CO ladders are key to make progress here.

It should be noted that there are several reasons why the comparison with the dust luminosity as a molecular gas tracer may break down in the first place. If the mass-weighted dust temperature in our sources is higher compared to the sample from Scoville et al. (2016) this would increase the dust luminosity at fixed gas mass, relieving the need for thermalized CO. However, even if the luminosity-weighted dust temperature varies, the mass-weighted dust temperature will not vary so strongly (Scoville et al., 2016). It is also not clear that our galaxies would have a very different dust-opacity slope (β). A discrepancy between the dust and CO emission could also happen if the dust emission is distinct from the CO emission (e.g., in the case of a constant gas-to-dust ratio, but a strong dust temperature gradient, or opacity effects). It is not clear that our galaxies would be very distinct from the calibration sample in this respect. However, we are probing a fainter regime in $L_\nu(850\,\mu\text{m})$, where the calibration sample is mostly local, while the sources at comparable redshifts are generally higher luminosity. Furthermore, our data at 1.2 mm and 3.0 mm probes further down the Rayleigh-Jeans tail than some of the earlier observations. The Scoville relation also breaks for galaxies with a strongly sub-solar metallicity and for that reason Scoville et al. (2016) restrict their sample to galaxies with $M_* \geq 2 \times 10^{10}$ M$_\odot$. However, the ASPECS galaxies are generally more massive than this and have (super-)solar metallicities (Boogaard et al., 2019). Finally, we do not exclude the possibility that the apparent discrepancy (on average) is driven by low number statistics, as the majority of the sample is consistent within the intrinsic scatter in the relation.

Measurement of r_{31} at $z = 2.0 - 2.7$

Stacking the CO(3–2)-selected galaxies at $\langle z \rangle = 2.5$, we directly derive an $r_{31} = 0.77 \pm 0.14$, which is supported by the average value from the LVG modeling of all individual sources at $z = 2.0 - 2.7$ ($r_{31} = 0.80 \pm 0.14$). This value is significantly higher than found in the lower redshift BzK-selected SFGs at $z = 1.5$ (Daddi et al. 2015; $r_{31} = 0.42 \pm 0.15$; ranging from $0.27 - 0.57$), which has implications for the measurement of the cosmic molecular gas density (we will come back to this in § 4.7.5). Studying two massive main-sequence galaxies at $z = 2.3$, Bolatto et al. (2015) found higher ratios consistent with thermalized CO: $r_{31} = 0.92 \pm 0.11$ and $r_{31} = 1.17 \pm 0.17$ (plus two lower limits of ≥ 0.57 and ≥ 0.79). The SMGs at $z = 2$ show a wide range of excitation values, as discussed in Riechers et al. (2020). Early studies found a relatively low average ($r_{31} = 0.52 \pm 0.09$ Ivison et al., 2011; Bothwell et al., 2013), while more recently, Sharon et al. (2016) found an average of $r_{31} = 0.78 \pm 0.27$. At higher redshift, Spilker et al. (2014) reports $r_{31} = 0.87 \pm 0.06$, although these lensed sources are arguably more extreme. Overall, the different samples at $z = 2 - 3$ show a significant spread in their r_{31} ratio (see also Riechers et al. 2020), driven by different selection methods picking up galaxies with different ambient conditions in their ISM. In that context, ASPECS provides a well-defined sample for further investigation—flux-limited in CO(3–2) and followed up in CO(1–0)—which probes fainter $L_{\rm IR}$ than the typical samples of SMGs. A contribution from the AGN is not expected to dominate the low-J lines and we do not find a clear correlation between r_{31} and the presence of an X-ray AGN.

Consistency with the model results

The fairly high excitation in the low-J lines is generally consistent with the densities of $\geq 10^4$ cm^{-3} found in the (constant density) PDR modeling of the low-J CO and [C I] lines (though we caution that the different types of models should not be blindly compared, given the differences in underlying assumptions). From a radiative transfer perspective, it is rather easy to excite CO(2–1), even at modest densities and temperatures, and slightly less so for CO(3–2). Note the effective floor on the gas temperature at each redshift is set by the Cosmic Microwave Background, which measures $T_{\rm CMB} = 6$ K at $z = 1.2$ and 10 K at $z = 2.5$. For comparison, the temperatures corresponding to the energy level differences for the (dominant) $\Delta J = 1$ collisional excitations are $T_{1\rightarrow 2} = (E_2 - E_1)/k_B = 11.1$ K and $T_{2\rightarrow 3} = 16.6$ K, respectively, where k_B is the Boltzmann constant. As such, unless galaxies harbor extended low-excitation reservoirs (addressed in § 4.A), the levels of low-J excitation found in this work are not unexpected.

4.7.4 Broader implications of the flux-limited survey

Because ASPECS is a flux-limited survey, without any target preselection, it also provides additional information on the CO excitation in the whole population of gas mass-selected galaxies, beyond just the detected sources. The observed CO luminosity at different redshifts depends on the product of $r_{J1} M_{\rm mol} \alpha_{\rm CO}^{-1}$ (Equation 4.4) and hence three selection effects are at play. At a given redshift we would first detect the sources with the highest gas mass (at fixed $\alpha_{\rm CO}$) and the highest luminosity at a given gas mass, i.e., the sources with the highest excitation in their low-J lines. Given that we detect approximately half of the massive main-sequence galaxies at $z = 1 - 3$ (Boogaard et al., 2019), this implies that the galaxies that we did not detect will have a less massive gas reservoir (and/or higher $\alpha_{\rm CO}$) and/or lower CO excitation in the $J = 2$ and $J = 3$ levels. For that reason, in particular for galaxies toward the lower stellar mass and SFR end of the ASPECS sample at a given redshift (i.e., the faint end of the survey), where we are less complete, the average excitation of the low-J levels may be lower. By the same argument, the fact that we do not detect any galaxies in the mid-/high-J CO lines alone that are in principle detectable in the low-J CO(2–1) or CO(3–2) lines, implies that the excitation in their mid-/high-J levels will not be significantly above the detected samples at the respective redshifts, for galaxies with comparable gas masses (at fixed $\alpha_{\rm CO}$).

4.7.5 Implications for the cosmic molecular gas density

By measuring the CO luminosity in galaxies without any preselection over a well-defined cosmic volume, ASPECS is conducting the deepest census of the cosmic molecular gas density, $\rho_{\rm H_2}(z)$, to date (Decarli et al., 2016a, 2019, 2020). This relies on the excitation corrections from the $J \geq 2$ lines back to CO(1–0). In the initial results from ASPECS, these have been assumed to follow a single CO ladder, as measured for BzK-selected SFGs by Daddi et al. (2015) at $\langle z \rangle = 1.5$, up to CO(4–3),[38] as these were considered to be the closest analogs of the sources observed with ASPECS at the time.[39] With our study of the CO excitation in the ASPECS galaxies—the actual sources that defined $\rho_{\rm H_2}(z)$—we can now revisit these assumptions in more detail.

Our result that the average excitation increases between $z < 2$ and $z \geq 2$ has important implications for $\rho_{\rm H_2}(z)$. Our results support the earlier assumptions for the excitation corrections at $z < 2$. Adopting the new CO ladders (Table 4.3) does not significantly alter the constraints on $\rho_{\rm H_2}$ at $z < 2$, with the largest change being a 25% decrease at $z = 0.7 - 1.2$ (based on r_{41}). In contrast, the significantly higher excitation at $z \geq 2$ implies a factor 2× decrease in $\rho_{\rm H_2}$ compared to earlier results, for CO(3–2) at $z = 2.0 - 3.1$ (see also Riechers et al. 2020) and CO(4–3) at $z = 3.0 - 4.5$. It should be noted that we currently do lack direct constraints on the excitation for CO(4–3)-selected samples at $z = 3.0 - 4.5$. However, based on the results from this paper, we do not expect the average excitation for the sources contributing to the measurement of $\rho_{\rm H_2}$ to be lower than at $z = 2.5$ (and certainly not as low as in Daddi et al. 2015). Note that this decrease is in line with the models underpredicting the earlier measurements of $\rho_{\mathrm{H}_2}(z > 2)$ (e.g., Popping et al., 2019).

---

[38] Daddi et al. (2015) did not measure the excitation in CO(4–3), but interpolating their CO ladder yields $r_{41} = 0.31 \pm 0.06$ (see Decarli et al., 2016b).

[39] The full range of results was considered to be bracketed between two extreme cases: Milky Way-like low excitation conditions and thermalized CO, see Appendix B in Decarli et al. (2019)

In summary, we make new recommendations for the average CO ladders to be used for the measurement of the cosmic molecular gas density (the two-component models from Table 4.3). The constraints on $\rho_{\mathrm{H}_2}(z)$ using the new excitation corrections are presented and discussed in Decarli et al. (2020). Our results, combined with those of Riechers et al. (2020), show that direct measurement of the CO(1–0) transition (where accessible) as well as constructing more complete CO ladders, in order to characterize the CO excitation and physical conditions in the cold ISM, are essential to make progress in further constraining the cosmic molecular gas density.

4.8 Summary and Conclusions

This paper presents a study of the carbon monoxide (CO) excitation, atomic carbon ([C I]) emission, and interstellar medium (ISM) conditions in a sample of 22 SFGs at $z = 0.46 - 3.60$. These galaxies have been observed as part of the ASPECS-LP, designed to provide a cosmic inventory of molecular gas by selecting galaxies purely by their CO and dust-continuum emission in ALMA Bands 3 and 6, without any preselection. These galaxies are known to lie on, above, and below the main sequence of SFGs at their respective redshifts (Aravena et al., 2019, 2020; Boogaard et al., 2019). We detect a total of 34 CO $J \rightarrow J - 1$ lines with $J = 1$ up to 8 (+ 21 upper limits, up to $J = 10$) and 6 [C I] $^3P_1 \rightarrow {}^3P_0$ and $^3P_2 \rightarrow {}^3P_1$ lines (+ 12 upper limits). This includes follow-up observations of seven sources at $z = 1.99 - 2.70$ in CO(1–0) from VLASPECS (Riechers et al., 2020), that we analyze here in concert with the ASPECS data.

The ASPECS galaxies have lower infrared luminosities (L_{IR}) and SFR surface densities (Σ_{SFR}) than earlier, targeted samples of SFGs and submillimeter galaxies (including lensed samples) at similar redshifts (Daddi et al., 2015; Bothwell et al., 2013; Spilker et al., 2014). We study the CO excitation of the CO(2–1) and CO(3–2) selected samples and compare them to the average CO ladders of the targeted samples. We focus on two redshift bins, $\langle z \rangle = 1.2$ and $\langle z \rangle = 2.5$, at which we cover both a low/mid-J CO transition and a mid/high-J CO transition with ASPECS.

We find that half of the galaxies at $\langle z \rangle = 1.2$ show remarkably similar excitation, up to CO(5–4), similar to that observed in a sample of four BzK-color-selected SFGs at $\langle z \rangle = 1.5$ (Daddi et al., 2015), while the remaining sources are consistent with lower excitation. The range in excitation suggests that a warm and/or dense component, indicated by the higher excitation, is not omnipresent in galaxies at these redshifts. We detect the high-$J \geq 6$ lines in several galaxies at $\langle z \rangle = 2.5$, indicating that the high-J excitation is comparable to the levels in local starbursts and slightly lower than SMGs at similar redshifts (Bothwell et al., 2013), although half of the sources selected by their CO(3–2) emission are not detected in their high-J lines.

Stacking all the CO and [C I] transitions that we cover with ASPECS (including non-detections), we find our galaxies at $\langle z \rangle = 1.2$ show, on average, lower excitation than BzK-selected galaxies. This is consistent with a picture in which the CO excitation is driven by the SFR surface density, $\Sigma_{\rm SFR}$, broadly matching model predictions (although the models do not fully reproduce our observations). For the galaxies at $\langle z\rangle = 2.5$, the stacking reveals an average $r_{31} = 0.77 \pm 0.14$ and $r_{71} = 0.19 \pm 0.04$, broadly comparable to SMGs at this epoch, as well as local starburst galaxies

We present the average excitation corrections for cold gas mass-selected galaxies at $z = 1.0 - 1.6$ and $z = 2.0 - 2.7$, based on the interpolation of the CO ladders using (single- and) two-component LVG models. These models predict $r_{21} = 0.75 \pm 0.11$ at $z < 2$, similar to the BzK-selected SFGs (Daddi et al., 2015).

We place our sources on the empirical correlations between $L'_{\rm CO(1-0)}$ and dust luminosity at rest-frame 850 μm, probing significantly lower $L_\nu(850\,\mu{\rm m})$ than the earlier samples at $z > 0$, and find good agreement for the CO(3–2)-selected sources. However, we find that the dust luminosity on average overpredicts the CO(1–0) luminosity for the CO(2–1)-selected sample. This either implies that the average r_{21} at $\langle z\rangle = 1.2$ is higher, or that the assumptions going into the correlation break down for these sources.

Comparing our [C I](1–0) and [C I](2–1) observations to the literature, we find that the $L_{\rm [C\,I]}/L_{\rm IR}$ ratio of our sample is similar to main-sequence galaxies, as observed by Valentino et al. (2018). We find an average neutral atomic carbon abundance of $[{\rm C\,I}]/[{\rm H_2}] = (1.9 \pm 0.4) \times 10^{-5}$. This is comparable to the abundance measured in the main-sequence galaxies and the MW, but lower than what is measured in SMGs (although this apparent discrepancy is degenerate with the assumption of a different $\alpha_{\rm CO}$; Valentino et al. 2018). Modeling the CO, [C I] and $L_{\rm IR}$ emission using the PDRToolbox indicates densities $\geq 10^4$ cm^{-3}, generally consistent with the (fairly high) excitation in the low-J lines.

The interpolated CO ladders suggest that the intrinsic excitation is higher for the sources at $z \geq 2$ compared to $z < 2$, even in the lower-J lines such as CO(3–2). The excitation difference is robust against the ASPECS selection function and correlated with $L_{\rm IR}$ and $\Sigma_{\rm SFR}$. This implies an intrinsic evolution in the ISM conditions of massive SFGs between these redshifts, which we link to an increase in the surface density of star formation (and gas) in SFGs with redshift.

Because ASPECS is a flux-limited survey, it also provides additional information on the CO excitation in the whole population of gas mass-selected galaxies. Being most sensitive to galaxies with the highest excitation at a given gas mass (at fixed $\alpha_{\rm CO}$), this suggests that the average excitation in sources with comparable gas masses (at fixed $\alpha_{\rm CO}$) may be lower toward the faint end of the survey. At the same time, the non-detection of galaxies in their mid-/high-J alone (which are in principle detectable in their low-J lines), implies that the average excitation is not much higher.

The galaxies studied in this paper are the same as those constraining the CO luminosity function and the cosmic molecular gas density, $\rho_{\rm H_2}$, as measured by ASPECS. The increased excitation in the CO-selected galaxies at $z \geq 2$ compared to those at $z < 2$ implies a decrease in the inferred $\rho_{\rm H_2}(z \geq 2)$ compared to earlier measurements (Decarli et al., 2016a, 2019). We make recommendations for the average CO excitation in CO-flux-limited samples of galaxies, to be adopted in the constraints on $\rho_{\rm H_2}(z)$ from the complete ASPECS survey, presented in Decarli et al. (2020).

The observations presented here have extended the sample of star-forming galaxies at $z = 1 - 3$ with constraints on their CO excitation and atomic carbon emission. As these are the same galaxies through which the CO luminosity function is measured, characterizing them in detail is key to further our constraints on the cosmic molecular gas density. Further study of such well-defined (flux-limited) samples with multi-line observations will be instrumental to gain a complete picture of the ISM conditions in star-forming galaxies across cosmic time.

Acknowledgments

We would like to thank the anonymous referee for an insightful and constructive report. The author is also grateful to Francesco Valentino for providing early access to the data from Valentino et al. (2020a), that appeared on the arXiv while this paper was under review. This paper makes use of the following ALMA data: ADS/JAO.ALMA#2016.1.00324.L. ALMA is a partnership of ESO (representing its member states), NSF (USA) and NINS (Japan), together with NRC (Canada), NSC and ASIAA (Taiwan), and KASI (Republic of Korea), in cooperation with the Republic of Chile. The Joint ALMA Observatory is operated by ESO, AUI/NRAO, and NAOJ. The National Radio Astronomy Observatory is a facility of the National Science Foundation operated under cooperative agreement by Associated Universities, Inc. F.W. acknowledges support from ERC grant 740246 (Cosmic_Gas). Este trabajo cont ó con el apoyo de CONICYT + PCI + INSTITUTO MAX PLANCK DE ASTRONOMIA MPG190030. D.R. acknowledges support from the National Science Foundation under grant Nos. AST-1614213 and AST-1910107. D.R. also acknowledges support from the Alexander von Humboldt Foundation through a Humboldt Research Fellowship for Experienced Researchers. I.R.S. acknowledges support from STFC (ST/T000244/1). M.K. acknowledges support from the International Max Planck Research School for Astronomy and Cosmic Physics at Heidelberg University (IMPRS-HD). T.D.-S. acknowledges support from the CASSACA and CONICYT fund CAS-CONICYT Call 2018. H.I. acknowledges support from JSPS KAKENHI grant No. JP19K23462.

Facilities: ALMA, VLA, VLT: Yepun (MUSE). *Software*: TOPCAT (Taylor, 2005), GNUASTRO (Akhlaghi & Ichikawa, 2015), IPYTHON (Perez & Granger, 2007), NUMPY (van der Walt et al., 2011), MATPLOTLIB (Hunter, 2007), ASTROPY (The Astropy Collaboration et al., 2013, 2018).

Appendix 4.A Similar widths for the low-J and high-J CO lines

Previous studies have suggested that some SMGs at $z = 2 - 4$ have line widths in CO(1–0) that are larger than in the higher-J transitions (e.g., Ivison et al., 2011, although the difference is rather subtle, about $\sim 15\%$, which is within the limits of our data). Together with the observation that the excitation models to the high-J CO lines underpredicted the total molecular gas mass in these sources (by a factor of $\sim 1.5 - 4.5$; Riechers et al., 2011a), this suggested the presence of extended low-excitation gas reservoirs in some SMGs, but, notably, not in all cases (e.g., Riechers et al., 2011b; Hodge et al., 2012). If there would be extended emission in CO(1–0), this complicates estimates of total molecular gas mass from the higher-J lines.

We find that the line widths of the different CO and [C I] lines are consistent (see Figure 4.2), including the CO(1–0) lines. There is one outlier, 3mm.12, which has a potential low-S/N broad component that should be confirmed by future observations (Riechers et al. 2020; this line has $S/N < 3$ in the fit where the line widths are tied together). The strong CO luminosity relative to the dust emission (see § 4.5.4), even when assuming thermalized CO, suggests that we are not missing a large volume of molecular gas in CO(2–1) and CO(3–2) that would be probed by the dust. Furthermore, from an excitation perspective it is very unlikely to have gas that radiates purely in CO(1–0) and not at all in CO(2–1), which is only attainable at very low $n_{\mathrm{H_2}}$ and T_{kin}. Looking at other SFGs at the same redshift, in the BzK-selected galaxies at $z = 1.5$ (Daddi et al., 2015) the line widths are also found to be very similar between CO(2–1) (Daddi et al., 2010a) and CO(1–0) (Aravena et al., 2014, although the errors on the latter are significant). Similarly, Bolatto et al. (2015) found consistent line widths and spatial extent between CO(3–2) and CO(1–0) in two massive main-sequence galaxies at $z = 2.3$. In summary, while we cannot conclusively rule out their presence with the current observations, we do not see clear evidence of a large volumes of cold molecular gas that are not traced by the relatively low-J CO lines. This supports the use of these transitions in inferring the molecular gas mass.

Appendix 4.B Spectral line fits

Gaussian fits to the spectral lines of CO and [C I], performed as detailed in § 4.3.1, are shown in Figure 4.15. The best-fit parameters are reported in Table 4.6. For each source, we fit a single redshift and line width for all lines simultaneously.

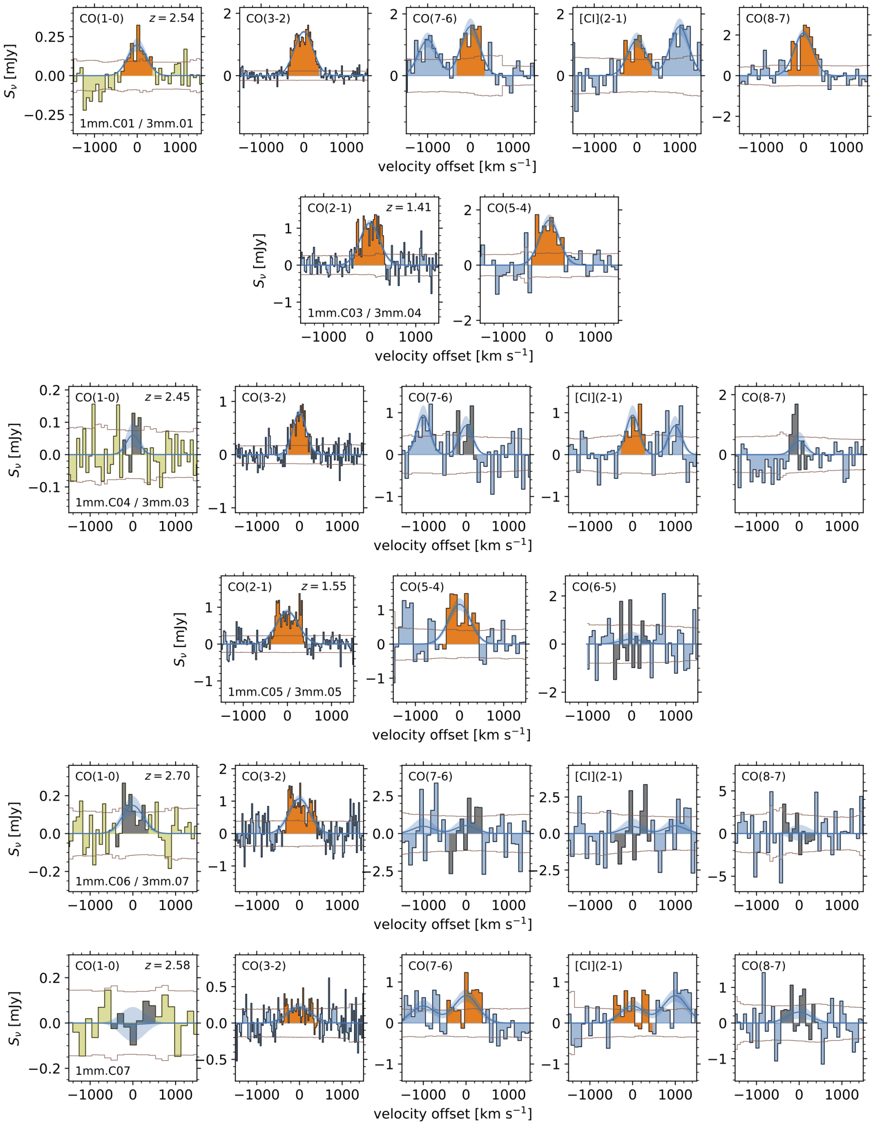

Figure 4.15: Gaussian fits to the ^{12}CO and [C I] lines in the ASPECS galaxies. The groups of panels (max 2 per row) show the different transitions (indicated top left) in a single galaxy (identified in the bottom left of the leftmost panel). The spectra are shown in blue (ASPECS) and yellow (VLA) and are binned in the *Ka* band and Band 6 for visualization purposes (except for 3mm.08 and 3mm.11 with very narrow lines). The brown line shows the $\pm 1\sigma$ root-mean-square noise. The best-fit for all lines (tied together in redshift and line width) and a 1σ confidence interval are shown by the blue line and shading. The channels indicated in orange (gray) fall within $1.4 \times$ FWHM (i.e., 90% of the flux) for a detection (non-detection).

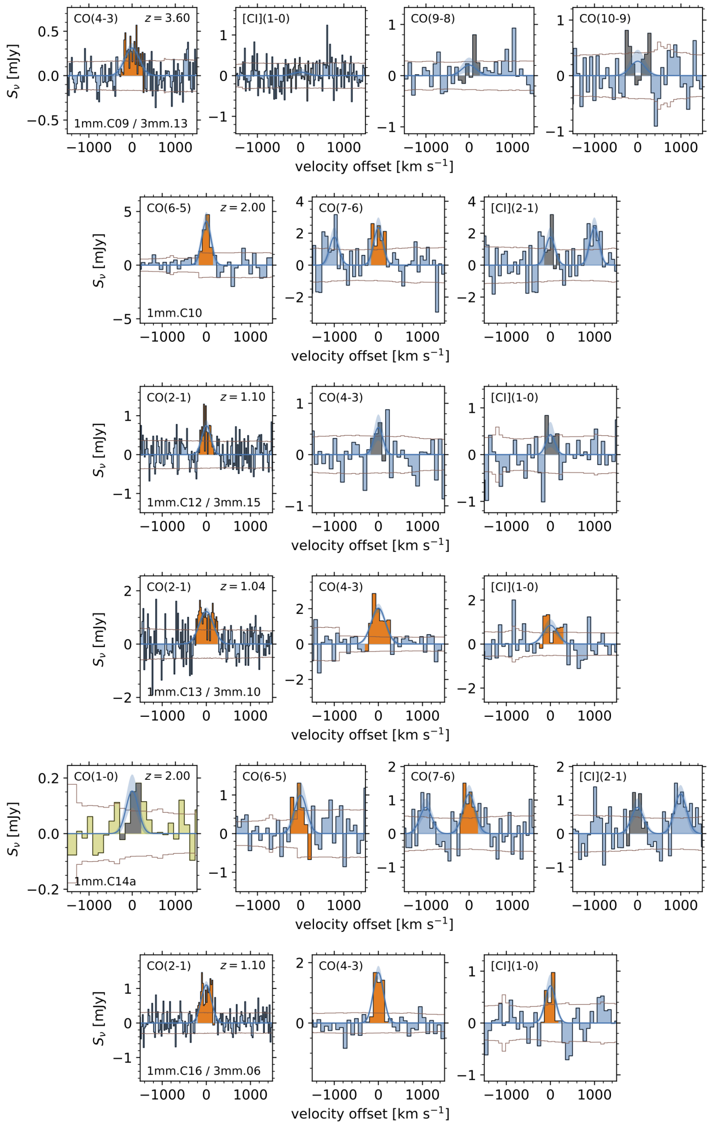

Figure 4.15: *(continued)*

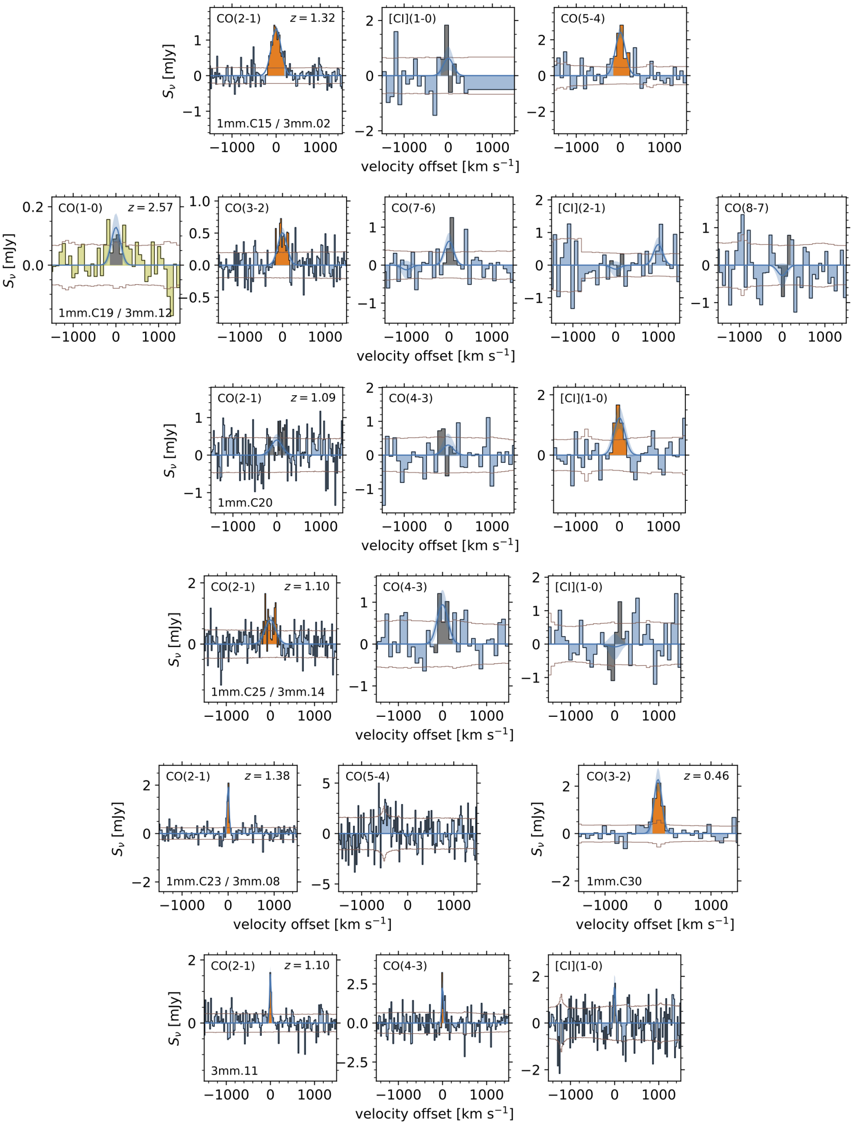

Figure 4.15: *(continued)*

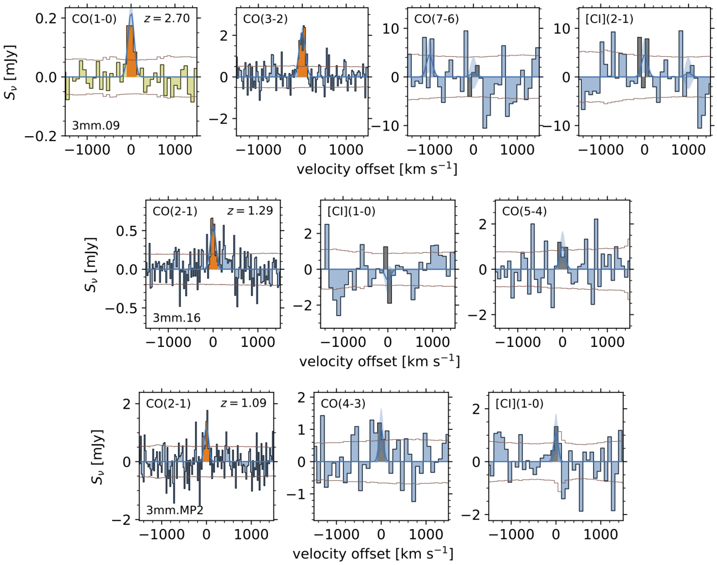

Figure 4.15: *(continued)*

Table 4.6: Spectral line properties determined with Gaussian fits

ID 1mm (1)	ID 3mm (2)	z (3)	FWHM ($\mathrm{km\,s^{-1}}$) (4)	Line (5)	Frequency (GHz) (6)	S^V ($\mathrm{Jy\,km\,s^{-1}}$) (7)	L' ($10^9\ \mathrm{K\,km\,s^{-1}\,pc^2}$) (8)	r_{J1} (9)	r_{J2} (10)
1mm.C01	3mm.01	2.5437 ± 0.0001	518 ± 18	CO(3–2)	97.582 ± 0.002	0.78 ± 0.02	25.9 ± 0.8	0.79 ± 0.17	. . .
				CO(7–6)	227.633 ± 0.006	0.88 ± 0.15	5.4 ± 0.9	0.16 ± 0.04	. . .
				[C I](2–1)	228.392 ± 0.006	0.64 ± 0.13	3.9 ± 0.8	. . .	. . .
				CO(8–7)	260.127 ± 0.007	1.16 ± 0.12	5.4 ± 0.5	0.17 ± 0.04	. . .
				CO(1–0)	32.529 ± 0.001	0.11 ± 0.02	32.7 ± 6.8	. . .	. . .
1mm.C03	3mm.04	1.4142 ± 0.0001	498 ± 39	CO(2–1)	95.491 ± 0.005	0.60 ± 0.04	15.8 ± 1.2	. . .	. . .
				CO(5–4)	238.697 ± 0.013	0.86 ± 0.11	3.6 ± 0.5	. . .	0.23 ± 0.03
1mm.C04	3mm.03	2.4535 ± 0.0002	367 ± 31	CO(3–2)	100.130 ± 0.004	0.31 ± 0.02	9.7 ± 0.7	1.46 ± 0.91	. . .
				CO(7–6)	233.577 ± 0.010	0.27 ± 0.09	1.6 ± 0.5	0.23 ± 0.16	. . .
				[C I](2–1)	234.356 ± 0.010	0.37 ± 0.09	2.1 ± 0.5	. . .	. . .
				CO(8–7)	266.920 ± 0.012	0.18 ± 0.12	0.8 ± 0.5	0.12 ± 0.11	. . .
				CO(1–0)	33.378 ± 0.002	0.02 ± 0.01	6.7 ± 4.2	. . .	. . .
1mm.C05	3mm.05	1.5503 ± 0.0002	587 ± 48	CO(2–1)	90.397 ± 0.006	0.55 ± 0.04	17.2 ± 1.3	. . .	. . .
				CO(5–4)	225.962 ± 0.015	0.73 ± 0.11	3.6 ± 0.6	. . .	0.21 ± 0.04
				CO(6–5)	271.135 ± 0.018	0.13 ± 0.20	0.4 ± 0.7	. . .	. . .
1mm.C06	3mm.07	2.6956 ± 0.0004	572 ± 68	CO(3–2)	93.570 ± 0.009	0.65 ± 0.07	24.1 ± 2.6	0.81 ± 0.28	. . .
				CO(7–6)	218.273 ± 0.021	0.32 ± 0.31	2.2 ± 2.1	0.07 ± 0.07	. . .
				[C I](2–1)	219.001 ± 0.021	0.29 ± 0.34	2.0 ± 2.3	. . .	. . .
				CO(8–7)	249.431 ± 0.024	0.06 ± 0.57	0.3 ± 2.9	0.01 ± 0.10	. . .
				CO(1–0)	31.191 ± 0.003	0.09 ± 0.03	29.9 ± 10.1	. . .	. . .
1mm.C07	. . .	2.5805 ± 0.0006	658 ± 109	CO(3–2)	96.577 ± 0.017	0.16 ± 0.03	5.3 ± 1.1	-4.19 ± 54.58	. . .
				CO(7–6)	225.288 ± 0.040	0.47 ± 0.10	2.9 ± 0.6	-2.31 ± 30.13	. . .
				[C I](2–1)	226.040 ± 0.040	0.29 ± 0.10	1.8 ± 0.6	. . .	. . .
				CO(8–7)	257.448 ± 0.046	0.22 ± 0.13	1.0 ± 0.6	-0.82 ± 10.63	. . .
				CO(1–0)	32.194 ± 0.006	-0.00 ± 0.05	-1.3 ± 16.5	. . .	. . .
1mm.C09	3mm.13	3.6008 ± 0.0005	397 ± 80	CO(4–3)	100.208 ± 0.011	0.13 ± 0.02	4.4 ± 0.8	. . .	
				[C I](1–0)	106.972 ± 0.012	0.04 ± 0.04	1.1 ± 1.0	. . .	. . .
				CO(9–8)	225.375 ± 0.026	0.09 ± 0.06	0.6 ± 0.4	. . .	. . .
				CO(10–9)	250.386 ± 0.028	0.11 ± 0.09	0.6 ± 0.5	. . .	. . .
1mm.C10	. . .	1.9975 ± 0.0002	248 ± 44	CO(6–5)	230.682 ± 0.015	1.09 ± 0.22	5.9 ± 1.2	. . .	. . .
				CO(7–6)	269.106 ± 0.018	0.63 ± 0.17	2.5 ± 0.7	. . .	. . .
				[C I](2–1)	270.004 ± 0.018	0.47 ± 0.17	1.9 ± 0.7	. . .	. . .

Table 4.6: *(continued)*

ID 1mm (1)	ID 3mm (2)	z (3)	FWHM (km s^{-1}) (4)	Line (5)	Frequency (GHz) (6)	S^V (Jy km s^{-1}) (7)	L' (10^9 K km s^{-1} pc^2) (8)	r_{J1} (9)	r_{J2} (10)
1mm.C12	3mm.15	1.0963 ± 0.0001	235 ± 50	CO(2–1)	109.975 ± 0.008	0.19 ± 0.04	3.0 ± 0.6	· · ·	· · ·
				CO(4–3)	219.934 ± 0.016	0.13 ± 0.06	0.5 ± 0.3	· · ·	0.18 ± 0.09
				[C I](1–0)	234.779 ± 0.016	0.11 ± 0.07	0.4 ± 0.2	· · ·	· · ·
1mm.C13	3mm.10	1.0364 ± 0.0001	380 ± 42	CO(2–1)	113.207 ± 0.007	0.49 ± 0.06	7.1 ± 0.9	· · ·	· · ·
				CO(4–3)	226.396 ± 0.013	0.82 ± 0.10	3.0 ± 0.4	· · ·	0.42 ± 0.07
				[C I](1–0)	241.678 ± 0.014	0.35 ± 0.11	1.1 ± 0.4	· · ·	· · ·
1mm.C14a	· · ·	1.9966 ± 0.0003	332 ± 64	CO(6–5)	230.755 ± 0.021	0.35 ± 0.11	1.9 ± 0.6	0.18 ± 0.09	· · ·
				CO(7–6)	269.191 ± 0.025	0.42 ± 0.10	1.7 ± 0.4	0.16 ± 0.07	· · ·
				[C I](2–1)	270.089 ± 0.025	0.28 ± 0.09	1.1 ± 0.4	· · ·	· · ·
				CO(1–0)	38.468 ± 0.004	0.05 ± 0.02	10.7 ± 4.2	· · ·	· · ·
1mm.C16	3mm.06	1.0952 ± 0.0001	275 ± 27	CO(2–1)	110.029 ± 0.004	0.32 ± 0.03	5.2 ± 0.5	· · ·	· · ·
				CO(4–3)	220.042 ± 0.008	0.49 ± 0.07	2.0 ± 0.3	· · ·	0.38 ± 0.06
				[C I](1–0)	234.894 ± 0.009	0.21 ± 0.06	0.7 ± 0.2	· · ·	· · ·
1mm.C15	3mm.02	1.3167 ± 0.0001	266 ± 19	CO(2–1)	99.512 ± 0.003	0.37 ± 0.03	8.4 ± 0.6	· · ·	· · ·
				[C I](1–0)	212.442 ± 0.006	0.18 ± 0.12	0.9 ± 0.6	· · ·	· · ·
				CO(5–4)	248.747 ± 0.007	0.69 ± 0.08	2.5 ± 0.3	· · ·	0.30 ± 0.04
1mm.C19	3mm.12	2.5739 ± 0.0002	254 ± 43	CO(3–2)	96.756 ± 0.006	0.14 ± 0.02	4.6 ± 0.8	0.43 ± 0.18	· · ·
				CO(7–6)	225.707 ± 0.014	0.17 ± 0.06	1.1 ± 0.4	0.10 ± 0.05	· · ·
				[C I](2–1)	226.460 ± 0.014	-0.03 ± 0.06	-0.2 ± 0.4	· · ·	· · ·
				CO(8–7)	257.926 ± 0.016	-0.07 ± 0.09	-0.4 ± 0.4	-0.03 ± 0.04	· · ·
				CO(1–0)	32.254 ± 0.002	0.04 ± 0.01	10.7 ± 4.0	· · ·	· · ·
1mm.C20	· · ·	1.0931 ± 0.0002	287 ± 83	CO(2–1)	110.140 ± 0.013	0.12 ± 0.05	2.0 ± 0.8	· · ·	· · ·
				CO(4–3)	220.264 ± 0.026	0.09 ± 0.10	0.4 ± 0.4	· · ·	0.19 ± 0.22
				[C I](1–0)	235.131 ± 0.028	0.38 ± 0.11	1.3 ± 0.4	· · ·	· · ·
1mm.C25	3mm.14	1.0982 ± 0.0002	289 ± 65	CO(2–1)	109.874 ± 0.010	0.24 ± 0.05	3.9 ± 0.8	· · ·	· · ·
				CO(4–3)	219.732 ± 0.020	0.29 ± 0.11	1.2 ± 0.4	· · ·	0.30 ± 0.13
				[C I](1–0)	234.564 ± 0.021	-0.03 ± 0.12	-0.1 ± 0.4	· · ·	· · ·
1mm.C23	3mm.08	1.3821 ± 0.0000	50 ± 7	CO(2–1)	96.778 ± 0.001	0.11 ± 0.01	2.7 ± 0.3	· · ·	· · ·
				CO(5–4)	241.912 ± 0.002	-0.01 ± 0.06	-0.0 ± 0.2	· · ·	-0.02 ± 0.09
1mm.C30	· · ·	0.4580 ± 0.0001	176 ± 36	CO(3–2)	237.170 ± 0.012	0.43 ± 0.08	0.5 ± 0.1	· · ·	· · ·
· · ·	3mm.11	1.0964 ± 0.0000	44 ± 7	CO(2–1)	109.970 ± 0.001	0.07 ± 0.01	1.2 ± 0.2	· · ·	· · ·
				CO(4–3)	219.924 ± 0.002	0.12 ± 0.03	0.5 ± 0.1	· · ·	0.40 ± 0.11

Table 4.6: *(continued)*

ID 1mm (1)	ID 3mm (2)	z (3)	FWHM ($\mathrm{km\,s^{-1}}$) (4)	Line (5)	Frequency (GHz) (6)	S^V ($\mathrm{Jy\,km\,s^{-1}}$) (7)	L' ($10^9\ \mathrm{K\,km\,s^{-1}\,pc^2}$) (8)	r_{J1} (9)	r_{J2} (10)
				[C I](1–0)	234.769 ± 0.002	0.08 ± 0.03	0.3 ± 0.1	…	…
…	3mm.09	2.6976 ± 0.0001	165 ± 22	CO(3–2)	93.520 ± 0.003	0.38 ± 0.05	13.9 ± 1.7	1.09 ± 0.27	…
				CO(7–6)	218.158 ± 0.007	0.14 ± 0.58	1.0 ± 3.9	0.08 ± 0.31	…
				[C I](2–1)	218.885 ± 0.007	0.78 ± 0.63	5.3 ± 4.2	…	…
				CO(1–0)	31.175 ± 0.001	0.04 ± 0.01	12.8 ± 2.7	…	…
Faint.1mm.C20	3mm.16	1.2938 ± 0.0001	144 ± 32	CO(2–1)	100.504 ± 0.005	0.09 ± 0.02	1.9 ± 0.4	…	…
				[C I](1–0)	214.559 ± 0.010	-0.09 ± 0.12	-0.4 ± 0.6	…	…
				CO(5–4)	251.225 ± 0.012	0.15 ± 0.11	0.5 ± 0.4	…	0.28 ± 0.21
…	MP.3mm.2	1.0873 ± 0.0001	115 ± 33	CO(2–1)	110.448 ± 0.005	0.15 ± 0.04	2.3 ± 0.6	…	…
				CO(4–3)	220.878 ± 0.010	0.12 ± 0.08	0.5 ± 0.3	…	0.21 ± 0.15
				[C I](1–0)	235.788 ± 0.011	0.13 ± 0.10	0.5 ± 0.3	…	…

Notes. (1) ASPECS-LP 1mm ID. (2) ASPECS-LP 3mm ID. (3) Redshift. (4) Line full width at half maximum (FWHM). (5) Line identification. (6) Observed line frequency. (7) Integrated line flux, $S^V = \int S_\nu dv$ (sometimes called $S\Delta v$). (8) Line luminosity (Equation 4.2). (9) Line luminosity ratio with CO(1–0) (Equation 4.3). (10) Line luminosity ratio with CO(2–1).

5 | The ALMA Spectroscopic Survey in the HUDF: Multiband constraints on line-luminosity functions and the cosmic density of molecular gas

Abstract

We present a CO and atomic fine-structure line-luminosity function analysis using the ALMA Spectroscopic Survey in the *Hubble* Ultra Deep Field (ASPECS). ASPECS consists of two spatially overlapping mosaics that cover the entire ALMA 3 mm and 1.2 mm bands. We combine the results of a line-candidate search of the 1.2 mm data cube with those previously obtained from the 3 mm cube. Our analysis shows that $\sim$ 80% of the line flux observed at 3 mm arises from CO(2–1) or CO(3–2) emitters at $z = 1 - 3$ ('cosmic noon'). At 1.2 mm, more than half of the line flux arises from intermediate-J CO transitions ($J_{\rm up} = 3 - 6$); $\sim$ 12% from neutral carbon lines; and $<$ 1% from singly-ionized carbon, [C II]. This implies that future [C II] intensity mapping surveys in the epoch of reionization will need to account for a highly significant CO foreground. The CO luminosity functions probed at 1.2 mm show a decrease in the number density at a given line luminosity (in units of L') at increasing $J_{\rm up}$ and redshift. Comparisons between the CO luminosity functions for different CO transitions at a fixed redshift reveal subthermal conditions on average in galaxies up to $z \sim 4$. In addition, the comparison of the CO luminosity functions for the same transition at different redshifts reveals that the evolution is not driven by excitation. The cosmic density of molecular gas in galaxies, $\rho_{\rm H_2}$, shows a redshift evolution with an increase from high redshift up to $z \sim 1.5$ followed by a factor $\sim$ 6 drop down to the present day. This is in qualitative agreement with the evolution of the cosmic star formation rate density, suggesting that the molecular gas depletion time is approximately constant with redshift, after averaging over the star-forming galaxy population.

R. Decarli, M. Aravena, L. A. Boogaard, C. Carilli, J. González-López, F. Walter, *et al.*
The Astrophysical Journal, 902, 110 (2020)

5.1 Introduction

Stars form in the dense, molecular phase of the interstellar medium (ISM; see, e.g., reviews in Kennicutt & Evans 2012, Carilli & Walter 2013, Dobbs et al. 2014, Combes 2018, Tacconi et al. 2020, and Hodge & da Cunha 2020). Molecular gas is thus a key ingredient of galaxy formation, and it plays a critical role in shaping the history of cosmic star formation (e.g., Lilly et al., 1995; Madau et al., 1996; Hopkins & Beacom, 2006; Madau & Dickinson, 2014). Gauging the amount of molecular gas in galaxies available for star formation, as well as its physical conditions and excitation properties, is thus pivotal in our understanding of the formation and evolution of galaxies. For instance, the cosmic star formation rate density, $\rho_{\rm SFR}$, may result from an evolution of the amount of molecular gas stored in galaxies, averaged over cosmological volume, $\rho_{\rm H_2}$, or from an evolution in the efficiency at which molecular gas is converted into stars (as set by the inverse of the depletion time, $t_{\rm dep}$, i.e., the timescale required for the galaxy to exhaust its current gaseous reservoirs, under the assumption that stars keep forming at the current rate), or by a combination of both.

Molecular hydrogen, H_2, is a poor radiator (e.g., Omont, 2007); therefore, observations of the molecular phase of the ISM typically rely on other molecules, in particular the carbon monoxide, $^{12}C^{16}O$ (hereafter, CO), which is abundant in the star-forming ISM and efficiently radiates via rotational transitions even at modest excitation energies (corresponding to excitation temperatures of a few tens of K, as observed in the cold, star-forming medium). Low-J CO transitions ($J_{\rm up} \lesssim 4$) have rest-frame frequencies, ν_0, of 100–500 GHz (rest wavelength $\lambda_0 = 0.6$ mm–3 mm), and are often used to gauge the mass in molecular gas, as their luminosity is only modestly dependent on the gas physics (in particular, excitation temperature and density). Intermediate-J CO transitions ($5 \lesssim J_{\rm up} \lesssim 7$; $\nu_0 = 500-900$ GHz, $\lambda_0 = 0.3-0.6$ mm) and high-J CO transitions ($J_{\rm up} \gtrsim 8$, $\nu_0 > 900$ GHz), on the other hand, owe their luminosity to the higher excitation, warmer or denser medium—thus they are better tracers of starbursting activity, nuclear activity, or shocks (see discussions in, e.g., Weiss et al., 2007a; Carilli & Walter, 2013; Daddi et al., 2015; Kamenetzky et al., 2018; Boogaard et al., 2020).

Surveys of molecular gas in high-redshift galaxies are blossoming thanks to the unprecedented observational capabilities offered by the Jansky Very Large Array (VLA), the IRAM NOrthern Expanded Millimeter Array (NOEMA), and the Atacama Large Millimeter Array (ALMA). The number of CO-detected galaxies at $z > 0.5$ has increased significantly in the last few years, and now exceeds 250 (see, e.g., the compilation in Tacconi et al., 2018). Most of these detections come from targeted investigations, i.e., investigations of the molecular content of known galaxies preselected based on their redshift, stellar mass, far-infrared luminosity, star formation rate (SFR), nuclear activity, apparent luminosity, etc. These studies have been instrumental in effectively establishing empirical relations between gas content and a number of galaxy properties (e.g., Greve et al., 2005; Daddi et al., 2010b; Tacconi et al., 2010, 2013, 2018; Aravena et al., 2012; Genzel et al., 2010, 2011, 2015; Bothwell et al., 2013; Dessauges-Zavadsky et al., 2017).

Molecular scans, i.e., interferometric observations of blank fields over a wide frequency range at millimeter wavelengths, represent a powerful complementary approach. By searching for molecular gas emission irrespective of the position and redshift, they effectively result in a line flux-limited survey of a well-defined cosmological volume, and do not depend on any preselection. The first molecular scan that reached sufficient depth to secure CO detections in typical galaxies at $z > 1$ came from a $>$ 100-hr long campaign targeting a $\sim$ 1 arcmin^2 region of the *Hubble* Deep Field North (Williams et al., 1996) in the 3 mm band using the IRAM/Plateau de Bure Interferometer (PdBI; Walter et al., 2012, 2014; Decarli et al., 2014). The ALMA Spectroscopic Survey in the *Hubble* Ultra Deep Field, ASPECS, built on the success of the PdBI program by performing two frequency scans at 3 mm and 1.2 mm. The ASPECS-Pilot program (Walter et al., 2016; Aravena et al., 2016b,c; Decarli et al., 2016a,b; J. Bouwens et al., 2016; Carilli et al., 2016) offered a first glimpse at the molecular gas content in galaxies residing in one of the best-studied regions of the extragalactic sky, the *Hubble* Ultra Deep Field (Beckwith et al., 2006). The ASPECS-Pilot survey was then expanded into an ALMA Large Program (LP) targeting a 4.6 arcmin^2 area, with the same survey strategy (González-López et al., 2019, 2020; Decarli et al., 2019; Boogaard et al., 2019, 2020; Aravena et al., 2019, 2020; Popping et al., 2019, 2020; Uzgil et al., 2019; Magnelli et al., 2020; Inami et al., 2020; Walter et al., 2020). Among other results, ASPECS provided robust constraints on the low-J CO luminosity functions up to $z \sim 4$, and an estimate of the evolution of the cosmic density of molecular gas in galaxies, $\rho_{\mathrm{H}_2}(z)$. A follow-up program dubbed VLASPECS used the NSF's Karl G. Jansky Very Large Array, VLA, to secure 30.6–38.7 GHz coverage over part of the ASPECS footprint, thus providing a low-J anchor to CO excitation models for galaxies by directly measuring CO(1–0) luminosities in the redshift range $z = 2.0 - 2.7$ (Riechers et al., 2020).

Other molecular scan efforts appeared in the literature in the last couple of years: The COLDz survey used $>$ 320 hr of the VLA time to sample CO(1–0) emission at $z \approx 2 - 3$ ('cosmic noon') as well as CO(2–1) at $z \approx 5 - 7$ over $\sim$ 60 arcmin^2 in parts of the COSMOS (Scoville et al., 2007) and GOODS-North (Giavalisco et al., 2004) fields (Pavesi et al., 2018; Riechers et al., 2019, 2020). Lenkić et al. (2020) used the Plateau de Bure High-z Blue-Sequence Survey 2 (PHIBSS2) data (Tacconi et al., 2018) to search for serendipitous emission in the cubes, besides the central targets. These studies place first direct constraints on the CO luminosity function in galaxies at $z \sim 2$, and revealed a higher molecular content in galaxies at these redshifts compared to the local universe: $\rho_{\mathrm{H}_2}(z = 2 - 3) \approx (1 - 20) \times 10^7$ M$_\odot$ Mpc^{-3}. A few serendipitous molecular line detections have been reported in the the fields of sub-millimeter galaxies (Wardlow et al., 2018; Cooke et al., 2018), in an ALMA deep field around SSA22 (Hayatsu et al., 2017) and around graviational lensing clusters (Yamaguchi et al., 2017; González-López et al., 2017b). Finally, Klitsch et al. (2019) used the high signal-to-noise ratio (S/N) of mm-bright calibrators in the ALMA archive to search for CO absorption features. They do not detect any extragalactic source, which sets constraints on both the CO luminosity functions and $\rho_{\mathrm{H}_2}(z)$ up to $z \sim 1.7$. In addition to CO-based estimates, various studies have inferred molecular gas mass functions and $\rho_{\mathrm{H}_2}(z)$ via estimates based on the dust continuum, but this relies on an empirically-calibrated gas-to-dust conversion (e.g., Scoville et al., 2017; Liu et al., 2019; Magnelli et al., 2020).

In this paper, we capitalize on the completed ASPECS dataset in order to constrain the luminosity functions and average cosmic content of molecular gas in galaxies throughout cosmic time. First, we present the new 1.2 mm dataset (§ 5.2.1), the ancillary data (§ 5.2.2), and the approach adopted in the analysis (§ 5.3). Then, we complement the 1.2 mm dataset

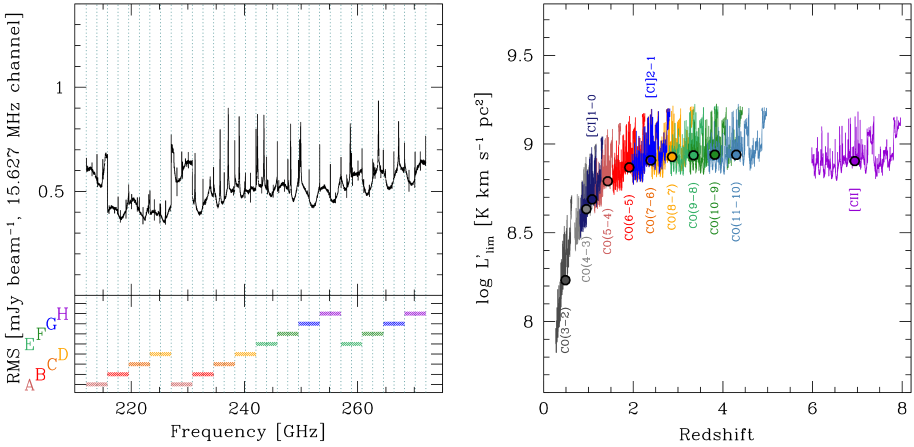

Figure 5.1: Sensitivity limits of the ASPECS 1.2 mm cube. *Left:* Channel rms as a function of frequency. For a 15.6 MHz channel, the typical rms is ~ 0.5 mJy beam^{-1} throughout the entire band. The frequency settings used in the observations (labeled A–H) and the edges of each spectral window are also marked. *Right:* Line-luminosity limits (in units of K km s^{-1} pc^{2}) as a function of redshift. Here we assume a 5σ limit for a line width of 200 km s^{-1}. The dots highlight the fiducial limit, obtained as the median sensitivity throughout the band.

with the information from the 3 mm part of ASPECS in a homogeneous analysis of molecular and atomic line emission from the cold ISM in high-redshift galaxies (§ 5.4). We present our conclusions in § 5.5. Throughout this paper we adopt a ΛCDM cosmological model with $H_0 = 70$ km s^{-1} Mpc^{-1}, $\Omega_{\rm m} = 0.3$ and $\Omega_\Lambda = 0.7$ (consistent with the measurements by the Planck Collaboration et al., 2016).

5.2 Observations

5.2.1 ALMA data

The ASPECS LP survey is an ALMA Cycle 4 Large Program comprising two bands, at 3 mm and 1.2 mm. The former is presented and discussed elsewhere (González-López et al., 2019; Decarli et al., 2019; Boogaard et al., 2019; Aravena et al., 2019; Popping et al., 2019; Uzgil et al., 2019; Inami et al., 2020). The latter consists of a mosaic of 85 pointings in the eXtremely Deep Field (XDF, Illingworth et al. 2013; also dubbed *Hubble* Deep Field 2012 or HUDF12, Koekemoer et al. 2013) for a total area of 4.2 arcmin^2 down to 10% sensitivity, or 2.9 arcmin^2 within the 50% primary beam response. The observing strategy involves covering the full mosaic area at each telescope visit. The pointings were arranged in classical hexagonal patterns at 11$''$ separation, which ensures Nyquist sampling throughout the entire frequency range of the observations and results in a spatially-uniform sensitivity throughout the majority of the footprint.

Table 5.1: Emission lines, corresponding redshift bins, volume-weighted average redshift, cosmic volume (in comoving units, within the area of $> 50\%$ sensitivity), and typical 5σ line-luminosity limit at $\langle z \rangle$, assuming a line width of 200 km s^{-1} in ASPECS LP 1.2 mm (observed range: 212–272 GHz).

Line (1)	Redshift (2)	$\langle z \rangle$ (3)	Volume (Mpc^3) (4)	limit L (10^7 L$_\odot$) (5)	limit L' (10^8 K km s^{-1} pc^2) (6)
CO(3–2)	0.2711–0.6306	0.49	921.3	0.023	1.710
CO(4–3)	0.6947–1.1740	0.96	2960.9	0.135	4.299
CO(5–4)	1.1183–1.7173	1.43	5106.3	0.378	6.174
CO(6–5)	1.5418–2.2606	1.91	6923.8	0.781	7.384
CO(7–6)	1.9651–2.8037	2.39	8470.4	1.358	8.088
CO(8–7)	2.3884–3.3467	2.87	9597.2	2.121	8.464
CO(9–8)	2.8115–3.8895	3.35	10478.0	3.085	8.647
CO(10–9)	3.2345–4.4321	3.82	11012.3	4.262	8.712
CO(11–10)	3.6574–4.9745	4.30	11371.6	5.660	8.696
$[\mathrm{C\,I}]_{1-0}$	0.8091–1.3207	1.08	3540.8	0.186	4.878
$[\mathrm{C\,I}]_{2-1}$	1.9750–2.8164	2.40	8509.3	1.374	8.102
$[\mathrm{C\,II}]$	5.9861–7.9619	6.94	12621.6	17.61	8.018

Observations were carried out in two parts, a first pass in 2017, March–April (roughly 20% of the total data volume spread among all of the requested frequency settings) and the remainder in 2018, May–July. The 2017 observations were collected with average weather conditions, with precipitable water vapour 2.5–3.0 mm; on the other hand, the 2018 observations were gathered in excellent weather conditions, with precipitable water vapour ~ 0.6 mm in most of the executions. The array was in compact, C40-1 or C40-2 configurations, with baselines in the range 15 m–320 m.

The observations sampled eight different frequency tunings, continuously encompassing the entire 212–272 GHz window (see Figure 5.1). Quasars J0329–2357, J0334–4008, J0348–2749, and J0522–3627 were employed as pointing, phase, amplitude, and bandpass calibrators.

We processed the raw data using the CASA calibration pipeline for ALMA (v.5.1.1; see McMullin et al., 2007). No additional flagging was applied. We inverted the visibilities using the task `tclean`, and adopting natural weighting. The resulting beam is $\sim 1.5'' \times 1.1''$. Along the spectral axis, the cube was resampled using 15.627 MHz wide channels (≈ 19 km s^{-1} at 242 GHz). Cleaning was performed down to 2σ per channel after putting cleaning boxes on all the sources with $S/N > 5$ in their continuum emission. We reach a sensitivity of ~ 0.5 mJy beam^{-1} per 15.627 MHz channel roughly constant throughout the 1.2 mm band (see Figure 5.1). We also created a continuum-subtracted version of the cube, after identifying and excluding the channels with the brightest emission lines (see González-López et al. 2020 for details). Finally, we created a tapered version of the cube, where we degrade the angular resolution by setting the `restoringbeam=2″` in the task `tclean`. We use this tapered cube to extract 1D spectra of the detected galaxies, following González-López et al. (2019).

5.2.2 Ancillary data

The targeted field lies in the *Hubble* Ultra Deep Field (HUDF), arguably the best studied extragalactic field in the sky. We employ the 3D-*HST* photometric catalog by Skelton et al. (2014), which relies on optical *Hubble*/Advanced Camera for Surveys data (Beckwith et al., 2006), deep near-infrared *Hubble*/Wide Field Camera 3 observations from the Cosmic Assembly Near-infrared Deep Extragalactic Legacy Survey (CANDELS; Grogin et al. 2011; Koekemoer et al. 2011), enriched with multiwavelength photometry and spectroscopy from various surveys (see Boogaard et al., 2019, and references therein). In particular, the MUSE *Hubble* Ultra Deep Survey (Bacon et al., 2017) provides integral field spectroscopy of a $3' \times 3'$ field (encompassing the whole HUDF) over the wavelength range 4750–9300 Å. More than 1500 galaxies have secured redshifts from MUSE (Inami et al., 2017), $\sim$ 700 of which are within the area of the ASPECS LP 1.2 mm mosaic with >50% primary beam response.

When comparing ALMA observations to other catalogs, we account for a known systematic astrometry offset ($\Delta\mathrm{RA} = +0.076''$, $\Delta\mathrm{Dec} = -0.279''$) between optical and mm/radio data (Rujopakarn et al., 2016; Dunlop et al., 2017).

5.3 Analysis and Results

5.3.1 Line search at 1.2 mm

We search for emission lines in the original and the continuum-subtracted ASPECS LP 1.2 mm cubes using FINDCLUMPS (Walter et al., 2016; Decarli et al., 2019; González-López et al., 2019). The code performs a floating average of channels over various kernel widths (with one channel corresponding to $\approx$ 19 km s^{-1} at the center of the bandwidth). Each averaged channel is searched for both positive and negative peaks. The S/N of a line candidate is computed as the ratio between the flux density measured at the centroid of the line candidate and the rms of the map used in the line identification. We refer to the line search results from the continuum-subtracted cube for line candidates that lie within 2″ from a bright continuum source from the compilation in González-López et al. (2020), and to the results from the original cube for anywhere else in the mosaic.

Positive peaks are a combination of signal from astrophysical sources and noise, while negative peaks are only due to noise. The latter are thus used to statistically infer the reliability or 'fidelity' of a line candidate, given its width (σ_{line}) and signal to noise (S/N):

$$\mathrm{Fidelity}(\mathrm{S/N}, \sigma_{\mathrm{line}}) = 1 - \frac{N_{\mathrm{neg}}(\mathrm{S/N}, \sigma_{\mathrm{line}})}{N_{\mathrm{pos}}(\mathrm{S/N}, \sigma_{\mathrm{line}})} \tag{5.1}$$

where $N_{\mathrm{pos,neg}}$ is the number of line candidates in a given S/N and σ_{line} bin. Only $\mathrm{S/N} > 4$ line candidates are considered in this analysis. For each line width bin, we fit the observed distribution of the noise peaks with the tails of a Gaussian function centered at zero, and the additional signal due to real sources as a power law. The fit is performed in two steps, first by modeling the negative distributions in σ_{line} bins, then by fitting the positive distributions capitalizing on the posterior parameters of the negative fits for the noise component of the

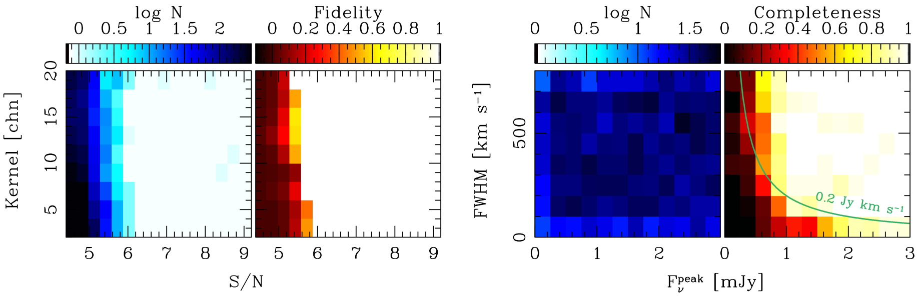

Figure 5.2: *First panel:* Number of observed (positive) line candidates from the line search as a function of S/N and kernel width that maximized the S/N of the line candidate in the line search. *Second panel:* Best fits of the fidelity dependence on S/N and kernel width. The fidelity of line candidate is close to unity at S/N $>$ 5.8, and drops rapidly to zero at S/N $<$ 5. The fidelity at a given S/N increases with increasing line widths, as expected because of the fewer independent noise realizations in the cubes. *Third panel:* Number of simulated lines injected in the cube for completeness assessments, as a function of line peak flux, $F_\nu^{\rm peak}$, and width (parametrized as FWHM). Only lines located within the footprint at $>$ 50% response in the cube. *Fourth panel:* Completeness of the line search. The completeness is $\gtrsim$ 90% for virtually any line with integrated flux larger than 0.2 Jy km s^{-1} (indicated by a green solid line) and peak fluxes of $>$ 1 mJy.

observed distributions. This allows us to mitigate limitations due to the low number of entries in some bins, while properly accounting for their statistical relevance. Following Pavesi et al. (2018), González-López et al. (2019), and Decarli et al. (2019), we conservatively treat these estimates of the fidelity as upper limits; e.g., in each realization of the luminosity functions, a line with a fidelity of 40% has up to 40% chance to be used in the analysis. The upper-right panel of Figure 5.2 show the behaviour of the fidelity as a function of the adopted kernel width (i.e., the number of channels that maximizes the S/N of a line candidates—this is a proxy of the line width) as well as of the integrated S/N of the line candidate. The fidelity is close to 100% for any line at S/N $>$ 6, and drops rapidly to zero between S/N $= 5-6$, with narrower lines being typically less reliable than broader lines with the similar total S/N. We refer the reader to Decarli et al. (2019) and González-López et al. (2019) for detailed discussions on the assessment of the line reliability. Finally, we adopt a fidelity of unity (not treated as an upper limit) for the high-significance line candidates associated with known sources for which we have clear 1.2 mm continuum counterparts, as well as a spectroscopic redshift from MUSE or from our 3 mm line search. These sources are studied in detail in Boogaard et al. (2020) and Aravena et al. (2020). The final catalog from the line search consists of 234 line candidates with fidelity $>$ 0.2, 75 with fidelity $>$ 0.5, and 35 with fidelity $>$ 0.8.

We estimate the completeness by injecting simulated emission lines with a range of input parameters into the observed data cube. We adopt a 3D Gaussian profile for mock lines. In the spatial dimension, we assume the position angle and width of the major and minor axes of the synthesized beam (i.e., sources are spatially unresolved). We run the line search on the cube, and then define the completeness as a function of the input line parameters as the ratio between the number of retrieved versus injected sources. As input parameters, we consider the right ascension, α; the declination, δ; the observed frequency, $\nu_{\rm obs}$; the line width along the spectral axis, FWHM $= 2\sqrt{2\ \ln 2}\ \sigma_{\rm line}$; the line peak intensity, $F_\nu^{\rm peak}$. Sources are distributed uniformly in the sampled parameter space (corresponding to the actual 3D coverage of ASPECS LP 1.2 mm mosaic in terms of α, δ, and $\nu_{\rm obs}$; and ranging between 0–800 km s^{-1} and 0–3 mJy in terms of FWHM and $F_\nu^{\rm peak}$). A total of 8000 mock lines were injected, $>$ 3000 of which reside within the area with $>$ 50% primary beam response. The bottom panels of Figure 5.2 show the number of injected lines as a function of FWHM and $F_\nu^{\rm peak}$, and the associated completeness in bins of 100 km s^{-1} and 0.25 mJy in line width and peak flux. The other free parameters in our simulation do not appear to significantly affect the completeness of the line search (after accounting for the primary beam response). We drop all line candidates with a completeness of < 0.2 from our analysis. The median correction due to completeness is $<$ 30%.

5.3.2 Line fluxes

For each line candidate, we extract a 1-D spectrum from the pixel where the line spatial centroid is found. We then fit the extracted spectrum with a continuum and a Gaussian profile, using our custom Bayesian Monte Carlo Markov Chain procedure, using FINDCLUMPS results as priors (see Decarli et al., 2019).

As we push our search towards the detection limit of our survey, we might tend to preferentially pick sources that appear brighter than they are due to noise fluctuations. We investigate the impact of flux boosting by comparing the injected and recovered fluxes of mock lines (see § 5.3.1 for details on the line simulations). Figure 5.3 compares the measured versus injected fluxes as a function of the detection S/N. The measured flux is typically within 30% of the input flux (at 1σ) in the $4.5 < \mathrm{S/N} < 7$ regime. Flux boosting appears to be significant (i.e., the recovered flux exceeds 3σ of the distribution width)[40] in $\approx$ 10% of sources with S/N $<$ 5, and $\sim$ 1% of the sources at S/N $>$ 6. Because of the modest fidelity of sources with S/N $<$ 5.8, we consider flux boosting negligible for the purpose of our analysis.

5.3.3 Line identification and redshifts

Sources with a near-infrared counterpart

Table 5.1 lists the transitions we are sensitive to, in various redshift bins.[41] In order to identify the rest-frame transition associated with a given line candidate, we first cross-match our line candidate compilation with catalogs from ancillary data (see § 5.2.2). All the entries in our galaxy catalog have a redshift estimate (with a wide range of accuracy, from very high for MUSE-identified sources with several bright emission lines to very poor for faint, photometric dropouts detected only in a handful of broad band filters). For each line candidate,

---

[40] The impact of flux boosting is likely larger for spatially-extended sources (see, e.g. Pavesi et al., 2018). However, our analysis assumes unresolved emission in the tapered cube for all of the sources.

[41] The ASPECS LP 1.2 mm coverage formally includes also the CO(2–1) transition at $z < 0.0874$. However, the sampled volume within this redshift range is $\sim 3.9 \times 10^{-4}$ Mpc^3, insufficient for this analysis.

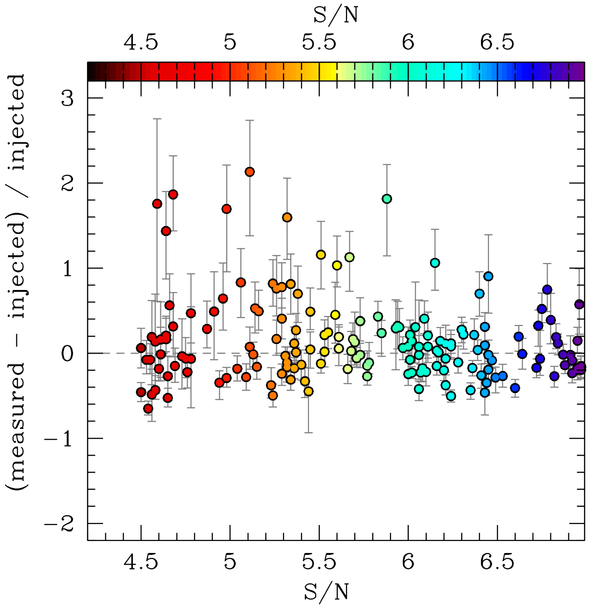

Figure 5.3: The impact of flux boosting on our analysis, estimated by comparing the injected and measured fluxes of mock lines. Small symbols show a random subset of individual mock lines, larger symbols are median values in bins of ΔS/N = 0.5. Flux boosting affects the flux measurement of $\approx$ 10% of lines at S/N < 5, and is completely negligible at S/N > 6.

we consider as potential counterpart sources within 1″ from the line spatial centroid. We identify the transition as the one that would yield the closest line redshift, $z_{\rm line}$, to the one reported in the ancillary catalog, $z_{\rm cat}$. We consider good matches line candidates that are found within 1″ from a known optical/near-infrared counterpart, and with a redshift separation of $|\delta z| = |z_{\rm cat} - z_{\rm line}|/(1 + z_{\rm line}) < 0.1$ (0.01 for sources with a spectroscopic redshift). All of the fidelity > 0.8 lines in the search have a clear counterpart (see Figure 5.4).

Ignoring the effects of gravitational lensing, we can estimate the impact of chance associations (i.e., the probability of intersecting a galaxy at a random point in our datacube) as:

$$P(\text{chance}) = \sum_i \frac{A_{\rm beam}}{A_{\rm footprint}} \, \frac{2\sigma_z}{(1+z)\,\Delta z_i} \tag{5.2}$$

where $A_{\rm beam}$ and $A_{\rm footprint}$ are the areas of the synthesized beam and of the ASPECS LP 1.2 mm footprint, respectively; σ_z is the uncertainty in the redshift, which we assume to be 0.1; Δz_i is the redshift coverage of ASPECS LP 1.2 mm in transition i; and the index i runs through the various transitions considered in our analysis. After summing over all of the transitions, we find that the probability of chance association is ~ 4.3%, i.e., from all the line candidates with a counterpart entering our analysis, only a handful of chance associations are expected (and virtually zero if one considers spectroscopic redshift uncertainties instead).

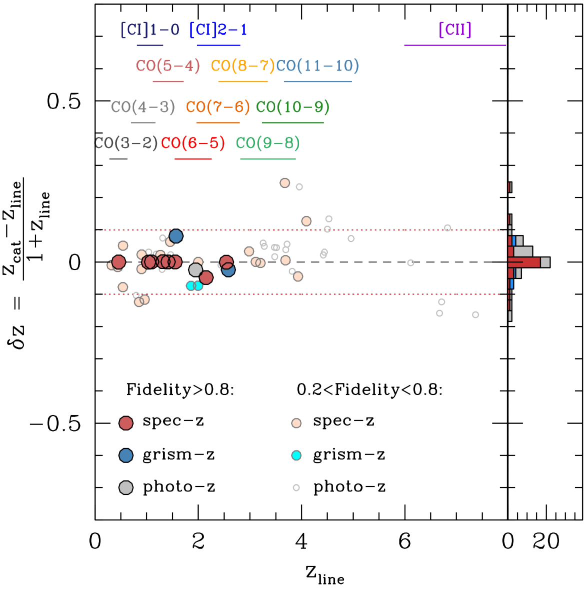

Figure 5.4: Redshift match from the line search in the ASPECS LP 1.2 mm mosaic, z_{line}, and the ancillary catalog values, z_{cat}, based on the 3D-HST catalog (Skelton et al., 2014), augmented with the most up to date spectroscopic information (see § 5.2.2 for details). We consider good matches cases where $|\delta z| < 0.1$ (< 0.01 for sources with spectroscopic redshifts). All of the high fidelity lines have a matching redshift in the catalog. The redshift ranges mapped by the various transitions considered in this work are marked as horizontal bars.

Figure 5.5 shows a pie chart of the fidelity-corrected total flux of all the line candidates with an optical/near-infrared counterpart and with fidelity > 0.5. The 3 mm flux distribution is dominated by CO(2–1) (53%) and CO(3–2) (27%), observed at $z = 1 - 3$, while higher-J lines contribute progressively less [CO(4–3): 10%; CO(5–4): 7%; CO(6–5): 3%]. On the other hand, more than half of the total flux measured in lines (62%) in the ASPECS LP 1.2 mm mosaic comes from intermediate-J CO transitions ($3 \leq J_{\text{up}} \leq 6$); 25% arises from higher-J CO transitions; 12% from [C I]; and less than 1% from [C II]. The uncertainties on these fractions are of ∼ 25% for the CO lines, and ∼ 50% for the carbon lines, as estimated from the Poissonian uncertainties. The fact that the contribution of [C II] flux to the total line flux is < 1% in band 6 implies significant challenges for intensity mapping experiments of [C II] emission in the epoch of reionization (e.g., Crites et al., 2014; Lagache et al., 2018; Sun et al., 2018; Yue et al., 2015; Yue & Ferrara, 2019; Chung et al., 2020) as the signal will be dominated by CO foreground emission.

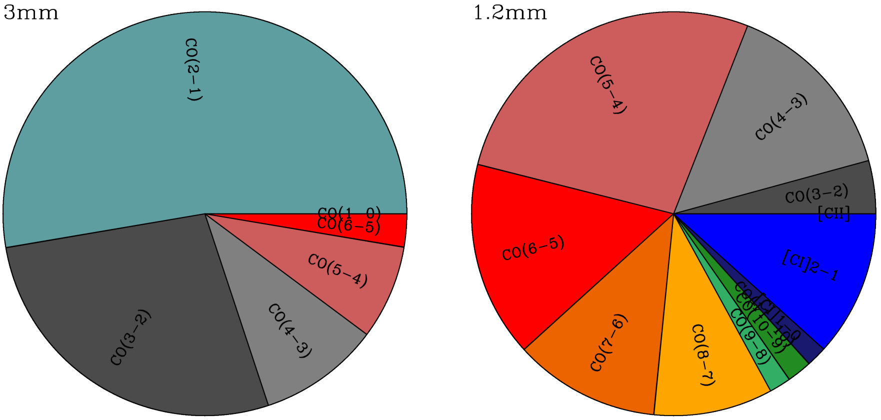

Figure 5.5: Pie charts of the fidelity-corrected flux distribution of the lines detected in the ASPECS LP 3 mm (*left*) and 1.2 mm (*right*) cubes. The 3 mm cube is dominated by low-J CO transitions observed at $z = 1 - 3$. At 1.2 mm, about 62% of the total line emission arises from CO transitions with intermediate $J = 3 - 6$. Higher-J transitions account for 25% of the total line flux in the 1.2 mm band. The two [C I] lines account for $\sim$ 12% of the total line emission, while [C II] contributes $<$ 1%.

Sources without a near-infrared counterpart

The identification of lines without an optical/near-infrared counterpart (roughly 1/3 of the line candidates with fidelity > 0.8) is done via a bootstrap approach, following, e.g., Decarli et al. (2019). Here we assume that the probability distribution of a line identification is proportional to the volume sampled in each transition, scaled by a weight set to be equal to $r_{J1} = (0.46, 0.25, 0.12, 0.04)$ for $J_{\rm up} = (3, 4, 5, 6)$, and to 0.01, 0.05 and 0.003 for $J_{\rm up} > 6$, $[\text{C I}]_{1-0}$ and $[\text{C I}]_{2-1}$, respectively. These weights have been derived from the average CO spectral energy distribution derived for the ASPECS sources by Boogaard et al. (2020). The weights for [C I] lines are defined based on a fiducial flux ratio between [C I] lines and neighboring CO transitions (see, e.g., Walter et al., 2011; Boogaard et al., 2020). Finally, we do not include [C II], based on the flux distribution shown in Figure 5.5 and the analyses presented in B. Uzgil, et al. (in prep.) and Loiacono et al. (2020). We discuss different choices of assigning CO transtions (i.e., redshifts) to sources with no near-infrared counterpart in § 5.C.

5.3.4 Line luminosities and molecular gas masses

Line fluxes are transformed into luminosities following, e.g., Carilli & Walter (2013):

$$\frac{L'}{\rm K\,km\,s^{-1}\,pc^2} = \frac{3.257\times10^7}{1+z}\,\frac{F_{\rm line}}{\rm Jy\,km\,s^{-1}}\left(\frac{\nu_0}{\rm GHz}\right)^{-2}\left(\frac{D_{\rm L}}{\rm Mpc}\right)^2 \qquad (5.3)$$

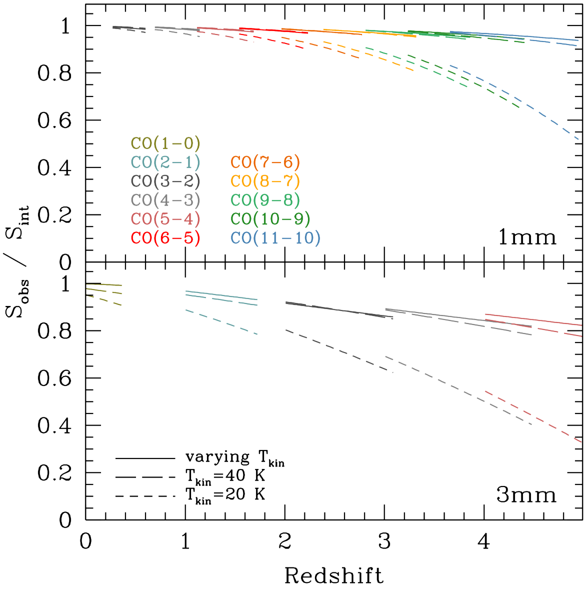

Figure 5.6: The effect of the CMB on the observed line fluxes. The correction is computed under the assumption of local thermal equilibrium, for different values of the gas kinetic temperature, $T_{\rm kin} = 20\,$K, 40 K, and for a redshift-dependent description as in Magnelli et al. (2014). The correction is always $\lesssim 20\%$ up to $z \sim 3$ for any $T_{\rm kin} > 20\,$K, and $< 10\%$ up to $z \sim 5$ for any $T_{\rm kin} > 40\,$K.

where $F_{\rm line}$ is the integrated line flux, ν_0 is the rest-frame frequency of the line, and $D_{\rm L}$ is the luminosity distance. We also compute line luminosities in solar units as:

$$\frac{L}{{\rm L}_\odot} = \frac{1.04 \times 10^3}{1+z} \frac{F_{\rm line}}{\rm Jy\,km\,s^{-1}} \frac{\nu_0}{\rm GHz} \left(\frac{D_{\rm L}}{\rm Mpc}\right)^2 . \tag{5.4}$$

As our observations probe the rest-frame far-infrared wavelengths of high-redshift galaxies, the Cosmic Microwave Background (CMB) might have an impact on the observed line fluxes. It provides an extra contribution to excitation temperature of the lines, but it also represents a background against which sources are observed. We follow the formalism presented in da Cunha et al. (2013) to compute the correction between the observed versus intrinsic line fluxes. The correction depends on the intrinsic excitation temperature in the gas. Here we assume local thermal equilibrium ($T_{\rm kin} = T_{\rm exc}$). Figure 5.6 shows the correction terms for two fixed temperature values $T_{\rm kin} = 20, 40\,$K, and for a redshift-dependent $T_{\rm kin}$ following the dust temperature evolution presented in Magnelli et al. (2014). We find that the correction is always $< 20\%$ for any temperature of interest $T_{\rm kin} > 20\,$K, up to $z \sim 3$, and $< 10\%$ for any $T_{\rm kin} > 40\,$K, for all the 1.2 mm CO lines. In Figure 5.6 we also show that the correction would be larger for lines observed at 3 mm, but still $< 20\%$ at any $z \lesssim 4$ for $T_{\rm kin} = 40\,$K. Because the exact correction depends on the (unknown) excitation temperature of the gas in our sources and on the (unverified) validity of the local thermal equilibrium, and given how small the corrections are, we opt not to apply any CMB-related correction in the remainder of our analysis.

The lower-J CO transitions are converted into CO(1–0) luminosities by adopting the CO[J-(J-1)]-to-CO(1–0) luminosity ratios, r_{J1}, from the analysis of the CO excitation in CO-detected galaxies in ASPECS LP by Boogaard et al. (2020): L' [CO(1–0)] = L'/r_{J1}, with $r_{J1} = \{0.75\pm0.11, 0.46\pm0.07, 0.31\pm0.07\}$, for $J_{\rm up} = \{2, 3, 4\}$. We also correct the results from ASPECS LP 3 mm (Decarli et al., 2019) accordingly for galaxies at $z < 2$. At higher redshifts, we adopt $r_{J1} = \{0.80 \pm 0.14, 0.61 \pm 0.13\}$, for $J_{\rm up} = \{3, 4\}$. As discussed in Boogaard et al. (2020), the redshift dependence reflects the higher IR luminosity and IR surface brightness in the higher-redshift ASPECS LP sample (see also Aravena et al., 2020). We are consistent within uncertainties with the measurements of individual sources. As in Decarli et al. (2019), we include bootstrapped realizations of the uncertainties on r_{J1} in the conversion.

Finally, the CO(1–0) luminosities are converted into corresponding H$_2$ mass: $M_{\rm H_2} = \alpha_{\rm CO}\, L'_{\rm CO(1--0)}$ (see Bolatto et al., 2013, for a review). The bulk of the flux emission in our observations arises from typical galaxies with close-to-solar metallicity (Boogaard et al., 2019; Aravena et al., 2019, 2020), for which a Galactic conversion factor should apply. Following the literature consensus, we adopt $\alpha_{\rm CO} = 3.6\,{\rm M}_\odot\,({\rm K\,km\,s^{-1}\,pc^2})^{-1}$ (e.g., Daddi et al., 2010b). All the results based on $\alpha_{\rm CO}$ would scale linearly if a different (but constant) value is adopted.

Atomic carbon transitions can also be used to infer constraints on the gas mass (see, e.g., Weiß et al., 2005; Walter et al., 2011; Alaghband-Zadeh et al., 2013; Bothwell et al., 2017; Popping et al., 2017b; Valentino et al., 2018). In the assumption of optically-thin line emission, the luminosity of the two [C I] transitions is related to the mass in neutral carbon as follows:

$$M_{\rm [C\,I]}/{\rm M}_\odot = 5.706\times10^{-4}\,\frac{Q_{\rm ex}}{3}\,e^{23.6/T_{\rm ex}}\,L'_{\rm [C\,I]\,1-0} \tag{5.5}$$

$$M_{\rm [C\,I]}/{\rm M}_\odot = 5.273\times10^{-3}\,\frac{Q_{\rm ex}}{5}\,e^{62.5/T_{\rm ex}}\,L'_{\rm [C\,I]\,2-1} \tag{5.6}$$

where $Q_{\rm ex} = 1 + 3\,e^{-23.6/T_{\rm ex}} + 5\,e^{-62.5/T_{\rm ex}}$ is the partition function, $T_{\rm ex}$ is the excitation temperature in K, and line luminosities are quoted in units of K km s^{-1} pc^2. The mass estimates in Equation 5.5 and Equation 5.6 can be related to the molecular gas mass, under the assumption that all of the carbon is in neutral form. Assuming an abundance ratio $[{\rm C\,I}]/[{\rm H_2}] = 1.9\times10^{-5}$ (Boogaard et al. 2020, consistent with the $10^{-4.8\pm0.2}$ value reported by Valentino et al. 2018), we obtain $M_{\rm H_2} = M_{\rm [C\,I]}/(6\,[{\rm C\,I}]/[{\rm H_2}])$, where the factor of six accounts for the mass ratio between molecular Hydrogen and the carbon atom. In our analysis, we assume $T_{\rm ex} = 29\pm6$ K (Walter et al., 2011).

The [C I] transitions have a number of advantages as molecular gas masses. In particular, $M_{\rm [C\,I]}$ in Equation 5.5 is nearly linear with $L'_{\rm [C\,I]\,1-0}$ for $T_{\rm ex} \gtrsim 15$ K (a realistic scenario at high redshift), and optical depth is virtually never an issue once averaged over galactic scales. In principle, the mass estimates inferred via Equation 5.5 and Equation 5.6 are lower limits on $M_{\rm H_2}$, because of the assumption that all of the carbon is in neutral form; however, the same assumption is usually at the root of the abundance estimates, i.e., the uncertainty cancels out. An additional caveat to consider is that, because [C I] is mostly optically thin, these [C I]-based mass estimates are more sensitive to assumptions on carbon abundance and to the fraction of [C I] emitted from the neutral versus molecular medium than CO-based estimates.

5.3.5 Luminosity functions and $\rho_{\rm H_2}$

In the construction of the CO luminosity functions, we follow the approach adopted in Decarli et al. (2019). Namely, we create 5000 realizations of the luminosity functions, folding in all of the uncertainties: formal flux measurement errors from the Gaussian fit, the uncertainties in the line identification (and the implications in terms of luminosity distance), the probability of a line to be spurious (as quantified via the fidelity), etc. In each realization, we keep only a subset of line candidates, based on their fidelity: We extract a number between 0 and 1 from a uniform distribution, and if the value is smaller than the line fidelity, we keep the line candidate in that realization. The resulting catalogs of lines are binned in luminosity, using 0.5 dex bins. Poissonian uncertainties are estimated for each bin, following Gehrels (1986). The number of entries and its uncertainties are then scaled to account for completeness and divided by the effective volume of the survey. Following Riechers et al. (2019) and Decarli et al. (2019), we create five versions of the luminosity functions, shifted by 0.1 dex one from the other, in order to expose the intra-bin variations despite the modest statistics in each bin. The luminosity functions (and their uncertainties) thus obtained are then averaged among all the realizations.

Figure 5.7 shows the resulting luminosity functions for each transition considered in this study: CO $J_{\rm up} = 1$ to 4, and [C I]$_{1-0}$ from 3 mm, and CO $J_{\rm up} = 3$ to 10, [C I]$_{1-0}$, [C I]$_{2-1}$, as well as [C II]. Tabulated values are reported in § 5.A. We limit our analysis to line candidates brighter than the formal 5σ limit (see Figure 5.1 and Table 5.1), and we only plot bins that are fully accommodated above this luminosity threshold and have an average of at least one entry throughout the realizations.

Finally, we convert the CO(1–0)–CO(4–3) line luminosities observed in either ASPECS band into H_2 masses as described in the previous subsection, we sum over the line candidates used in each realization of the luminosity function, and thus we infer the total molecular gas per cosmological volume, $\rho_{\rm H_2}$ (see Table 5.2). We remark that in the estimate of $\rho_{\rm H_2}$, we do not extrapolate the LFs outside the observed line-luminosity ranges, but rather sum over the individual detections (corrected for fidelity and completeness).

5.4 Discussion

5.4.1 CO luminosity functions

Figure 5.7 shows the constraints on the luminosity functions for all the transitions covered in our analysis. Multiple lines are identified for all the mid-J CO transitions (up to $J_{\rm up} = 7$). The CO(8–7) line is securely detected only in one case in the entire ASPECS volume. None of the higher-J CO lines is significantly detected individually, thus only low-fidelity candidates enter the luminosity function analysis for these transitions. Since our line-luminosity limit (in units of L') is rather flat with redshift at $z > 1$ (see Figure 5.1), this result per se can be

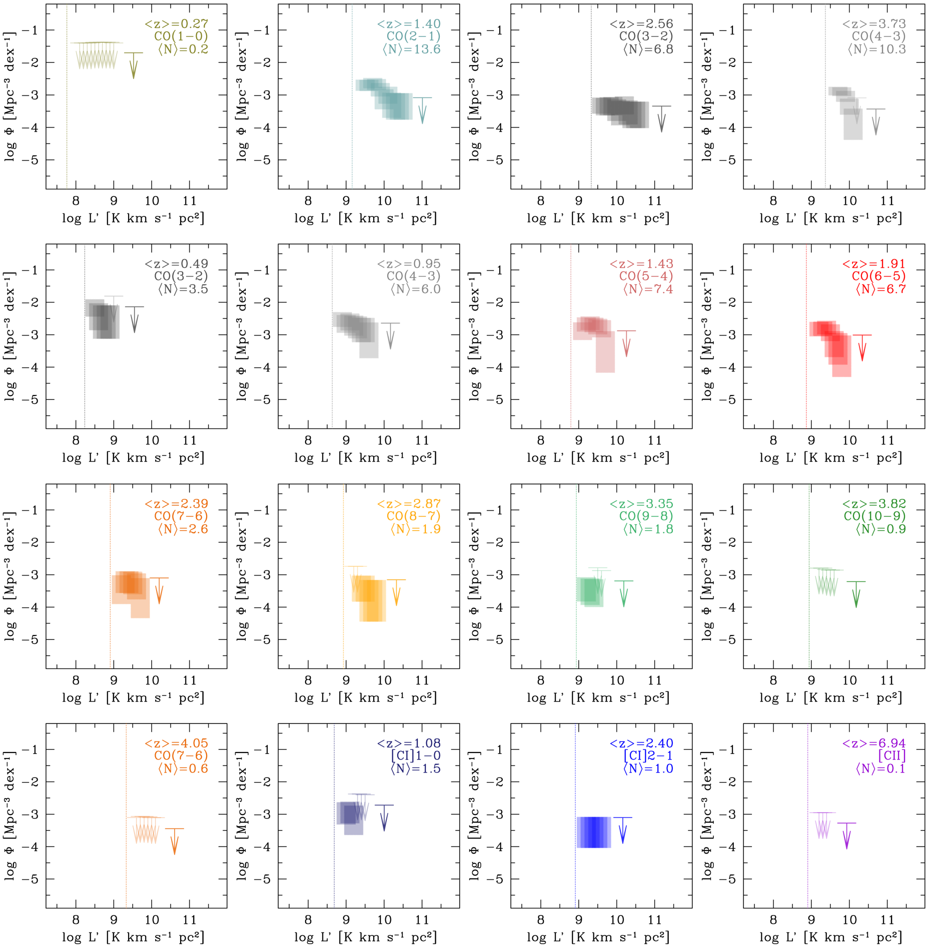

Figure 5.7: Constraints on the CO, [C I], and [C II] luminosity functions from ASPECS. The vertical extent of the boxes shows the average $\pm 1\sigma$ range in each 0.5 dex bin. For each transition, we report the volume-averaged redshift, and the average number of line candidates used in the various LF realizations. Bins with an average of $>$ 1 line candidate entry per realization are shown as boxes, while arrows mark the corresponding 3σ limits for all of the other bins. The vertical bars show the formal 5σ line-luminosity limit (see Table 5.1).

Table 5.2: The cosmic molecular gas density (mass of molecular gas in galaxies per cosmological volume) as constrained by ASPECS.

Redshift (1)	ρ_{H_2}, 1σ [10^7 M$_\odot$ Mpc^{-3}] (2)	ρ_{H_2}, 2σ [10^7M$_\odot$ Mpc^{-3}] (3)	Tracer (4)
	new from ASPECS LP 1.2 mm		
0.271–0.631	0.572–2.148	0.286–3.181	CO(3–2)
0.695–1.174	2.772–7.371	1.652–10.02	CO(4–3)
0.809–1.321	0.210–1.397	0.078–2.240	$[\mathrm{C\,I}]_{1-0}$
1.975–2.816	0.150–2.882	0.020–4.977	$[\mathrm{C\,I}]_{2-1}$
	updated from ASPECS LP 3 mm		
0.003–0.369	0.015–0.281	0.002–0.485	CO(1–0)
1.006–1.738	4.053–7.489	2.953–9.462	CO(2–1)
2.008–3.107	1.844–4.438	1.164–6.007	CO(3–2)
3.011–4.475	1.686–3.289	1.193–4.220	CO(4–3)

attributed to subthermalized conditions in the ISM of typical galaxies at least at $J_{\mathrm{up}} \gtrsim 7$ or a drop in the gas masses or metallicities of galaxies at $z > 1$. In the following section we further explore these scenarios.

Same redshift, different CO transition

Figure 5.8 compares the CO luminosity function constraints from the two bands of ASPECS. At $\langle z \rangle \approx 1.43$, the ASPECS frequency coverage is such that we observe the CO(2–1) transition at 3 mm and the CO(5–4) transition at 1.2 mm. The inferred CO luminosity functions show an offset of about 0.5 dex in luminosity for a fixed number density. This immediately implies subthermalized conditions of the molecular ISM in the targeted galaxies ($r_{52} \lesssim 0.3$, consistent with the value of $r_{52} \approx 0.16$ derived by Boogaard et al. 2020).

Same CO transition, different redshifts

The ASPECS frequency coverage also allows us to trace the same line transition, CO(3–2), both at $\langle z \rangle \approx 0.49$ at 1.2 mm, and at $\langle z \rangle \approx 2.61$ at 3 mm. Because of the $\sim 16.2\times$ smaller volume and $\sim 7.7\times$ lower luminosity distance, we sample different ranges of the CO(3–2) luminosity function in the two redshift bins, with the low-redshift data mostly constraining the $L' < 10^9$ K km s^{-1} pc^2 regime and the high-redshift data pinning down the bright end at $L' > 2 \times 10^9$ K km s^{-1} pc^2. However, the difference in number density throughout the observed range strongly points towards an evolution of the CO(3–2) luminosity function between $z \sim 2.6$ and $z \sim 0.5$. This is even clearer once we compare the observed CO LFs with the empirical predictions based on the *Herschel* IR LFs from Vallini et al. (2016) shown in Figure 5.8. The *Herschel* IR LFs were scaled via an empirical relation of the form: $\log L'/(\mathrm{K\,km\,s^{-1}\,pc^2}) = 0.54 + 0.81 \log L_{\mathrm{IR}}/\mathrm{L}_\odot$ (Sargent et al., 2014). The observed CO LF at $z \sim 0.5$ appears to sample just above the expected knee of the CO LFs. The observed CO(3–2) LF at $z \sim 2.6$ is in good agreement with the prediction for $z \sim 2$ around the expected

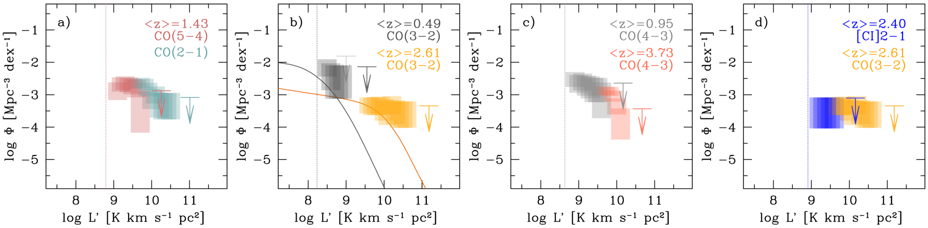

Figure 5.8: Comparison between CO and [C I]$_{2-1}$ luminosity functions. (a) The CO(2–1) (grey blue) and CO(5–4) (dark red) luminosity functions in the common redshift range around $\langle z \rangle = 1.43$. The CO(2–1) luminosity function appears in systematic excess with respect to the CO(5–4), hinting at generally subthermalized conditions ($r_{52} < 0.3$, see text for details). (b) The CO(3–2) luminosity functions observed at 3 mm and 1.2 mm at $\langle z \rangle = 2.61$ and $\langle z \rangle = 0.49$, respectively. For comparison, the empirical predictions of the CO(3–2) luminosity functions based on *Herschel* IR luminosity functions by Vallini et al. (2016) are shown in grey ($z \sim 0$) and orange ($z \sim 2$) lines. The CO(3–2) LF appears to evolve from $z \sim 2.6$ to the present age. ASPECS data point to an evolution in the CO(3–2) luminosity function consistent with the empirical predictions, although the difference in the sampled luminosity ranges in the two redshift bins limits the robustness of this finding. (c) Similar to the previous panel, but for the CO(4–3) luminosity functions observed at $z \sim 0.95$ at 1.2 mm and at $z \sim 3.7$ at 3 mm. (d) Comparison between the [C I]$_{2-1}$ and CO(3–2) luminosity functions at $z \sim 2.5$. We find an offset of $\gtrsim 0.5$ dex between the two luminosity functions, broadly in agreement with similar ratios between the two line luminosities reported in the literature from studies of individual sources (see § 5.4.2).

knee, and it lies >2 dex higher (in terms of number density) than the low-z predictions for $L' \sim 10^{10}$ K km s^{-1} pc^2. This result provides further, direct support to an evolution in the CO LFs, and therefore in gas content of galaxies, in this case irrespective of uncertainties in the CO excitation. We also show the comparison between the CO(4–3) LFs observed at $z \sim 0.95$ at 1.2 mm and $z \sim 3.7$ at 3 mm. A similar LF evolution might also be present in CO(4–3), but the available data do not allow us to exclude a non-evolving scenario.

5.4.2 [C I] and [C II] luminosity functions

In Figure 5.7, we also show the observed constraints on the [C I]$_{1-0}$ LF at $\langle z \rangle = 1.08$, on the [C I]$_{2-1}$ LF at $\langle z \rangle = 2.40$, and on the [C II] LF at $\langle z \rangle = 6.94$ from ASPECS 1.2 mm. With the exception of the strong [C I]$_{2-1}$ detection associated with the galaxy ASPECS LP 1mm.C01 (Boogaard et al., 2020; Aravena et al., 2020), only relatively low fidelity candidates are consistent with being [C I] or [C II] transitions. We further explore ASPECS contraints on the [C II] LF in B. Uzgil, et al. (in prep.).

Figure 5.8 shows the comparison between the [C I]$_{2-1}$ LF from our 1.2 mm cube, and the CO(3–2) LF from the ASPECS LP 3 mm. The two LFs probe roughly the same redshift range, so the comparison of the two LFs yields an insight on the average physical conditions in the ISM of the detected galaxies. We find a global shift of $\gtrsim 0.5$ dex between the two LFs, which is roughly consistent with the median ratio of 0.69 ± 0.16 dex for [C I]$_{2-1}$/CO(3–2) reported in targeted observations of SMGs and quasar host galaxies at $z = 2 - 6$ in Walter et al. (2011).

For comparison, Jiao et al. (2017) find a ratio of 0.9 dex in local ULIRGs.

We refer to Boogaard et al. (2020) for a more detailed discussion of the astrophysical implication of the observed CO to [C I] line ratios, and to B. Uzgil, et al. (in prep.) for a further exploration of the upper limits on the [C II] LF.

5.4.3 ρ_{H_2} vs redshift

We use the combined ASPECS data to infer the cosmic-averaged molecular gas density of galaxies, ρ_{H_2}, as a function of cosmic time (see § 5.3.5). Compared to previous incarnations of our analysis (e.g., Walter et al., 2014; Decarli et al., 2016a, 2019), we here adopt the updated constraints on the CO excitation from Boogaard et al. (2020), which also includes the VLASPECS results (Riechers et al., 2020). Our analysis yields a nearly continuous sampling of $\rho_{\mathrm{H}_2}(z)$ from $z \approx 0$ to $z \sim 4.5$ in a self-consistent manner. The ASPECS data show a smooth increase of $\rho_{\mathrm{H}_2}(z)$ from early cosmic time up to $z \sim 1.5$, followed by a $\sim 6\times$ decline to the present day (see Figure 5.9 and Table 5.2). The new excitation correction (Boogaard et al., 2020) brings the $\rho_{\mathrm{H}_2}(z)$ constraints from CO into excellent agreement with our dust-based measurements from ASPECS (Magnelli et al., 2020). The ρ_{H_2} constraints at $z \lesssim 0.5$ from ASPECS are rather loose, as a result of the small volume probed (see § 5.B).

We note that the results shown in Figure 5.9 are based on a constant α_{CO} or gas-to-dust ratio. The arguments presented in § 5.3.4 for a Galactic value may not be valid at $z \gtrsim 3$, where direct constraints on the metallicity of typical CO- and dust-emitting galaxies lack. A lower metallicity would imply a higher α_{CO} and gas-to-dust ratio, yielding higher ρ_{H_2} estimates.

We also derive [C I]-based estimates of $\rho_{\mathrm{H}_2}(z)$ (see Table 5.2). The two [C I]-based estimates at $z \sim 1$ and $z \sim 2.5$ appear lower by a factor $\sim 5\times$ and $\sim 2\times$, respectively, compared to the corresponding CO-based estimates. This discrepancy is likely due to sensitivity limitations, and highlights the challenge of using [C I] as molecular gas tracer of the bulk of the galaxy population at high redshift (for dedicated [C I] studies in main sequence galaxies at high redshift, see, e.g., Valentino et al., 2018; Valentino et al., 2020b).

In Figure 5.9 we place the ASPECS measures of $\rho_{\mathrm{H}_2}(z)$ in the context of similar investigations in the literature. Our new measurements, listed in Table 5.2, improve and expand on the results from previous molecular scans using the Plateau de Bure Interferometer (Walter et al., 2014), the VLA (Riechers et al., 2019), and ALMA (Decarli et al., 2016a, 2019), as well as the constraints from field sources in the PHIBSS data (Lenkić et al., 2020), and from calibrator fields in the ALMACAL survey (Klitsch et al., 2019). Our comparison also includes dust-based $\rho_{\mathrm{H}_2}(z)$ measurements from Scoville et al. (2017), Liu et al. (2019), and from ASPECS (Magnelli et al., 2020). Overall, the molecular gas constraints from volume-limited surveys agree within the uncertainties over $\sim 90\%$ of the cosmic history. The general agreement in these results, based on different fields, suggests that the impact of cosmic variance and of systematics is modest. In § 5.B we quantitatively assess its role within our dataset. The studies by Scoville et al. (2017) and Liu et al. (2019) find a qualitatively similar evolution of $\rho_{\mathrm{H}_2}(z)$, although with different normalizations. These ρ_{H_2} estimates rely on different assumptions of stellar mass functions, functional form of the main sequence, gas fractions, internal calibrations, and integration limits. Homogenizing these is beyond the scope of the present work, therefore we here only show their 'bona fide' estimates as published.

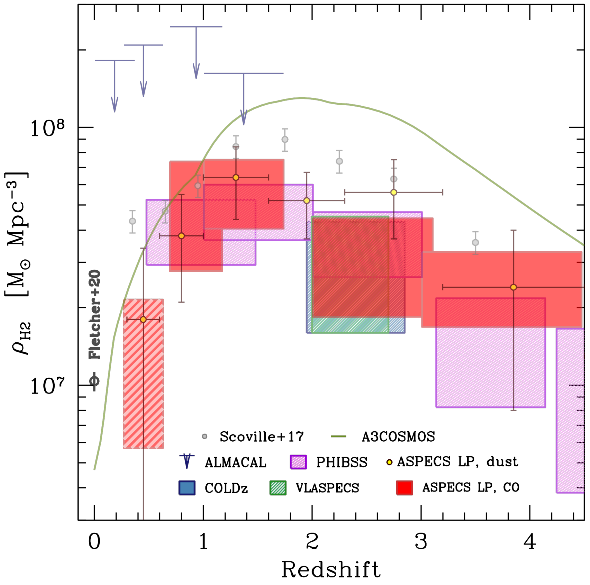

Figure 5.9: The evolution of the cosmic molecular gas density, $\rho_{H_2}(z)$, from ASPECS LP compared to similar studies in the literature: CO-based measurements from VLASPECS (Riechers et al., 2020), COLDz (Riechers et al., 2019), PHIBSS fields (Lenkić et al., 2020), ALMACAL (Klitsch et al., 2019); and dust-based measurements from ASPECS (Magnelli et al., 2020), A3COSMOS (Liu et al., 2019), and from Scoville et al. (2017, see their footnote 2). The $\rho_{H_2}(z = 0)$ measurement by Fletcher et al. (2020) is also shown for reference. All of the uncertainties are shown at 1σ significance. The ASPECS LP constraints at $z \lesssim 0.5$ are shaded to highlight the non-negligible impact of cosmic variance at these redshifts. The available datasets all point towards a steep decrease in ρ_{H_2} from cosmic noon to the local universe preceded by a smooth increase from higher redshift. Different surveys targeting different regions of the sky appear to find the same trend, implying that cosmic variance does not dominate the results (see § 5.B).

The observed evolution of ρ_{H_2} appears to mimic the history of the cosmic star formation rate density, ρ_{SFR} (see, e.g., Madau & Dickinson, 2014). The ratio between ρ_{H_2} and ρ_{SFR} results in a volume-average of the "depletion time" $\langle t_{dep} \rangle$, i.e., the timescale required for galaxies to deplete their reservoirs of molecular gas, if star formation continues at the current rate, and there is no further gas accretion or outflows. Our results hint to a relatively constant $\langle t_{dep} \rangle$. In Walter et al. (2020) we explore the astrophysical implications of this result in the context of galaxy evolution.

5.5 Conclusions

We present the ultimate CO luminosity functions from the ASPECS large program, and the resulting constraints for the cosmic evolution of the molecular gas density. The main conclusions of this study of the molecular and atomic line emission in ASPECS LP are as follows.

i. The line flux distributions due to various CO and neutral/ionized carbon lines in our analysis show that roughly 80% of the line flux at 3 mm is associated with CO(2–1) or CO(3–2) at the age of cosmic noon, and 60% of the line flux at 1.2 mm is due to intermediate-J CO transition ($J_{\rm up} = 3 - 6$) at $z \lesssim 2$. Higher-J CO transitions are negligible at 3 mm but account for 25% of the total line flux at 1.2 mm. Neutral carbon contributes to $\sim$ 12% of the integrated line flux at 1.2 mm. Finally, singly-ionized carbon [C ii] at $6 \lesssim z \lesssim 8$ accounts for $<$ 1% of the line flux at 1.2 mm. This result poses a major challenge for intensity mapping experiments targeting [C ii] at the end of the epoch of reionization, as the expected line foreground is two orders of magnitudes stronger (in terms of total flux in lines) than the [C ii] signal.

ii. The CO luminosity functions probed at 1.2 mm evolve as a function of redshift, with a decrease in the number density at a given line luminosity (in units of L'). This implies substantially subthermal excitation in galaxies throughout the last ~10 Gyr of cosmic history.

iii. The direct comparison between the luminosity functions for the same CO transition seen in the 1.2 mm and 3 mm cubes of the ASPECS LP reinforces the idea that the typical galaxy at $z \approx 1.43$ shows subthermalized molecular gas emission, and that there is a significant evolution in the luminosity function for CO(2–1) takes place between $z \sim 2.8$ and $z \sim 0.5$ irrespective of any CO excitation assumption. A comparison between the [C i]$_{2-1}$ and CO(3–2) luminosity functions in the redshift range $z \sim 2.5$ suggests that the line ratio is in line with the values reported for IR-bright galaxies in targeted studies.

iv. The cosmic density of molecular gas in galaxies, $\rho_{\rm H_2}$, smoothly increases from early cosmic time up $z \sim 2 - 3$, followed by a factor $\sim$ 6 drop to the present age. This is in qualitative agreement with the cosmic SFR density, suggesting that the depletion time of galaxies is approximately constant in redshift once averaged over the galaxy population.

v. Modeling and the comparison with similar surveys suggest that cosmic variance does not play a dominant role in our estimates of $\rho_{\rm H_2}$ at $z \gtrsim 0.5$.

The emerging consensus on the evolution of $\rho_{\rm H_2}$ is the result of many hundreds of hours of integration with PdBI/NOEMA, VLA, and ALMA. Using these facilities to significantly expand on the latest campaigns is still possible, but observationally expensive. Future upgrades in the capabilities of available instruments (from the forthcoming completion of NOEMA, to the plans outlined in the ALMA 2030 Roadmap, Carpenter et al. 2020, and in the next generation VLA white books, Murphy et al. 2018) are required in order to make the next transformational step in this field.

Acknowledgements

F.W. and M.N. acknowledge support by the ERC Advanced Grant Cosmic-Gas (740246). Este trabajo cont ó con el apoyo de CONICYT + PCI + INSTITUTO MAX PLANCK DE ASTRONOMIA MPG190030. T.D.-S. acknowledges support from the CASSACA and CONICYT fund CAS-CONICYT Call 2018. J.H. acknowledges support of the VIDI research programme with project number 639.042.611, which is (partly) financed by the Netherlands Organisation for Scientific Research (NWO). D.R. acknowledges support from the National Science Foundation under grant numbers AST-1614213 and AST-1910107 and from the Alexander von Humboldt Foundation through a Humboldt Research Fellowship for Experienced Researchers. H.I. acknowledges support from JSPS KAKENHI Grant Number JP19K23462. I.R.S. acknowledges support from STFC (ST/T000244/1). This paper makes use of the following ALMA data: 2016.1.00324.L. ALMA is a partnership of ESO (representing its member states), NSF (USA) and NINS (Japan), together with NRC (Canada), NSC and ASIAA (Taiwan), and KASI (Republic of Korea), in cooperation with the Republic of Chile. The Joint ALMA Observatory is operated by ESO, AUI/NRAO and NAOJ.

Facilities: ALMA

Authorship statement

This chapter presents and discusses the main result from ASPECS: the cosmic density of molecular gas. The central analysis of ASPECS was conducted in close collaboration by a small core team of authors, who each lead part of a series of interrelated papers that were published simultaneously in The Astrophysical Journal (including chapter 4). The lead author of this chapter is R. Decarli, who was in charge of conducting the analysis and writing the manuscript. The main contributions from L. A. Boogaard concern the detailed assessment of the high-fidelity lines, the analysis of the line flux distributions and associated tests involving the lines without counterpart and their impact on the cosmic molecular gas density, the adopted CO excitation, and the discussion of the intercomparison of the luminosity functions of carbon monoxide and atomic carbon, as well as reviewing and discussing the manuscript.

Appendix 5.A Tabulated luminosity functions

Table 5.3 and Table 5.4 list the ASPECS constraints on the luminosity functions of CO, [C I] and [C II].

Table 5.3: Luminosity functions of the observed CO transitions.

log L' (K km s^{-1} pc^2) (1)	log Φ (dex^{-1} Mpc^{-3}) (2)	log L' (K km s^{-1} pc^2) (3)	log Φ (dex^{-1} Mpc^{-3}) (4)	log L' (K km s^{-1} pc^2) (5)	log Φ (dex^{-1} Mpc^{-3}) (6)
CO(1–0), 3 mm		CO(3–2), 1.2 mm		CO(7–6), 1.2 mm	
8.5	< −1.38	8.5	−2.44 −1.91	9.2	−3.91 −3.02
8.6	< −1.38	8.6	−2.86 −2.03	9.3	−3.57 −2.89
8.7	< −1.38	8.7	−3.12 −2.09	9.4	−3.57 −2.89
8.8	< −1.38	8.8	−3.12 −2.09	9.5	−3.60 −2.91
8.9	< −1.38	8.9	−3.12 −2.09	9.6	−3.76 −2.96
9.0	< −1.40	9.0	< −1.81	9.7	−4.34 −3.11
CO(2–1), 3 mm		CO(4–3), 1.2 mm		CO(8–6), 1.2 mm	
9.5	−2.87 −2.53	8.9	−2.76 −2.30	9.2	< −2.74
9.6	−2.88 −2.53	9.0	−2.94 −2.39	9.3	< −2.74
9.7	−2.80 −2.48	9.1	−2.87 −2.35	9.4	−3.83 −3.03
9.8	−2.85 −2.51	9.2	−3.03 −2.41	9.5	−3.83 −3.03
9.9	−3.05 −2.63	9.3	−3.11 −2.44	9.6	−4.45 −3.16
10.0	−3.44 −2.83	9.4	−3.23 −2.48	9.7	−4.45 −3.16
10.1	−3.27 −2.75	9.5	−3.23 −2.48	9.8	−4.45 −3.16
10.2	−3.71 −2.93	9.6	−3.72 −2.62		
10.3	−3.76 −2.95				
10.4	−3.76 −2.95				
10.5	−3.76 −2.95				
CO(3–2), 3 mm		CO(5–4), 1.2 mm		CO(9–8), 1.2 mm	
9.6	−3.58 −3.08	9.1	−3.16 −2.62	9.2	−3.83 −3.08
9.7	−3.63 −3.09	9.2	−2.90 −2.46	9.3	−3.93 −3.12
9.8	−3.63 −3.07	9.3	−2.86 −2.44	9.4	−4.00 −3.14
9.9	−3.62 −3.07	9.4	−2.93 −2.47	9.5	< −2.78
10.0	−3.80 −3.13	9.5	−2.99 −2.51	9.6	< −2.87
10.1	−3.94 −3.19	9.6	−3.08 −2.55		
10.2	−3.60 −3.04	9.7	−4.17 −2.89		
10.3	−3.91 −3.17				
10.4	−4.02 −3.21				
10.5	−4.02 −3.21				
10.6	−4.02 −3.21				
CO(4–3), 3 mm		CO(6–5), 1.2 mm		CO(10–9), 1.2 mm	
9.7	−3.01 −2.75	9.2	−3.05 −2.60	9.2	< −2.80
9.8	−3.03 −2.77	9.3	−3.04 −2.60	9.3	< −2.80
9.9	−3.21 −2.88	9.4	−2.99 −2.57	9.4	< −2.84
10.0	−3.61 −3.12	9.5	−3.20 −2.68	9.5	< −2.86
10.1	−4.38 −3.42	9.6	−3.69 −2.89	9.6	< −2.86
10.2	< −3.09	9.7	−3.92 −2.95		
		9.8	−4.31 −3.02		

Notes. (Columns: 1, 3, 5) Luminosity bin center; each bin is 0.5 dex wide. (Columns: 2, 4, 6) minimum and maximum values of the luminosity function confidence levels at 1σ, or 3σ upper limits on the luminosity functions.

Table 5.4: Luminosity functions of the observed [C I] and [C II] lines.

$\log L'$ ($\mathrm{K\,km\,s^{-1}\,pc^{2}}$) (1)	$\log \Phi$ ($\mathrm{dex^{-1}\,Mpc^{-3}}$) (2)	$\log L'$ ($\mathrm{K\,km\,s^{-1}\,pc^{2}}$) (3)	$\log \Phi$ ($\mathrm{dex^{-1}\,Mpc^{-3}}$) (4)
[C I]$_{1-0}$, 3 mm		[C I]$_{2-1}$, 1.2 mm	
9.6	< -3.10	9.2	-4.04 -3.08
9.7	< -3.07	9.3	-4.04 -3.08
9.8	< -3.07	9.4	-4.04 -3.08
9.9	< -3.08	9.5	-4.04 -3.08
10.0	< -3.11	9.6	-4.04 -3.08
10.1	< -3.11		
[C I]$_{1-0}$, 1.2 mm		[C II], 1.2 mm	
9.0	-3.32 -2.63	9.1	< -2.95
9.1	-3.28 -2.61	9.2	< -2.95
9.2	-3.64 -2.73	9.3	< -2.95
9.3	< -2.38	9.4	< -2.95
9.4	< -2.38	9.5	< -2.97

Notes. (Columns: 1, 3) Luminosity bin center; each bin is 0.5 dex wide. (Columns: 2, 4) minimum and maximum values of the luminosity function confidence levels at 1σ, or 3σ upper limits on the luminosity functions.

Appendix 5.B Cosmic variance

A critical limitation of pencil-beam surveys such as ASPECS is the impact of cosmic variance. Noticeably, a large fraction of the galaxies detected in CO(2–1) emission in ASPECS LP 3 mm belongs to a large overdensity at $z \approx 1.09$ (see Boogaard et al., 2019). Here we quantify how the clustering of sources impact our results. The expected number of galaxies in a volume-limited survey is:

$$N = \int_{V_1} \int_{V_2} (1 + \xi)\, n_1 n_2 \, dV_1 \, dV_2 \tag{5.7}$$

where n_i is the number density of galaxies, obtained by integrating the luminosity (or mass) function of galaxies down to the detection threshold of the survey, V_i is the survey volume, and ξ is the 3D 2-points correlation function, which accounts for the excess of galaxy counts compared to the average field due to galaxy clustering. In the linear clustering regime, ξ is often modeled as a power-law: $\xi(r) = (r/r_0)^{-\gamma}$. The variance on the expected numbers, Var[N], is usually referred to as cosmic variance. It comprizes of a Poissonian term, and a term due to the variations in the number counts due to clustering:

$$\sigma_v^2 = \frac{\langle N^2 \rangle - \langle N \rangle^2 - \langle N \rangle}{\langle N \rangle^2} = \frac{1}{V^2} \int_{V_1} \int_{V_2} \xi \, dV_1 \, dV_2 \tag{5.8}$$

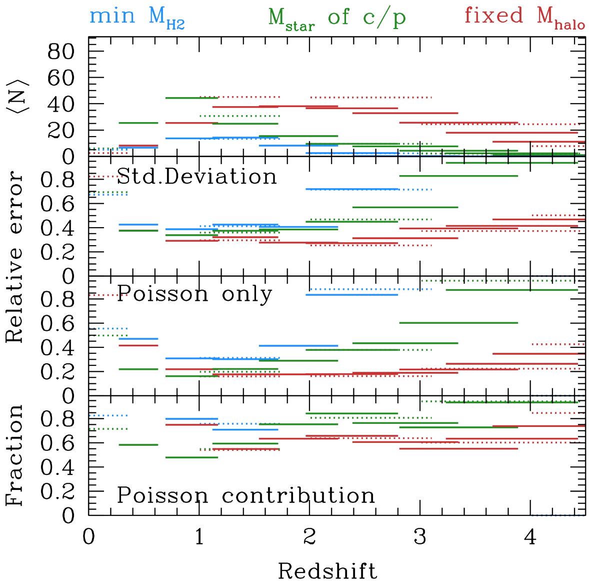

Figure 5.10: Impact of cosmic variance on the expected number counts of galaxies in our survey, based on the models presented in Popping et al. (2020), as a function of redshift. Blue, green, and red lines show galaxies selected based on the predicted CO luminosity (via the simulated H_2 mass), on the stellar mass of their optical/near-infrared counterparts, and on the halo mass, respectively (see text for details). The *top panel* shows the average number of galaxies in each redshift bin probed with ASPECS LP 1.2 mm (solid lines) and 3 mm (dotted lines). The *second panel* shows the root square of the total cosmic variance. The *third panel* shows the Poissonian term alone. Finally, the *bottom panel* shows the fraction of the standard deviation that is due to Poisson. We find that the Poisson contribution dominates the cosmic variance (> 50% of the standard deviation) at any redshift, irrespective of the selection function. This implies that the impact of clustering (i.e., the non-Poissonian component of the cosmic variance) is small, and often negligible in ASPECS.

As discussed in Decarli et al. (2016a) and Decarli et al. (2019), the Poissonian uncertainties are accounted for in the construction of the CO luminosity functions and in our estimates of ρ_{H_2}. The clustering term in Equation 5.8 implies that, even in presence of large source counts, field-to-field variations are expected due to large-scale structures and clustering. This might introduce a systematic bias in the estimates of LFs based on datasets centered on preselected targets (see also Loiacono et al., 2020). Here we quantify how our results depend on the choice of the targeted region.

Directly solving the integral in Equation 5.8 would require assumptions on the clustering of CO-bright sources, for which no direct observational constraint is available yet. An alternative and commonly-adopted approach is to rely on theoretical models of galaxy formation to create multiple realizations of galaxy populations in various volume samplings. Cosmic variance is then directly computed using the actual variations of N. Here we follow the latter method by capitalizing on data-driven simulations presented in Popping et al. (2020). From these simulations we create 100 samplings of the simulated box with a geometry matched to the ASPECS survey volume. We then apply different cuts on the galaxy samples to mimic the selection criteria of ASPECS (see below). Finally, we compute the average and variance in the number of selected galaxies from all the realizations. The variance is a combination of the intrinsic scatter due to the cosmic structures within the simulation, and of Poissonian scattering. The contribution of the latter is directly computed following Gehrels (1986), thus we can infer the impact of large-scale structures in the count rates used in our LFs.

The results of this analysis are presented in Figure 5.10, where we show the average number of galaxies, the standard deviation (i.e., the squared root of the total variance in the number of galaxies), the Poissonian fluctuations, and the fraction of the uncertainties that is attributed to Poissonian fluctuations. Concerning the selection function, for a given transition, ASPECS applies a selection based on the line flux. As this is not trivially derived in models (see extensive discussions in, e.g., Lagos et al., 2011; Popping et al., 2014, 2019), here we opt for three different approaches: First, we apply a simple, redshift independent cut in the dark matter halo mass, $M_{\rm halo} > 10^{11.5}\,{\rm M}_\odot$. Then we consider a cut based on the minimum stellar mass of detected optical/near-infrared counterparts as a function of redshift. The threshold is $M_{\rm star} > 10^{9.0}\,{\rm M}_\odot$ at $z \approx 0.5$, $M_{\rm star} > 10^{9.7}\,{\rm M}_\odot$ at $z \approx 1.4$, $M_{\rm star} > 10^{10.1}\,{\rm M}_\odot$ at $z \approx 2.4$, $M_{\rm star} > 10^{10.3}\,{\rm M}_\odot$ at $z \approx 3.5$, at $M_{\rm star} > 10^{10.5}\,{\rm M}_\odot$ at $z \approx 4.5$. Finally, we consider a cut based on the CO 5σ luminosity thresholds shown in Figure 5.1, using the predicted CO luminosity in models, based on the simulated H_2 mass, under the same r_{J1} and $\alpha_{\rm CO}$ assumptions as used elsewhere in this work (see § 5.3.4). We find that the number of galaxies we expect to detect is < 15 in each redshift bin for the CO luminosity cut, while the stellar mass cut at the halo mass cut yield larger numbers of expected galaxies (up to ~ 50 around cosmic noon). However, even in these cases, Poissonian uncertainties appear to dominate the total error budget, i.e., the Poisson contribution accounts for $> 50\%$ of the standard deviation in the number of galaxies at any redshift, irrespective of the selection function. Variance purely due to the large-scale structure in the universe (second panel from the top in Figure 5.10) plays a significant role only at $z \lesssim 0.5$ (in all cases) and $z \gtrsim 3-4$ (depending on the adopted the adopted selection cut. The overall low impact of cosmic variance is likely to be attributed to the peculiar pencil beam geometry of the survey, with the line-of-sight dimension stretching over ~ 1000 Mpc in most redshift bins. The Poissonian fluctuations are already accounted for in the LFs and estimates of $\rho_{\rm H_2}(z)$. The remainder term, due to the clustering of sources, is small in the redshift range of interest, its actual value strongly depends on the (unknown) reliability of our forward-modeling of the selection function. Therefore, we opt not to include this further term into our estimates of the uncertainties. In support to the negligible contribution of cosmic variance, Magnelli et al. (2020) and Bouwens et al. (2020) find an excellent match between the stellar mass functions and cosmic SFR density in the ASPECS footprint and the ones inferred in the literature from much wider regions in different (physically disconnected) fields at any $z \gtrsim 0.5$.

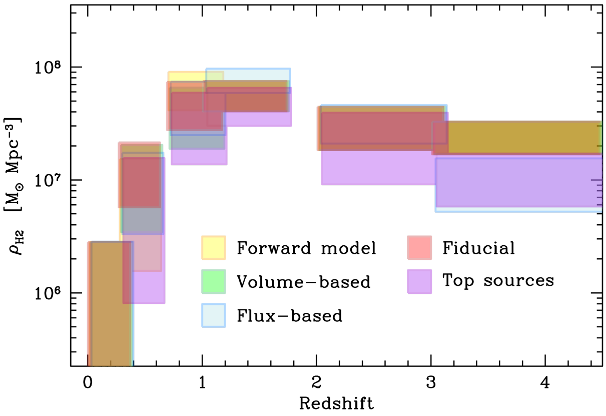

Figure 5.11: The evolution of the molecular gas cosmic density in galaxies as a function of redshift, shown under different treatments of the line candidates without a counterpart. Red boxes: our bona-fide constraints, as shown in Figure 5.9. Green boxes: the probability distribution of line identification scales with the sampled volume in each transition, for both ASPECS bands. Yellow boxes: the probability distribution of line identification scales as the volume for 3 mm transitions, and as the predicted number of detections assuming the corresponding CO LFs from 3 mm at similar redshifts, and the large velocity gradient modeling of the CO spectral energy distribution from Boogaard et al. (2020). Blue boxes: the probability distribution scales as the observed flux distributions shown in Figure 5.5. Purple boxes: Constraints on ρ_{H_2} based exclusively on the sources detected in the 1.2 mm dust continuum.

Appendix 5.C Identification of line candidates without near-infrared counterparts

Here we explore how our treatment of the line candidates without a counterpart affects our results on the molecular gas content in the universe, $\rho_{H_2}(z)$. The expected number of lines from a specific transition is given by the integral over the corresponding above the luminosity limit set in Figure 5.1, scaled for the cosmological volume sampled in such transition. In addition, the lack of a counterpart in our multiwavelength catalog implies an additional, unknown selection function that favors high-redshift scenarios. The modest information content in the data concerning the actual redshift of line candidates without a counterpart implies that the posterior distributions might be affected by our prior assumptions. Hence, we test how different options affect our final results.

Beside our fiducial approach described in § 5.3.5, we consider four scenarios: 1) We assume that the probability distribution of line identification is proportional to volume; 2) We assume the same volume-based argument at 3 mm, and infer expected LFs (and hence, expected number of sources) for 1.2 mm transitions based on the CO LFs from Saintonge et al. (2017) (extrapolated to $z \sim 0.5$) and from Decarli et al. (2019) (at $z \gtrsim 0.9$), paired with the large velocity gradient analysis on individual ASPECS sources from Boogaard et al. (2020); 3) For both bands we assume that the probability distribution scales according to the flux

Table 5.5: The cosmic molecular gas density (mass of molecular gas in galaxies per cosmological volume) as constrained by ASPECS under different methods to identify line candidates without counterparts (see text for details).

Redshift	$\log \rho_{H_2}$ ($M_\odot$ Mpc^{-3})			
	Forward model	Volume-based	Flux-based	Top sources
(1)	(2)	(3)	(4)	(5)
0.003–0.369	5.171–6.449	5.171–6.449	5.177–6.453	
0.271–0.631	6.196–7.184	6.537–7.312	6.522–7.240	5.911–7.194
0.695–1.174	7.617–7.957	7.278–7.819	7.398–7.871	7.138–7.772
1.006–1.738	7.608–7.874	7.608–7.874	7.769–7.984	7.481–7.816
2.008–3.107	7.266–7.647	7.266–7.647	7.322–7.663	6.961–7.595
3.011–4.475	7.227–7.517	7.227–7.517	6.720–7.190	6.766–7.235

Notes. The quoted values refer to the 1σ upper- and lower condifence boundaries.

distribution of line candidates with a counterpart (see Figure 5.5); 4) Finally, we restrict our analysis to lines with a 1.2 mm continuum counterpart (see González-López et al., 2020; Aravena et al., 2020). These different approaches have their strengths and drawbacks. The volume-based arguments use the least prior information, but they do not account for the different luminosity limits and for the evolution of the LFs, nor for the intrinsic ratios of line luminosities. The flux-based method has the advantage of resulting in a realistic distribution of the line fluxes for sources without a counterpart, but inherently assumes that the sources with and without a counterpart share a similar redshift and flux distribution, which is unlikely. The forward-modeling method has the advantage of exploiting the information available at 3 mm and from local studies to constrain the 1.2 mm LFs, but it relies on extrapolation of observed LFs in different redshift bins, and is partially circular, in that the excitation constraints are based on the same 1.2 mm data. Finally, limiting the analysis to secure sources provides us with a robust lower limit, but this approach does not fully capitalize on the signal present in the data.

Figure 5.11 compares the $\rho_{H_2}(z)$ evolution that results from each assumption (see also Table 5.5). To first order, the ρ_{H_2} evolution is unaffected by our treatment of the sources without a counterpart in the catalog. The spread between the ρ_{H_2} estimates is most prominent at $z \lesssim 0.5$ as a result of low number statistics. Discrepancies are always well within the uncertainties. The main offset comes from restricting our analysis to the secure sources with a 1.2 mm dust continuum, which typically results in a $\sim 1.5\times$ underestimate of ρ_{H_2}.

6 | The average molecular gas content of star-forming galaxies at $z = 3 - 4$

Abstract

We study the molecular gas content of 24 star-forming galaxies at $z = 3 - 4$, with a median stellar mass of $10^{9.1}$ $\mathrm{M}_{\odot}$, from the MUSE *Hubble* Ultra Deep Field (HUDF) Survey. Selected by their Lyα λ1216-emission and H_{F160W}-band magnitude, the galaxies show an average $\langle \mathrm{EW}^{0}_{\mathrm{Ly}\alpha} \rangle \approx 20$ Å, lower than typical Lyman Alpha Emitters, and a rest-frame UV spectrum more similar to Lyman Break Galaxies. We use rest-frame optical spectroscopy from KMOS and MOSFIRE, and the UV features observed with MUSE, to determine the systemic redshifts, which are offset from Lyα by $\langle \Delta v(\mathrm{Ly}\alpha) \rangle = 346$ km s^{-1}, with a 100 to 600 km s^{-1} range. Stacking ^{12}CO $J = 4 \rightarrow 3$ and [C I] $^{3}P_{1} \rightarrow {}^{3}P_{0}$ (and higher-J CO lines) from the ALMA Spectroscopic Survey of the HUDF (ASPECS), we determine 3σ upper limits on the line luminosities of 4.0×10^{8} K km s^{-1}pc^{2} and 5.6×10^{8} K km s^{-1}pc^{2}, respectively (for a 300 km s^{-1} linewidth). Stacking the 1.2 mm dust continuum flux densities, we find a 3σ upper limit of 9 μJy. The inferred gas fractions, under the assumption of a 'Galactic' CO-to-H$_2$ conversion factor and gas-to-dust ratio, are in tension with previously determined scaling relations. This implies a substantially higher $\alpha_{\mathrm{CO}} \geq 10$ and $\delta_{\mathrm{GDR}} \geq 1200$, consistent with the sub-solar metallicity estimated for these galaxies ($12 + \log(\mathrm{O/H}) \approx 7.8 \pm 0.2$). The low metallicity of $z \geq 3$ star-forming galaxies may thus make it very challenging to unveil their cold gas through CO or dust emission, warranting further exploration of alternative tracers, such as [C II].

L. A. Boogaard, R. J. Bouwens, D. Riechers, P. van der Werf, *et al.*
The Astrophysical Journal, submitted for publication

6.1 Introduction

The recent decade has witnessed a tremendous advance in the characterization of the cold molecular gas content of star forming galaxies at $z > 1$. Evidence is now mounting that the cold gas fraction of massive star-forming galaxies strongly increases up to at least $z \approx 3$ (e.g., Tacconi et al., 2010, 2013, 2018; Genzel et al., 2010, 2015; Geach et al., 2011; Dessauges-Zavadsky et al., 2015, 2020; Aravena et al., 2019, 2020). As the cold H_2 gas itself is radiatively dark, the molecular gas has to be traced by the emission from the ground-state rotational transition of Carbon Monoxide (^{12}CO, hereafter CO), or other tracers such as the emission from neutral atomic carbon ([C I]) or the long-wavelength dust continuum. Yet, observations of CO in (optically selected) star-forming galaxies at $z > 3$ remain challenging and have been limited to massive Lyman Break- or main sequence-selected galaxies and/or strongly lensed systems, with known redshifts (Baker et al., 2004; Coppin et al., 2007; Riechers et al., 2010; Magdis et al., 2012, 2017; Tan et al., 2013; Livermore et al., 2012; Saintonge et al., 2013; Dessauges-Zavadsky et al., 2015, 2017; Pavesi et al., 2019; Cassata et al., 2020), sometimes serendipitously detected and only identified as such *a posteriori* (Gowardhan et al., 2019).

The Atacama Large Millimeter Array Large Program ASPECS (The ALMA Spectroscopic Survey in the *Hubble* Ultra Deep Field (HUDF); Walter et al. 2016; Decarli et al. 2019) provides a unique opportunity to study the gas content of star forming galaxies at $z \geq 3$. ASPECS consists of spectral scans in ALMA Band 3 (85–115 GHz) and 6 (212–272 GHz), probing molecular gas and dust in galaxies without any target preselection. These data unveil emission from CO, [C I] and dust-continuum in several star-forming galaxies at $z = 1 - 4$ (González-López et al., 2019, 2020; Boogaard et al., 2019, 2020), providing key constraints on the empirical scaling relations describing the evolution of the gas and dust content in galaxies (Aravena et al., 2019, 2020), the evolution of the cosmic molecular gas density (Decarli et al., 2019, 2020) and the baryon cycle (Walter et al., 2020).

Key to the exploration of the ASPECS data are the large number of spectroscopic redshifts provided by the Multi Unit Spectroscopic Explorer (MUSE) HUDF Survey (Bacon et al., 2017). Through its unparalleled sensitivity for faint emission lines, MUSE has detected many galaxies at $z \geq 3$, where the bright H I Lyα λ1216 line enters the integral-field spectrograph (4750 − 9300Å; $\lambda/\Delta\lambda \approx 3000$; Inami et al. 2017), probing the faint end of the Lyα luminosity function down to below $0.1\,L^{*}_{\mathrm{Lya}}$ (Drake et al., 2017).

Exploiting the large number of redshifts from MUSE, we can push the gas mass-sensitivity of ASPECS at $z \geq 3$ to its limits through stacking (in particular, CO $J = 4 \rightarrow 3$ becomes accessible at $z \geq 3.0115$). Indeed, Inami et al. (2020) have shown that at lower redshifts, $z = 1 - 2$, we can recover CO emission below the formal sensitivity threshold of ASPECS, by stacking on the accurate systemic redshifts from MUSE.

However, the MUSE redshifts at $z \geq 3$ obtained from Lyα cannot be used for stacking. Because Lyα is a resonant transition, the photons are easily scattered by the neutral gas in- and surrounding a galaxy, shifting the peak of the emission away from the systemic velocity by several hundred km s^{-1} (e.g., Shapley et al., 2003; Verhamme et al., 2018; Muzahid et al., 2020). This means that the line emission tracing the molecular gas could be completely washed out by the noise if non-systemic Lyα-redshifts are used for stacking.

Fortunately, because we have approximate redshifts from Lyα, these targets can be effectively followed-up simultaneously with multi-object, near-infrared spectrographs, such as the K-band Multi Object Spectrograph (KMOS) at the Very Large Telescope and the Multi-Object Spectrometer For Infra-Red Exploration (MOSFIRE) at the Keck Observatory. These data can constrain the systemic redshift by targeting the rest-frame optical lines such as Hβ λ4863 and [O III] $\lambda\lambda$4960, 5008 in the K-band (out to $z = 3.812$).

In this paper, we constrain the molecular gas content of star-forming galaxies at $3.0115 < z < 3.812$, by stacking their molecular gas signal through the outlined three step process. We 1) identify the galaxies from MUSE and 2) determine their systemic redshifts through rest-frame NIR spectroscopy with KMOS/MOSFIRE (as well as rest-UV features from MUSE; § 6.2). We then 3) turn to ALMA to stack the CO and [C I] signal from the ASPECS data, as well as the 1.2 mm dust continuum (§ 6.3). We do not detect any (line) emission in the stacks (at the 3σ level) and discuss the implications of this non-detection on metallicity, the CO-to-H_2 conversion factor (α_{CO}) and gas-to-dust ratio (δ_{GDR}) in § 6.4. The results highlight that the metallicity evolution of star-forming galaxies makes it increasingly challenging to infer the molecular gas content at higher redshifts, which warrants the further theoretical and observational exploration of alternative tracers, in particular the [C II] λ158 μm line.

Throughout this paper, we report wavelengths in vacuo and magnitudes in the AB system (Oke & Gunn, 1983), and adopt a Chabrier (2003) initial mass function. We use log to denote $\log_{10}$ and ln for the natural logarithm. We adopt a concordance cosmology with $H_0 = 70\,\mathrm{km\,s^{-1}\,Mpc^{-1}}$, $\Omega_m = 0.3$ and $\Omega_\Lambda = 0.7$, in good agreement with the measurements from Planck Collaboration et al. (2016).

6.2 Observations and sample selection

6.2.1 Parent sample selection and physical properties

We construct a parent sample of galaxies from the MUSE HUDF Survey Data Release 2 catalog,[42] which is an updated and revised version of the DR1 catalog (Bacon et al., 2017; Inami et al., 2017). In short, the catalog contains both emission line-selected sources (from ORIGIN; Mary et al., 2020) and continuum-selected sources (from the *Hubble Space Telescope (HST)* catalog by Rafelski et al. 2015) for which the redshifts are determined automatically. These sources have subsequently been verified by several independent groups of experts that inspect the redshift, the multiwavelength counterpart associations, and assign a confidence flag (ZCONF; where confidence $\geq$ 2 implies a secure redshift, determined by at least two spectral features). Specifically, we use the following criteria:

- Select all objects with $3.0115 < z < 3.812$ and ZCONF ≥ 2, that have a *HST* counterpart in the Rafelski et al. (2015) catalog.

- Restrict to objects that lie within the 4.55 arcmin^2 region of the ASPECS Band 3 mosaic where the sensitivity is $\geq$ 40% of the primary beam peak sensitivity at 99.5 GHz.

---

[42] DR2 v0.1; R. Bacon, *et al.*, in prep.

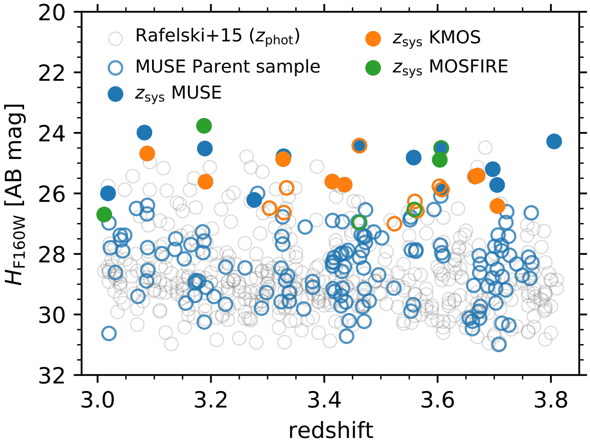

Figure 6.1: The H_{F160W}-band magnitude of the galaxies considered in this paper as a function of redshift. The open circles show the parent sample of all galaxies with $3.0115 \leq z < 3.812$ within the ASPECS field ($\geq$ 40% of the primary beam peak sensitivity) that have a MUSE redshift (from Lyα λ1216) in blue, while the gray circles show all galaxies in the same field with a photometric redshift (Rafelski et al., 2015). Galaxies targeted for KMOS or MOSFIRE follow-up are shown in orange and green, respectively. The filled circles show galaxies for which we obtained a systemic redshift measurement from MUSE (blue), KMOS (orange) or MOSFIRE (green).

- Remove three X-ray detected sources that are classified as having an active galactic nucleus (AGN; MUSE-1051, MUSE-1056 and MUSE-6672), based on the *Chandra* 7 MS data (Luo et al., 2017).

There are a total of 168 galaxies in the parent sample constructed this way. The H_{F160W} magnitude of the parent sample is shown as a function of redshift in Figure 6.1. Because of the sensitivity of MUSE to faint emission line sources, it consists almost exclusively of galaxies that are selected by their Lyα λ1216-emission. Only six galaxies are not marked as such: one is MUSE-50, which does show double peaked Lyα-emission on top of strong Lyα-absorption, as well as strong UV lines. The other five indeed show little Lyα-emission: one is a faint C IV $\lambda\lambda$1548, 1551-only-emitter, while the other four have bright enough UV continuum to have their systemic redshifts determined from absorption lines (see § 6.2.2).

Because the Lyα emission may peak in the halo of a galaxy, the association of a MUSE source with an *HST* counterpart can be ambiguous and is typically resolved on during the redshift determination process. The associations adopted here are listed in Table 6.2 and are in all cases supported by a second tracer of the systemic redshift. In the case of MUSE-6518, the photometry is completely blended with a $z = 0.83$ foreground object and we do not use it to obtain physical properties.

We determine a stellar mass (M_*) and star-formation rate (SFR) for all galaxies in the parent sample by fitting eleven bands of *HST* (Rafelski et al., 2015) and four bands of *Spitzer*/IRAC photometry, using the high-z extension of the spectral energy distribution fitting code MAG-

PHYS (Da Cunha et al., 2008, 2015). As in Labbé et al. (2006, 2010, 2015), the deblended *Spitzer*/IRAC photometry was measured with MOPHONGO, using the *HST* observations as a template, in the deep $\sim$ 200-hour data from the GREATS program (M. Stefanon, et al., in prep.). The latter provides constraints on the rest-frame optical part of the spectral energy distribution redward of the 4000-Å break and is critical to pin down the stellar masses of our galaxies. The results are listed in Table 6.2, for the galaxies in the systemic redshift sample.

As part of the DR2, the spectra of all galaxies are modeled with PYPLATEFIT (R. Bacon, *et al.*, in prep.), the Python implementation of the spectrum fitting code PLATEFIT, originally developed for the *Sloan Digital Sky Survey* (Tremonti et al., 2004; Brinchmann et al., 2004, 2008). The most salient features of PYPLATEFIT, relevant to this work, are that it can simultaneously model both the emission- and absorption lines, as well as the stellar continuum, allowing for velocity differences between groups of lines (such as Lyα and other UV lines). All lines are modeled using Gaussians except Lyα, for which a (double) asymmetric Gaussian[43] is used (double if the Lyα line is double-peaked).

6.2.2 Measurement of systemic redshifts

We obtain systemic redshifts for galaxies in our parent sample from either the rest-frame UV features using MUSE or the rest-frame optical emission lines with near-IR spectroscopy. For the near-IR follow-up, targets were selected by their $H_{\rm F160W}$ magnitude (as a proxy for stellar mass) and the absence of a systemic redshift from MUSE in the DR1 reductions. Fainter targets were sometimes observed because brighter targets were no longer accessible given the small size of the HUDF and physical limitations in the positioning arms and slits of multi-object spectrographs.

MUSE

For a subset of galaxies we can determine the systemic redshift directly from the MUSE spectra, using the weaker rest-frame UV emission lines, or absorption features. We identify objects in the parent sample that are cataloged as having S/N $>$ 3 in at least one UV emission line. We focus specifically on O III] $\lambda\lambda$1661, 1666 S III] $\lambda\lambda$1883, 1892, C III] $\lambda\lambda$1907, 1909 and a selection of absorption lines,[44] that trace the systemic redshift. We also fit narrow He II λ1640 together with the emission lines, finding it at a similar velocity offset as the other UV lines. We do not use the resonant lines, such as C IV $\lambda\lambda$1548, 1551, which can be offset from the systemic velocity like Lyα. To identify absorption line redshifts, we inspect all objects with $V_{\rm F606W} \leq 27$ and/or $i_{\rm F775W} \leq 27$, finding that we can determine these in several galaxies down to $i_{\rm F775W} = 26$. We use PYPLATEFIT to fit the selected spectra, performing 200 bootstrap iterations to obtain a more robust estimate of the uncertainties (both on Lyα and the other features). We only keep the objects that remain at S/N $>$ 3.5 in at least one emission line or

---

[43] Also known as the Skew normal distribution, $f(x) = 2\phi(x)\Phi(\gamma x)$, where $\phi(x)$ is the standard normal (Gaussian) distribution, $\Phi(x)$ is the cumulative distribution function for a standard normal distribution, and γ is the skewness parameter.

[44] Si II λ1260, O II λ1302, Si II λ1304, C II λ1335, Si IV $\lambda\lambda$1394, 1403, Fe II $\lambda\lambda$1608, 1611, Al II λ1671 and Al II $\lambda\lambda$1854, 1862.

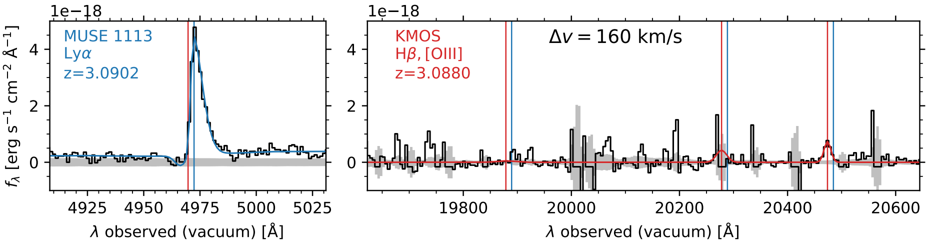

Figure 6.2: Rest-frame ultraviolet and optical spectra for the first galaxy in the sample with near-infrared follow-up. The *left* panel shows the MUSE spectrum surrounding the Lyα line. The *right* panel shows the continuum subtracted KMOS spectrum around the Hβ λ4863 and [O III] $\lambda\lambda$4960, 5008 lines. In both panels the vertical blue and red lines indicate the redshift of Lyα and the systemic redshift, respectively, determined from the fit to the spectrum (shown in the same color). This particular galaxy is detected in Lyα λ1216 and [O III] λ5008, but not in Hβ λ4863, showing a positive velocity offset between the red peak of Lyα and the systemic redshift (note [O III] λ4960 falls on top of a skyline). Spectra of the remaining galaxies with KMOS or MOSFIRE observations are shown in Figure 6.12 in § 6.B.

the sum of the absorption features. In addition, we keep MUSE-1360 as a tentative candidate, having both a tentative detection in the KMOS data and an absorption line redshift at $\mathrm{S/N} = 3$. The $z_{\mathrm{Lyff}}^{\mathrm{red}}$ and z_{sys}, with their bootstrapped uncertainties, are provided in Table 6.2 (where $z_{\mathrm{Lyff}}^{\mathrm{red}}$ is the redshift of the red peak of Lyα). We note that three of these sources were also part of the study of Lyα-velocity offsets by Verhamme et al. (2018).

In principle, one could estimate the systemic redshift by using half of the peak separation for Lyα-lines with a blue bump (Verhamme et al., 2018). Indeed, a few galaxies in our sample also show blue bump-emission. However, systematic searches for blue-bump Lyα-emitters are still on-going and we therefore do not include such a sample at this stage. Furthermore, the presence of a blue bump requires specific radiative transfer conditions and selecting a sample in such a way may introduce a bias in the stack.

KMOS

The KMOS observations were taken in two ESO periods, as part of 099.A-0858(A) (PI: Bouwens) and 0101.A-0725(A) (PI: Boogaard). We used the HK grating (with a spectral resolution of $\lambda/\Delta\lambda \approx 1800$) in 5 Observing Blocks (OBs) per period, with an ABA ABA AB sky-offset pattern between the science (A) and sky (B) frames with 300 s integrations and 0.″2 dithering offsets. In total we targeted 17 galaxies, with (final) on source times ranging between 200 and 250 minutes. We also included a bright quasar on all masks to control the astrometry, from which we measure the image quality to be around 0.″75 and 0.″85 in the reduced P99 and P101 data, respectively.

We reduce the data using the ESO KMOS pipeline version 2.1.0 (Davies et al., 2013), using the standard star observations for the zeropoint, response and telluric correction. We enable the `background` flag to correct for differences in the residual background level between the exposures by applying a constant offset, estimated by taking the mode of the pixel values after excluding the brightest 25%. We discard the data from one detector for the second A frame of the first OB in period 99, which shows a strong background offset. We experimented with further reducing the sky line residuals using the `sky-tweak` and `molecfit` options of the pipeline, but found that these sometimes introduces artifacts in the data. As our lines were selected to be away from the sky lines as much as possible, we therefore do not apply these corrections. Because of the density of the skylines around [O ii] λ3727 in the H-band, we focus on the Hβ λ4863 and [O iii] $\lambda\lambda$4960, 5008 in the K-band. We apply radial velocity corrections[45] to shift every reduced A-B frame to the solar system barycentric frame (the mean $\langle v_r \rangle = 17.3$ km s^{-1}).

We correct for positional shifts between the different OBs by centering on the continuum position of the reference quasar, which we model with a 2D Gaussian. As objects were placed on different IFUs between periods, their position relative to the reference quasar change. We therefore first combine and analyze the data from each period separately. To identify the spatial position of each (emission line-only) object on its IFU in each period, we (i) extract spectra at the a-priori expected position (that is, the quasar position or the center of the cube) using the 2D fit of the reference quasar as a spatial model, (ii) identify the brightest spectral line, [O iii] λ5008, based on the Lyα redshift and determine its central wavelength and line width using a Gaussian fit, (iii) collapse the cube over the channels with line emission to make a 'narrow band', through multiplication with the Gaussian fit along the wavelength axis, and (iv) identify the spatial position in the narrow band image. We iterate steps (i)-(iv) until we converge on spatial position. Finally, we combine the data from both periods using the best positions and repeat the same steps to obtain the final spectra.

We conservatively only consider the objects for which we can identify the line(s) in each half of the data separately, which gives strong confidence that the line(s) are not (caused by) sky line residuals. We exclude one source where the blueshift of the lines relative to Lyα resulted in them being too close to the skylines to determine the centroid and four more sources where a tentative feature was only seen in one period. In total, we confidently detect the rest-frame optical line(s) in 7/17 galaxies. As an example, we show the MUSE and KMOS spectrum for one of the galaxies in Figure 6.2. The spectra of the remaining galaxies are shown in Figure 6.12 in § 6.B.

Finally, we determine the redshift by simultaneously fitting Gaussians (in vacuo) to the Hβ λ4863 and [O iii] $\lambda\lambda$4960, 5008 lines (using LMFIT; Newville et al. 2019b). We use the inverse of the error spectrum as weights and subtract a running median continuum from the spectrum prior to the fitting. The resulting redshifts are reported in Table 6.2.

MOSFIRE

The MOSFIRE observations were taken in the night of 28 November 2018 as part of program 2018B_N182 (PI: Riechers). We observed a single K band mask with 0.″7 slits ($\lambda/\Delta\lambda \approx 3610$). We used an AB dither pattern with 180 second exposures, totaling to 108 minutes of exposure time on source, with an average seeing of 0.″7. The data were reduced using the

---

[45] $\lambda' = \lambda\sqrt{(1 + v_r/c)/(1 - v_r/c)}$, where λ' and λ are the corrected and uncorrected wavelengths, respectively, c is the speed of light and v_r is the radial velocity correction to the solar system barycenter, computed with `astropy.coordinates.SkyCoord.radial_velocity_correction`.

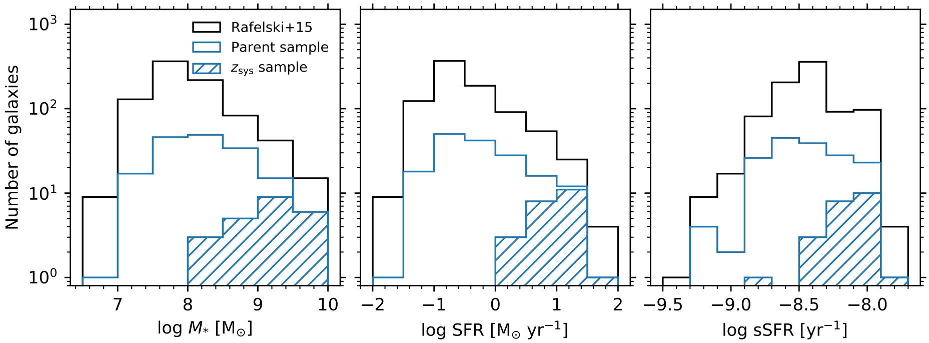

Figure 6.3: Histograms of the stellar mass (M_*), star formation rate (SFR) and specific SFR (sSFR = SFR/M_*) of the galaxies for which we determine a systemic redshift ($z_{\rm sys}$), compared to the parent sample from MUSE at $3.0115 \le z < 3.812$ and all galaxies from the photometric redshift catalog by Rafelski et al. (2015).

standard MOSFIRE Data Reduction Pipeline (Release 2018),[46] using the Neon arc lamps for the wavelength calibration. As our objects generally do not show any continuum, we first manually identify (candidate) emission lines in the rectified, two dimensional spectra (based on the Lyα redshift). We then optimally extract the one dimensional spectra using a Gaussian model for the spatial profile. As all data were taken on a single night, we apply the radial velocity correction to the final spectra ($v_r = -9.2\,\mathrm{km\,s^{-1}}$).[47]

In total, we detect the rest-frame optical lines in 4/7 of the galaxies on the mask that are part of our parent sample (including MUSE-6518, with blended *HST* photometry). Their spectra are shown in Figure 6.12. We measure the redshifts as described in § 6.2.2 and report the results in Table 6.2.

6.2.3 Final systemic redshift sample

In total, we use MUSE, KMOS and MOSFIRE to obtain systemic redshifts for 24 galaxies, 20 of which are originally identified by their Lyα-emission, with an average redshift of $\langle z \rangle = 3.45$. The $H_{\rm F160W}$ magnitude of the final sample is shown in comparison to the MUSE parent sample in Figure 6.1. We have a systemic redshift for most galaxies in the parent sample down to $H_{\rm F160W} = 26$. Because the parent sample is Lyα-selected, this raises the question how representative our sample is for the broader population of galaxies at these epochs. We therefore compare our (parent) sample to all galaxies at the same redshift and over the same field, from the photometric redshift catalog by (Rafelski et al., 2015, updated with the MUSE redshifts), after excluding the X-ray AGN (Luo et al., 2017, as we did for the parent sample), see Figure 6.1.

We show a histogram of the physical properties of the galaxies in Figure 6.3. The median

---

[46] https://github.com/Keck-DataReductionPipelines/MosfireDRP

[47] See footnote 45

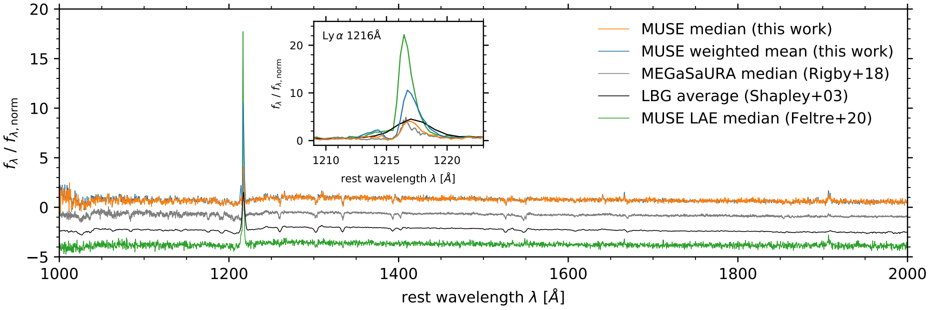

Figure 6.4: Composite MUSE spectrum of the sample, from both weighted mean (blue) and median (orange) stacking (at 0.3 Å resolution) using the systemic (non-Lyα) redshifts. We compare to the average Lyman Break Galaxy (LBG) spectrum at $z \sim 3$ (black) from (Shapley et al., 2003, 1 Å resolution), the composite spectrum of 14 strongly lensed, star-forming galaxies at $1.6 < z < 3.6$ from the MEGaSAURA sample (Rigby et al. 2018; the pivot normalized, median stack at 0.1 Å resolution) and the composite MUSE spectrum of all 220 LAEs at $2.9 < z < 4.6$ (Feltre et al., 2020, median stack; note their weighted mean stack is very similar, with slightly stronger Lyα emission). We normalize all spectra to the median flux density at 1267–1276 Å and offset the literature spectra by −1.5, −3, and −4.5 for clarity. The inset shows a zoom-in of the Lyα-line without vertical offsets. Overall, the composite MUSE spectrum is very similar to the LBGs and MEGaSAURA, showing comparable UV continuum and absorption features, slightly stronger UV emission lines, and a comparable strength of the Lyα-line in the median spectrum (notably showing a blue bump). In contrast, the median stack of all LAEs from Feltre et al. (2020) shows significantly stronger Lyα-emission, even when compared to the weighted mean spectrum of our galaxies.

stellar mass and SFR of the sample is $10^{9.1}$ $M_\odot$ and 10 $M_\odot$ yr^{-1}. The sample encompasses $\geq$ 50% of the galaxies in the MUSE parent sample in the bins down to $M_* \geq 10^9$ $M_\odot$ and SFR ≥ 3 $M_\odot$ yr^{-1}, and $\geq$ 20% of the galaxies in the broader photometric catalog, down to the same limits.

Our galaxies are faint Lyα-emitters in comparison to narrow band-selected samples. The typical Lyα luminosity of our sample is $L_{\rm Ly\alpha} = 10^{42}$ erg s^{-1} $\approx 0.2\,L^*_{\rm Ly\alpha}$ at $z = 3.5$ (e.g., Ouchi et al., 2008; Drake et al., 2017; Herenz et al., 2019). The average rest-frame equivalent-width[48] $\langle {\rm EW}^0_{\rm Ly\alpha}\rangle \approx 20$ Å of our sample is also small, especially when considering that ≈ 25 Å is the typical lower limit for the definition of a (narrow band-selected) Lyα-emitter (or LAE). This is likely due to our selection towards objects that are bright in $H_{\rm F160W}$. As such, our galaxies are not necessarily comparable to the typical sample of LAEs, but arguably more similar to the average population of (low-mass) star-forming galaxies

To illustrate this point, we stack the MUSE spectrum of all the galaxies in our sample, using the systemic redshifts, following Feltre et al. (2020). We perform a median and weighted mean stack, after normalizing each of the spectra by the median flux density at 1267 − 1276 Å (matching Rigby et al. 2018). The result is shown in Figure 6.4. We compare the composite

---

[48] The rest-frame equivalent width is computed by PYPLATEFIT, from the total flux in Lyα (including a possible blue bump) over the modeled continuum flux density at 1216Å (defined such that a positive value indicates emission).

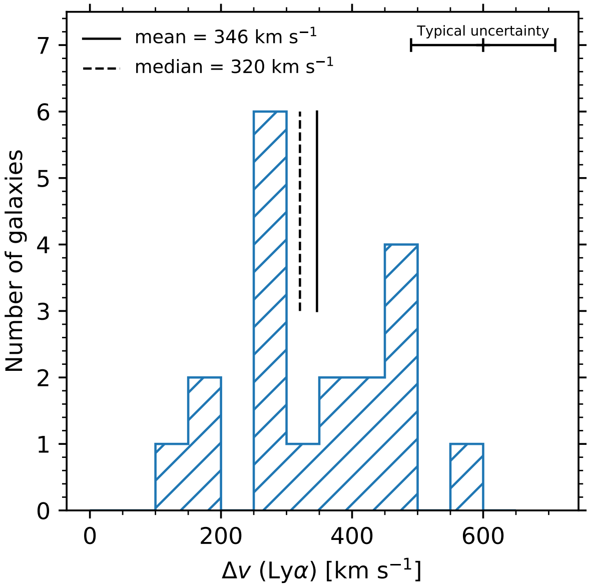

Figure 6.5: Histogram of the velocity offset of Lyα λ1216 with respect to the systemic redshift, Δv(Lyα). The vertical lines indicate the mean and median velocity offset in the sample. The typical $\pm 1\sigma$-uncertainty on the velocity offset is indicated in the top right.

MUSE spectrum to the average spectrum of $z \sim 3$ Lyman Break Galaxies (LBGs; Shapley et al., 2003), the composite spectrum of 14 strongly lensed, star-forming galaxies at $1.6 < z < 3.6$ from the MegaSaura sample (Rigby et al., 2018) and the composite MUSE spectrum of all 220 LAEs at $2.9 < z < 4.6$ from Feltre et al. (2020). Overall, the similarities in the literature spectra of LBGs and star-forming galaxies and the (median) composite spectrum of our sample, with significantly weaker Lyα-emission than the average LAE spectrum, support the case that our galaxies are more similar to the population of star-forming galaxies at these epochs.

6.3 Results

6.3.1 Velocity offsets

We plot the velocity offset of Lyα λ1216 with respect to the systemic redshift in Figure 6.5, defined as $\Delta v(\mathrm{Ly}\alpha) = c(z^{\mathrm{red}}_{\mathrm{Lyff}} - z_{\mathrm{sys}})/(1 + z_{\mathrm{sys}})$, where c is the speed of light. Our galaxies show a mean velocity offset of $\langle \Delta v(\mathrm{Ly}\alpha) \rangle = 346\,\mathrm{km\,s^{-1}}$, with a range from 100 to 600 km s^{-1}.

For comparison, the mean $\Delta v(\mathrm{Ly}\alpha) \approx 200 - 250\,\mathrm{km\,s^{-1}}$ in the LAE samples at $z = 2 - 3$ (Erb et al., 2014; Trainor et al., 2015), while the $z \sim 3$ LBG sample from Shapley et al. (2003)

Table 6.1: Lines stacked in this paper.

Transition (1)	ν_0 (GHz) (2)	$z_{\rm min}$ (3)	Band (4)	N (5)	$S_\nu \Delta v$ (mJy km s^{-1}) (6)	$S_\nu \Delta v$ (mJy km s^{-1}) (7)	L' (K km s^{-1} pc^2) (8)
Systemic redshift sample (Figure 6.6)							
CO $J = 4 \rightarrow 3$	461.04	3.0115	3	23	-3.2 ± 4.2	<12.7	$<4.0 \times 10^8$
[C I] $^3P_1 \rightarrow {}^3P_0$	492.16	3.2823	3	16	4.9 ± 6.8	<20.5	$<5.6 \times 10^8$
CO $J = 9 \rightarrow 8$	1036.91	2.8122	6	23	33.3 ± 12.7	<38.1	$<2.3 \times 10^8$
CO $J = 10 \rightarrow 9$	1151.99	3.2352	6	16	7.4 ± 16.6	<49.8	$<2.5 \times 10^8$
Lyα-selected galaxies only							
CO $J = 4 \rightarrow 3$	461.04	3.0115	3	18	-7.3 ± 5.0	<15.0	$<4.7 \times 10^8$
[C I] $^3P_1 \rightarrow {}^3P_0$	492.16	3.2823	3	12	11.0 ± 7.9	<23.8	$<6.5 \times 10^8$
CO $J = 9 \rightarrow 8$	1036.91	2.8122	6	19	39.5 ± 14.0	<42.2	$<2.6 \times 10^8$
CO $J = 10 \rightarrow 9$	1151.99	3.2352	6	13	16.2 ± 18.8	<56.5	$<2.8 \times 10^8$

Notes. $\langle z \rangle = 3.45$, $\Delta v = 300$ km s^{-1}. (1) Stacked transition (2) Rest frequency (3) Minimum redshift at which the transition is covered by ASPECS. (4) Band that contains transition. (5) Number of objects in stack. (6) Line flux in stack. (7) 3σ upper limit on line flux. (8) 3σ upper limit on line luminosity.

shows a greater mean velocity offset of 650 km s^{-1}. The relatively large velocity offsets imply a larger H I column density and lower Lyα escape fraction, consistent with the low EW$^0_{\rm Ly\alpha}$ of our galaxies (Shapley et al., 2003; Erb et al., 2014; Yang et al., 2017b).

The broad distribution in Figure 6.5 also reflects the smoothing function by which the stacking signal would be diluted if $z^{\rm red}_{\rm Ly\alpha}$ would be used for stacking, in particular because the ALMA data has a higher velocity resolution. This highlights the need for systemic redshifts.

6.3.2 ALMA Stacking

With the systemic redshifts in hand, we turn to the ALMA data. We use the ASPECS Band 3 (González-López et al., 2019; Decarli et al., 2019) and Band 6 (González-López et al., 2020; Decarli et al., 2020) datacubes at their native resolution ($\approx$ 20 km s^{-1} in both cases). The root-mean-square (rms) error spectra reach ≈ 0.2 and 0.5 mJy beam^{-1} channel^{-1} in Band 3 and Band 6, respectively (at the center of the field, varying with frequency).

Before extracting the spectra, we first shift the ALMA cubes from the Kinematic Local Standard of Rest (LSRK) to the Barycentric frame, using the CASA task `imreframe` ($\Delta v = -16.78$ km s^{-1}), such that all our spectroscopic data are on the same velocity frame. We then extract pixel spectra at the *HST* positions (Rafelski et al., 2015) of our galaxies, after correcting for the known astrometric offset ($\Delta\alpha = 0\farcs076$, $\Delta\delta = -0\farcs279$; Dunlop et al. 2017, consistent with Franco et al. 2020). These spectra should contain all the flux as our sources are expected to be unresolved by the ASPECS synthesised beam ($1\farcs8 \times 1\farcs5$ in Band 3 and $1\farcs5 \times 1\farcs1$ in Band 6). Their spatial extent in the rest-frame UV is significantly smaller, with a median effective radius in $H_{\rm F160W}$ of $\approx 0\farcs2$ (van der Wel et al., 2012).

Inspecting the spectra around the systemic redshift, none of the galaxies are individually detected in their CO or [C I] emission lines at the 3σ level. We therefore stack the spectra

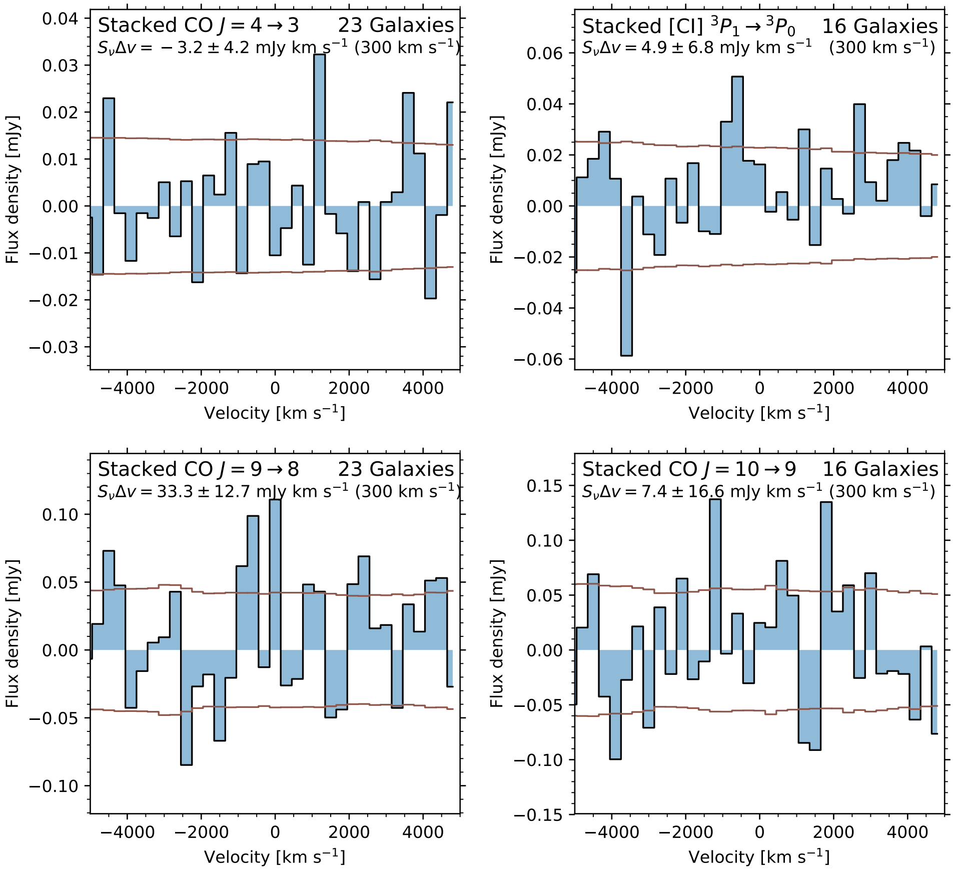

Figure 6.6: Stacked spectra of the ^{12}CO and [C I] transitions of the full sample. The spectrum is shown in blue and the brown line shows the root-mean-square noise (propagated through the $1/\sigma^2$-weighting of the stack). The stacked transition, the number of galaxies in the stack, the integrated line flux in the zero-velocity channel and the channel width (300 km s^{-1}) are indicated in each panel. We do not detect any emission in any of the transitions and provide 3σ upper limits in Table 6.1.

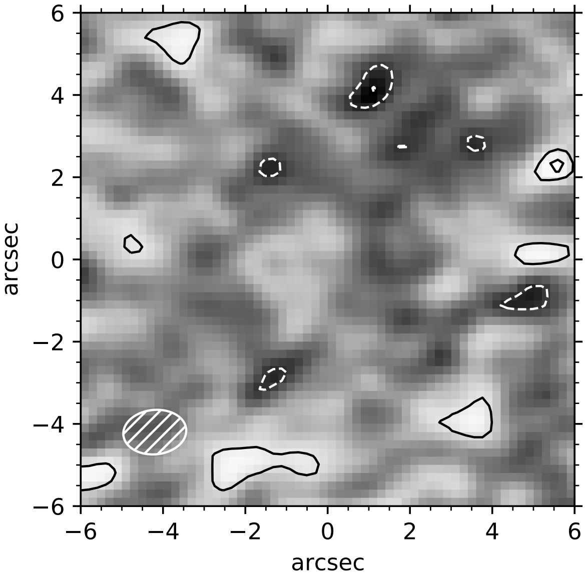

Figure 6.7: Stack of the 1.2 mm dust continuum. The cutout size is $12'' \times 12''$ and the synthesised beam is indicated in the bottom left corner. Contours are drawn starting at $\pm 2\sigma$ in steps of $\pm 1\sigma$ (dashed contours indicate negative signal). No emission is detected at the 3σ level, implying an upper limit of $9\,\mu$Jy.

as follows (Boogaard et al., 2020, cf. Spilker et al. 2014). We first create a grid in velocity space, centered around zero, with 300 km s^{-1} wide channels. The channel width was chosen based on the mean rest-frame UV/optical line-width ($\approx$ 200 km s^{-1}), such that $> 90\%$ of the stacked line flux is expected to fall within the single central channel. We convert each observed spectrum to velocity space, centered around the line, and bin it onto the velocity grid. We then stack the spectra by taking the $1/\sigma^2$-weighted mean in each velocity channel (where σ is the error) and determine the uncertainty by propagating the error spectrum in the same manner. We finally measure the flux density and the corresponding uncertainty in the zero-velocity channel.

The stacked spectra are shown in Figure 6.6. None of the lines are detected in the stack at a signal-to-noise ratio greater than three. The stack of CO $J = 9 \rightarrow 8$ shows some signal at the $2 - 3\sigma$ level, but we do not consider this a detection. We compute 3σ upper limits on the integrated line flux, $S_\nu \Delta v$, from the uncertainty in the zero-velocity channel of the stacked spectrum (at $300\,\mathrm{km\,s^{-1}}$ resolution). We determine the corresponding upper limits on the line luminosities via

$$L' = 3.255 \times 10^7\, S_\nu \Delta v\, d_L^2\, \nu_{\mathrm{obs}}^{-2} (1+z)^{-3}\ \mathrm{K\,km\,s^{-1}\,pc^2} \tag{6.1}$$

(Solomon et al., 1992b; Carilli & Walter, 2013), adopting the luminosity distance (d_L) and observed frequency (ν_{obs}) at the average redshift of the sample, $z = 3.45$. The results can be found in Table 6.1. We also perform additional stacks, including only the galaxies with the highest stellar masses ($M_* \geq 10^{9.0}$, $\geq 10^{9.5}$ and $\geq 10^{10}\,\mathrm{M}_\odot$) and the highest star formation rates (SFR ≥ 3.2 and $\geq 10\,\mathrm{M}_\odot\,\mathrm{yr}^{-1}$), but do not obtain any detections.

None of the galaxies are individually detected at the 3σ level in the deep 1.2 mm dust continuum map (González-López et al., 2020; Aravena et al., 2020). In addition to the line stack, we therefore also perform a weighted mean stack of the 1.2 mm dust continuum data for the full sample (following the approach from J. Bouwens et al., 2016; Bouwens et al., 2020, again applying the astrometric offset). We do not obtain a detection, measuring a flux of $S_\nu = 1 \pm 3\,\mu\mathrm{Jy}$ (Figure 6.7), implying an upper limit of $\leq 9\,\mu\mathrm{Jy}$ (3σ).

6.4 Discussion

6.4.1 Molecular gas masses

Stacking the $\langle z \rangle = 3.45$ star-forming galaxies in the HUDF by their systemic redshifts, we find that $L'_{\mathrm{CO}\,J=4\rightarrow3} \leq 4.7 \times 10^8\,\mathrm{K\,km\,s^{-1}\,pc^2}$. This result puts an upper limit on the molecular gas mass via

$$M_{\mathrm{mol}} = \alpha_{\mathrm{CO}} r_{J1}^{-1} L'_{\mathrm{CO}\,J\rightarrow J-1}, \tag{6.2}$$

where α_{CO} is known as the CO-to-H$_2$ conversion factor (a light-to-mass ratio) and r_{J1} is the excitation correction, needed to convert the observed CO luminosity to $L'_{\mathrm{CO}\,J=1\rightarrow0}$. There is no direct measurement of the CO excitation in the galaxies under consideration. Valentino et al. (2020a) measured an average $r_{41} = 0.36 \pm 0.06$ in their sample of star-forming galaxies at $z = 1.25$, while Tacconi et al. (2018) assume an average $r_{41} = 0.42$, constant with redshift. Boogaard et al. (2020), however, have shown that there is significant evolution in the CO excitation of gas mass-selected samples, with the average r_{41} increasing from 0.3 up to 0.6 between $z = 1{-}2$ and $z = 2{-}3$. Indeed, Dessauges-Zavadsky et al. (2017) find $r_{41} = 0.60 \pm 0.17$ in the strongly lensed MACSJ0032-arc at $z = 3.6$, with a similar $M_* \approx 10^{9.7}\,\mathrm{M}_\odot$ as our sample average (though significantly higher SFR $\approx 50\,\mathrm{M}_\odot\,\mathrm{yr}^{-1}$). If the excitation scales with SFR surface density (Daddi et al., 2015; Valentino et al., 2020a; Boogaard et al., 2020), this may suggest the excitation to be lower in our galaxies on average. We therefore loosely assume that $r_{41} = 0.5 \pm 0.2$, broadly encompassing the literature values. Note that higher excitation implies a smaller gas mass (Equation 6.2). As we are dealing with an upper limit on the gas mass in the first place, we effectively assume a lower limit on the excitation of $r_{41} \geq 0.3$, in good agreement with observations.

A major uncertainty in the molecular gas estimate comes from α_{CO}. For star forming galaxies at high redshift 'Galactic' conversion factors are typically assumed, consistent with observations in massive star forming galaxies (Daddi et al., 2010a). However, the value of α_{CO} has been observed to increase strongly at low metallicity (Z; Maloney & Black 1988; Israel 1997), where the decreased shielding leads to dissociation of CO deeper into the clouds (e.g., Wolfire et al. 2010, see Bolatto et al. 2013 for a review). Several calibrations for the metallicity dependence of the CO-to-H$_2$ conversion factor exist in the literature, both determined empirically (e.g., Leroy et al., 2011; Magdis et al., 2012; Schruba et al., 2012; Genzel et al., 2012; Sandstrom et al., 2013) as well as theoretically (e.g., Wolfire et al. 2010, see also Bolatto et al. 2013).

We adopt the relation from Genzel et al. (2015, also adopted by Tacconi et al. 2018; Dessauges-Zavadsky et al. 2020),

$$\alpha_{\rm CO}(Z) = \alpha_{\rm CO}^{\rm MW} \times \sqrt{10^{-1.27(12+\log({\rm O/H})-8.67)}} \tag{6.3}$$

$$\times \sqrt{0.67 \exp\left(0.36 \times 10^{-(12+\log({\rm O/H})-8.67)}\right)}, \tag{6.4}$$

which is the geometrical mean of the curves from Genzel et al. (2012, which follows a power-law, as the other literature relations do) and Bolatto et al. (2013, which has a steeper, exponential increase towards very low metallicities). Here, $12 + \log({\rm O/H})$ is the gas-phase oxygen abundance, measured on the Pettini & Pagel (2004) scale (for conversion between metallicity scales see Kewley & Ellison 2008), calibrated to a solar abundance of $12 + \log({\rm O/H})_\odot = 8.67$ (Asplund et al., 2009), and $\alpha_{\rm CO}^{\rm MW} = 4.36\,{\rm M}_\odot({\rm K\,km\,s^{-1}\,pc^2})^{-1}$, which includes a factor 1.36 for helium (Strong & Mattox, 1996).

To obtain metallicities in the absence of a direct tracer, the mass metallicity relation can be used (see § 6.4.2 for discussion). Genzel et al. (2015) determined the following mass-metallicity relation.

$$12 + \log({\rm O/H})_{\rm PP04} = a - 0.087\left(\log M_* - b(z)\right)^2, \tag{6.5}$$

where $a = 8.74(0.06)$ and $b(z) = 10.4\,(0.05) + 4.46\,(0.3)\log(1 + z) - 1.78\,(0.4)\log^2(1 + z)$ (uncertainties in brackets), which is determined by combining several relations at different redshifts (Erb et al., 2006; Maiolino et al., 2008; Zahid et al., 2014; Wuyts et al., 2014). Notably, this relation approaches that of Maiolino et al. (2008) determined at $z = 3.5$.

Alternatively, we can determine $M_{\rm mol}$ from [C I], under the assumption of an excitation temperature $T_{\rm ex}$ and a neutral atomic carbon abundance (Weiß et al. 2005; see Boogaard et al. 2020 for a detailed description). We adopt $T_{\rm ex} = 30$ K (Walter et al., 2011, note that the atomic carbon mass is not a strong function of excitation temperature above $T_{\rm ex} = 20$ K) and an abundance of $[{\rm C\,I}]/[{\rm H_2}] = 2 \times 10^{-5}$ (Valentino et al., 2018; Boogaard et al., 2020). We will revisit the latter assumption in § 6.4.2.

The dust can be used as a third tracer of the molecular gas mass. We compute the dust mass by relying on assumption that the Rayleigh-Jeans (RJ) tail of the dust blackbody at long wavelengths is nearly always optically thin (Scoville et al., 2016). Specifically, we follow Magnelli et al. (2020) and assume a mass-weighted mean dust temperature of $\langle T_{\rm dust}\rangle_{\rm M} = 25$ K and a dust emissivity spectral index of $\beta = 1.8$. As argued by Scoville et al. (2016), the cold dust is the dominant contributor to the dust mass and the RJ-tail of the dust emission, and recent studies by *Planck* and *Herschel* have found the temperature to be in the range of 15–35 K (e.g., Abergel et al., 2011; Magnelli et al., 2014). Varying beta between $1.5 - 2.0$ (the range typically assumed for the larger grains that dominate the far-infrared emission, e.g., Da Cunha et al. 2008) impacts the dust masses by 20–40%. Varying the dust temperature between 15–35 K has a more significant impact on the inferred gas masses, ranging from a factor 5.0 to 0.5, because the observations at rest-frame 275 μm start probing the emission away from the RJ-tail and closer to the peak (this is further discussed in § 6.4.2). We correct for the impact of the Cosmic Microwave Background on the equilibrium dust temperature and observed flux density (da Cunha et al., 2013), which increases the inferred mass by 10%.

To convert the dust masses to gas masses, we assume a metallicity dependent gas-to-dust ratio ($\delta_{\mathrm{GDR}} \simeq M_{\mathrm{mol}}/M_{\mathrm{dust}}$), with $\delta_{\mathrm{GDR}}(\mathrm{Z}_\odot) = 100$ (Draine et al., 2007), making the common assumption that the gas in our galaxies at $z = 3.45$ is predominately molecular (e.g., Daddi et al., 2010b; Genzel et al., 2015; Tacconi et al., 2018). The $\delta_{\mathrm{GDR}} \propto Z^\gamma$ has been observed to decrease close to linearly towards sub-solar metallicities (with $\gamma \approx -1$, e.g., Leroy et al., 2011; Magdis et al., 2012; Sandstrom et al., 2013; Saintonge et al., 2013). However, there is increasing evidence of a steeper relation for metallicities below $12 + \log(\mathrm{O/H}) \approx 8.0 - 8.1$; Rémy-Ruyer et al. (2014) find $\gamma \approx -3.1$ in local galaxies, while observations at $z \sim 2$ suggest that $\gamma < -2.2$ (Coogan et al., 2019), in agreement with the fiducial model from Popping et al. (2017a). We explore both regimes, assuming the power-law $\delta_{\mathrm{GDR}}(Z)$ relation from Tacconi et al. (2018) for a shallower increase with metallicity. For a steeper $\delta_{\mathrm{GDR}}(Z)$ at low metallicity, we adopt the broken power law relation from Rémy-Ruyer et al. (2014, the $X_{\mathrm{CO},Z}$-case), which we scale to the same assumptions ($12 + \log(\mathrm{O/H})_\odot = 8.67$; $\delta_{\mathrm{GDR}}(\mathrm{Z}_\odot) = 100$):

$$\delta_{\mathrm{GDR}}(Z) = \begin{cases} 10^{2+\gamma_{\mathrm{H}}(x-8.67)} & \text{for } x > 8.1 \\ 10^{0.8+\gamma_{\mathrm{L}}(x-8.67)} & \text{for } x \leq 8.1, \end{cases} \tag{6.6}$$

with $x = 12 + \log(\mathrm{O/H})$. Here $\gamma_{\mathrm{H}} = -1$ and $\gamma_{\mathrm{L}} = -3.1$ are the power law slopes at high and low metallicity, respectively. The relation from Tacconi et al. (2018) is obtained from Equation 6.6 by taking the $x > 8.1$ solution at all metallicities, with $\gamma_{\mathrm{H}} = -0.85$.

6.4.2 Low metallicity driving a high molecular gas mass-to-light ratio

We show the constraints on the molecular gas mass in the context of the gas-to-stellar mass-ratio ($\mu_{\mathrm{gas}} = M_{\mathrm{mol}}/M_*$) and the gas fraction ($f_{\mathrm{gas}} = M_{\mathrm{mol}}/(M_{\mathrm{mol}} + M_*)$), including a literature sample of CO observations at low and high redshift, in Figure 6.8. At the basis of the literature sample, we take the mass-selected sample of Sloan Digital Sky Survey galaxies at $z = 0$ from xCOLDGASS (Saintonge et al., 2017), together with the massive, main-sequence selected galaxies at $z = 0.5 - 2.5$ from the Plateau de Bure HIgh-z Blue Sequence Survey (PHIBSS1+2) from the Tacconi et al. (2018) compilation, and the galaxies from ASPECS at $z = 1.0 - 3.6$ (Aravena et al., 2019; Boogaard et al., 2019). We supplement these with studies that contain observations of CO in (strongly lensed) star-forming galaxies at $z \geq 3$ from Magdis et al. (2012, 2017, using the updated values from Tan et al. 2013), Dessauges-Zavadsky et al. (2015, 2017, which include two sources from Riechers et al. 2010), Gowardhan et al. (2019) and Cassata et al. (2020, based on the sources from Schinnerer et al. 2016). We convert the literature observations to the metallicity dependent α_{CO} (Equation 6.4; using the mass metallicity relation when needed, Equation 6.5) and adopt $r_{21} = 0.77$ and $r_{31} = 0.55$ (± 0.1; to remain consistent with Tacconi et al. 2018), though we keep the excitation corrections as assumed by the authors in case these are better constrained through additional line measurements (Boogaard et al., 2020; Cassata et al., 2020).[49]

---

[49] For example, in the case of ASPECS, the measured $\langle r_{31} \rangle = 0.8$ (Riechers et al., 2020; Boogaard et al., 2020), implies a factor 1.5× higher gas masses than the average value from Tacconi et al. (2018). Note however that, as

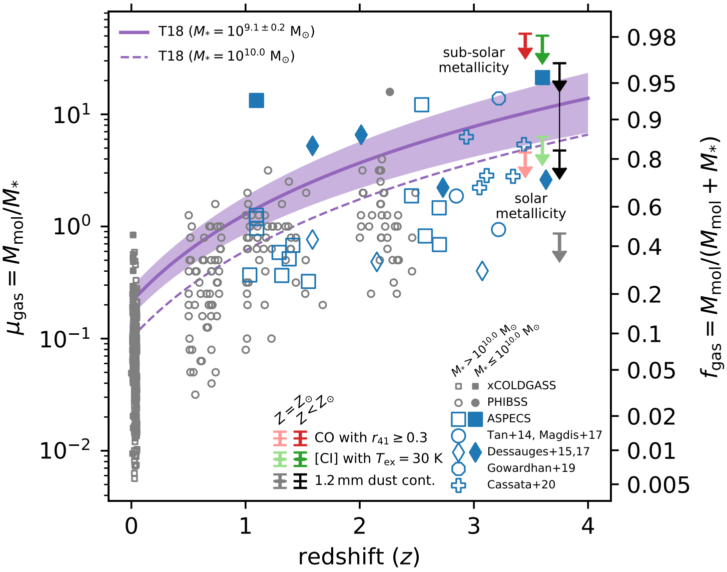

Figure 6.8: The gas-to-stellar mass ratio ($\mu_{\rm gas}$) and gas fraction ($f_{\rm gas}$) as a function of redshift. We show a literature sample of star-forming galaxies with CO measurements, focusing on $z \geq 3$, separating galaxies with $M_* \leq 10^{10}$ M$_\odot$ (filled symbols) and $M_* > 10^{10}$ M$_\odot$(open symbols). Nearly all galaxies from literature are significantly more massive than the $\langle z \rangle = 3.45$ star forming galaxies studied here, which have a median $M_* = 10^{9.1}$ M$_\odot$ and SFR $= 10$ M$_\odot$ yr^{-1}. The upper limit on the gas fraction from CO is shown in red, with the limits at low and high gas fraction corresponding to solar metallicity ($\alpha_{\rm CO}^{\rm MW} = 4.36$; light red) and sub-solar metallicity ($\alpha_{\rm CO} = 50$; dark red), respectively, assuming $r_{41} \geq 0.3$. The green limit shows the constraints from [C I], for a typical abundance of 2×10^{-5} and a factor 8× lower in lighter and darker shading, respectively. The gray and black limits show the constraint from the 1.2 mm dust continuum assuming, in order of increasing gas fraction, $\delta_{\rm GDR} = 100$, 550 and 3300, corresponding to solar metallicity and sub-solar metallicity with different assumptions for the scaling of $\delta_{\rm GDR} \propto Z^\gamma$. We add horizontal offsets to the upper limits from different tracers for clarity. For comparison, we also show the predictions from Tacconi et al. (2018) for main-sequence galaxies with stellar masses $M_* = 10^{9.1\pm0.2}$ M$_\odot$ (solid line with shading; 0.2 dex around the median mass of our sample, where shading also includes the uncertainties in the fit of the scaling relation), and $10^{10.0}$ M$_\odot$ (dashed; above the most massive galaxy in our sample). Under the assumption of solar metallicity conversion factors, the constraints are in tension with the scaling relations from Tacconi et al. (2018) for galaxies in our mass range, while for sub-solar metallicity conversion factors the upper limits are in comfortable agreement.

---

argued in § 6.4.1, differences in the excitation do not affect the upper limit on the gas mass of our star-forming galaxies at $\langle z \rangle = 3.45$, unless the excitation is significantly lower than our (conservative) lower limit.

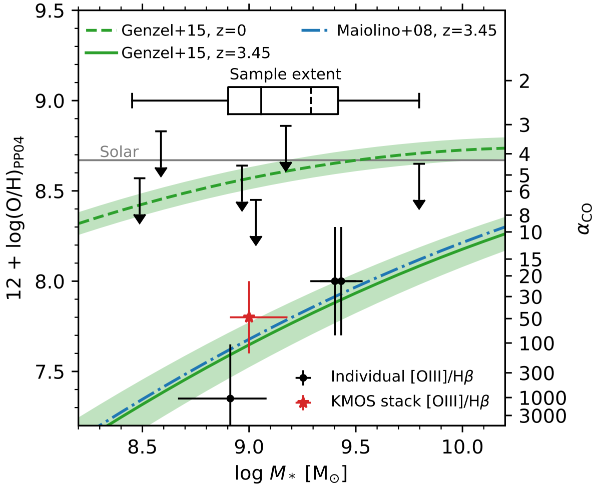

Figure 6.9: Plot of the mass–metallicity (MZ) relation and corresponding $\alpha_{\mathrm{CO}}(Z)$ (Equations 6.4 and 6.5; Genzel et al. 2015), as function of stellar mass (M_*). The constraints on the MZ relation at $z = 3.45$ come from Maiolino et al. (2008). Metallicity is plotted as $12 + \log(\mathrm{O/H})$ on the Pettini & Pagel (2004) scale. The inset shows a boxplot with the whiskers indicating the full stellar mass extent of the sample, the box the interquartile range, the solid line the median, and the dashed line the (linear) mean M_* of the sample. The black points show direct constraints (3σ limits) on the metallicity of a few galaxies via [O III] $\lambda5008$/Hβ $\lambda4863$, with 0.3 dex uncertainty, using the direct method (Curti et al., 2017), conservatively assuming the upper branch solution for the upper limits. The red star shows the average metallicity from the stack of the KMOS spectra (Figure 6.10) at the mean stellar mass (error bars correspond to the 16th and 84th percentile). Overall, the measurements are consistent with the MZ relation at the typical redshift of the sample.

Assuming conversion factors that apply at solar metallicity ($\alpha_{\mathrm{CO}}^{\mathrm{MW}} = 4.36$, $\delta_{\mathrm{GDR}} = 100$), the stacking results imply gas fractions that appear to be in tension with the observed gas fractions in galaxies at $z \geq 3$ at a similar stellar mass (see Figure 6.8). This is in particular true for stringent limit based the dust, which places our low-mass galaxies among the lowest gas fractions observed at $z = 3 - 4$, with $f_{\mathrm{gas}} \leq 0.5$. For CO, the tension becomes more clear once we take into account that our galaxies are over an order of magnitude lower in stellar mass than the typical galaxy studied in molecular gas at high redshift. The gas fraction in star-forming galaxies is observed to increase towards lower masses and expected to be substantial for low-mass galaxies at these epochs (Scoville et al., 2016; Tacconi et al., 2018; Liu et al., 2019). For reference, we plot the predicted gas fraction for a main sequence galaxy with $M_* = 10^{9.1\pm0.2}\ \mathrm{M}_\odot$ from Tacconi et al. (2018),[50] taking into account an extra 0.2 dex uncertainty in the average stellar mass, as well as for $M_* = 10^{10}\ \mathrm{M}_\odot$ (that is, more massive than the most massive galaxy in our sample). Taking into account the evolution of the gas fraction in low-mass galaxies, the upper limit based on the CO is also tension with the expected gas fraction.

---

[50] We adopt the "$\beta = 0$" scaling relation from Tacconi et al. (2018), assuming a main sequence as observed by Whitaker et al. 2014.

At face value, this result suggests that the galaxies in our sample have unexpectedly low molecular gas fractions. However, a more likely explanation is that the assumption of a Galactic $\alpha_{\rm CO}$ and gas-to-dust ratio does not hold for these systems. Indeed, significantly higher conversion factors would be naturally explained by sub-solar metallicities for these systems.

In Figure 6.9, we show the MZ relation from Equation 6.5 at the average redshift of our sample. We find that the metallicity at the median mass (16th, 84th percentile) of the sample is $12 + \log{\rm (O/H)} = 7.7^{+0.3}_{-0.2}$. However, the MZ relation is only an approximate tracer of the metallicity. More directly, the [O III] λ5008/Hβ λ4863-ratio can be used to trace the metallicity, albeit with significant scatter, as the ratio monotonically increases with decreasing metallicity, up to a turnover at $12 + \log{\rm (O/H)} \sim 8.0$ (e.g., Curti et al., 2017; Sanders et al., 2020). Because of this turnover, there are two metallicities solutions at a fixed ratio; one on the upper branch (high metallicity) and one on the lower branch (low metallicity). We robustly detect Hβ in two objects, finding high ratios of log([O III]/Hβ) ≈ 0.8 for two (MUSE-1019 and MUSE-6878). This roughly implies a metallicity at the turnover, $12 + \log{\rm (O/H)} \sim 8.0$, via the direct method (Curti et al., 2017).[51] We also tentatively detect Hβ λ4863 in a third object (MUSE-6895), yielding a lower ratio (0.35), which implies a high metallicity if it is on the upper branch of the metallicity calibration, in tension with its stellar mass. However, assuming that it follows the (extrapolated) lower branch, this would imply a much lower metallicity of $12 + \log{\rm (O/H)} \sim 7.35$ (and an extremely high $\alpha_{\rm CO} \gg 100$), in better agreement with the stellar mass. For the remaining galaxies, we only find (weak) upper limits on the metallicity (conservatively assuming all are on the higher branch).

To obtain an estimate of the average metallicity in the sample, we stack the KMOS spectra using weighted mean and median stacking. Because of the uncertainties in the background level (see § 6.2.2), we do not normalize the spectra but stack the continuum subtracted spectra instead, which may introduce a bias towards the brighter objects that go into the stack. Note that, due to the shifting to a common redshift, the skyline residuals are spread throughout the stack, though this problem should be mitigated in the median stack. The stacked spectra are shown in Figure 6.10. We tentatively detect Hβ λ4863, measuring log([O III]/Hβ) $\approx 0.9 \pm 0.3$, which broadly implies a metallicity of $12 + \log{\rm (O/H)} \approx 7.6 - 8.0$. We do caution against over-interpreting the stack, given the uncertainties mentioned above. It should also be stressed that the mass-metallicity relation only holds on average. For example, Dessauges-Zavadsky et al. (2017), found that the lensed arc at $z = 3.6$ has a higher inferred metallicity from its measured [O III]/Hβ-ratio than predicted from the MZ. Overall though, the metallicities for the individual galaxies and from the stack are in reasonable agreement with the predictions from the MZ relation (Figure 6.9), pointing to an average metallicity of $12 + \log{\rm (O/H)} \approx 7.8 \pm 0.2$ for the galaxies in our sample.

The average metallicity of our sample implies a significantly higher value of $\alpha_{\rm CO} \approx 50$, which places our upper limit in comfortable agreement with the predicted gas fractions (see Figure 6.8). Notice that the strong, non-linear increase in the conversion factor with

---

[51] http://www.arcetri.astro.it/metallicity/calibrazioni.pl

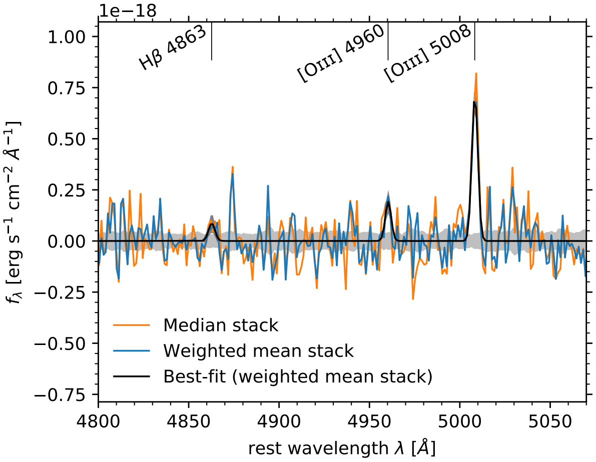

Figure 6.10: Stacked NIR spectra of the galaxies observed with KMOS (continuum subtracted). We show the median stack (orange), the weighted mean stack (blue, with propagated errors in gray) and the best-fit to the weighted mean stack (in black, with uncertainties). We tentatively detect Hβ λ4863, measuring $\log([\text{O III}]/\text{H}\beta) \approx 0.9 \pm 0.3$, which broadly implies a metallicity of $12 + \log(\text{O/H}) \approx 7.6 - 8.0$ (Curti et al., 2017).

metallicity (Equation 6.4) makes the exact value uncertain, particularly in the low-mass range. Furthermore, we caution that there is still debate about the exact relation between α_{CO} and metallicity at low metallicity, mostly due to the difficulty of constraining α_{CO} at low metallicity. In any case, a minimal value of $\alpha_{\text{CO}} \geq 10$ is required to place the 3σ upper limit on the Tacconi et al. (2018) relation, more than 2 times the Galactic value.

The shallower relations between gas-to-dust ratio and metallicity yield gas-to-dust ratios that are insufficient to reconcile the observed limit with the scaling relations, which requires a $\delta_{\text{GDR}} \geq 1200$. For example, we find $\delta_{\text{GDR}} \approx 550$ based on (Tacconi et al., 2018, see Equation 6.6). This points towards a steeper relation between the δ_{GDR} and metallicity in the low-metallicity regime, as suggested by, for example, Rémy-Ruyer et al. (2014) and Coogan et al. (2019) (see § 6.4.1). Adopting the relation from Rémy-Ruyer et al. (2014, Equation 6.6) yields a significantly higher $\delta_{\text{GDR}} \approx 3300$, again placing our upper limit in comfortable agreement with the expected gas fraction. Alternatively, a dust temperature of $T_{\text{dust}} < 20\,\text{K}$ (as opposed to 25 K), can also reconcile the difference with a lower δ_{GDR}. However, given the stronger radiation field expected at low metallicity, it is not clear that the dust temperatures would be much lower than assumed.

Independent of CO and the dust, we reach the same conclusions using [C I] instead. While a typical abundance ratio of 2×10^{-5} predicts similarly low gas masses as CO, assuming an 8× lower abundance (loosely based on the metallicity) easily yields a limit that is fully consistent with the scaling relations, with a ≈ 2× lower abundance being minimally required (see Figure 6.8).

6.4.3 Contribution to the cosmic molecular gas density

The galaxies under study are below the detection threshold of current $\rho_{\rm mol}(z)$ surveys (e.g., Riechers et al., 2019; Decarli et al., 2019, 2020). Still, their potentially high gas mass-to-light ratios imply that they could have a significant contribution to the total cosmic molecular gas density. Assuming the average gas masses derived from the stacks are representative of all 67 galaxies in the photometric catalog down to $H_{\rm F160W} = 26$ (cf. Figure 6.1), we compute the total contribution of these galaxies to the cosmic molecular gas density, $\rho(3.0115 < z < 3.812)$. We adopt the solar, the minimum, and the sub-solar conversion factors from § 6.4.2, and $r_{41} = 0.5$. The result can be seen in Figure 6.11. Because the upper limits are not stringent enough, the results are inconclusive. On one hand, they do not exclude the possibility that a significant amount of molecular gas is missed due to the high gas mass-to-light ratio of star forming galaxies at these redshifts. On the other hand, it is equally possible that their contribution is significantly smaller, implying that their molecular gas signal lies well below the detection threshold, even in stacks. We also determine upper limits for the more massive galaxies in the sample only (with $M_* \geq 10^9$ M$_\odot$ and $\geq 10^{9.5}$ M$_\odot$, computing their average conversion factors from the mass-metallicity relation). The limits on $\rho_{\rm mol}$ are slightly stronger for these sub-samples because, while the stacks are slightly less constraining, the estimated $\alpha_{\rm CO}$ and $\delta_{\rm GDR}$ are lower, as well as the number of sources in the volume. The results fall in between the minimum and sub-solar values of magnitude limited sample, but do not alter the conclusions overall.

6.4.4 Implications for observing cold gas in low metallicity galaxies at high redshift

The evolution of the metallicity of star-forming galaxies with redshift has significant implications for the detectability of molecular gas at $z \geq 3$. Even in the local universe, detecting CO in low metallicity dwarf galaxies has been challenging (e.g., Schruba et al., 2012; Hunt et al., 2015). The substantial CO-to-H$_2$ conversion factor and gas-to-dust ratios inferred for our low-mass, low metallicity galaxies imply that detecting the molecular gas reservoir in these galaxies will be very challenging on an individual basis, even with modern instruments. Similar conclusions are also reached for more massive galaxies at sub-solar metallicities (e.g. Tan et al., 2013; Coogan et al., 2019). Tan et al. (2013) have shown that under the assumption of a MZ-$\alpha_{\rm CO}$ relation similar to the one adopted here, the expected CO luminosity for a star-forming galaxy on the main sequence rapidly declines, due to the metallicity evolution. This raises the interesting question of how the molecular gas content can be best constrained in sub-solar metallicity star-forming galaxies at high redshift.

There are significant uncertainties in deriving a total dust and gas mass from the dust continuum in the low metallicity regime. Variations in the process and balance of dust formation and destruction at low metallicity, as well as differences in grain composition and size distribution can have a major impact on the gas-to-dust ratio, the dust emissivity and emerging dust spectrum (e.g., Rémy-Ruyer et al. 2014, see also Draine et al. 2007). In addition to these complications, the fainter part Rayleigh-Jeans tail at long wavelengths has to be probed, such that the blackbody is dominated by cold dust which dominates the mass

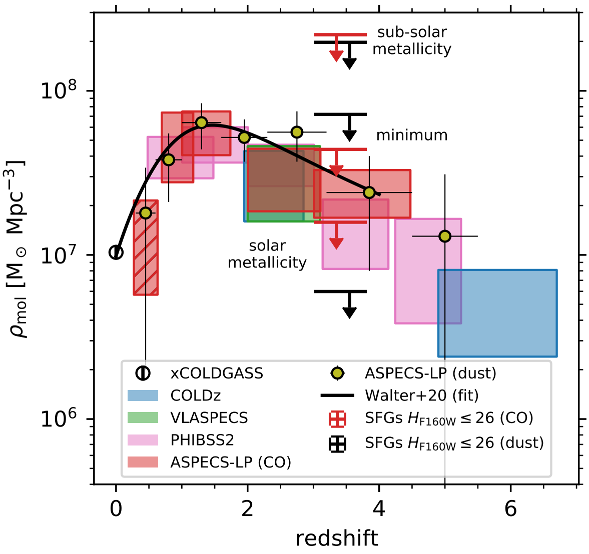

Figure 6.11: Cosmic molecular gas density as a function of redshift. The literature data is from Fletcher et al. (2020) (xCOLDGASS), Riechers et al. (2019) (COLDz), Riechers et al. (2020) (VLASPECS), Lenkić et al. (2020) (PHIBSS2), Decarli et al. (2020) (ASPECS-LP CO), Magnelli et al. (2020) (ASPECS-LP dust) and we also show the best-fit from Walter et al. (2020). We show the best-estimate upper limit on the cosmic molecular density for all galaxies with $H_{\rm F160W} \leq 26$ at $3.0115 < z < 3.812$, as derived from CO (red; assuming $r_{41} = 0.5$) and the dust-continuum (black). The different limits are for conversion factors ($\alpha_{\rm CO}$, $\delta_{\rm GDR}$) = (3.6, 100), (10, 1200), (50, 3300), corresponding to solar metallicity, the minimum value based on § 6.4.2, and the best-estimate sub-solar metallicity. The upper limits do not rule out a large amount of molecular gas in lower mass galaxies (that would have been missed in previous surveys, due to their high gas mass-to-light ratio), but are equally consistent with a smaller contribution to the total molecular gas budget.

and the uncertainty in the (unknown) mass-weighted dust-temperature is minimized (e.g. Scoville et al., 2016).

At low metallicity, CO also becomes an increasingly poor tracer of the total molecular gas reservoir. Because of the lower dust abundance at low metallicity, CO is dissociated and ionized into C and C$^+$ deeper into the clouds, while the H_2 self-shields against photodissociation (Gnedin & Draine, 2014), resulting in an increasing volume of H_2 gas that is not traced by CO at low metallicity (e.g., Wolfire et al., 2010). This provides motivation to investigate and develop the theoretical underpinning for other species as tracers of the molecular gas, such as the fainter [C I] lines (e.g., Weiß et al. 2003, 2005; Papadopoulos et al. 2004; see also Valentino et al. 2018; Boogaard et al. 2020), but in particular also [C II] $\lambda 158\,\mu$m.

The bright [C II] $^3P_{3/2} \rightarrow {}^3P_{1/2}$ line at 158 μm is one of the foremost cooling lines of the ISM, also at low metallicity (where it is outranked only by the high ionization line [O III] $\lambda 88\,\mu$m at 35 eV; e.g., Cormier et al., 2015, 2019) and its high luminosity allows it to be observed in star-forming galaxies out to the highest redshifts (Ouchi et al., 2013; Ota et al., 2014; Maiolino et al., 2015; Capak et al., 2015; Knudsen et al., 2016; Pentericci et al., 2016; Bradač et al., 2017; Matthee et al., 2017, 2019; Carniani et al., 2018a,b, 2020; Smit et al., 2018; Hashimoto et al., 2018; Laporte et al., 2019; Le Fèvre et al., 2020; Béthermin et al., 2020; Harikane et al., 2020; Bakx et al., 2020). With an ionization potential of 11.3 eV (that is, lower than H I at 13.6 eV), [C II] can arise in both the neutral and ionized medium, though it becomes an increasingly better tracer of the neutral ISM towards lower metallicities (Croxall et al. 2017; Cormier et al. 2019, see also Díaz-Santos et al. 2017) potentially due to the carbon in the H II-regions being further ionized into C^{++} (as witnessed by the shift in the ionization balance to high ionization lines, also see in some high-z sources, e.g., Pavesi et al. 2016; Harikane et al. 2020, see also Carniani et al. 2020). While, as a cooling line, [C II] is in principal sensitive to the heating rate (and not the molecular gas mass), it may be calibrated as a molecular gas tracer (Zanella et al., 2018). As such, [C II] can potentially outperform other tracers of the molecular gas mass, in particular in low metallicity environments (e.g. Madden et al., 2020). As [C II] is already seeing use as tracer of the molecular gas at high redshift (e.g., Dessauges-Zavadsky et al., 2020), its use to this end should be further investigated both observationally and theoretically.

6.5 Summary and conclusions

We present constraints on the molecular gas signal for a sample of 24 star-forming galaxies at $\langle z \rangle = 3.45$, with a median $M_* = 10^{9.1}$ $\mathrm{M}_\odot$, in the *Hubble* Ultra Deep Field (HUDF). Based on their Lyα- and H_{F160W}-selection (Figure 6.1), they show relatively low $\mathrm{EW}^0_{\mathrm{Ly}\alpha} \approx 20$ Å ($L_{\mathrm{Ly}\alpha} = 0.2\,L^*_{\mathrm{Ly}\alpha}$), and rest-frame UV spectra similar to star-forming galaxies at the same epoch (see Figure 6.4). We efficiently follow-up Lyα-selected galaxies from the MUSE HUDF Survey, with near-infrared spectroscopy from KMOS and MOSFIRE to determine their systemic redshifts (Figure 6.2 and Figure 6.12) and stack the molecular line emission from the ALMA Spectroscopic Survey in the HUDF (ASPECS). Our main results are as follows:

- We determine systemic redshifts from the rest-frame UV and rest-frame optical features, finding an average velocity offset of $\langle \Delta v(\mathrm{Ly}\alpha) \rangle = 346$ km s^{-1} (with a 100 to 600 km s^{-1} range) consistent with the relatively low $\mathrm{EW}^0_{\mathrm{Ly}\alpha}$ of the sample (Figure 6.5).

- Stacking the signal from ^{12}CO $J = 4 \rightarrow 3$ and [C I] $^3P_1 \rightarrow {}^3P_0$ (as well as the ^{12}CO $J = 9 \rightarrow 8$ and $J = 10 \rightarrow 9$ lines), we do not find any detections and determine 3σ upper limits on the line luminosities of 4.0×10^8 K km s^{-1}pc^2 and 5.6×10^8 K km s^{-1}pc^2, respectively, for a linewidth of 300 km s^{-1} (see Figure 6.6 and Table 6.1; also for the limits on the higher-J lines). Stacking the 1.2 mm dust continuum, we find a 3σ upper limit on the flux density of $S_\nu \leq 9$ μJy (Figure 6.7).

- Comparing the inferred molecular fraction from CO and the dust continuum to scaling relations, we find that assuming a 'Galactic' $\alpha^{\mathrm{MW}}_{\mathrm{CO}} = 4.36$ and $\delta_{\mathrm{GDR}} = 100$ significantly underpredicts the expected molecular gas mass (Figure 6.8). In order to reconcile our measurements with the published scaling relations from Tacconi et al. (2018) would require an $\alpha_{\rm CO} \geq 10$ and $\delta_{\rm GDR} \geq 1200$. This result either implies that our galaxies have unexpectedly low gas fractions or that the assumption of solar-metallicity conversion factors break down.

- Using the mass-metallicity relation, as well as constraints from [O III] λ5008/Hβ λ4863 (Figure 6.10), we predict an average metallicity of our sample of $12 + \log(\rm O/H) = 7.8 \pm 0.2$, that is, significantly sub-solar. This implies a high $\alpha_{\rm CO} \approx 50$ making our result consistent with the expected (high) gas fractions at $z = 3.5$ (Figure 6.9).
- An approximately linear scaling relation between the gas-to-dust ratio and metallicity ($\delta_{\rm GDR} \propto \gamma^{-0.85}$; Tacconi et al., 2018) yields $\delta_{\rm GDR} \approx 550$, which is insufficient to reconcile the limit based on the dust with the Tacconi et al. (2018) scaling relations. Using a steeper relation at low metallicity ($\delta_{\rm GDR} \propto \gamma^{-3.1}$ at $12 + \log(\rm O/H) \leq 8.1$; Rémy-Ruyer et al., 2014) instead yields $\delta_{\rm GDR} \approx 3300$, making our upper limit consistent again (Figure 6.8).
- Independent of the CO, we find the same tension from the [C I] luminosity, which implies a [C I]/[H$_2$] abundance lower than in massive star-forming galaxies such as the Milky Way (Figure 6.8).
- Based on the results, we compute the upper limit on the contribution of all galaxies with $H_{\rm F160W} \leq 26$ to the cosmic molecular gas density $\rho_{\rm mol}(z = 3.0115 - 3.812)$. The upper limits are not constraining enough to exclude the possibility of a significant contribution of these galaxies, that lie below the detection threshold of current surveys, to the cosmic molecular gas density.

The results of this work exemplify the difficulty to obtain molecular gas mass estimates in low metallicity environments, which are expected to be more prevalent in typical star forming galaxies at $z \geq 3$. Given the uncertainties associated with the dust and CO at low metallicity we argue for the further observational and theoretical development of alternative tracers of the molecular gas reservoir, such as the bright [C II] λ158 μm line, that should be more easily observable with ALMA. Obtaining accurate constraints on the gas-phase metallicity of high-redshift galaxies will key in this regard and one of the key pieces of information that the *James Webb Space Telescope* will be able to provide.

Acknowledgments

L.A.B. is grateful to Corentin Schreiber for assisting with the near-infrared spectroscopy during the early stages of this work. L.A.B. acknowledges support from the Leids Kerkhoven-Bosscha Fonds under subsidy numbers 18.2.074 and 19.1.147. D.R. acknowledges support from the National Science Foundation under grant numbers AST-1614213 and AST-1910107. D.R. also acknowledges support from the Alexander von Humboldt Foundation through a Humboldt Research Fellowship for Experienced Researchers. A.F. acknowledges the support from grant PRIN MIUR 2017-20173ML3WW_001. J.B. acknowledges support by Fundação para a Ciêcia e a Tecnologia (FCT) through the research grants UID/FIS/04434/2019, UIDB/04434/2020, UIDP/04434/2020. H.I. acknowledges support from JSPS KAKENHI Grant Number JP19K23462. This work is based on observations collected at the European Southern Observatory under ESO programs 094.A-2089(B), 095.A-0010(A), 096.A-0045(A), 096.A-0045(B), 099.A-0858(A), and 0101.A-0725(A). This paper makes use of the following ALMA data: ADS/JAO.ALMA#2016.1.00324.L. ALMA is a partnership of ESO (representing its member states), NSF (USA) and NINS (Japan), together with NRC (Canada), NSC and ASIAA (Taiwan), and KASI (Republic of Korea), in cooperation with the Republic of Chile. The Joint ALMA Observatory is operated by ESO, AUI/NRAO and NAOJ. The National Radio Astronomy Observatory is a facility of the National Science Foundation operated under cooperative agreement by Associated Universities, Inc. This work was supported by a NASA Keck PI Data Award, administered by the NASA Exoplanet Science Institute. Data presented herein were obtained at the W. M. Keck Observatory from telescope time allocated to the National Aeronautics and Space Administration through the agency's scientific partnership with the California Institute of Technology and the University of California. The Observatory was made possible by the generous financial support of the W. M. Keck Foundation. The authors wish to recognize and acknowledge the very significant cultural role and reverence that the summit of Maunakea has always had within the indigenous Hawaiian community. We are most fortunate to have the opportunity to conduct observations from this mountain.

Facilities: ALMA, VLT: Yepun (MUSE), VLT: Antu (KMOS), Keck I (MOSFIRE). *Software:* TOPCAT (Taylor, 2005), GNUASTRO (Akhlaghi & Ichikawa, 2015), IPYTHON (Perez & Granger, 2007), NUMPY (van der Walt et al., 2011), MATPLOTLIB (Hunter, 2007), ASTROPY (The Astropy Collaboration et al., 2013, 2018), CASA (McMullin et al., 2007).

Appendix 6.A Table

The coordinates, (systemic) redshifts, and physical properties of the sample of $3.0115 < z < 3.812$ star-forming galaxies are listed in Table 6.2.

Table 6.2: Coordinates, (systemic) redshifts, and physical properties of the sample of $3.0115 < z < 3.812$ star-forming galaxies.

ID (1)	RAF ID (2)	α_{J2000} (3)	δ_{J2000} (4)	$z^{\rm red}_{\rm Lyff}$ (5)	$\delta(z^{\rm red}_{\rm Lyff})$ (km s^{-1}) (6)	$z_{\rm sys}$ (7)	$\delta(z_{\rm sys})$ (km s^{-1}) (8)	Source (9)	$\Delta v({\rm Ly}\alpha)$ (km s^{-1}) (10)	$\log M_*$ (M$_\odot$) (11)	log SFR (M$_\odot$ yr^{-1}) (12)
50	9110	53.16284897	-27.77162645	3.33015 ± 0.00086	59.5	3.32349 ± 0.00027	18.7	MUSE EM	461.8 ± 62.5	$9.15^{+0.10}_{-0.12}$	$1.122^{+0.10}_{-0.10}$
82	6627	53.1515512	-27.7853475	3.60777 ± 0.00006	3.9	3.60493 ± 0.00080	52.1	MUSE EM	184.9 ± 52.3	$9.00^{+0.10}_{-0.10}$	$0.792^{+0.10}_{-0.17}$
106	9863	53.16372638	-27.77907551	3.28171 ± 0.00009	6.3	3.27648 ± 0.00012	8.4	MUSE EM	366.6 ± 10.5	$8.45^{+0.10}_{-0.10}$	$0.547^{+0.10}_{-0.10}$
118	23839	53.15708801	-27.78026883	3.02127 ± 0.00056	41.7	3.01727 ± 0.00017	12.7	MUSE EM	298.5 ± 43.7	$8.78^{+0.10}_{-0.20}$	$0.462^{+0.10}_{-0.10}$
1019	8002	53.16492565	-27.76512153	3.19361 ± 0.00088	62.9	3.18669 ± 0.00002	1.4	MOSFIRE	495.5 ± 63.0	$9.43^{+0.10}_{-0.10}$	$1.387^{+0.10}_{-0.10}$
...	...	...	...	...	...	3.18579 ± 0.00026	18.6	MUSE ABS	560.1 ± 65.7	...	...
1059	8203	53.15344247	-27.76611934	3.80588 ± 0.00005	3.1	3.80122 ± 0.00199	124.3	MUSE ABS	291.0 ± 124.4	$9.70^{+0.10}_{-0.10}$	$1.267^{+0.10}_{-0.10}$
1087	3506	53.16790037	-27.7979532	3.46259 ± 0.00019	12.8	3.45675 ± 0.00097	65.2	MUSE ABS	392.8 ± 66.6	$9.55^{+0.10}_{-0.10}$	$1.112^{+0.10}_{-0.10}$
1088	6012	53.15257181	-27.79384452	...	...	3.08224 ± 0.00039	28.6	MUSE ABS	...	$9.65^{+0.10}_{-0.10}$	$1.472^{+0.10}_{-0.10}$
1113	8528	53.16993928	-27.76833978	3.09022 ± 0.00005	3.7	3.08803 ± 0.00281	206.1	KMOS	160.6 ± 206.2	$9.17^{+0.17}_{-0.10}$	$0.917^{+0.10}_{-0.10}$
...	...	...	...	...	...	3.08520 ± 0.00065	47.7	MUSE ABS	368.4 ± 47.9	...	...
1138	8308	53.14850621	-27.77728375	3.61287 ± 0.00266	172.9	3.60520 ± 0.00047	30.6	MUSE ABS	499.3 ± 175.9	$9.40^{+0.11}_{-0.10}$	$1.567^{+0.10}_{-0.10}$
1215	9247	53.1487158	-27.77294489	3.33215 ± 0.00155	107.3	3.32623 ± 0.00104	72.1	KMOS	410.2 ± 129.4	$9.87^{+0.10}_{-0.10}$	$1.092^{+0.17}_{-0.10}$
...	...	...	...	...	...	3.32594 ± 0.00053	36.7	MUSE ABS	430.4 ± 113.5	...	...
1253	8783	53.17824938	-27.77399604	3.67218 ± 0.00096	61.6	3.66765 ± 0.00421	270.4	KMOS	291.0 ± 277.6	$8.59^{+0.10}_{-0.10}$	$0.587^{+0.10}_{-0.10}$
...	...	...	...	...	...	3.66896 ± 0.00067	43.0	MUSE EM	206.8 ± 75.2	...	...
1360	37765	53.17926551	-27.78289487	3.66696 ± 0.00161	103.4	3.66479 ± 0.00284	182.5	MUSE ABS	139.5 ± 209.9	$9.06^{+0.12}_{-0.10}$	$1.027^{+0.10}_{-0.28}$
1530	7002	53.17666134	-27.78380467	3.19270 ± 0.00112	80.1	3.18896 ± 0.00036	25.8	KMOS	267.7 ± 84.2	$8.97^{+0.10}_{-0.10}$	$0.772^{+0.10}_{-0.10}$
1833	3673	53.1524905	-27.79770827	3.01437 ± 0.00178	132.9	3.00842 ± 0.00009	6.7	MOSFIRE	445.0 ± 133.3	$8.49^{+0.14}_{-0.10}$	$0.362^{+0.10}_{-0.36}$
6375	22525	53.14339467	-27.78800227	3.41682 ± 0.00160	108.6	3.41287 ± 0.01914	1300.3	KMOS	268.3 ± 1306.0	$8.79^{+0.10}_{-0.10}$	$0.882^{+0.10}_{-0.10}$
6518†	52206	53.14325211	-27.7868279	3.75265 ± 0.00062	39.1	3.74969 ± 0.00020	12.6	MOSFIRE	186.8 ± 41.1	...	...
6666	24954	53.15957552	-27.7767193	3.43869 ± 0.00021	14.2	3.43494 ± 0.00024	16.2	KMOS	253.5 ± 21.6	$9.03^{+0.10}_{-0.10}$	$0.902^{+0.10}_{-0.12}$
...	...	...	...	...	...	3.43492 ± 0.00008	5.4	MUSE EM	254.8 ± 15.2	...	...
6878	7843	53.13953672	-27.78067557	3.60787 ± 0.00090	58.6	3.60020 ± 0.00064	41.7	MUSE ABS	499.8 ± 72.0	$9.40^{+0.10}_{-0.11}$	$1.387^{+0.10}_{-0.13}$
...	...	...	...	...	...	3.60295 ± 0.00006	3.9	MOSFIRE	320.4 ± 58.7	...	...
6883	9832	53.17629722	-27.77891257	3.19503 ± 0.00222	158.6	3.18724 ± 0.00040	28.6	MUSE ABS	557.7 ± 161.5	$9.56^{+0.10}_{-0.10}$	$1.407^{+0.10}_{-0.10}$

Table 6.2: *(continued)*

ID (1)	RAF ID (2)	α_{J2000} (3)	δ_{J2000} (4)	$z_{\rm Lyff}^{\rm red}$ (5)	$\delta(z_{\rm Lyff}^{\rm red})$ (km s^{-1}) (6)	$z_{\rm sys}$ (7)	$\delta(z_{\rm sys})$ (km s^{-1}) (8)	Source (9)	Δv(Lyα) (km s^{-1}) (10)	log M_* (M$_\odot$) (11)	log SFR (M$_\odot$ yr^{-1}) (12)
6895	5742	53.1759691	-27.79261283	3.71273 ± 0.00194	123.4	3.70409 ± 0.00079	50.3	MUSE ABS	550.6 ± 133.5	$8.41^{+0.10}_{-0.10}$	$0.497^{+0.10}_{-0.10}$
· · ·	· · ·	· · ·	· · ·	· · ·	· · ·	3.70522 ± 0.00020	12.7	KMOS	478.5 ± 124.3	· · ·	· · ·
8041	8635	53.1755829	-27.76874786	· · ·	· · ·	3.69700 ± 0.00172	109.8	MUSE ABS	· · ·	$9.52^{+0.10}_{-0.10}$	$1.317^{+0.10}_{-0.16}$
8091	5468	53.14920592	-27.79147296	· · ·	· · ·	3.55707 ± 0.00116	76.3	MUSE ABS	· · ·	$9.27^{+0.10}_{-0.10}$	$1.242^{+0.10}_{-0.10}$
8103	5741	53.17592521	-27.79246095	· · ·	· · ·	3.70527 ± 0.00027	17.2	MUSE EM	· · ·	$8.60^{+0.10}_{-0.10}$	$0.677^{+0.10}_{-0.16}$

Notes. (1) MUSE ID (2) Rafelski et al. (2015) ID (3) Right Ascension (4) Declination (5) Redshift measured from Lyα λ1216 (the red peak, in the case of a double-peaked line) (6) Velocity uncertainty on redshift (7) Systemic redshift (8) Velocity uncertainty on systemic redshift (9) Source of systemic redshift (MUSE EMission or ABSorption, KMOS, MOSFIRE) (10) Lyα velocity offset, $\Delta v({\rm Ly}\alpha) = c(z_{\rm Lyff}^{\rm red} - z_{\rm sys})/(1 + z_{\rm sys})$. (11) Stellar mass and (12) Star Formation Rate from MAGPHYS, with a minimum uncertainty of 0.1 dex.

† Blended with a $z = 0.83$ foreground object.

Appendix 6.B Spectra

The rest-frame UV (MUSE) and near-IR (KMOS, MOSFIRE) spectra of all galaxies in the sample are shown in Figure 6.12 (except for the galaxy already shown in Figure 6.2).

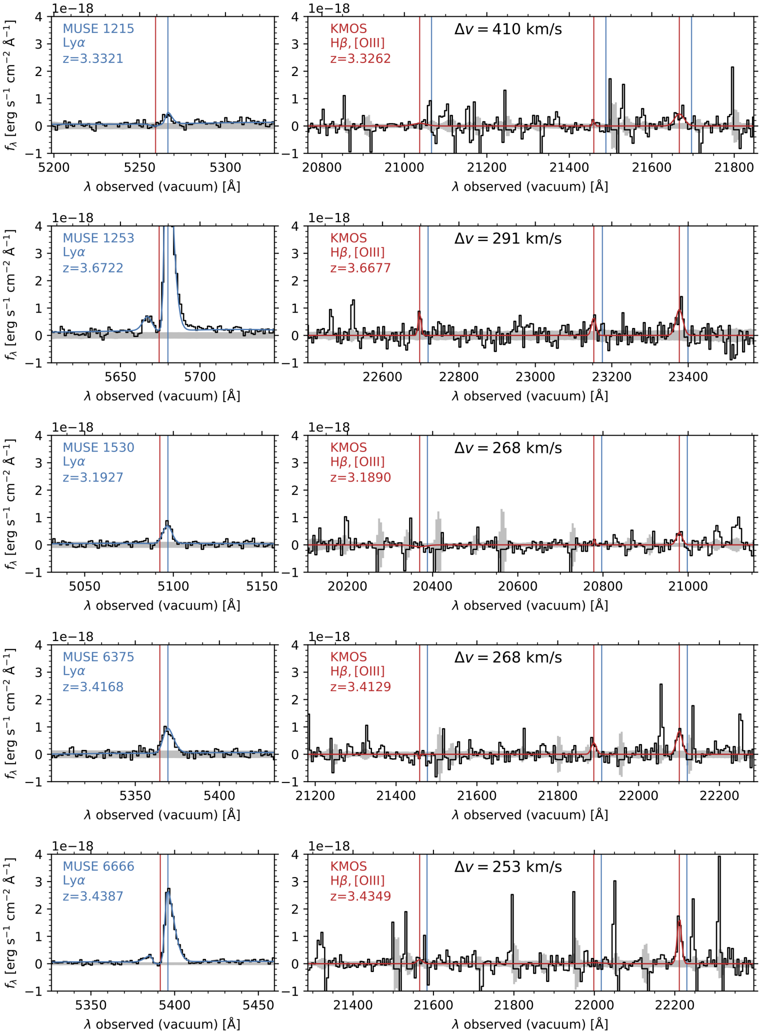

Figure 6.12: Rest-frame ultraviolet and optical spectra for the galaxies with near-infrared follow up. The *left* panel shows the MUSE spectrum surrounding the Lyα line. The *right* panel shows the continuum subtracted KMOS or MOSFIRE spectrum (indicated in the figure) around the Hβ λ4863 and [O III] $\lambda\lambda$4960, 5008 lines. In both panels the vertical blue and red lines indicate the redshift of Lyα and the systemic redshift, respectively, determined from the fit to the spectrum (shown in the same color). All spectra show a positive velocity offset between the red peak of Lyα and the systemic redshift.

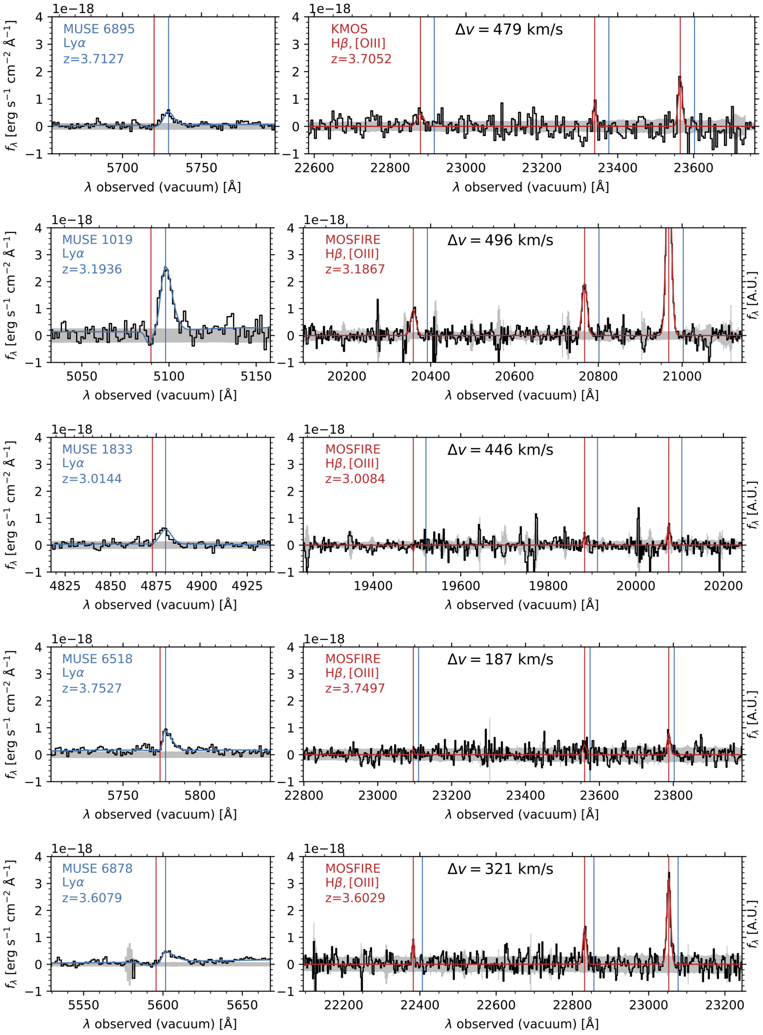

Figure 6.12: *(continued)*

Bibliography

Abazajian K. N., et al., 2009, ApJS, 182, 543

Abergel A., et al., 2011, A&A, 536, A21

Abramson L. E., et al., 2014, ApJ, 785, L36

Abramson L. E., Gladders M. D., Dressler A., Oemler A., Poggianti B., Vulcani B., 2016, ApJ, 832, 7

Akhlaghi M., Ichikawa T., 2015, ApJS, 220, 1

Alaghband-Zadeh S., et al., 2013, MNRAS, 435, 1493

Ali B., et al., 1991, PASA, 103, 1182

Andreani P., Retana-Montenegro E., Zhang Z.-Y., Papadopoulos P., Yang C., Vegetti S., 2018, A&A, 615, A142

Andreon S., Hurn M. a., 2010, MNRAS, 1937, 1922

Aravena M., et al., 2010, ApJ, 718, 177

Aravena M., et al., 2012, MNRAS, 426, 258

Aravena M., et al., 2014, MNRAS, 442, 558

Aravena M., et al., 2016a, MNRAS, 457, 4406

Aravena M., et al., 2016b, ApJ, 833, 68

Aravena M., et al., 2016c, ApJ, 833, 71

Aravena M., et al., 2019, ApJ, 882, 136

Aravena M., et al., 2020, ApJ, 901, 79

Asplund M., Grevesse N., Sauval A. J., Scott P., 2009, ARA&A, 47, 481

BIPM 2019, Le Système international d'unités / The International System of Units ('The SI Brochure'), ninth edn. Bureau international des poids et mesures, http://www.bipm.org/en/si/si_brochure/

Bacon R., et al., 2010, in McLean I. S., Ramsay S. K., Takami H., eds, Society of Photo-Optical Instrumentation Engineers (SPIE) Conference Series Vol. 7735, Ground-based and Airborne Instrumentation for Astronomy III. p. 773508, doi:10.1117/12.856027

Bacon R., et al., 2014, The Messenger, 157, 13

Bacon R., et al., 2015, A&A, 575, A75

Bacon R., et al., 2017, A&A, 608, A1

Baker A. J., Tacconi L. J., Genzel R., Lehnert M. D., Lutz D., 2004, ApJ, 604, 125

Bakx T. J., et al., 2020, MNRAS, 493, 4294

Baldwin J. A., Phillips M. M., Terlevich R., 1981, PASA, 93, 5

Barkana R., Loeb A., 2001, Phys. Rep., 349, 125

Beckwith S. V. W., et al., 2006, AJ, 132, 1729

Behroozi P. S., Wechsler R. H., Conroy C., 2013a, ApJ, 762, L31

Behroozi P. S., Wechsler R. H., Conroy C., 2013b, ApJ, 770, 57

Béthermin M., et al., 2015, A&A, 573, 1

Béthermin M., et al., 2020, A&A, 643, A2

Bigiel F., et al., 2008, AJ, 136, 2846

Birkin J. E., et al., 2020, arXiv e-prints, p. arXiv:2009.03341

Birnboim Y., Dekel A., Neistein E., 2007, MNRAS, 380, 339

Bisbas T. G., Papadopoulos P. P., Viti S., 2015, ApJ, 803, 37

Bisbas T. G., van Dishoeck E. F., Papadopoulos P. P., Szűcs L., Bialy S., Zhang Z.-Y., 2017, ApJ, 839, 90

Bisigello L., Caputi K. I., Grogin N., Koekemoer A., 2018, A&A, 609, A82

Blain A. W., Smail I., Ivison R. J., Kneib J. P., Frayer D. T., 2002, Phys. Rep., 369, 111
Blanchard A., Valls-Gabaud D., Mamon G., 1992, A&A, 264, 365
Blumenthal G. R., Faber S. M., Primack J. R., Rees M. J., 1984, Nature, 311, 517
Bolatto A. D., Leroy A. K., Rosolowsky E., Walter F., Blitz L., 2008, ApJ, 686, 948
Bolatto A. D., Wolfire M., Leroy A. K., 2013, ARA&A, 51, 207
Bolatto A. D., et al., 2015, ApJ, 809, 175
Boogaard L. A., 2020, in da Cunha E., Hodge J., Afonso J., Pentericci L., Sobral D., eds, IAU Symposium Vol. 352, IAU Symposium. pp 326–330, doi:10.1017/S1743921319008913
Boogaard L. A., et al., 2018, A&A, 619, A27
Boogaard L. A., et al., 2019, ApJ, 882, 140
Boogaard L. A., et al., 2020, ApJ, 902, 109
Bothwell M. S., et al., 2013, MNRAS, 429, 3047
Bothwell M. S., et al., 2017, MNRAS, 466, 2825
Bouche N., Gardner J. P., Katz N., Weinberg D. H., Dave R., Lowenthal J. D., 2005, ApJ, 628, 89
Bouché N., et al., 2010, ApJ, 718, 1001
Bourne N., Dunlop J. S., Simpson J. M., Rowlands K. E., Geach J. E., McLeod D. J., 2019, MNRAS, 482, 3135
Bouwens R. J., et al., 2012, ApJ, 754, 83
Bouwens R. J., et al., 2015, ApJ, 803, 34
Bouwens R., et al., 2020, ApJ, 902, 112
Bradač M., et al., 2017, ApJ, 836, L2
Brinchmann J., et al., 2004, MNRAS, 351, 1151
Brinchmann J., Kunth D., Durret F., 2008, A&A, 485, 657
Brisbin D., et al., 2019, A&A, 628, A104
Brown R. L., vanden Bout P. A., 1991, AJ, 102, 1956
Bundy K., Fukugita M., Ellis R. S., Targett T. A., Belli S., Kodama T., 2009, ApJ, 697, 1369
Caffau E., Ludwig H. G., Steffen M., Freytag B., Bonifacio P., 2011, Sol. Phys., 268, 255
Calzetti D., Armus L., Bohlin R. C., Kinney A. L., Koornneef J., Storchi-Bergmann T., 2000, ApJ, 533, 682
Cañameras R., et al., 2018, A&A, 620, A61
Cantalupo S., 2010, MNRAS, 403, 16
Capak P. L., et al., 2015, Nature, 522, 455
Carilli C. L., Walter F., 2013, ARA&A, 51, 1
Carilli C. L., et al., 2010, ApJ, 714, 1407
Carilli C. L., et al., 2016, ApJ, 833, 73
Carniani S., et al., 2018a, MNRAS, 478, 1170
Carniani S., Maiolino R., Smit R., Amorín R., 2018b, ApJ, 854, L7
Carniani S., et al., 2020, MNRAS, 499, 5136
Carpenter J., Iono D., Testi L., Whyborn N., Wootten A., Evans N., 2019, arXiv e-prints, p. arXiv:1902.02856
Carpenter J., Iono D., Kemper F., Wootten A., 2020, arXiv e-prints, p. arXiv:2001.11076
Casertano S., et al., 2000, AJ, 120, 2747
Casey C. M., Narayanan D., Cooray A., 2014, Phys. Rep., 541, 45
Casey C. M., et al., 2018, ApJ, 862, 77
Cassata P., et al., 2020, ApJ, 891, 83
Cattaneo A., Mamon G. A., Warnick K., Knebe A., 2011, A&A, 533, 1
Cattaneo A., et al., 2017, MNRAS, 471, 1401
Chabrier G., 2003, PASA, 115, 763
Charlot S., Fall S. M., 2000, ApJ, 539, 718
Chary R., Elbaz D., 2001, ApJ, 556, 562
Chomiuk L., Povich M. S., 2011, AJ, 142, 197
Chung D. T., Viero M. P., Church S. E., Wechsler R. H., 2020, ApJ, 892, 51
Combes F., 2018, A&A Rev., 26, 1
Conroy C., 2013, ARA&A, 51, 393
Conroy C., White M., Gunn J. E., 2010, ApJ, 708, 58
Coogan R. T., et al., 2019, MNRAS, 485, 2092
Cooke E. A., et al., 2018, ApJ, 861, 100
Coppin K. E. K., et al., 2007, ApJ, 665, 936

Cormier D., et al., 2015, A&A, 578, A53

Cormier D., et al., 2019, A&A, 626, A23

Correa C. A., Wyithe J. S. B., Schaye J., Duffy A. R., 2015a, MNRAS, 450, 1514

Correa C. A., Stuart J., Wyithe B., Schaye J., Duffy A. R., 2015b, MNRAS, 452, 1217

Crain R. A., et al., 2015, MNRAS, 450, 1937

Crites A. T., et al., 2014, in Holland W. S., Zmuidzinas J., eds, Society of Photo-Optical Instrumentation Engineers (SPIE) Conference Series Vol. 9153, Millimeter, Submillimeter, and Far-Infrared Detectors and Instrumentation for Astronomy VII. p. 91531W, doi:10.1117/12.2057207

Croxall K. V., et al., 2017, ApJ, 845, 96

Curti M., Cresci G., Mannucci F., Marconi A., Maiolino R., Esposito S., 2017, MNRAS, 465, 1384

Da Cunha E., Charlot S., Elbaz D., 2008, MNRAS, 388, 1595

Da Cunha E., et al., 2015, ApJ, 806, 110

Daddi E., et al., 2004, ApJ, 617, 746

Daddi E., et al., 2007, ApJ, 670, 156

Daddi E., et al., 2010a, ApJ, 713, 686

Daddi E., et al., 2010b, ApJ, 714, L118

Daddi E., et al., 2015, A&A, 577, A46

Dale D. A., Helou G., 2002, ApJ, 576, 159

Damen M., et al., 2009, ApJ, 705, 617

Danielson A. L., et al., 2011, MNRAS, 410, 1687

Danielson A. L. R., et al., 2017, ApJ, 840, 78

Dannerbauer H., et al., 2009, ApJ, 698, 178

Dannerbauer H., et al., 2019, AJ, 158, 34

Davé R., 2008, MNRAS, 385, 147

Davé R., Finlator K., Oppenheimer B. D., 2012, MNRAS, 107, 98

Davidzon I., et al., 2017, A&A, 605, A70

Davies R. I., et al., 2013, A&A, 558, A56

Davies L. J. M., et al., 2016, MNRAS, 461, 458

Decarli R., et al., 2014, ApJ, 782, 78

Decarli R., et al., 2016a, ApJ, 833, 69

Decarli R., et al., 2016b, ApJ, 833, 70

Decarli R., et al., 2017, Nature, 545, 457

Decarli R., et al., 2018, ApJ, 854, 97

Decarli R., et al., 2019, ApJ, 882, 138

Decarli R., et al., 2020, ApJ, 902, 110

Dekel A., Mandelker N., 2014, MNRAS, 444, 2071

Dekel a., et al., 2009, Nature, 457, 451

Dekel A., Zolotov A., Tweed D., Cacciato M., Ceverino D., Primack J. R., 2013, MNRAS, 435, 999

Dessauges-Zavadsky M., et al., 2015, A&A, 577, A50

Dessauges-Zavadsky M., et al., 2017, A&A, 605, A81

Dessauges-Zavadsky M., et al., 2020, A&A, 643, A5

Díaz-Santos T., et al., 2017, ApJ, 846, 32

Dickman R. L., Snell R. L., Schloerb F. P., 1986, ApJ, 309, 326

Dobbs C. L., Pringle J. E., Naylor T., 2014, MNRAS, 437, L31

Dominguez A., et al., 2015, MNRAS, 451, 839

Dopita M. A., et al., 2006a, ApJS, 167, 177

Dopita M. A., et al., 2006b, ApJ, 639, 788

Draine B. T., 2011, Physics of the Interstellar and Intergalactic Medium

Draine B. T., Li A., 2001, ApJ, 551, 807

Draine B. T., et al., 2007, ApJ, 663, 866

Drake A. B., et al., 2017, A&A, 608, A6

Dudzevičiūtė U., et al., 2020, MNRAS, 494, 3828

Dunlop J. S., et al., 2017, MNRAS, 466, 861

Dutton A. A., Van Den Bosch F. C., Dekel A., 2010, MNRAS, 1710, no

Eales S., et al., 2018, MNRAS, 473, 3507

Einstein A., 1917, Sitzungsberichte der Königlich Preußischen Akad. der Wissenschaften (Berlin), pp 142–152
Elbaz D., et al., 2007, A&A, 468, 33
Elbaz D., et al., 2011, A&A, 533, A119
Erb D. K., Steidel C. C., Shapley A. E., Pettini M., Reddy N. A., Adelberger K. L., 2006, ApJ, 646, 107
Erb D. K., et al., 2014, ApJ, 795, 33
Fakhouri O., Ma C. P., 2008, MNRAS, 386, 577
Faucher-Giguère C. A., Keres D., Ma C. P., 2011, MNRAS, 417, 2982
Feltre A., et al., 2018, A&A, 617, A62
Feltre A., et al., 2020, A&A, 641, A118
Fixsen D. J., Bennett C. L., Mather J. C., 1999, ApJ, 526, 207
Fletcher T. J., Saintonge A., Soares P. S., Pontzen A., 2020, MNRAS, 8, 1
Forbes J. C., Krumholz M. R., Burkert A., Dekel A., 2014, MNRAS, 443, 168
Foreman-Mackey D., 2016, Journal of Open Source Software, 1, 24
Foreman-Mackey D., Hogg D. W., Lang D., Goodman J., 2013, PASA, 125, 306
Förster Schreiber N. M., Wuyts S., 2020, ARA&A, 58, 1
Förster Schreiber N. M., et al., 2009, ApJ, 706, 1364
Franco M., et al., 2018, A&A, 620, A152
Franco M., et al., 2020, A&A, 643, A53
Frerking M. A., Keene J., Blake G. A., Phillips T. G., 1989, ApJ, 344, 311
Furlong M., et al., 2015, MNRAS, 450, 4486
Galliano F., Galametz M., Jones A. P., 2018, ARA&A, 56, 673
Gao Y., Solomon P. M., 2004, ApJS, 152, 63
Gavazzi G., et al., 2015, A&A, 580, A116
Geach J. E., Smail I., Moran S. M., MacArthur L. A., Lagos C. d. P., Edge A. C., 2011, ApJ, 730, L19
Gehrels N., 1986, ApJ, 303, 336
Genel S., et al., 2008, ApJ, 688, 789
Genel S., et al., 2014, MNRAS, 445, 175
Genzel R., et al., 2010, MNRAS, 407, 2091
Genzel R., et al., 2011, ApJ, 733, 101
Genzel R., et al., 2012, ApJ, 746, 69
Genzel R., et al., 2015, ApJ, 800, 20
Gerin M., Phillips T. G., 2000, ApJ, 537, 644
Giavalisco M., et al., 2004, ApJ, 600, L93
Gladders M. D., Oemler A., Dressler A., Poggianti B., Vulcani B., Abramson L., 2013, ApJ, 770, 64
Glover S. C., Clark P. C., Micic M., Molina F., 2015, MNRAS, 448, 1607
Gnedin N. Y., 2000, ApJ, 20, 535
Gnedin N. Y., Draine B. T., 2014, ApJ, 795, 4
González-López J., et al., 2017a, A&A, 597, A41
González-López J., et al., 2017b, A&A, 608, A138
González-López J., et al., 2019, ApJ, 882, 139
González-López J., et al., 2020, ApJ, 897, 91
Goodman J., Weare J., 2010, Communications in Applied Mathematics and Computational Science, 5, 65
Gowardhan A., Riechers D., Pavesi R., Daddi E., Dannerbauer H., Neri R., 2019, ApJ, 875, 6
Greve T. R., et al., 2005, MNRAS, 359, 1165
Greve T. R., et al., 2014, ApJ, 794, 142
Grogin N. A., et al., 2011, ApJS, 197, 35
Groves B., Brinchmann J., Walcher C. J., 2012, MNRAS, 419, 1402
Gruppioni C., et al., 2013, MNRAS, 432, 23
Guo K., Zhong Zheng X., Fu H., 2013, ApJ, 778, 23
Haas M. R., et al., 2013a, MNRAS, 435, 2931
Haas M. R., et al., 2013b, MNRAS, 435, 2955
Habing H., 1968, Bull. Astron. Inst. Netherlands, 19, 421
Haggard D., et al., 2010, ApJ, 723, 1447
Harikane Y., et al., 2020, ApJ, 896, 93
Harrington K. C., et al., 2018, MNRAS, 474, 3866

Hashimoto T., et al., 2018, Nature, 557, 392
Hatsukade B., et al., 2018, PASJ, 70, 1
Hayatsu N. H., et al., 2017, PASJ, 69, 1
Henriques B. M., et al., 2015, MNRAS, 451, 2663
Herenz E. C., Wisotzki L., 2017, A&A, 602, A111
Herenz E. C., et al., 2019, A&A, 621, A107
Hildebrand R., 1983, QJRAS, 24, 267
Hirschmann M., De Lucia G., Fontanot F., 2016, MNRAS, 461, 1760
Hodge J. A., da Cunha E., 2020, arXiv e-prints, p. arXiv:2004.00934
Hodge J. A., et al., 2012, ApJ, 760, 11
Hogg D. W., Bovy J., Lang D., 2010, arXiv e-prints, p. arXiv:1008.4686
Hollenbach D. J., Tielens A. G. G. M., 1999, Reviews of Modern Physics, 71, 173
Hopkins A. M., Beacom J. F., 2006, ApJ, 651, 142
Hopkins P. F., Richards G. T., Hernquist L., 2007, ApJ, 654, 731
Hopkins P. F., et al., 2014, MNRAS, 445, 581
Hopkins P. F., Torrey P., Faucher-Gigùre C. A., Quataert E., Murray N., 2016, MNRAS, 458, 816
Hubble E. P., 1926, ApJ, 64, 321
Hummer D. G., Storey P. J., 1987, MNRAS, 224, 801
Hunt L. K., et al., 2015, A&A, 583, A114
Hunter J. D., 2007, Computing in Science & Engineering, 9, 90
Ikeda M., Oka T., Tatematsu K., Sekimoto Y., Yamamoto S., 2002, ApJS, 139, 467
Ilbert O., et al., 2015, A&A, 579, A2
Illingworth G. D., et al., 2013, ApJS, 209, 6
Inami H., et al., 2017, A&A, 608, A2
Inami H., et al., 2020, ApJ, 902, 113
Israel F., 1997, A&A, 328, 471
Israel F. P., Rosenberg M. J. F., van der Werf P., 2015, A&A, 578, A95
Ivison R. J., et al., 2011, MNRAS, 412, 1913
J. Bouwens R., et al., 2016, ApJ, 833, 72
Jiao Q., Zhao Y., Zhu M., Lu N., Gao Y., Zhang Z.-Y., 2017, ApJ, 840, L18
Jiao Q., et al., 2019, ApJ, 880, 133
Jin S., et al., 2019, ApJ, 887, 144
Juneau S., Dickinson M., Alexander D. M., Salim S., 2011, ApJ, 736, 104
Kaasinen M., et al., 2019, ApJ, 880, 15
Kaasinen M., et al., 2020, ApJ, 899, 37
Kamenetzky J., Rangwala N., Glenn J., Maloney P. R., Conley A., 2014, ApJ, 795, 174
Kamenetzky J., Rangwala N., Glenn J., 2017, MNRAS, 471, 2917
Kamenetzky J., Privon G. C., Narayanan D., 2018, ApJ, 859, 9
Kannan R., et al., 2014, MNRAS, 437, 3529
Karim a., et al., 2011, ApJ, 730, 61
Kauffmann G., et al., 2003, MNRAS, 341, 33
Kaufman M. J., Wolfire M. G., Hollenbach D. J., 2006, ApJ, 644, 283
Kelly B. C., 2007, ApJ, 665, 1489
Kelson D. D., 2014, arXiv e-prints, p. arXiv:1406.5191
Kennicutt R. C., 1998a, ARA&A, 36, 189
Kennicutt R. C., 1998b, ApJ, 498, 541
Kennicutt R. C., Evans N. J., 2012, ARA&A, 50, 531
Kere D., Katz N., Weinberg D. H., Dave R., 2005, MNRAS, 363, 2
Kewley L. J., Dopita M. A., 2002, ApJS, 142, 35
Kewley L. J., Ellison S. L., 2008, ApJ, 681, 1183
Kewley L. J., Dopita M. A., Sutherland R. S., Heisler C. A., Trevena J., 2001, ApJ, 556, 121
Kewley L. J., Geller M. J., Jansen R. a., 2004, AJ, 127, 2002
Kirkpatrick A., Sharon C., Keller E., Pope A., 2019, ApJ, 879, 41
Klitsch A., et al., 2019, MNRAS, 490, 1220
Knudsen K. K., et al., 2016, MNRAS, 462, L6

Koekemoer A. M., et al., 2011, ApJS, 197, 36

Koekemoer A. M., et al., 2013, ApJS, 209, 3

Kohno K., et al., 2016, in Kaviraj S., ed., IAU Symposium Vol. 319, Galaxies at High Redshift and Their Evolution Over Cosmic Time. pp 92–95, doi:10.1017/S1743921315010364

Kormendy J., Ho L. C., 2013, ARA&A, 51, 511

Kreckel K., et al., 2018, ApJ, 863, L21

Kriek M., et al., 2009, ApJ, 700, 221

Kurczynski P., et al., 2016, ApJ, 820, L1

Labbé I., Bouwens R., Illingworth G. D., Franx M., 2006, ApJ, 649, L67

Labbé I., et al., 2010, ApJL, 708, 26

Labbé I., et al., 2015, ApJ, Suppl. Ser., 221, 23

Lagache G., Cousin M., Chatzikos M., 2018, A&A, 609, A130

Lagos C. D. P., Baugh C. M., Lacey C. G., Benson A. J., Kim H. S., Power C., 2011, MNRAS, 418, 1649

Lamareille F., Mouhcine M., Contini T., Lewis I., Maddox S., 2004, MNRAS, 350, 396

Laporte N., et al., 2019, MNRAS, 487, L81

Le Fèvre O., et al., 2020, A&A, 643, A1

Lee N., et al., 2015, ApJ, 801, 80

Leja J., van Dokkum P. G., Franx M., Whitaker K. E., 2015, ApJ, 798, 115

Leja J., Johnson B. D., Conroy C., van Dokkum P. G., Byler N., 2017, ApJ, 837, 170

Leja J., et al., 2019, ApJ, 877, 140

Lenkić L., et al., 2020, AJ, 159, 190

Leroy A. K., et al., 2008, AJ, 136, 2782

Leroy A. K., et al., 2011, ApJ, 737, 12

Leroy A. K., et al., 2013, AJ, 146, 19

Levesque E. M., Richardson M. L. A., 2014, ApJ, 780, 4

Li A., Draine B. T., 2001, ApJ, 554, 778

Liang L., et al., 2018, MNRAS, 478, L83

Lilly S. J., Tresse L., Hammer F., Crampton D., Le Fevre O., 1995, ApJ, 455, 108

Lilly S. J., Le Fèvre O., Hammer F., Crampton D., 1996, ApJ, 460, 55

Lilly S. J., Carollo C. M., Pipino A., Renzini A., Peng Y., 2013, ApJ, 772, 119

Liu D., et al., 2015, ApJL, 810, L14

Liu D., et al., 2019, ApJ, 887, 235

Livermore R. C., et al., 2012, ApJL, 758, 1

Loeb A., Barkana R., 2001, ARA&A, 39, 19

Loiacono F., et al., 2020, arXiv e-prints, p. arXiv:2006.04837

Lu Y., Mo H. J., 2007, MNRAS, 377, 617

Lu Y., Mo H. J., Wechsler R. H., 2015, MNRAS, 446, 1907

Lu N., et al., 2017, ApJS, 230, 1

Luo B., et al., 2017, ApJS, 228, 2

Madau P., Dickinson M., 2014, ARA&A, 52, 415

Madau P., Ferguson H. C., Dickinson M. E., Giavalisco M., Steidel C. C., Fruchter A., 1996, MNRAS, 283, 1388

Madden S. C., et al., 2020, A&A, 643, A141

Magdis G. E., et al., 2012, ApJ, 760, 6

Magdis G., et al., 2017, A&A, 603, 1

Magnelli B., et al., 2014, A&A, 561, A86

Magnelli B., et al., 2020, ApJ, 892, 66

Maiolino R., et al., 2008, A&A, 488, 463

Maiolino R., et al., 2015, MNRAS, 452, 54

Maloney P., Black J. H., 1988, ApJ, 325, 389

Mannucci F., Cresci G., Maiolino R., Marconi a., Gnerucci a., 2010, MNRAS, 408, 2115

Mary D., Bacon R., Conseil S., Piqueras L., Schutz A., 2020, A&A, 635, A194

Maseda M. V., et al., 2017, A&A, 608, A4

Matthee J., Schaye J., 2019, MNRAS, 484, 915

Matthee J., et al., 2017, ApJ, 851, 145

Matthee J., et al., 2019, ApJ, 881, 124

McKee C. F., Ostriker E. C., 2007, ARA&A, 45, 565
McMullin J. P., Waters B., Schiebel D., Young W., Golap K., 2007, in Shaw R. A., Hill F., Bell D. J., eds, Astronomical Society of the Pacific Conference Series Vol. 376, Astronomical Data Analysis Software and Systems XVI. p. 127
Meijerink R., Spaans M., Israel F. P., 2007, A&A, 461, 793
Mitchell P. D., Lacey C. G., Cole S., Baugh C. M., 2014, MNRAS, 444, 2637
Mitra S., Davé R., Finlator K., 2015, MNRAS, 452, 1184
Mitra S., Davé R., Simha V., Finlator K., 2017, MNRAS, 464, 2766
Mo H. J., Yang X., Van Den Bosch F. C., Katz N., 2005, MNRAS, 363, 1155
Moustakas J., Kennicutt, Jr. R. C., Tremonti C. a., 2006, ApJ, 642, 775
Murphy E. J., et al., 2018, in Murphy E., ed., Astronomical Society of the Pacific Conference Series Vol. 517, Science with a Next Generation Very Large Array. p. 3
Muzahid S., et al., 2020, MNRAS, 496, 1013
Naab T., Ostriker J. P., 2017, ARA&A, 55, 59
Nagao T., Maiolino R., Marconi A., 2006, A&A, 459, 85
Nanayakkara T., et al., 2017, MNRAS, 468, 3071
Narayanan D., Krumholz M. R., 2014, MNRAS, 442, 1411
Neeleman M., et al., 2016, ApJ, 820, L39
Neistein E., Dekel A., 2008, MNRAS, 388, 1792
Nelson D., et al., 2018, MNRAS, 475, 624
Nesvadba N. P., et al., 2019, A&A, 624, 1
Newville M., et al., 2019a, lmfit/lmfit-py 0.9.13, doi:10.5281/zenodo.2620617
Newville M., et al., 2019b, lmfit/lmfit-py 1.0.0, doi:10.5281/zenodo.3588521
Noeske K. G., et al., 2007a, ApJ, 660, L43
Noeske K. G., et al., 2007b, ApJ, 660, L47
Obreschkow D., Heywood I., Klöckner H.-R., Rawlings S., 2009, ApJ, 702, 1321
Ojha R., et al., 2001, ApJ, 548, 253
Okamoto T., Gao L., Theuns T., 2008, MNRAS, 390, 920
Oke J. B., Gunn J. E., 1983, ApJ, 266, 713
Oliver S., et al., 2010, MNRAS, 2294, 2279
Omont A., 2007, Reports on Progress in Physics, 70, 1099
Oppenheimer B. D., et al., 2010, MNRAS, 406, 2325
Osterbrock D. E., Ferland G. J., 2006, Astrophysics of gaseous nebulae and active galactic nuclei
Ota K., et al., 2014, ApJ, 792, 34
Ouchi M., et al., 2008, ApJS, 176, 301
Ouchi M., et al., 2013, ApJ, 778, 102
Paalvast M., et al., 2018, A&A, 618, A40
Pannella M., et al., 2009, ApJ, 698, L116
Papadopoulos P. P., Thi W. F., Viti S., 2004, MNRAS, 351, 147
Pavesi R., et al., 2016, ApJ, 832, 151
Pavesi R., et al., 2018, ApJ, 864, 49
Pavesi R., Riechers D. A., Faisst A. L., Stacey G. J., Capak P. L., 2019, ApJ, 882, 168
Peng Y.-j., et al., 2010, ApJ, 721, 193
Peng Y.-j., Lilly S. J., Renzini A., Carollo M., 2014, ApJ, 790, 95
Pentericci L., et al., 2016, ApJ, 829, L11
Penzias A. A., Wilson R. W., 1965, ApJ, 142, 419
Perez F., Granger B. E., 2007, Computing in Science and Engineering, 9, 21
Perlmutter S., et al., 1999, ApJ, 517, 565
Péroux C., Howk J. C., 2020, ARA&A, 58, 363
Pettini M., Pagel B. E. J., 2004, MNRAS, 348, L59
Pham D. T., Castellani M., 2009, Proceedings of the Institution of Mechanical Engineers, Part C: Journal of Mechanical Engineering Science, 223, 2919
Pillepich A., et al., 2018, MNRAS, 475, 648
Planck Collaboration et al., 2016, A&A, 594, A13
Planck Collaboration et al., 2020, A&A, 641, A6
Popping G., Somerville R. S., Trager S. C., 2014, MNRAS, 442, 2398

Popping G., Somerville R. S., Galametz M., 2017a, MNRAS, 471, 3152
Popping G., et al., 2017b, A&A, 602, A11
Popping G., et al., 2019, ApJ, 882, 137
Popping G., et al., 2020, ApJ, 891, 135
Pound M., Wolfire M., 2008, in Argyle R., Bunclark P., Lewis J., eds, Astronomical Society of the Pacific Conference Series Vol. 394, Astron. Data Anal. Softw. Syst. XVII. p. 654
Privon G. C., Narayanan D., Davé R., 2018, ApJ, 867, 102
Quinn T., Katz N., Efstathiou G., 1996, MNRAS, 278, L49
Rafelski M., et al., 2015, AJ, 150, 31
Rakic O., Schaye J., Steidel C. C., Rudie G. C., 2011, MNRAS, 414, 3265
Rangwala N., et al., 2011, ApJ, 743, 94
Reddy N. A., et al., 2015, ApJ, 806, 259
Rémy-Ruyer A., et al., 2014, A&A, 563, A31
Renzini A., Peng Y., 2015, ApJL, 801, L29
Riechers D. A., Carilli C. L., Walter F., Momjian E., 2010, ApJL, 724, 1
Riechers D. A., Hodge J., Walter F., Carilli C. L., Bertoldi F., 2011a, ApJ, 739, L31
Riechers D. A., et al., 2011b, ApJ, 739, L32
Riechers D. A., et al., 2013, Nature, 496, 329
Riechers D. A., et al., 2019, ApJ, 872, 7
Riechers D. A., et al., 2020, ApJ, 896, L21
Riess A. G., et al., 1998, AJ, 116, 1009
Rigby J. R., et al., 2018, ApJ, 853, 87
Robotham A. S. G., Obreschkow D., 2015, PASA, 32, e033
Rodighiero G., et al., 2010, A&A, 518, L25
Rodríguez-Puebla A., Primack J. R., Behroozi P., Faber S. M., 2016, MNRAS, 455, 2592
Rodríguez-Puebla A., Primack J. R., Avila-Reese V., Faber S. M., 2017, MNRAS, 470, 651
Rosenberg M. J. F., et al., 2014, A&A, 564, A126
Rosenberg M. J. F., et al., 2015, ApJ, 801, 72
Rujopakarn W., et al., 2016, ApJ, 833, 12
Rujopakarn W., et al., 2019, ApJ, 882, 107
Saintonge A., et al., 2013, ApJ, 778, 2
Saintonge A., et al., 2016, MNRAS, 462, 1749
Saintonge A., et al., 2017, ApJS, 233, 22
Salim S., et al., 2007, ApJS, 173, 267
Salmi F., et al., 2012, ApJ, 754, L14
Salmon B., et al., 2015, ApJ, 799, 183
Sanders D. B., Mirabel I. F., 1996, ARA&A, 34, 749
Sanders R. L., et al., 2020, MNRAS, 491, 1427
Sandstrom K. M., et al., 2013, ApJ, 777, 5
Santini P., et al., 2009, A&A, 504, 751
Santini P., et al., 2015, ApJ, 801, 97
Santini P., et al., 2017, ApJ, 847, 76
Sargent M. T., et al., 2014, ApJ, 793, 19
Schaye J., et al., 2010, MNRAS, 402, 1536
Schaye J., et al., 2015, MNRAS, 446, 521
Schinnerer E., et al., 2016, ApJ, 833, 112
Schmidt M., 1959, ApJ, 129, 243
Schneider N., Simon R., Kramer C., Kraemer K., Stutzki J., Mookerjea B., 2003, A&A, 406, 915
Schramm D. N., Turner M. S., 1998, Reviews of Modern Physics, 70, 303
Schreiber C., et al., 2015, A&A, 575, A74
Schreiber C., et al., 2016, A&A, 589, A35
Schreiber C., Elbaz D., Pannella M., Ciesla L., Wang T., Franco M., 2018, A&A, 609, A30
Schroetter I., et al., 2016, ApJ, 833, 39
Schruba A., et al., 2011, AJ, 142, 37
Schruba A., et al., 2012, AJ, 143, 138

Scoville N., et al., 2007, ApJS, 172, 1
Scoville N., et al., 2014, ApJ, 783, 84
Scoville N., et al., 2016, ApJ, 820, 83
Scoville N., et al., 2017, ApJ, 837, 150
Shapley a. E., Steidel C. C., Pettini M., Adelberger K. L., 2003, ApJ, 588, 65
Sharon C. E., et al., 2016, ApJ, 827, 1
Shivaei I., Reddy N. A., Steidel C. C., Shapley A. E., 2015, ApJ, 804, 1
Silverman J. D., et al., 2015, ApJL, 812, L23
Silverman J. D., et al., 2018, ApJ, 867, 92
Skelton R. E., et al., 2014, ApJS, 214, 24
Smail I., Ivison R. J., Blain A. W., 1997, ApJ, 490, L5
Smit R., et al., 2018, Nature, 553, 179
Solomon P., Vanden Bout P., 2005, ARA&A, 43, 677
Solomon P. M., Rivolo A. R., Barrett J., Yahil A., 1987, ApJ, 319, 730
Solomon P. M., Radford S. J. E., Downes D., 1992a, Nature, 356, 318
Solomon P. M., Downes D., Radford S. J. E., 1992b, ApJ, 398, L29
Somerville R. S., Davé R., 2015, ARA&A, 53, 51
Somerville R. S., Hopkins P. F., Cox T. J., Robertson B. E., Hernquist L., 2008, MNRAS, 391, 481
Somerville R. S., Popping G., Trager S. C., 2015, MNRAS, 453, 4337
Sorba R., Sawicki M., 2018, MNRAS, 476, 1532
Sparre M., et al., 2015, MNRAS, 447, 3548
Sparre M., et al., 2017, MNRAS, 466, 88
Späth H., 2004, Mathematical Communications, 9, 27
Speagle J. S., Steinhardt C. L., Capak P. L., Silverman J. D., 2014, ApJS, 214, 15
Spilker J. S., et al., 2014, ApJ, 785, 149
Stark D. P., Schenker M. A., Ellis R., Robertson B., McLure R., Dunlop J., 2013, ApJ, 763, 129
Straatman C. M. S., et al., 2016, ApJ, 830, 1
Strom A. L., Steidel C. C., Rudie G. C., Trainor R. F., Pettini M., Reddy N. A., 2017, ApJ, 836, 164
Strong A., Mattox J., 1996, A&A, 308, L21
Stutzki J., et al., 1997, ApJ, 477, L33
Sun G., et al., 2018, ApJ, 856, 107
Tacchella S., et al., 2016, MNRAS, 457, 2790
Tacconi L. J., et al., 2010, Nature, 463, 781
Tacconi L. J., et al., 2013, ApJ, 768, 74
Tacconi L. J., et al., 2018, ApJ, 853, 179
Tacconi L. J., Genzel R., Sternberg A., 2020, ARA&A, 58, 157
Talia M., et al., 2018, MNRAS, 476, 3956
Tan Q., et al., 2013, ApJ, 776, L24
Tasca L. A. M., et al., 2015, A&A, 581, A54
Taylor M. B., 2005, in Shopbell P., Britton M., Ebert R., eds, Astronomical Society of the Pacific Conference Series Vol. 347, Astronomical Data Analysis Software and Systems XIV. p. 29
The Astropy Collaboration et al., 2013, A&A, 558, A33
The Astropy Collaboration et al., 2018, AJ, 156, 123
Tielens A. G., 2008, ARA&A, 46, 289
Tielens A. G. G. M., Hollenbach D., 1985a, ApJ, 291, 722
Tielens A. G. G. M., Hollenbach D., 1985b, ApJ, 291, 747
Tomczak A. R., et al., 2014, ApJ, 783, 85
Tomczak A. R., et al., 2016, ApJ, 817, 118
Torrey P., Vogelsberger M., Genel S., Sijacki D., Springel V., Hernquist L., 2014, MNRAS, 438, 1985
Trainor R. F., Steidel C. C., Strom A. L., Rudie G. C., 2015, ApJ, 809, 89
Tremonti C. a., et al., 2004, ApJ, 613, 898
Tumlinson J., Peeples M. S., Werk J. K., 2017, ARA&A, 55, 389
Uzgil B. D., et al., 2019, ApJ, 887, 37
Valentino F., et al., 2018, ApJ, 869, 27
Valentino F., et al., 2020a, A&A, 641, A155

Valentino F., et al., 2020b, ApJ, 890, 24
Vallini L., Gruppioni C., Pozzi F., Vignali C., Zamorani G., 2016, MNRAS, 456, L40
Vallini L., et al., 2019, MNRAS, 14, 1
Venemans B. P., et al., 2018, ApJ, 866, 159
Venemans B. P., et al., 2019, ApJ, 874, L30
Verhamme A., et al., 2018, MNRAS, 478, L60
Vogelsberger M., et al., 2014, Nature, 509, 177
Walter F., Weiß A., Downes D., Decarli R., Henkel C., 2011, ApJ, 730, 18
Walter F., et al., 2012, ApJ, 752, 93
Walter F., et al., 2014, ApJ, 782, 79
Walter F., et al., 2016, ApJ, 833, 67
Walter F., et al., 2020, ApJ, 902, 111
Wang T., et al., 2017, A&A, 601, A63
Wardlow J. L., et al., 2018, MNRAS, 479, 3879
Weilbacher P. M., et al., 2020, A&A, 641, A28
Weiß A., Henkel C., Downes D., Walter F., 2003, A&A, 409, L41
Weiß A., Downes D., Henkel C., Walter F., 2005, A&A, 429, L25
Weiss A., Downes D., Walter F., Henkel C., 2007a, in Baker A., Glenn J., Harris A., Mangum J., Yun M., eds, Astronomical Society of the Pacific Conference Series Vol. 375, From Z-Machines to ALMA (sub)millim. Spectrosc. Galaxies. p. 25
Weiss A., et al., 2007b, A&A, 467, 955
Weiß A., et al., 2013, ApJ, 767, 88
Whitaker K. E., van Dokkum P. G., Brammer G., Franx M., 2012, ApJ, 754, L29
Whitaker K. E., et al., 2014, ApJ, 795, 104
Whitaker K. E., et al., 2015, ApJ, 811, L12
White S. D. M., Frenk C. S., 1991, ApJ, 379, 52
White S. D. M., Rees M. J., 1978, MNRAS, 183, 341
Williams R. E., et al., 1996, AJ, 112, 1335
Williams R. E., et al., 2000, AJ, 120, 2735
Wolfire M. G., Hollenbach D., McKee C. F., 2010, ApJ, 716, 1191
Wootten A., Thompson A. R., 2009, IEEE Proceedings, 97, 1463
Wuyts S., et al., 2013, ApJ, 779, 135
Wuyts E., et al., 2014, ApJL, 789, 1
Xue Y. Q., et al., 2011, ApJS, 195, 10
Yamaguchi Y., et al., 2017, ApJ, 845, 108
Yang C., et al., 2017a, A&A, 608, A144
Yang H., et al., 2017b, ApJ, 844, 171
York D. G., et al., 2000, AJ, 120, 1579
Young J. S., Scoville N. Z., 1991, ARA&A, 29, 581
Yue B., Ferrara A., 2019, MNRAS, 490, 1928
Yue B., Ferrara A., Pallottini A., Gallerani S., Vallini L., 2015, MNRAS, 450, 3829
Zahid H. J., et al., 2014, ApJ, 791, 130
Zanella A., et al., 2018, MNRAS, 481, 1976
da Cunha E., et al., 2013, ApJ, 766, 13
van de Voort F., Schaye J., Booth C. M., Haas M. R., Dalla Vecchia C., 2011, MNRAS, 414, 2458
van de Voort F., Schaye J., Altay G., Theuns T., 2012, MNRAS, 421, 2809
van der Walt S., Colbert S. C., Varoquaux G., 2011, Computing in Science and Engineering, 13, 22
van der Wel A., et al., 2012, ApJS, 203, 24
van der Wel A., et al., 2014, ApJ, 788, 28
van der Werf P. P., et al., 2010, A&A, 518, L42

Publication list

Conference proceedings

39. *Nature and physical properties of gas-mass selected galaxies using integral field spectroscopy*
Leindert A. Boogaard, 2020, In Elisabete da Cunha, Jacqueline Hodge, José Afonso, Laura Pentericci, and David Sobral, editors, *Uncovering Early Galaxy Evolution in the ALMA and JWST Era*, volume 352, pages 326–330

Refereed publications

Publications marked with a star (*) are included in this thesis.

38. *MusE GAs FLOw and Wind (MEGAFLOW) VII: A NOEMA pilot program to probe molecular gas in galaxies with measured circumgalactic gas flows.*
Jonathan Freundlich, Nicolas Bouché, Thierry Contini, Emanuele Daddi, Johannes Zabl, Ilane Schroetter, **Leindert Boogaard**, and Johan Richard, 2021, MNRAS, 501, 1900–1910

37.* *The ALMA Spectroscopic Survey in the Hubble Ultra Deep Field: Multiband Constraints on Line-luminosity Functions and the Cosmic Density of Molecular Gas.*
Roberto Decarli, Manuel Aravena, **Leindert Boogaard**, Chris Carilli, Jorge González-López, Fabian Walter, Paulo C. Cortes, Pierre Cox, Elisabete da Cunha, Emanuele Daddi, Tanio Díaz-Santos, Jacqueline A. Hodge, Hanae Inami, Marcel Neeleman, Mladen Novak, Pascal Oesch, Gergö Popping, Dominik Riechers, Ian Smail, Bade Uzgil, Paul van der Werf, Jeff Wagg, and Axel Weiss, 2020, ApJ, 902, 110

36. *The ALMA Spectroscopic Survey Large Program: The Infrared Excess of z = 1.5-10 UV-selected Galaxies and the Implied High-redshift Star Formation History.*
Rychard Bouwens, Jorge González-López, Manuel Aravena, Roberto Decarli, Mladen Novak, Mauro Stefanon, Fabian Walter, **Leindert Boogaard**, Chris Carilli, Ugnė Dudzevičiūtė, Ian Smail, Emanuele Daddi, Elisabete da Cunha, Rob Ivison, Themiya Nanayakkara, Paulo Cortes, Pierre Cox, Hanae Inami, Pascal Oesch, Gergö Popping, Dominik Riechers, Paul van der Werf, Axel Weiss, Yoshi Fudamoto, and Jeff Wagg, 2020, ApJ, 902, 112

35.* *The ALMA Spectroscopic Survey in the Hubble Ultra Deep Field: CO Excitation and Atomic Carbon in Star-forming Galaxies at z = 1-3.*
Leindert A. Boogaard, Paul van der Werf, Axel Weiss, Gergö Popping, Roberto Decarli, Fabian Walter, Manuel Aravena, Rychard Bouwens, Dominik Riechers, Jorge González-López, Ian Smail,

Chris Carilli, Melanie Kaasinen, Emanuele Daddi, Pierre Cox, Tanio Díaz-Santos, Hanae Inami, Paulo C. Cortes, and Jeff Wagg, 2020, ApJ, 902, 109

34. *The ALMA Spectroscopic Survey in the Hubble Ultra Deep Field: Constraining the Molecular Content at* $\log(M_*/M_\odot) \sim 9.5$ *with CO Stacking of MUSE-detected* $z \sim 1.5$ *Galaxies*.
Hanae Inami, Roberto Decarli, Fabian Walter, Axel Weiss, Chris Carilli, Manuel Aravena, **Leindert Boogaard**, Jorge Gonzaĺez-López, Gergö Popping, Elisabete da Cunha, Roland Bacon, Franz Bauer, Thierry Contini, Paulo C. Cortes, Pierre Cox, Emanuele Daddi, Tanio Díaz-Santos, Melanie Kaasinen, Dominik A. Riechers, Jeff Wagg, Paul van der Werf, and Lutz Wisotzki, 2020, ApJ, 902, 113

33. *The Evolution of the Baryons Associated with Galaxies Averaged over Cosmic Time and Space*.
Fabian Walter, Chris Carilli, Marcel Neeleman, Roberto Decarli, Gergö Popping, Rachel S. Somerville, Manuel Aravena, Frank Bertoldi, **Leindert Boogaard**, Pierre Cox, Elisabete da Cunha, Benjamin Magnelli, Danail Obreschkow, Dominik Riechers, Hans-Walter Rix, Ian Smail, Axel Weiss, Roberto J. Assef, Franz Bauer, Rychard Bouwens, Thierry Contini, Paulo C. Cortes, Emanuele Daddi, Tanio Diaz-Santos, Jorge González-López, Joseph Hennawi, Jacqueline A. Hodge, Hanae Inami, Rob Ivison, Pascal Oesch, Mark Sargent, Paul van der Werf, Jeff Wagg, and L. Y. Aaron Yung, 2020, ApJ, 902, 111

32. *The MUSE Hubble Ultra Deep Field Survey. XV. The mean rest-UV spectra of* Lyα *emitters at* $z > 3$.
Anna Feltre, Michael V. Maseda, Roland Bacon, Jayadev Pradeep, Floriane Leclercq, Haruka Kusakabe, Lutz Wisotzki, Takuya Hashimoto, Kasper B. Schmidt, Jeremy Blaizot, Jarle Brinchmann, **Leindert Boogaard**, Sebastiano Cantalupo, David Carton, Hanae Inami, Wolfram Kollatschny, Raffaella A. Marino, Jorryt Matthee, Themiya Nanayakkara, Johan Richard, Joop Schaye, Laurence Tresse, Tanya Urrutia, Anne Verhamme, and Peter M. Weilbacher, 2020, A&A, 641, A118

31. *The ALMA Spectroscopic Survey in the Hubble Ultra Deep Field: The Nature of the Faintest Dusty Star-forming Galaxies*.
Manuel Aravena, **Leindert Boogaard**, Jorge Gónzalez-López, Roberto Decarli, Fabian Walter, Chris L. Carilli, Ian Smail, Axel Weiss, Roberto J. Assef, Franz Erik Bauer, Rychard J. Bouwens, Paulo C. Cortes, Pierre Cox, Elisabete da Cunha, Emanuele Daddi, Tanio Díaz-Santos, Hanae Inami, Rob Ivison, Mladen Novak, Gergö Popping, Dominik Riechers, Paul van der Werf, and Jeff Wagg, 2020, ApJ, 901, 79

30. *A Comparison of the Stellar, CO, and Dust-continuum Emission from Three Star-forming HUDF Galaxies at* $z \sim 2$.
Melanie Kaasinen, Fabian Walter, Mladen Novak, Marcel Neeleman, Ian Smail, **Leindert Boogaard**, Elisabete da Cunha, Axel Weiss, Daizhong Liu, Roberto Decarli, Gergö Popping, Tanio Diaz-Santos, Paulo Cortés, Manuel Aravena, Paul van der Werf, Dominik Riechers, Hanae Inami, Jacqueline A. Hodge, Hans-Walter Rix, and Pierre Cox, 2020, ApJ, 899, 37

29. *Stellar populations and physical properties of starbursts in the antennae galaxy from self-consistent modelling of MUSE spectra*.
M. L. P. Gunawardhana, J. Brinchmann, P. M. Weilbacher, P. Norberg, A. Monreal-Ibero, T. Nanayakkara, M. den Brok, **L. Boogaard**, and W. Kollatschny, 2020, MNRAS, 497, 3860–3895

28. *The nature of CR7 revealed with MUSE: a young starburst powering extended* Lyα *emission at* $z = 6.6$.
Jorryt Matthee, Gabriele Pezzulli, Ruari Mackenzie, Sebastiano Cantalupo, Haruka Kusakabe, Floriane Leclercq, David Sobral, Johan Richard, Lutz Wisotzki, Simon Lilly, **Leindert Boogaard**, Raffaella Marino, Michael Maseda, and Themiya Nanayakkara, 2020, MNRAS, 498, 3043–3059

27. *The ALMA Spectroscopic Survey in the HUDF: Deep 1.2 mm Continuum Number Counts.*
Jorge González-López, Mladen Novak, Roberto Decarli, Fabian Walter, Manuel Aravena, Chris Carilli, **Leindert Boogaard**, Gergö Popping, Axel Weiss, Roberto J. Assef, Franz Erik Bauer, Rychard Bouwens, Paulo C. Cortes, Pierre Cox, Emanuele Daddi, Elisabete da Cunha, Tanio Díaz-Santos, Rob Ivison, Benjamin Magnelli, Dominik Riechers, Ian Smail, Paul van der Werf, and Jeff Wagg, 2020, ApJ, 897, 91

26. *VLA-ALMA Spectroscopic Survey in the Hubble Ultra Deep Field (VLASPECS): Total Cold Gas Masses and CO Line Ratios for $z = 2 - 3$ Main-sequence Galaxies.*
Dominik A. Riechers, **Leindert A. Boogaard**, Roberto Decarli, Jorge González-López, Ian Smail, Fabian Walter, Manuel Aravena, Christopher L. Carilli, Paulo C. Cortes, Pierre Cox, Tanio Díaz-Santos, Jacqueline A. Hodge, Hanae Inami, Rob J. Ivison, Melanie Kaasinen, Jeff Wagg, Axel Weiß, and Paul van der Werf, 2020, ApJL, 896, L21

25. *Elevated ionizing photon production efficiency in faint high-equivalent-width Lyman α emitters.*
Michael V. Maseda, Roland Bacon, Daniel Lam, Jorryt Matthee, Jarle Brinchmann, Joop Schaye, Ivo Labbe, Kasper B. Schmidt, **Leindert Boogaard**, Rychard Bouwens, Sebastiano Cantalupo, Marijn Franx, Takuya Hashimoto, Hanae Inami, Haruka Kusakabe, Guillaume Mahler, Themiya Nanayakkara, Johan Richard, and Lutz Wisotzki, 2020, MNRAS, 493, 5120–5130

24. *The MUSE-Faint survey. I. Spectroscopic evidence for a star cluster in Eridanus 2 and constraints on MACHOs as a constituent of dark matter.*
Sebastiaan L. Zoutendijk, Jarle Brinchmann, **Leindert A. Boogaard**, Madusha L. P. Gunawardhana, Tim-Oliver Husser, Sebastian Kamann, Andrés Felipe Ramos Padilla, Martin M. Roth, Roland Bacon, Mark den Brok, Stefan Dreizler, and Davor Krajnović, 2020, A&A, 635, A107

23. *The ALMA Spectroscopic Survey in the HUDF: A Model to Explain Observed 1.1 and 0.85 mm Dust Continuum Number Counts.*
Gergö Popping, Fabian Walter, Peter Behroozi, Jorge González-López, Christopher C. Hayward, Rachel S. Somerville, Paul van der Werf, Manuel Aravena, Roberto J. Assef, **Leindert Boogaard**, Franz E. Bauer, Paulo C. Cortes, Pierre Cox, Tanio Díaz-Santos, Roberto Decarli, Maximilien Franco, Rob Ivison, Dominik Riechers, Hans-Walter Rix, and Axel Weiss, 2020, ApJ, 891, 135

22. *The ALMA Spectroscopic Survey in the HUDF: The Cosmic Dust and Gas Mass Densities in Galaxies up to $z \sim 3$.*
Benjamin Magnelli, **Leindert Boogaard**, Roberto Decarli, Jorge Gónzalez-López, Mladen Novak, Gergö Popping, Ian Smail, Fabian Walter, Manuel Aravena, Roberto J. Assef, Franz Erik Bauer, Frank Bertoldi, Chris Carilli, Paulo C. Cortes, Elisabete da Cunha, Emanuele Daddi, Tanio Díaz-Santos, Hanae Inami, Robert J. Ivison, Olivier Le Fèvre, Pascal Oesch, Dominik Riechers, Hans-Walter Rix, Mark T. Sargent, Paul van der Werf, Jeff Wagg, and Axel Weiss, 2020, ApJ, 892, 66

21. *Evidence for ram-pressure stripping in a cluster of galaxies at $z = 0.7$.*
A. Boselli, B. Epinat, T. Contini, V. Abril-Melgarejo, L. A. Boogaard, E. Pointecouteau, E. Ventou, J. Brinchmann, D. Carton, H. Finley, L. Michel-Dansac, G. Soucail, and P. M. Weilbacher, 2019, A&A, 631, A114

20. *The ALMA Spectroscopic Survey in the HUDF: CO Luminosity Functions and the Molecular Gas Content of Galaxies through Cosmic History.*
Roberto Decarli, Fabian Walter, Jorge Gónzalez-López, Manuel Aravena, **Leindert Boogaard**, Chris Carilli, Pierre Cox, Emanuele Daddi, Gergö Popping, Dominik Riechers, Bade Uzgil, Axel Weiss, Roberto J. Assef, Roland Bacon, Franz Erik Bauer, Frank Bertoldi, Rychard Bouwens,

Thierry Contini, Paulo C. Cortes, Elisabete da Cunha, Tanio Díaz-Santos, David Elbaz, Hanae Inami, Jacqueline Hodge, Rob Ivison, Olivier Le Fèvre, Benjamin Magnelli, Mladen Novak, Pascal Oesch, Hans-Walter Rix, Mark T. Sargent, Ian Smail, A. Mark Swinbank, Rachel S. Somerville, Paul van der Werf, Jeff Wagg, and Lutz Wisotzki, 2019, ApJ, 882, 138

19.* *The ALMA Spectroscopic Survey in the HUDF: Nature and Physical Properties of Gas-mass Selected Galaxies Using MUSE Spectroscopy.*
Leindert A. Boogaard, Roberto Decarli, Jorge González-López, Paul van der Werf, Fabian Walter, Rychard Bouwens, Manuel Aravena, Chris Carilli, Franz Erik Bauer, Jarle Brinchmann, Thierry Contini, Pierre Cox, Elisabete da Cunha, Emanuele Daddi, Tanio Díaz-Santos, Jacqueline Hodge, Hanae Inami, Rob Ivison, Michael Maseda, Jorryt Matthee, Pascal Oesch, Gergö Popping, Dominik Riechers, Joop Schaye, Sander Schouws, Ian Smail, Axel Weiss, Lutz Wisotzki, Roland Bacon, Paulo C. Cortes, Hans-Walter Rix, Rachel S. Somerville, Mark Swinbank, and Jeff Wagg, 2019, ApJ, 882, 140

18. *The ALMA Spectroscopic Survey in the Hubble Ultra Deep Field: Evolution of the Molecular Gas in CO-selected Galaxies.*
Manuel Aravena, Roberto Decarli, Jorge Gónzalez-López, **Leindert Boogaard**, Fabian Walter, Chris Carilli, Gergö Popping, Axel Weiss, Roberto J. Assef, Roland Bacon, Franz Erik Bauer, Frank Bertoldi, Richard Bouwens, Thierry Contini, Paulo C. Cortes, Pierre Cox, Elisabete da Cunha, Emanuele Daddi, Tanio Díaz-Santos, David Elbaz, Jacqueline Hodge, Hanae Inami, Rob Ivison, Olivier Le Fèvre, Benjamin Magnelli, Pascal Oesch, Dominik Riechers, Ian Smail, Rachel S. Somerville, A. M. Swinbank, Bade Uzgil, Paul van der Werf, Jeff Wagg, and Lutz Wisotzki, 2019, ApJ, 882, 136

17. *The Atacama Large Millimeter/submillimeter Array Spectroscopic Survey in the Hubble Ultra Deep Field: CO Emission Lines and 3 mm Continuum Sources.*
Jorge González-López, Roberto Decarli, Riccardo Pavesi, Fabian Walter, Manuel Aravena, Chris Carilli, **Leindert Boogaard**, Gergö Popping, Axel Weiss, Roberto J. Assef, Franz Erik Bauer, Frank Bertoldi, Richard Bouwens, Thierry Contini, Paulo C. Cortes, Pierre Cox, Elisabete da Cunha, Emanuele Daddi, Tanio Díaz-Santos, Hanae Inami, Jacqueline Hodge, Rob Ivison, Olivier Le Fèvre, Benjamin Magnelli, Pascal Oesch, Dominik Riechers, Hans-Walter Rix, Ian Smail, A. M. Swinbank, Rachel S. Somerville, Bade Uzgil, and Paul van der Werf, 2019, ApJ, 882, 139

16. *The ALMA Spectroscopic Survey in the HUDF: the Molecular Gas Content of Galaxies and Tensions with IllustrisTNG and the Santa Cruz SAM.*
Gergö Popping, Annalisa Pillepich, Rachel S. Somerville, Roberto Decarli, Fabian Walter, Manuel Aravena, Chris Carilli, Pierre Cox, Dylan Nelson, Dominik Riechers, Axel Weiss, **Leindert Boogaard**, Richard Bouwens, Thierry Contini, Paulo C. Cortes, Elisabete da Cunha, Emanuele Daddi, Tanio Díaz-Santos, Benedikt Diemer, Jorge González-López, Lars Hernquist, Rob Ivison, Olivier Le Fèvre, Federico Marinacci, Hans-Walter Rix, Mark Swinbank, Mark Vogelsberger, Paul van der Werf, Jeff Wagg, and L. Y. Aaron Yung, 2019, ApJ, 882, 137

15. *Resolved UV and [C II] Structures of Luminous Galaxies within the Epoch of Reionization.*
J. Matthee, D. Sobral, **L. A. Boogaard**, H. Röttgering, L. Vallini, A. Ferrara, A. Paulino-Afonso, F. Boone, D. Schaerer, and B. Mobasher, 2019, ApJ, 881, 124

14. *The mean Hα EW and Lyman-continuum photon production efficiency for faint $z \approx 4$-5 galaxies.*
Daniel Lam, Rychard J. Bouwens, Ivo Labbé, Joop Schaye, Kasper B. Schmidt, Michael V. Maseda, Roland Bacon, **Leindert A. Boogaard**, Themiya Nanayakkara, Johan Richard, Guillaume Mahler, and Tanya Urrutia, 2019, A&A, 627, A164

13. *Exploring* He *II* *λ1640 emission line properties at* $z \sim 2 - 4$.
Themiya Nanayakkara, Jarle Brinchmann, **Leindert Boogaard**, Rychard Bouwens, Sebastiano Cantalupo, Anna Feltre, Wolfram Kollatschny, Raffaella Anna Marino, Michael Maseda, Jorryt Matthee, Mieke Paalvast, Johan Richard, and Anne Verhamme, 2019, A&A, 624, A89

12. *The MUSE-Wide Survey: survey description and first data release.*
T. Urrutia, L. Wisotzki, J. Kerutt, K. B. Schmidt, E. C. Herenz, J. Klar, R. Saust, M. Werhahn, C. Diener, J. Caruana, D. Krajnović, R. Bacon, **L. Boogaard**, J. Brinchmann, H. Enke, M. Maseda, T. Nanayakkara, J. Richard, M. Steinmetz, and P. M. Weilbacher, 2019, A&A, 624, A141

11. *The MUSE-Wide Survey: A determination of the Lyman α emitter luminosity function at* $3 < z < 6$.
Edmund Christian Herenz, Lutz Wisotzki, Rikke Saust, Josephine Kerutt, Tanya Urrutia, Catrina Diener, Kasper Borello Schmidt, Raffaella Anna Marino, Geoffroy de la Vieuville, **Leindert Boogaard**, Joop Schaye, Bruno Guiderdoni, Johan Richard, and Roland Bacon, 2019, A&A, 621, A107

10.* *The MUSE Hubble Ultra Deep Field Survey. XI. Constraining the low-mass end of the stellar mass - star formation rate relation at* $z < 1$.
Leindert A. Boogaard, Jarle Brinchmann, Nicolas Bouché, Mieke Paalvast, Roland Bacon, Rychard J. Bouwens, Thierry Contini, Madusha L. P. Gunawardhana, Hanae Inami, Raffaella A. Marino, Michael V. Maseda, Peter Mitchell, Themiya Nanayakkara, Johan Richard, Joop Schaye, Corentin Schreiber, Sandro Tacchella, Lutz Wisotzki, and Johannes Zabl, 2018, A&A, 619, A27

9. *Properties and redshift evolution of star-forming galaxies with high* [O *III*]/[O *II*]/ *ratios with MUSE at* $0.28 < z < 0.85$. M. Paalvast, A. Verhamme, L. A. Straka, J. Brinchmann, E. C. Herenz, D. Carton, M. L. P. Gunawardhana, **L. A. Boogaard**, S. Cantalupo, T. Contini, B. Epinat, H. Inami, R. A. Marino, M. V. Maseda, L. Michel-Dansac, S. Muzahid, T. Nanayakkara, G. Pezzulli, J. Richard, J. Schaye, M. C. Segers, T. Urrutia, M. Wendt, and L. Wisotzki, 2018, A&A, 618, A40

8. *MUSE Spectroscopic Identifications of Ultra-faint Emission Line Galaxies with* $M_{\rm UV} \sim -15$.
Michael V. Maseda, Roland Bacon, Marijn Franx, Jarle Brinchmann, Joop Schaye, **Leindert A. Boogaard**, Nicolas Bouché, Rychard J. Bouwens, Sebastiano Cantalupo, Thierry Contini, Takuya Hashimoto, Hanae Inami, Raffaella A. Marino, Sowgat Muzahid, Themiya Nanayakkara, Johan Richard, Kasper B. Schmidt, Anne Verhamme, and Lutz Wisotzki, 2018, ApJL, 865:L1

7. *The MUSE Hubble Ultra Deep Field Survey. XII.* Mg *II* *emission and absorption in star-forming galaxies.*
Anna Feltre, Roland Bacon, Laurence Tresse, Hayley Finley, David Carton, Jérémy Blaizot, Nicolas Bouché, Thibault Garel, Hanae Inami, **Leindert A. Boogaard**, Jarle Brinchmann, Stéphane Charlot, Jacopo Chevallard, Thierry Contini, Leo Michel-Dansac, Guillaume Mahler, Raffaella A. Marino, Michael V. Maseda, Johan Richard, Kasper B. Schmidt, and Anne Verhamme, 2018, A&A, 617, A62

6. *Ionised gas structure of 100 kpc in an over-dense region of the galaxy group COSMOS-Gr30 at* $z = 0.7$.
B. Epinat, T. Contini, H. Finley, **L. A. Boogaard**, A. Guérou, J. Brinchmann, D. Carton, L. Michel-Dansac, R. Bacon, S. Cantalupo, M. Carollo, S. Hamer, W. Kollatschny, D. Krajnović, R. A. Marino, J. Richard, G. Soucail, P. M. Weilbacher, and L. Wisotzki, 2018, A&A, 609, A40

5. *The MUSE Hubble Ultra Deep Field Survey. VII.* Fe *II** *emission in star-forming galaxies.*
Hayley Finley, Nicolas Bouché, Thierry Contini, Mieke Paalvast, **Leindert Boogaard**, Michael Maseda, Roland Bacon, Jérémy Blaizot, Jarle Brinchmann, Benoît Epinat, Anna Feltre, Raffaella Anna Marino, Sowgat Muzahid, Johan Richard, Joop Schaye, Anne Verhamme, Peter M. Weilbacher, and Lutz Wisotzki, 2017, A&A, 608, A7

4. *The MUSE Hubble Ultra Deep Field Survey. II. Spectroscopic redshifts and comparisons to color selections of high-redshift galaxies*.
   H. Inami, R. Bacon, J. Brinchmann, J. Richard, T. Contini, S. Conseil, S. Hamer, M. Akhlaghi, N. Bouché, B. Clément, G. Desprez, A. B. Drake, T. Hashimoto, F. Leclercq, M. Maseda, L. Michel-Dansac, M. Paalvast, L. Tresse, E. Ventou, W. Kollatschny, **L. A. Boogaard**, H. Finley, R. A. Marino, J. Schaye, and L. Wisotzki, 2017, A&A, 608, A2

3. *The MUSE Hubble Ultra Deep Field Survey. IV. Global properties of* C iii] *emitters*.
   Michael V. Maseda, Jarle Brinchmann, Marijn Franx, Roland Bacon, Rychard J. Bouwens, Kasper B. Schmidt, **Leindert A. Boogaard**, Thierry Contini, Anna Feltre, Hanae Inami, Wolfram Kollatschny, Raffaella A. Marino, Johan Richard, Anne Verhamme, and Lutz Wisotzki, 2017, A&A, 608, A4

2. *The MUSE Hubble Ultra Deep Field Survey. III. Testing photometric redshifts to 30th magnitude*.
   J. Brinchmann, H. Inami, R. Bacon, T. Contini, M. Maseda, J. Chevallard, N. Bouché, **L. Boogaard**, M. Carollo, S. Charlot, W. Kollatschny, R. A. Marino, R. Pello, J. Richard, J. Schaye, A. Verhamme, and L. Wisotzki, 2017, A&A, 608, A3

1. *Deep MUSE observations in the HDFS. Morpho-kinematics of distant star-forming galaxies down to* $10^8\,M_\odot$.
   T. Contini, B. Epinat, N. Bouché, J. Brinchmann, **L. A. Boogaard**, E. Ventou, R. Bacon, J. Richard, P. M. Weilbacher, L. Wisotzki, D. Krajnović, J. B. Vielfaure, E. Emsellem, H. Finley, H. Inami, J. Schaye, M. Swinbank, A. Guérou, T. Martinsson, L. Michel-Dansac, I. Schroetter, M. Shirazi, and G. Soucail, 2016, A&A, 591, A49

Nederlandse samenvatting

Kort overzicht

De vorming en evolutie van sterrenstelsels wordt aangedreven door de vorming van nieuwe sterren uit koud gas. Waarnemingen van jonge sterren in verre sterrenstelsels in het vroege universum, zoals in het *Hubble Ultra Deep Field*, hebben laten zien hoe de kosmische dichtheid van de stervormingssnelheid evolueert. Maar, terwijl het *gevolg* van stervorming—de jonge sterren—met steeds meer detail in kaart is gebracht, blijft de *oorzaak*—het koude gas dat de brandstof is voor de stervorming—ongrijpbaar. Dit proefschrift presenteert een observationele studie van het koude interstellaire medium van verre sterrenstelsels in het vroege universum, met behulp van de meest gevoelige submillimeter telescoop tot nu toe, de *Atacama Large Millimeter Array*, en nieuwe *integral-field* spectrografen, zoals de *Multi Unit Spectroscopic Explorer* op de *Very Large Telescope*. Het brengt de eigenschappen van stervormende sterrenstelsels en hun moleculaire gas in kaart en beschrijft de evolutie van de kosmische dichtheid van moleculair gas—*de brandstof voor stervorming*.

Uitgebreide samenvatting

Van gevolg naar oorzaak

Het is bijna honderd jaar geleden dat Edwin Hubble aantoonde dat sommige 'nevels' in feite aparte *sterrenstelsels* zijn; eilanden van sterren die op grote afstand staan van het sterrenstelsel waar onze Zon zich in bevindt, de *Melkweg*. Een sterrenstelsel zoals de Melkweg bevat miljarden sterren. Tussen de sterren in een sterrenstelsel bevindt zich gas en stof, dat het *interstellair medium* wordt genoemd. Sterrenstelsels kunnen grofweg worden onderverdeeld in twee categorieën: *stervormende* sterrenstelsels, met veel gas, en *passieve* sterrenstelsels, met weinig gas. Het gas bestaat voornamelijk uit waterstof en helium, dat verrijkt is met zwaardere elementen die zijn gevormd door kernfusie in de kernen van sterren. Het gas kan worden verhit (bijvoorbeeld door sterlicht) en afkoelen, en zich op die manier in verschillende fasen bevinden. In de koudste fase, waar individuele waterstofmoleculen (H) zich kunnen binden en moleculair waterstof (H_2) vormen, kunnen wolken van gas ineenstorten onder de zwaartekracht en zo nieuwe sterren vormen. Het koude gas in sterrenstelsels is dus de *brandstof voor stervorming*.

Dat het heelal gevuld is met sterrenstelsels wordt op een prachtige manier zichtbaar in de *Ultra Deep Field* opname van de *Hubble* ruimtetelescoop, die te zien is in Figuur 1.1 in hoofdstuk 1. Door dagenlang naar hetzelfde deel van de nachtelijke hemel te staren, wordt langzaam het zwakke licht zichtbaar dat is uitgezonden door verre sterrenstelsels, op een moment waarop het heelal nog veel minder oud was. Metingen aan onder andere de *kosmische achtergrondstraling* hebben laten zien dat het uitdijende heelal nu ongeveer 13.8 miljard jaar oud is en in het begin gevuld was met gas van een hoge temperatuur en dichtheid, tijdens wat de *big bang* wordt genoemd. Een van de grote vragen in de moderne sterrenkunde is hoe de sterrenstelsels sinds dit begin zijn gevormd en geëvolueerd tot de diverse populatie die we vandaag de dag zien.

De vorming en evolutie van sterrenstelsels is een complex fenomeen, met processen die werken op uiteenlopende afstanden en tijdschalen. Aan de ene kant vormen individuele groepen sterren zich gedurende miljoenen jaren diep in het koude interstellair medium, op schalen die veel kleiner zijn dan een enkel sterrenstelsel. Aan de andere kant duurt de opbouw van de populatie van sterren miljarden jaren en moet het gas dat hiervoor nodig is afkoelen en van grote afstanden in het sterrenstelsel vallen. Door de lange tijdschalen kan de vorming en evolutie van sterrenstelsels dan ook dan niet direct door de mensheid worden bestudeerd. In plaats daarvan maakt men gebruik van het feit dat het licht dat wordt uitgezonden door verre sterrenstelsels naar ons toe reist met de snelheid van het licht en dus tijd nodig heeft om onze telescopen te bereiken. We zien sterrenstelsels nu dus zoals ze eruit zagen in het verleden. Door de uitdijing van het heelal wordt de golflengte van dit licht onderweg langer en het licht daardoor roder. Door precieze metingen van dit effect, dat de *roodverschuiving* wordt genoemd, kan nauwkeurig de afstand tot verre sterrenstelsels worden bepaald en daarmee het tijdstip in het verleden dat ze hun licht uitzonden. Met deze informatie kan de evolutie van sterrenstelsels worden bestudeerd, door de hele populatie van sterrenstelsels op verschillende momenten in het verleden op een statistische manier met elkaar te verbinden en te vergelijken.

Een van de centrale vraagstukken binnen het vakgebied van de vorming en evolutie van sterrenstelsels is waar, wanneer en onder welke omstandigheden de sterren in sterrenstelsels zijn gevormd. Uitgebreide waarneemcampagnes met verschillende telescopen (zoals het *Hubble* Ultra Deep Field), theoretisch ondersteund door grote computersimulaties, hebben hierover heel veel aan het licht gebracht in de afgelopen jaren. Het *gevolg* van de stervorming—de mate waarin sterrenstelsels groeien—is steeds gedetailleerder in kaart gebracht. Daarentegen is kennis van de *oorzaak*—het koude gas dat de brandstof is voor de stervorming—beperkt gebleven. Dit komt omdat koud gas moeilijk te meten is in verre sterrenstelsels. De aanleiding voor dit proefschrift zijn de recente technologische ontwikkelingen, in de vorm van nieuwe telescopen en instrumenten, die het mogelijk maken om het koude gas in verre sterrenstelsels in ongekend detail te meten.

De instrumenten

De eerste telescoop die een belangrijke rol speelt is de *Atacama Large Millimeter/submillimeter Array* (ALMA), die in 2011 in gebruik is genomen. ALMA is een radio-interferometer, die bestaat uit 66 individuele telescopen (antennes) variërend van 7 tot 12 meter in diameter, die samen één gedetailleerd en gevoelig beeld vormen. Deze antennes staan verspreid over het Chajnantor-plateau, op meer dan 5000 meter hoogte in de Atacama woestijn in Chili. Het ongekende formaat van de telescoop in combinatie met het droge klimaat en de hoogte (wat minder verstorende atmosfeer tussen de telescoop en de ruimte betekent) stellen ALMA in staat om het zwakke signaal van koud gas en stof in verre sterrenstelsels te meten; straling die de aarde bereikt met golflengten van iets minder dan een millimeter.

De tweede telescoop is de *Very Large Telescope* (VLT) in Paranal, Chili, en dan specifiek het instrument MUSE (*Multi Unit Spectroscopic Explorer*) dat in 2014 in gebruik is genomen. MUSE is een *integral-field* spectrograaf die het zichtbare licht dat op elke pixel valt uiteen breekt in alle kleuren van de regenboog. Op deze manier kan een driedimensionale opname worden gemaakt (zie voor een voorbeeld Figuur 1.5). Hieruit kunnen kenmerken van het hete gas en het sterlicht kunnen worden gemeten, die gebruikt worden om de eigenschappen van het sterrenstelsel en de roodverschuiving, en dus de afstand, te meten. MUSE is dusdanig efficiënt dat uit de waarnemingen van het *Hubble* Ultra Deep Field tien keer zoveel roodverschuivingen konden worden gemeten dan eerder bekend waren.

Naast *Hubble* en de bovengenoemde telescopen worden in dit proefschrift nog een reeks aan andere telescopen en instrumenten gebruikt. Onder andere de ruimtetelescopen *Chandra*, *Spitzer* en *Herschel*, en nabij-infrarood spectrografen 'op de grond', zoals de *K-band Multi Object Spectrograph* (KMOS) op de VLT en de *Multi-Object Spectrometer For Infra-Red Exploration* (MOSFIRE) op de Keck telescoop in Hawai'i. Samen geven deze instrumenten een vollediger beeld van het licht dat sterrenstelsels uitzenden. Hieruit kunnen vervolgens de eigenschappen van sterrenstelsels worden afgeleid, zoals de totale massa in sterren, de snelheid waarmee nieuwe sterren gevormd worden, de mate waarin het gas verrijkt is met zwaardere elementen (het *metaalgehalte*[52]), en de mogelijke aanwezigheid van een sterk stralingsveld afkomstig van het gas rondom een superzwaar zwart gat. Deze eigenschappen zijn essentieel voor het interpreteren van de metingen aan het koude gas.

---

[52] In de sterrenkunde wordt naar alle elementen zwaarder dan waterstof en helium (de twee elementen die samen > 99% van het kosmische massabudget bevatten) verwezen als 'metalen'. De massafractie van metalen in een bepaalde omgeving wordt het metaalgehalte of de *metalliciteit* genoemd.

Recente resultaten

Onderzoek naar de vorming van sterren in verre sterrenstelsels heeft laten zien dat er 10 miljard jaar geleden ongeveer acht keer meer sterren in het heelal werden gevormd dan vandaag de dag (zie ook Figuur 1.6, dat de kosmische dichtheid van de stervormingssnelheid als een functie van de tijd laat zien). Een belangrijk vraag is wat dit ons leert over het proces van stervorming in sterrenstelsels: was stervorming efficiënter in verre sterrenstelsels in het vroege universum, of hadden ze bijvoorbeeld meer (koud) gas tot hun beschikking?

Voor individuele sterrenstelsels is er een verband waargenomen tussen de totale massa in sterren (alle sterren die tot nu toe gevormd zijn) en het aantal sterren dat nieuw gevormd wordt (de stervormingssnelheid). Dit verband wordt ook wel de *hoofdreeks van stervormende sterrenstelsels* genoemd.[53] Belangrijke vragen in deze context betreffen de oorzaak van dit verband, of het ook stand houdt voor sterrenstelsels met een hele lage massa en in hoeverre dit verband samenhangt met de hoeveelheid gas in sterrenstelsels.

Metingen met ALMA en andere telescopen hebben in de afgelopen jaren steeds meer bewijs verzameld voor een scenario waarin de hoeveelheid gas in stervormende sterrenstelsels groter was in het verleden dan in huidige stelsels. Omdat deze metingen zelfs op de grootste telescopen veel tijd kosten, zijn ze voornamelijk uitgevoerd door het gericht waarnemen van sterrenstelsels die verwacht worden (veel) gas te bevatten op basis van hun (stervormende) eigenschappen. Deze waarnemingen geven daarom een onvolledig beeld van welke stelsels daadwerkelijk het meeste koude gas bevatten en de totale hoeveelheid koud gas in het heelal. Om een vollediger beeld te krijgen zijn metingen nodig van de totale hoeveelheid koud gas in het heelal, of een representatief deel daarvan, tot een voldoende gevoelige limiet.

ALMA Spectroscopic Survey of the Hubble Ultra Deep Field

De *ALMA Spectroscopic Survey of the Hubble Ultra Deep Field* (ASPECS) is een driedimensionaal waarneemprogramma met ALMA, met als doel om de totale hoeveelheid koud gas in het heelal door te tijd heen te meten. Het is het eerste grote waarneemprogramma dat is toegekend aan extragalactische studies en beslaat in totaal 150 uur aan telescooptijd.

Omdat het koude H_2 gas dat betrokken is bij de stervorming zelf geen straling uitzendt moeten andere *tracers* van dit gas worden waargenomen. Een van de beste kandidaten hiervoor is koolstofmonoxide (CO), dat straling uitzendt op specifieke submillimeter golflengten (de zogenaamde rotationele overgangen) die niet worden tegengehouden door de aardse atmosfeer en dus goed waarneembaar zijn met een telescoop (Figuur 1.2). De mate waarin de hogere rotationele energieniveaus van CO aangeslagen worden (de CO *excitatie*) is afhankelijk van de temperatuur en de dichtheid van het gas (Figuur 1.3). De verhouding tussen CO en de totale massa van het koude gas is daarnaast onder andere afhankelijk van het metaalgehalte. Kennis van de eigenschappen van de sterrenstelsels is dus essentieel om hun massa in koud gas te bepalen. Het *Hubble* Ultra Deep Field is om onder andere deze reden uitgekozen als het ideale doelwit voor ASPECS, aangezien het door meeste grote telescopen uitgebreid is (en wordt) bestudeerd.

---

[53] Deze term is afgeleid van de *hoofdreeks* van sterren in het Hertzsprung-Russell diagram die in hun kern waterstof fuseren tot helium; al is deze parallel te betwisten (zie ook voetnoot 11).

ASPECS is zo opgezet dat het een volledige scan van het frequentiebereik uitvoert (in twee verschillende frequentiebanden) en is op deze manier gevoelig voor alle straling van CO in het kosmische volume (zie Figuur 1.7), zonder van te voren specifieke sterrenstelsels uit te kiezen. Het product van de waarnemingen zijn twee *datakubussen*, te zien in Figuur 1.10, met als assen de positie aan de hemel en de frequentie (die zich, via de roodverschuiving, vertaalt tot afstand). Tegelijkertijd geven deze kubussen ook de gevoeligste metingen van het koude stof in verre sterrenstelsels tot nu toe (Figuur 1.8). De analyse van het signaal van het koude gas (en ook het stof) uit deze data, en de conclusies die we hieruit kunnen trekken over het koude gas in verre sterrenstelsels, zijn het onderwerp van dit proefschrift.

Dit proefschrift

Dit proefschrift presenteert een reeks aan studies van het koude gas in verre sterrenstelsels in het *Hubble* Ultra Deep Field, mogelijk gemaakt door gevoelige waarneemprogramma's met MUSE en ALMA, in het bijzonder ASPECS. De hoofdstukken hebben de volgende onderwerpen.

Hoofdstuk 1 bevat de inleiding en achtergrondinformatie bij het proefschrift, en stelt de centrale vraagstelling aan de orde: hoe evolueert het koude interstellair medium van sterrenstelsels met de (kosmische) tijd, in relatie tot hun stervormende eigenschappen, en hoe dicteert dit de evolutie van sterrenstelsels?

Hoofdstuk 2 bestudeert allereerst de 'hoofdreeks' van stervormende sterrenstelsels. Het richt zich specifiek op sterrenstelsels met de laagste massa, die een fundamentele rol spelen in de groei van sterrenstelsels, maar nog niet uitgebreid bestudeerd zijn. Hiervoor gebruiken we nauwkeurig gemeten stervormingssnelheden voor alle sterrenstelsels (tot een bepaalde fluxlimiet) in combinatie met een nieuw-ontwikkeld, Bayesiaans statistisch model om tegelijkertijd de intrinsieke spreiding in de populatie te meten. Het resultaat dat de intrinsieke spreiding van stervormingssnelheden groter is dan voor massievere stelsels, kan verklaard worden door sterkere fluctuaties in de stervormingssnelheid van lage-massa stelsels met de tijd. Daarnaast vinden we een discrepantie met computersimulaties, die erop wijst dat modellen van *feedback* in lage-massa stelsels nog onvolledig zijn.

Hoofdstuk 3 verschuift de focus naar het koude gas. Dit hoofdstuk beantwoordt in zekere zin de meest simpele vraag die men kan stellen bij een waarneemprogramma zoals ASPECS: wat is de aard en wat zijn de fysieke eigenschappen van de sterrenstelsels waarin koud gas (via CO) gedetecteerd word? We identificeren alle emissie als roodverschoven CO lijnen, uitgezonden door koud gas in sterrenstelsels die zichtbaar zijn met *Hubble*. Met behulp van MUSE laten we zien dat de stelsels een gelijkaardig metaalgehalte hebben aan de Zon, wat ons in staat stelt om de CO emissie te vertalen naar de totale massa in koud gas. De resultaten laten zien dat ASPECS het moleculaire gas in de meeste massieve, stervormende sterrenstelsels rond 10 miljard jaar geleden in kaart brengt. De lage stervormingssnelheid van sommige stelsels waarin wel een significant reservoir van koud gas is gemeten laat zien dat eerdere waarnemingen een deel van de gasrijke populatie hebben gemist.

Hoofdstuk 4 bestudeert vervolgens de fysische condities in het koude interstellaire medium van de sterrenstelsels die gedetecteerd zijn door ASPECS, door middel van hun CO excitatie en de emissie van neutraal koolstof en van koud stof. Door de waarnemingen van ALMA te combineren met waarnemingen van de *Very Large Array* (New Mexico, VS), meten en voorspellen we (met behulp van modellen) de gemiddelde excitatie van CO in verschillende overgangen. Voor CO blijkt dat de excitatie, en dus de gemiddelde dichtheid en temperatuur van het koude medium, afneemt met de tijd (toeneemt met roodverschuiving). Tegelijkertijd laten de ASPECS-stelsels een lagere excitatie zien dan eerdere waarnemingen van optisch- en submillimeter-geselecteerde stelsels op vergelijkbare roodverschuiving. Beide fenomenen kunnen worden verklaard door een lagere (oppervlakte)dichtheid van de stervormingssnelheid in deze sterrenstelsels, ten opzichte van eerder waargenomen sterrenstelsels.

Hoofdstuk 5: Voortbouwend op de resultaten van hoofdstukken 3 en 4 komen alle aspecten in dit hoofdstuk samen, waar een inventarisatie en statistische analyse van het signaal van alle emissielijnen in de ASPECS data wordt uitgevoerd. We combineren de noodzakelijke informatie over de roodverschuiving en het metaalgehalte (hoofdstuk 3) met de kennis over de CO excitatie en de condities in het gas (hoofdstuk 4) om de kosmische dichtheid van moleculair gas te bepalen. Het centrale resultaat is dat deze toeneemt met tijd, tot een piek rond 9.5 miljard jaar geleden, en daarna afneemt tot vandaag de dag, vergelijkbaar met de kosmische dichtheid van de stervormingssnelheid. Dit impliceert dat de toename en afname van de kosmische dichtheid van de stervormingssnelheid inderdaad gerelateerd is aan de toename van de hoeveelheid gas in sterrenstelsels, en dat de tijdschaal waarop het gas verbruikt wordt grofweg constant is met roodverschuiving, gemiddeld genomen over de hele populatie van sterrenstelsels.

Hoofdstuk 6: In dit laatste hoofdstuk brengen we ASPECS nog één stap verder. Voor sterrenstelsels die worden gezien op het moment dat het heelal slechts 1.5 à 2 miljard jaar oud is, meet MUSE de roodverschuiving door middel van de Lyman α lijn van waterstof. Deze lijn wordt verstrooid door gas dat uit sterrenstelsels vloeit en kan daardoor licht verschoven zijn ten opzichte van het sterrenstelsel zelf. Door waarnemingen te doen met KMOS en MOSFIRE bepalen we precieze roodverschuivingen voor een deel van deze sterrenstelsels. Deze worden vervolgens gebruikt om het signaal van het koude gas en stof te combineren en zo gemiddeld zwakkere signalen te kunnen meten. De resultaten laten zien dat het gas en stof in deze vroege stelsels zeer moeilijk te detecteren is, omdat het metaalgehalte nog heel laag is. Tot slot worden daarom enkele andere methoden besproken waarmee het gas in deze verre sterrenstelsels kan worden gemeten.

Curriculum Vitae

Lein Adriaan Boogaard was born on January 5th, 1992 in Oegstgeest (The Netherlands). After graduating from the Gymnasium at the Visser 't Hooft Lyceum in Leiden in 2010, with a curriculum focused on science & technology, (classic) languages and music, he spent a year in Holsbybrunn (Sweden), completing the Torchbearers bible school in combination with an outdoor activity program. Returning to Leiden in 2011, he completed his bachelor's degree specifically in Astronomy (Sterrenkunde) at Leiden University in 2014, enjoying the opportunity to observe at the Isaac Newton Telescope in La Palma (Canary Islands). In 2016, he completed the 'research and astronomy' track of the Astronomy master's program in Leiden with honours (*cum laude*), with a specialisation in cosmology. Throughout the years, he has been actively involved in the education program, as a teaching assistant for bachelor's and master's courses, as teacher to dutch high school teachers in physics, and as student tutor.

The research-oriented education program in Leiden provided the opportunity to engage in several research projects, exploring different fields of astronomy (from small to large scales, both observational and theoretical). As part of his bachelor's thesis with Leon Trapman, he studied the gaps in transitional protoplanetary disks using first-cycle, high-frequency, submillimeter observations from the *Atacama Large Millimeter Array* (ALMA), under the supervision of dr. Michiel Hogerheijde. For the first master's thesis, he studied star formation in low-mass galaxies, under the supervision of dr. Jarle Brinchmann, using the first deep-field observations of *Multi Unit Spectroscopic Explorer* (MUSE) instrument on the *Very Large Telescope* (VLT), that had just been commissioned earlier that year, which also led to his involvement in the MUSE GTO team. He completed his master's with a second thesis in the group of prof. Joop Schaye, studying the escape of ionising radiation from simulated galaxies, under the supervision of dr. Joakim Rosdahl, who authored the simulation code (RAMSES-RT) that performed the radiation-hydrodynamics on an adaptive mesh.

In September 2016, he started his doctoral research under the supervision of prof. Paul van der Werf and dr. Rychard Bouwens, studying cold gas in distant galaxies. This work centred around the observations from the newly-awarded large program ASPECS, the ALMA Spectroscopic Survey of the *Hubble* Ultra Deep Field, in combination with spectroscopy from MUSE, KMOS and MOSFIRE, for which he spent time observing at the Very Large Telescope in Paranal (Chile) and at Keck on Hawai'i (USA). He has presented his work at international conferences and during public talks and outreach activities.

Starting March 2021, he will continue his research at the Max-Planck-Institut für Astronomie in Heidelberg (Germany), in the group of dr. Fabian Walter.

Acknowledgements

The completion of this thesis also marks an end of a decade at the Leiden Observatory, which I look back on with great pleasure and gratitude. In closing, I would like to thank a number of people who contributed to this thesis, directly or indirectly, fully aware that one cannot possibly hope to thank everyone who joined for part of the journey.

First and foremost, I would like to thank Paul van der Werf and Rychard Bouwens for their trust, encouragement, and enthusiasm throughout the years; closely involved when needed, while at the same time allowing me develop as an independent scientist and as a person. Being two very different people, I feel fortunate that I was given the opportunity to learn from both of you.

Thanks to Roberto Decarli, Fabian Walter, Manuel Aravena, Chris Carilli, Jorge González-López, Hanae Inami, Melanie Kaasinen, Mladen Novak, Gergö Popping, Dominik Riechers, Ian Smail, Axel Weiß, and all the other members of the ASPECS team for the good times and the great teamwork, with a stimulating atmosphere and many insightful discussions. In particular, I am grateful to Roberto for all his help, his positive attitude, encouragement, and perseverance, especially while dealing with our "expensive noise cubes". Thanks to Roland Bacon and the other members of the MUSE GTO consortium (how can I possibly list you all here?) for making such a pleasant and diverse team. The busy weeks were often a highlight of the year, especially for a starting scientist, and I am grateful for the diverse discussions and for receiving the opportunity to go observing overseas.

I am deeply grateful to Jarle Brinchmann, for being a mentor and an example over the years, and for the way in which he guided me into the world of astronomical research, which played a key role in my decision to become an astronomer. I would also like to thank Joki Rosdahl, for his enthusiasm in supervising my master's thesis and the decision to pursue a PhD. I am grateful to Michael Maseda for taking up the unofficial role of postdoc-mentor when I started my PhD and, together with Corentin Schreiber and Themiya Nanayakkara, for allowing me to share in their experience with optical and near-infrared spectroscopy. I also want to thank the (other) members of *Jarle's Group*, including Mieke Paalvast, David Carton, Madusha Gunawardhana and Bas Zoutendijk, for the weekly discussions and for allowing me to stick around at them, even when my work was driving me toward the colder phases of the interstellar medium.

In later years, I greatly enjoyed meetings and discussions with Kirsty Butler, Matus Rybak, Hiddo Algera, Dieuwertje van der Vlucht, Marta Frias, Cristina García, Sarah Leslie, Sander Schouws, and the other *Dust Mites* from the combined groups of Jacqueline Hodge, Serena

Viti, Rychard Bouwens and Paul van der Werf. I want to thank Kirsty, Matus, and Themiya for a great time in the office and for making it a lively place; thanks for the latter should certainly also be extended to the occasional fifth office mate, who actually occupied an office across the hallway. I enjoyed many insightful discussions with a number of colleagues at the observatory, including those attending the weekly *Galaxies Journal Club*, of which not yet mentioned: Marijn Franx, Joop Schaye, Stijn Debackere, Anna de Graaff, Jorryt Matthee, and Mauro Stefanon, as well as a number of international colleagues. Certainly not to be forgotten are the many teachers that I enjoyed over the years, as well as the computergroup and essential support staff, who give true meaning to the word *support*, in being indispensable to uphold the observatory and its facilities. I would like to acknowledge the Leids Kerhoven-Bosscha Fonds for supporting this work financially.

Tot slot wil ik een aantal mensen noemen waarvan de bijdrage aan dit proefschrift misschien minder direct te duiden is, maar daarom niet minder belangrijk. Hierbij denk ik in de eerste plaats aan de onmisbare steun van mijn familie, schoonfamilie en vrienden.

De groep studievrienden van het eerste uur sterrenkunde, waaronder Leon Trapman, Stijn Debackere, David Doelman, Kasper van Dam, Steven Bos en Bavo Croiset, wil ik bedanken voor de goede tijden binnen en buiten de collegezaal, en binnen en buiten de landsgrenzen; hierbij noem ik ook de groep van de elfde verdieping. Leon, wie had kunnen vermoeden dat één bachelorscriptie zou leiden tot twee zo diverse proefschriften? Arjen Wiersma ben ik dankbaar voor een verrijkend jaar in Zweden (voor ik aan mijn opleiding sterrenkunde begon) en voor het ontwerpen van de kaft van dit proefschrift. Ik ben dankbaar voor goede gesprekken met vrienden uit de studententijd en in de NGK Oegstgeest. De VROLIKE vrienden wil ik bedanken voor alle mooie momenten, niet alleen tijdens een spelletje. De Changin' Keys ben ik dankbaar voor de muzikale ontspanning. Ik hecht bijzonder veel waarde aan de bijeenkomsten en onderlinge vriendschappen van de mannen van Axios. Tante Jeanne ben ik dankbaar voor de korte schrijfretraite om dit voltooiing van proefschrift het laatste zetje te geven en, samen met Oom Bert, voor zo veel meer.

Het voelt als een voorrecht dat André van Delft en Pierre Schwering mij als paranimfen terzijde willen staan bij de verdediging. André, dank voor de vriendschap en de verwondering, ook wat betreft onze vele gedeelde interesses. Pierre, uit alle goede herinneringen staat me nog helder voor ogen dat ik voor het eerst de manen van Jupiter zag, door een telescoop op het dak van jullie huis. Wat had ik toen graag begrepen wat het betekent dat jouw vader, Piet Schwering, jaren geleden bij dezelfde Sterrewacht zijn proefschrift schreef.

Niet in de laatste plaats gaan mijn gedachten liefdevol uit naar mijn zusje en broertje, en naar mijn ouders, die mij van jongs af hebben gestimuleerd om op onderzoek uit te gaan en op eigen benen te staan, en alle kansen hebben gegeven om mijn dromen na te volgen.

Tot slot wil ik Elisabeth noemen, zonder wier liefdevolle steun en eindeloze geduld dit proefschrift waarschijnlijk nooit was afgekomen. Dank voor alles wat je me gegeven hebt, ook als de rest van het universum meer tijd van mij vroeg dan waar het recht op had. Marie, jij laat zien wat in het leven echt belangrijk is. Het heelal is groot, maar de liefde is groter.

Ten slotte, schenk aandacht aan alles wat waar is,
alles wat edel is, alles wat rechtvaardig is,
alles wat zuiver is, alles wat lieflijk is, alles wat eervol is,
kortom, aan alles wat deugdzaam is en lof verdient.

Filippenzen 4: 8